MOUNTAIN-PLAINS CONSORTIUM

MPC 20-413 | J.W. McRory, F.F. Pozo-Lora, Z. Benson and M. Maguire

Structural Fiber Reinforcement to Reduce Deck Reinforcement and Improve Long-Term Performance

MOUNTAIN-PLAINS CONSORTIUM REGION 8

A University Transportation Center sponsored by the U.S. Department of Transportation serving the Mountain-Plains Region. Consortium members:

Colorado State University
North Dakota State University
South Dakota State University
University of Colorado Denver
University of Denver
University of Utah
Utah State University
University of Wyoming

Technical Report Documentation Page

1. Report No.	2. Government Accession No.	3. Recipient's Catalog No.
MPC-581		

4. Title and Subtitle	5. Report Date
Structural Fiber Reinforcement to Reduce Deck Reinforcement and Improve Long-Term Performance	June 2020
	6. Performing Organization Code

7. Author(s)	8. Performing Organization Report No.
Jared W. McRory Fray F. Pozo-Lora Zachary Benson Marc Maguire	MPC 20-413

9. Performing Organization Name and Address	10. Work Unit No. (TRAIS)
Utah State University 4110 Old Main Hill Logan, UT 84322-4110	11. Contract or Grant No.

12. Sponsoring Agency Name and Address	13. Type of Report and Period Covered
Mountain-Plains Consortium North Dakota State University PO Box 6050, Fargo, ND 58108	Final Report
	14. Sponsoring Agency Code

15. Supplementary Notes

Supported by a grant from the US DOT, University Transportation Centers Program

16. Abstract

The use of deicing salts on highway bridges has decreased the service life of bridge decks due to the accelerated corrosion of the steel reinforcement. The use of Glass Fiber Reinforced Polymer (GFRP) in bridge decks as a means of corrosion-mitigation has been met with some success; however, GFRP is a linear-elastic material that does not exhibit any plastic behavior prior to rupture. This current work provides a description of an experiment conducted on 14 full-scale 4'x12' flexural bridge deck specimens and six full-scale14'x12' punching shear specimens. The decks contained steel-reinforcement, GFRP-reinforcement, or discrete GFRP-reinforcement combined with alkali-resistant fiberglass composite macrofibers.

The investigation consisted of two parts: the static testing and the cyclic and post-cyclic testing. The cyclic specimens experienced either 1 or 2 million cycles at the service level. The HRC decks exhibited more flexural ductility prior to the rupture of the concrete than both the steel- and GFRP-reinforced deck panels. Under fatigue loading, all of the decks performed within the AASHTO criteria for service level crack width and deflections. Therefore, based on the results, the HRC reinforcement strategy is viable for both ultimate and service limit states.

17. Key Word	18. Distribution Statement
bridge decks, cracking, fiber reinforced concrete, performance, reinforced concrete bridges, structural materials	Public distribution

19. Security Classif. (of this report)	20. Security Classif. (of this page)	21. No. of Pages	22. Price
Unclassified	Unclassified	218	n/a

Form DOT F 1700.7 (8-72) Reproduction of completed page authorized

STRUCTURAL FIBER REINFORCEMENT TO REDUCE DECK REINFORCEMENT AND IMPROVE LONG-TERM PERFORMANCE

by

Jared W. McRory
Fray F. Pozo-Lora
Zachary Benson
Marc Maguire, Ph.D.

Utah State University
Logan, Utah

June 2020

Acknowledgements

Special thanks go to those at the Mountain-Plains Consortium (MPC) as well as Owens Corning for their help throughout this project. A special thanks also goes to goes to Alvin Ericson at ReforceTech, Matt Offenberg, Ryan Koch and Doug Gremel at Owens Corning, and Robert Slade and Roy Eriksson at Eriksson Technologies for their help throughout this project. Thanks also go to Dr. Andrew Sorensen, Taylor Sorensen, Ony Al-Sarfin, Nick Markosian, Nick Langford, and other professors or graduate students at Utah State University who donated their time and resources to assist in this project.

Numerous undergraduate students also helped cast, test, and dispose of the specimens from this experiment, including Colby Bench, Tyler Daniels, Quinn Lythgoe, Nathan Raine, Ethan Schow, Jacob Leatham, and others. Without the help of these individuals, this project would never have happened. Many others helped with this project, and the authors would like to thank all who supported and aided in any way.

Disclaimer

The contents of this report reflect the views of the authors, who are responsible for the facts and the accuracy of the information presented. This document is disseminated under the sponsorship of the Department of Transportation, University Transportation Centers Program, in the interest of information exchange. The U.S. Government assumes no liability for the contents or use thereof.

ABSTRACT

The use of deicing salts on highway bridges has decreased the service life of bridge decks due to the accelerated corrosion of the steel reinforcement. The use of Glass Fiber Reinforced Polymer (GFRP) in bridge decks as a means of corrosion-mitigation has been met with some success; however, GFRP is a linear-elastic material that does not exhibit any plastic behavior prior to rupture. This current work provides a description of an experiment conducted on 14 full-scale 4’ x 12’ flexural bridge deck specimens and six full-scale 14’ x 12’ punching shear specimens. The decks contained steel-reinforcement, GFRP-reinforcement, or discrete GFRP-reinforcement combined with alkali-resistant fiberglass composite macrofibers.

The investigation consisted of two parts: static testing and the cyclic and post-cyclic testing. The cyclic specimens experienced either one or two million cycles at the service level. The HRC decks exhibited more flexural ductility prior to the rupture of the concrete than both the steel- and GFRP-reinforced deck panels. Under fatigue loading, every deck performed within the AASHTO criteria for service level crack width and deflections. Therefore, based on the results, the HRC reinforcement strategy is viable for both ultimate and service limit states.

TABLE OF CONTENTS

1. INTRODUCTION 1

1.1 Overview 1

1.2 Objective 1

1.3 Outline 2

2. LITERATURE REVIEW 3

2.1 Historical Background 3

2.1.1 Applications of FRP in Bridge Decks 3

2.1.2 Applications of Fiber-Reinforced Concrete in Bridge Decks 4

2.2 Durability 5

2.2.1 Durability of Steel 5

2.2.2 Durability of GFRP 6

2.3 Flexural Response 8

2.3.1 Flexural Design of Bridge Decks 8

2.3.2 GFRP Flexure 9

2.3.3 Fiber-Reinforced Concrete Flexure 11

2.3.4 Combined GFRP and FRC Considerations 14

2.4 Fatigue Response 15

2.4.1 Concrete Fatigue Background 15

2.4.2 FRP Fatigue 20

2.4.3 FRC Fatigue 24

2.5 Punching Shear Behavior 26

2.5.1 Steel Reinforced Punching Shear 26

2.5.2 GFRP Reinforced Punching Shear 27

2.5.3 FRC Punching Shear 30

2.6 Literature Summary 31

3. EXPERIMENTAL PROGRAM − FLEXURE 33

3.1 Introduction 33

3.2 Material Information and Testing Standards 33

3.2.1 Steel Rebar 33

3.2.2 GFRP Rebar 35

3.2.3 Concrete Mix Properties 36

3.2.4 Concrete Mechanical Properties 40

3.3 Flexural Bridge Deck Panels 44
3.3.1 Panel Design and Fabrication 44
3.3.2 Static Loading 48
3.3.3 Fatigue Loading 52
4. EXPERIMENTAL PROGRAM – PUNCHING SHEAR 56
4.1 Introduction 56
4.2 Concrete Mix Properties 56
4.3 Punching Shear Deck Panels 58
4.3.1 Panel Design and Fabrication 58
4.3.2 Static Testing 63
4.3.3 Fatigue Testing 67
5. EXPERIMENTAL RESULTS − FLEXURE 69
5.1 Introduction 69
5.2 Materials Testing 69
5.3 Static Testing Results 79
5.4 Fatigue Testing Results 84
5.5 Post-Fatigue Static Testing Results 97
6. EXPERIMENTAL RESULTS − PUNCHING SHEAR 106
6.1 Introduction 106
6.2 Materials Testing 106
6.3 Static Testing Results 110
6.4 Fatigue Testing Results 111
6.5 Post-Fatigue Static Testing Results 113
7. DISCUSSION – FLEXURAL DECKS 115
7.1 Introduction 115
7.2 Material Models 115
7.2.1 Steel Reinforcement 115
7.2.2 GFRP Reinforcement 118
7.2.3 Plain Concrete 119
7.2.4 FRC 123
7.3 Service Limit State 124
7.3.1 Deflection 124
7.3.2 Crack Width 127

7.4 Strength Limit State 128
7.4.1 Deflection 128
7.4.2 Moment Capacity 129
8. DISCUSSION − PUNCHING SHEAR 141
8.1 Introduction 141
8.2 Static Testing 141
8.3 Fatigue Testing 149
8.4 Post-Fatigue Testing 149
9. CONCLUSIONS 160
REFERENCES 163
APPENDIX A. BRIDGE DECK DESIGNS AND FATIGUE LOADING 172
APPENDIX B. MOMENT CURVATURE PROGRAM SCRIPT 199
APPENDIX C. PRELIMINARY COST ANALYSIS 204

LIST OF TABLES

Table 2.2.1 FRP Environmental Reduction Factors (ACI Committee 440, 2015) 8
Table 2.2.2 FRP Long-Term Stress Reductions (ACI Committee 440, 2015) 8
Table 2.3.1 Equivalent Strips – Adapted from Table 4.6.2.1.3-1 (AASHTO, 2018c) 9
Table 2.3.2 Comparison of FRC test procedures 13
Table 3.2.1 Cem-FIL MiniBars™ properties and behavior 37
Table 3.2.2 Design mix specifications for 5 ksi (34.5 MPa) mix 38
Table 3.2.3 Steel-reinforced concrete mix design 38
Table 3.2.4 GFRP-reinforced concrete mix design 39
Table 3.2.5 HRC mix design set #1 39
Table 3.2.6 HRC mix design set #2 40
Table 3.2.7 Water/cement ratio of the different mixes 40
Table 3.3.1 Reinforcement summary 45
Table 4.2.1 Mix design punching shear steel 56
Table 4.2.2 Mix design punching shear GFRP 57
Table 4.2.3 Mix design punching shear FRC 57
Table 4.2.4 w/c Ratio punching shear mixes 58
Table 4.3.1 Reinforcement layout 58
Table 5.2.1 Steel rebar testing results 70
Table 5.2.2 GFRP rebar testing results 71
Table 5.2.3 Concrete compression testing results 72
Table 5.2.4 Concrete static modulus testing results 72
Table 5.2.5 Concrete splitting tensile strength results 72
Table 5.2.6 HRC residual flexural tensile stress results 79
Table 5.3.1 Maximum moments and deflections at failure for static flexure decks 84
Table 5.4.1 Peak deflection values 97
Table 5.4.2 Peak crack width values 97
Table 5.4.3 Live load deflection values 97
Table 5.4.4 Live load crack opening values 97
Table 5.5.1 Maximum moments and deflections at failure for post-fatigue flexure 102
Table 6.2.1 Compressive strengths of punching shear concrete 106
Table 6.2.2 Modulus of elasticity of punching shear concrete 106
Table 6.2.3 Splitting tensile strength of punching shear concrete 106
Table 6.2.4 Residual flexural tensile stresses in punching shear FRC 110

Table 6.3.1 Maximum force and deflections for punching shear decks 111
Table 6.5.1 Maximum forces and deflections for post-fatigue punching shear decks 114
Table 7.3.1 Adequacy of bridge decks for live load deflection 127
Table 7.3.2 Adequacy of bridge decks for crack width 128
Table 7.4.1 Bridge deck deflection at failure 128
Table 7.4.2 Actual moment vs predicted moment for each specimen 135
Table 8.2.1 Bottom surface punching dimensions and shear angle 147
Table 8.2.2 Punching shear prediction models for static tests 148
Table 8.2.3 HRC prediction models without fiber contribution 149
Table 8.4.1 Bottom surface punching shear dimensions and shear angle (post-fatigue) 155
Table 8.4.2 Punching shear prediction models for post-fatigue static tests 156
Table 8.4.3 HRC punching shear predictions without fiber contribution (post-fatigue) 157
Table 8.4.4 Punching shear force and deflection comparisons before and after fatigue 159
Table C-1 Unit costs of reinforcing materials 204
Table C-2 Cost per square foot for each reinforcement scheme 204

LIST OF FIGURES

Figure 2.1.1 Steel-free bridge decks (Memon, 2005) 4
Figure 2.1.2 Second-generation steel-free bridge decks (Memon, 2005) 5
Figure 2.3.1 Resistance factor of FRP-reinforced concrete (ACI Committee 440, 2015) 11
Figure 2.3.2 ASTM C1609 test setup (ACI Committee 544, 2018) 12
Figure 2.3.3 EN 14651 beam setup (EN 14651, 2005) 12
Figure 2.3.4 FRC constitutive models from fib Model Code (CEB-FIB, 2013) 14
Figure 2.4.1 Stiffness degradation under cyclic compression, (Van Ornum, 1903) 16
Figure 2.4.2 S-N curve for varying stress ranges (John W Murdock & Kesler, 1958) 17
Figure 2.4.3 Cracking developed due to moving load, (Sonoda & Horikawa, 1982) 19
Figure 2.4.4 FRP fatigue specimen to prevent gripping damage, (Adimi et al., 2000) 20
Figure 2.4.5 Typical geometry and load cases, (Yost et al., 2015) 23
Figure 2.4.6 Static and fatigue setup, (Gopalaratnam et al., 2006) 25
Figure 3.2.1 Steel rebar tensile test setup 34
Figure 3.2.2 Necked region 34
Figure 3.2.3 Using a jig to keep GFRP bars vertical 35
Figure 3.2.4 GFRP tensile test setup 35
Figure 3.2.5 GFRP at rupture initiation 36
Figure 3.2.6 Fully ruptured GFRP specimen 36
Figure 3.2.7 Macrofibers used in this experiment 37
Figure 3.2.8 Adding fibers through a grate to prevent clumping 37
Figure 3.2.9 Compression test of an FRC cylinder 41
Figure 3.2.10 Crack opening displacement transducer 42
Figure 3.2.11 Specified pattern to fill up molds (EN 14651, 2005) 42
Figure 3.2.12 Filling up the mini beam molds 42
Figure 3.2.13 Saw used to notch FRC specimens 43
Figure 3.2.14 FRC mini beam test setup 44
Figure 3.2.15 Failed FRC specimen 44
Figure 3.3.1 Equivalent strip method – wheel load distribution 45
Figure 3.3.2 Steel reinforcement layout 46
Figure 3.3.3 GFRP reinforcement layout 46
Figure 3.3.4 HRC reinforcement layout 46
Figure 3.3.5 Internal vibration of deck panels 47
Figure 3.3.6 Steel-reinforced decks prior to pouring 48
Figure 3.3.7 Laying moist burlap on the panels 48
Figure 3.3.8 Pin support condition 49
Figure 3.3.9 Roller support condition (Spreader Beam) 49
Figure 3.3.10 Static flexure test setup 50
Figure 3.3.12 Static test setup (steel-reinforced deck) 51
Figure 3.3.13 Static test with centerline loading (GFRP deck) 51
Figure 3.3.14 Fatigue test setup 53
Figure 3.3.15 Fatigue test setup 2 53
Figure 3.3.16 Measuring deflections with potentiometer 54

Figure 3.3.17 LVDT spanning crack at bottom level of deck 54
Figure 3.3.18 Static test after fatigue loading 55
Figure 4.3.1 Adding the fibers at the batch plant 59
Figure 4.3.2 Steel punching shear deck prior to pouring 59
Figure 4.3.3 Pouring the steel punching shear deck with concrete hopper 60
Figure 4.3.4 Close-up of GFRP reinforcement on chairs prior to pouring 60
Figure 4.3.5 Pouring the GFRP punching shear decks 61
Figure 4.3.6 HRC punching shear decks before casting 61
Figure 4.3.7 HRC decks being poured with internal vibration 62
Figure 4.3.8 Finished GFRP punching shear deck 63
Figure 4.3.9 Curing the punching shear decks 63
Figure 4.3.10 Punching shear static test setup 64
Figure 4.3.11 Punching shear deck supports 65
Figure 4.3.12 Steel punching shear deck static test setup 65
Figure 4.3.13 GFRP punching shear static test setup 66
Figure 4.3.14 HRC punching shear static test setup 66
Figure 4.3.15 Fatigue test setup 67
Figure 4.3.16 Fatigue test setup 2 68
Figure 4.3.17 Fatigue test setup 3 68
Figure 5.2.1 Stress-strain curve for steel rebar (Imperial) 69
Figure 5.2.2 Stress-strain curve for steel rebar (SI) 70
Figure 5.2.3 Stress-strain curve for GFRP (Imperial) 71
Figure 5.2.4 Stress-strain curve for GFRP (SI) 71
Figure 5.2.5 Force-CMOD curve HRC set #1 (Imperial) 73
Figure 5.2.6 Force-CMOD curve HRC set #2 (SI) 73
Figure 5.2.7 Stress-CMOD curve HRC set #1 (Imperial) 74
Figure 5.2.8 Stress-CMOD curve HRC Set #1 (SI) 74
Figure 5.2.9 Average flexural tensile strength HRC set #1 (Imperial) 75
Figure 5.2.10 Average flexural tensile strength HRC set #1 (SI) 75
Figure 5.2.11 Force-CMOD curve HRC set #2 (Imperial) 76
Figure 5.2.12 Force-CMOD curve HRC set #2 (SI) 76
Figure 5.2.13 Stress-CMOD curve HRC set #2 (Imperial) 77
Figure 5.2.14 Stress-CMOD curve HRC set #2 (SI) 77
Figure 5.2.15 Average flexural tensile strength HRC set #2 (Imperial) 78
Figure 5.2.16 Average flexural tensile strength HRC Set #2 (SI) 78
Figure 5.3.1 Moment-deflection curves for steel-reinforced decks (Imperial) 80
Figure 5.3.2 Moment-deflection curves for steel-reinforced decks (SI) 80
Figure 5.3.3 Moment-deflection curves for GFRP-reinforced decks (Imperial) 81
Figure 5.3.4 Moment-deflection curves for GFRP-reinforced decks (SI) 81
Figure 5.3.5 Moment-deflection curves for HRC decks (Imperial) 82
Figure 5.3.6 Moment-deflection curves for HRC decks (SI) 82
Figure 5.3.7 Moment-deflection curves for all bridge decks (Imperial) 83
Figure 5.3.8 Moment-deflection curves for all bridge decks (SI) 83
Figure 5.4.1 Peak deflection vs. No. of cycles for 1 million cycles (Imperial) 85

Figure 5.4.2 Peak deflection vs. No. of cycles for 1 million cycles (SI) 85
Figure 5.4.3 Peak crack width vs. No. of cycles for 1 million cycles (Imperial) 86
Figure 5.4.4 Peak crack width vs. No. of cycles for 1 million cycles (SI) 86
Figure 5.4.5 Live load deflection vs. No. of cycles for 1 million cycles (Imperial) 87
Figure 5.4.6 Live load crack opening vs. No. of cycles for 1 million cycles (SI) 87
Figure 5.4.7 Live load crack opening vs. No. of cycles for 1 million cycles (Imperial) 88
Figure 5.4.8 Live load crack opening vs. No. of cycles for 1 million cycles (SI) 88
Figure 5.4.9 Peak deflection vs. No. of cycles for 2 million cycles (Imperial) 89
Figure 5.4.10 Peak deflection vs. No. of cycles for 2 million cycles (SI) 89
Figure 5.4.11 Peak crack width vs. No. of cycles for 2 million cycles (Imperial) 90
Figure 5.4.12 Peak crack width vs. No. of cycles for 2 million cycles (SI) 90
Figure 5.4.13 Live load deflection vs. No. of cycles for 2 million cycles (Imperial) 91
Figure 5.4.14 Live load deflection vs. No. of cycles for 2 million cycles (SI) 91
Figure 5.4.15 Live load crack opening vs. No. of cycles for 2 million cycles (Imperial) 92
Figure 5.4.16 Live load crack opening vs. No. of cycles for 2 million cycles (SI) 92
Figure 5.4.17 Peak deflection vs. No. of cycles – combined (Imperial) 93
Figure 5.4.18 Peak deflection vs. No. of cycles – combined (SI) 93
Figure 5.4.19 Peak crack opening vs. No. of cycles – combined (Imperial) 94
Figure 5.4.20 Peak crack opening vs. No. of cycles – combined (SI) 94
Figure 5.4.21 Live load deflection vs. No. of cycles – combined (Imperial) 95
Figure 5.4.22 Live load deflection vs. No. of cycles – combined (SI) 95
Figure 5.4.23 Live load crack opening vs. No. of cycles – Combined (Imperial) 96
Figure 5.4.24 Live load crack opening vs. No. of cycles – Combined (SI) 96
Figure 5.5.1 Moment-deflection response for post-fatigue steel decks (Imperial) 98
Figure 5.5.2 Moment-deflection response for post-fatigue steel decks (SI) 98
Figure 5.5.3 Moment-deflection response for post-fatigue HRC decks (Imperial) 99
Figure 5.5.4 Moment-deflection response for post-fatigue HRC decks (SI) 99
Figure 5.5.5 Moment-deflection response for post-fatigue GFRP decks (Imperial) 100
Figure 5.5.6 Moment-deflection response for post-fatigue GFRP decks (SI) 100
Figure 5.5.7 Moment-deflection response for post-fatigue decks (Imperial) 101
Figure 5.5.8 Moment-deflection response for post-fatigue decks (SI) 101
Figure 5.5.9 Moment-deflection before and after fatigue – steel (Imperial) 103
Figure 5.5.10 Moment-deflection before and after fatigue – steel (SI) 103
Figure 5.5.11 Moment-deflection before and after fatigue – GFRP (Imperial) 104
Figure 5.5.12 Moment-deflection before and after fatigue – GFRP (SI) 104
Figure 5.5.13 Moment-deflection before and after fatigue – HRC (Imperial) 105
Figure 5.5.14 Moment-deflection before and after fatigue – HRC (SI) 105
Figure 6.2.2 Force-CMOD curve HRC punching shear (SI) 107
Figure 6.2.3 Stress-CMOD curve HRC punching shear (Imperial) 108
Figure 6.2.4 Stress-CMOD curve HRC punching shear (SI) 108
Figure 6.2.5 Average flexural tensile strength HRC punching shear (Imperial) 109
Figure 6.2.6 Average flexural tensile strength HRC punching shear (SI) 109
Figure 6.3.1 Force-deflection curves for punching shear decks (Imperial) 110
Figure 6.3.2 Force-deflection curves for punching shear decks (SI) 111

Figure 6.4.1 Actuator deflection for punching shear fatigue decks (Imperial) 112
Figure 6.4.2 Actuator deflection for punching shear fatigue decks (SI) 112
Figure 6.5.1 Force-deflection for post-fatigue punching shear decks (Imperial) 113
Figure 6.5.2 Force-deflection for post-fatigue punching shear decks (SI) 113
Figure 7.2.1 Steel stress-strain constitutive relationship (Imperial) 117
Figure 7.2.2 Steel stress-strain constitutive relationship (SI) 117
Figure 7.2.3 GFRP stress-strain constitutive relationship (Imperial) 118
Figure 7.2.4 GFRP stress-strain constitutive relationship (SI) 119
Figure 7.2.5 Hognestad relationship (adapted from Hognestad, 1951) 120
Figure 7.2.6 Concrete compressive stress-strain constitutive relationship (Imperial) 121
Figure 7.2.7 Concrete compressive stress-strain constitutive relationship (SI) 121
Figure 7.2.8 Concrete in tension stress-strain constitutive relationship (Imperial) 122
Figure 7.2.9 Concrete in tension stress-strain constitutive relationship (SI) 123
Figure 7.2.10 FRC in tension stress strain constitutive relationship 124
Figure 7.3.1 Simply supported beam - 4-point flexure (adapted - AISC Manual 2017) 125
Figure 7.3.2 Live load deflection – fatigue loading 126
Figure 7.3.3 Live load deflection – normalized by E_c 126
Figure 7.4.1 Moment curvature program flow chart 130
Figure 7.4.2 Steel moment-curvature relationship before fatigue 131
Figure 7.4.3 GFRP moment-curvature relationship before fatigue 131
Figure 7.4.4 HRC set #1 moment-curvature relationship before fatigue 132
Figure 7.4.5 HRC set #2 moment-curvature relationship before fatigue 132
Figure 7.4.6 Steel moment-curvature relationship after fatigue 133
Figure 7.4.7 GFRP moment-curvature relationship after fatigue 133
Figure 7.4.8 HRC set #1 moment-curvature relationship after fatigue 134
Figure 7.4.9 HRC set #2 moment-curvature relationship after fatigue 134
Figure 7.4.10 Shear failure on first GFRP specimen 136
Figure 7.4.11 HRC failure after 2 million cycles 136
Figure 7.4.12 Bond failure on GFRP deck post-fatigue 137
Figure 7.4.13 Side view of 1 million cycle GFRP specimen at failure 137
Figure 7.4.14 Bottom view of GFRP specimen after failure 138
Figure 7.4.15 Steel deck at failure 139
Figure 7.4.16 GFRP deck at failure 139
Figure 7.4.17 HRC deck at failure 139
Figure 8.2.1 Force-deflection of punching shear decks (Imperial) 142
Figure 8.2.2 Force-deflection of punching shear decks (SI) 142
Figure 8.2.3 Normalized force-deflection of punching shear decks (Imperial) 143
Figure 8.2.4 Normalized force-deflection of punching shear decks (SI) 143
Figure 8.2.5 Top of steel punching shear deck 144
Figure 8.2.6 Top of GFRP punching shear deck 145
Figure 8.2.7 Top of HRC punching shear deck 145
Figure 8.2.8 Shear rupture of GFRP bar 146
Figure 8.2.9 Bottom surface of steel punching shear deck 146
Figure 8.2.10 Bottom surface of GFRP punching shear deck 147

Figure 8.2.11 Bottom surface of HRC punching shear deck 147
Figure 8.4.1 Force-deflection of punching shear decks after fatigue (Imperial)..... 151
Figure 8.4.2 Force-deflection of punching shear decks after fatigue (SI)..... 151
Figure 8.4.3 Normalized force-deflection of punching shear decks after fatigue (Imperial)..... 152
Figure 8.4.4 Normalized force-deflection of punching shear decks after fatigue (SI)..... 152
Figure 8.4.5 Top of steel post-fatigue punching shear deck 153
Figure 8.4.6 Top of GFRP post-fatigue punching shear deck..... 153
Figure 8.4.7 Top of HRC post-fatigue punching shear deck 154
Figure 8.4.8 Bottom of steel post-fatigue punching shear deck..... 154
Figure 8.4.9 Bottom of GFRP post-fatigue punching shear deck 155
Figure 8.4.10 Bottom of HRC post-fatigue punching shear deck..... 155
Figure 8.4.11 Force-deflection for punching shear decks before and after fatigue (Imperial) 158
Figure 8.4.12 Force-deflection for punching shear decks before and after fatigue (SI) 158
Figure B-1 Introduction page of moment-curvature program..... 199
Figure B-2 Sectional input 199
Figure B-3 Steel reinforced moment-curvature analysis 200
Figure B-4 GFRP reinforced moment-curvature analysis 200
Figure B-5 HRC moment-curvature analysis..... 201

EXECUTIVE SUMMARY

In 2017, the American Society of Civil Engineers (ASCE) stated that 9.1% of bridges in the United States are structurally deficient with total repair costs of approximately $123 billion (American Society of Civil Engineers, 2017). Koch et al. (2002) determined the annual direct costs of steel corrosion in bridge decks is $2 billion.

The corrosion of bridge deck reinforcement is an expected phenomenon due to the cracking that develops in the decks (Krauss & Rogalla, 1996). This behavior is amplified by the ingression of chlorides from deicing salts placed on roadways during severe environmental conditions. As the steel corrodes, it expands to a volume of about 1.8 to 6.4 times greater than the original non-oxidized reinforcement (Bhargava, Ghosh, Mori, & Ramanujam, 2006; Lundgren, 2002; Zhao, Ren, Dai, & Jin, 2011). This expansion induces tensile stresses that can result in surface spalling or cover delamination, requiring regular maintenance by way of patches, sealants, or complete deck replacement.

Full bridge deck replacements are almost always necessary prior to the service life of a bridge, with the majority of the DOTs stating in a 2009 NCHRP survey that the service life of a reinforced concrete bridge deck falls between 15 and 50 years with an average of about 30 years (Krauss, Lawler, & Steiner, 2009). Although no specific service life is detailed within the AASHTO specifications, a design life of 75 years was used to calibrate the specifications (AASHTO, 2018c). This is a minimum, however, and there is an initiative to extend this to greater than 100 years (Kulicki et al., 2015).

The use of glass fiber reinforced polymer (GFRP) in bridge decks as a means of corrosion mitigation has been met with some success; however, GFRP is a linear-elastic material that does not exhibit any plastic behavior prior to rupture. Although most bridge decks will only experience service loads with any level of frequency, this lack of ductility would equate to a brittle failure at the ultimate limit state.

This current work provides a description of an experiment conducted on 14 full-scale 4’ x 12’ flexural bridge deck specimens and six full-scale 14’ x 12’ punching shear deck specimens utilizing different reinforcement strategies. The decks contained steel-reinforcement, GFRP-reinforcement, or discrete GFRP-reinforcement combined with alkali-resistant macrofibers. The addition of the macrofibers with GFRP bars, or hybrid reinforced concrete (HRC), was an attempt at improving ductility in the otherwise brittle GFRP-reinforced decks. Preliminary cost analysis suggests that the HRC decks are cost neutral to epoxy coated rebar decks.

The investigation consisted of two parts: the static and cyclic testing of flexural specimens and the static and cyclic testing of flexural specimens. The cyclic specimens experienced either one or two million cycles at the service level loads, and these were subsequently tested monotonically to obtain the post-fatigue behavior.

The experimental results were compared with predictive models based on the constitutive relationships of each material with good agreement. A simple model under-predicts the flexural behavior by an average of 9%, while a more sophisticated moment curvature model is shown to over-predict the behavior by an average of 5%.

The HRC decks exhibited 29% and 119% more flexural ductility prior to the rupture of the concrete than the GFRP- and steel-reinforced deck panels, respectively. Under fatigue loading, all the decks performed within the AASHTO criteria for service level crack width and deflections. Therefore, based on the results, the HRC reinforcement strategy is viable for both ultimate and service limit states.

1. INTRODUCTION

1.1 Overview

In 2017, the American Society of Civil Engineers (ASCE) stated that 9.1% of bridges in the United States of America are structurally deficient with total repair costs of approximately $123 billion (American Society of Civil Engineers, 2017). Koch et al. (2002) determined that the annual direct costs of steel corrosion in bridge decks is $2 billion.

The corrosion of bridge deck reinforcement is an expected phenomenon due to the cracking that develops in the decks (Krauss & Rogalla, 1996). This behavior is amplified by the ingression of chlorides from deicing salts placed on roadways during severe environmental conditions. As the steel corrodes, it expands to a volume of about 1.8 to 6.4 times greater than the original non-oxidized reinforcement (Bhargava et al., 2006; Lundgren, 2002; Zhao et al., 2011). This expansion induces tensile stresses that can result in surface spalling or cover delamination, requiring regular maintenance by way of patches, sealants, or complete deck replacement.

Full bridge deck replacements are almost always necessary prior to the service life of a bridge, with the majority of the DOTs stating in a 2009 NCHRP survey that the service life of a reinforced concrete bridge deck falls between 15 and 50 years with an average of about 30 years (Krauss et al., 2009). Although no specific service life is detailed within the AASHTO specifications, a design life of 75 years was used to calibrate the specifications (AASHTO, 2018c). This is a minimum, however, and there is an initiative to extend this to greater than 100 years (Kulicki et al., 2015).

Several ideas have been studied and implemented to provide a longer service life in bridge decks to reduce life-cycle costs. Epoxy coated rebar has been the standard solution to corrosion mitigation since the 1970s, but several studies have shown that, although the coating helps, it does not solve the problem since corrosion still occurs (Frosch, Labi, & Sim, 2014; Kahhaleh, Vaca-Cortés, Jirsa, Wheat, & Carrasquillo, 1998; Manning, 1996; Samples & Ramirez, 1999).

Discrete fiber reinforced polymer (FRP) rebar has been successfully implemented in several bridge decks as a corrosion-free solution (Brahim Benmokrane, Desgagne, Lackey, & El-Salakawy, 2004). There are many advantages to FRP, and bridge decks reinforced with this composite material have shown positive initial results. However, concrete reinforced with FRP composites made of glass, carbon, aramid, or basalt fibers demonstrates an entirely elastic response with a brittle failure mechanism at ultimate load.

Pairing glass fiber reinforced polymer (GFRP) rebar with alkali-resistant glass fibers dispersed throughout the mix could provide a bridge deck with the corrosion resistance of FRP composites and the ductility and post-peak residual capacity of fiber reinforced concrete (FRC). Preliminary cost analysis shows that implementing HRC decks in place of epoxy coated rebar is cost neutral as shown in Appendix C. The figures contained in the cost analysis are subject to availability and supplier.

1.2 Objective

The purpose of this study was to quantify the static and fatigue response of three bridge deck reinforcing schemes consisting of steel rebar, GFRP rebar, and GFRP rebar combined with FRC. The flexural behavior of these deck types was examined and compared. Constitutive relationships of each material were approximated, and numerical solutions were used to predict ultimate load behavior by examining the moment curvature relationship of each section. Using the experimental results, recommendations are given as to the viability of the GFRP-FRC decks.

The ultimate goal of this project is to provide an alternative reinforcing strategy that increases long-term durability while still providing a sufficient measure of ductility. As the existing infrastructure is steadily phased out and replaced, long-term solutions should be implemented in their place.

1.3 Outline

Chapter 2 contains a review of relevant literature and history of FRP and FRC in concrete bridge decks. There is an abundance of research regarding FRP and FRC, and only the smallest fraction of it could be included in this document. After reviewing the literature, the experimental program and setup is detailed in Chapter 3. The experimental program for the punching shear decks is included in Chapter 4. These two experimental program chapters also include all material testing data and procedures used.

Chapter 5 provides the experimental results for both static and fatigue testing of the flexural specimens. Chapter 6 includes experimental results for the static and cyclic testing of the punching shear specimens. Chapter 7 encompasses a discussion that contains the creation of constitutive relationships and numerical prediction models and elaborates on the experimental data for the flexural data. Chapter 8 contains a discussion regarding the punching shear data. The final chapter gives a summary of the experiment and provides recommendations based on the research.

2. LITERATURE REVIEW

2.1 Historical Background

2.1.1 Applications of FRP in Bridge Decks

FRP composites have been in use in mechanical and aerospace applications since after World War II, and their use became even more commonplace during the technological advancements of the Cold War. It wasn't until the late 1970s that the FRP reinforcing bar was available on the market; by that point, epoxy-coated reinforcing steel was the corrosion prevention strategy of choice (ACI Committee 440, 2015).

In the 1980s, pultruded FRP bars became a popular alternative for structures subjected to aggressive chemical conditions, such as wastewater treatment plants, sea walls, floating docks, and underwater structures. The non-conductivity of FRP reinforcement was also utilized in electromagnetically sensitive structures, such as hospitals with MRI machines, substation reactor bases, airport runways, and laboratories (Brown & Bartholomew, 1993).

The Japanese were pioneers in the use of FRP in civil engineering applications, and by the mid-1990s they had dedicated a document containing design recommendations in 1997 (Japan Society of Civil Engineering, 1997). China also has adopted FRP composites for many uses and, according to the ACI, has become the largest recent FRP user in Asia. Europe's first uses of FRP reinforcement were in Germany: a pedestrian bridge in 1980 followed by a high-traffic, prestressed FRP highway bridge in 1986 (ACI Committee 440, 2015; Bedard, 1992). Since then, there has been a focused research effort by various European organizations, especially EUROCRETE, to understand and utilize FRP composites (Taerwe & Matthys, 1999).

Canada is a large proponent of FRP use, with a special emphasis in bridge deck applications. To ensure design familiarity with FRP materials, Canada integrated FRP into its bridge design manual CHBDC. Three FRP reinforced bridge decks in Canada were also installed with sensors, as well as the Morristown Bridge in the U.S., allowing researchers to continuously monitor structural response over time (Brahim Benmokrane et al., 2004; Brahim Benmokrane, El-Salakawy, El-Gamal, & Goulet, 2007; Brahim Benmokrane, El-Salakawy, El-Ragaby, & Lackey, 2006; El-Salakawy, Benmokrane, & Desgagné, 2003).

The Cookshire-Eaton bridge, completed in 2004, was the first bridge constructed in Canada with GFRP bars in the bridge deck for one span. The two-span bridge also had galvanized steel as a control in the other span, and the bridge was implemented with fiber-optic sensors (FOS) at critical sections of the bridge to monitor strains and internal temperatures. After monitoring, it was shown that GFRP-reinforced deck slabs provide competitive performance to steel decks (El-Salakawy, Benmokrane, El-Ragaby, & Nadeau, 2005).

In the United States, ACI committee 440, which focuses on internal and external FRP reinforcement, has published multiple design documents beginning in 1996 with *ACI 440R-96: Report on Fiber Reinforced Plastic Reinforcement for Concrete Structures*. To date, the committee has published an additional 19 documents involving FRP. In 2009, AASHTO developed a design guide for GFRP-reinforced concrete. This document, updated in 2018, includes provisions for deck slabs. Out of glass, aramid, carbon, and basalt fiber reinforcements, glass is typically more cost effective, and most bridge deck applications consist of GFRP rebar (ACI Committee 440, 2015).

The FHWA created the Innovative Bridge Research and Construction (IBRC) program in 1998, providing grants to DOTs to incentivize the use of innovative bridge construction materials and strategies. From 1999 to 2005, $128.7 million was awarded to around 400 projects. By 2005 alone, $55 million of this

grant money was awarded to projects involving FRP in 30 different states (National Academies of Sciences, Engineering, and Medicine, 2019).

2.1.2 Applications of Fiber-Reinforced Concrete in Bridge Decks

Fibers have been used in adobe and mud bricks for centuries to provide a better crack control system. It was not until 1874 that FRC was created (Picazo, Alberti, Enfedaque, & Gálvez, 2018). Many patents followed this period, but wide acceptance and research in FRC did not begin until the 1960s when researchers started to realize the benefits of the crack arrest behavior and increased tensile strength of FRC. Following this work in the 1960s, there was an explosion in research surrounding FRC. The market began to be saturated with macro- and micro-fibers of all different material types and orientations (Naaman, 2018).

By 1978, the use of FRC as a structural concrete had gained acceptance, and was being used in applications where repetitive loads were present, such as bridge decks (O'Neil, 1978). Concrete reinforced with epoxy-coated steel tends to have wider cracks due to the decreased bond (Cleary & Ramirez, 1991; Treece & Jirsa, 1989). Therefore, FRC has been used in combination with epoxy-coated rebar to provide crack control.

In 1991, Aftab Mufti developed a "steel-free" bridge deck system that consisted of an FRC slab containing no internal steel reinforcement (Memon, 2005; Mufti, Jaeger, Bakht, & Wegner, 1993). To provide sufficient lateral stiffness and ensure "arching action," or compressive membrane action, external steel straps are welded from girder to girder at the top flange as seen in Figure. The first bridge using an FRC slab with steel straps was implemented over the Salmon River in Nova Scotia. After six months, longitudinal cracks measuring approximately 1 mm developed in between the girders.

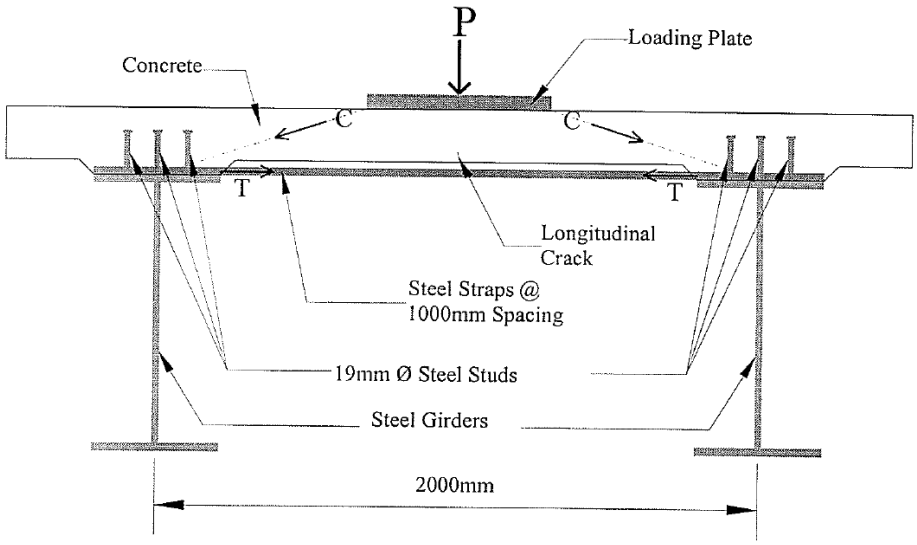

Figure 2.1.1 Steel-free bridge decks (Memon, 2005)

To eliminate these longitudinal cracks, a "second-generation" of steel-free decks also included an FRP crack control grid in conjunction with the FRC. The first of these decks was implemented in the Red River Bridge in 2003. In 2004, this same second-generation steel-free design was utilized in a bridge in Iowa, U.S. (Memon, 2005). Figure shows a typical detail for the second-generation steel-free bridge decks. Requirements for "steel-free" bridge decks have been codified in the CHBDC (Salem, El Aghoury, Sayed-Ahmed, & Moustafa, 2002).

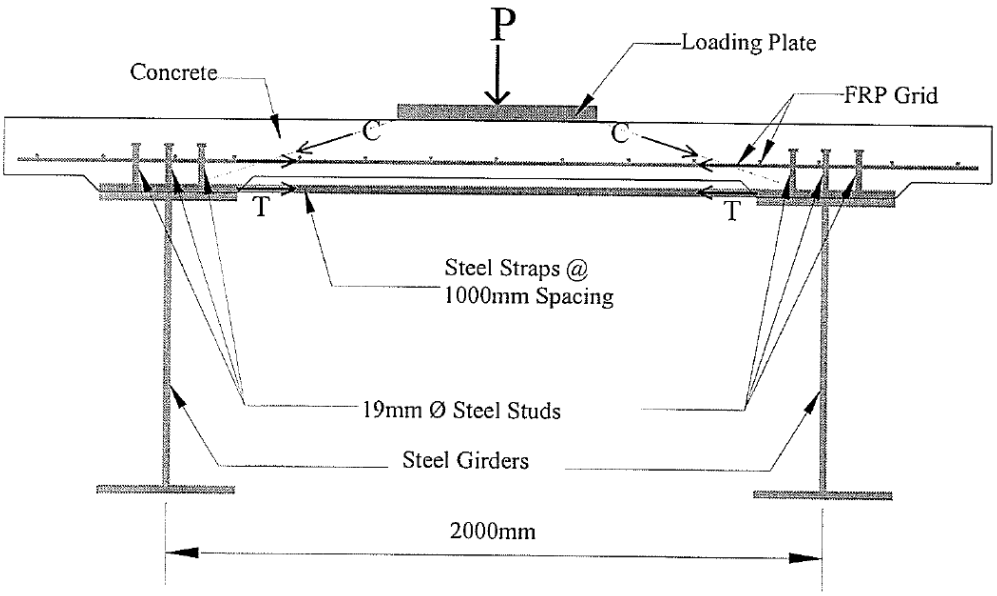

Figure 2.1.2 Second-generation steel-free bridge decks (Memon, 2005)

The Missouri Department of Transportation (MoDOT), in tandem with the University of Missouri-Rolla and the University of Missouri-Columbia, performed a study in 2006 similar to that conducted in this research project. A hybrid steel-free system reinforced with FRP and FRC was tested for bond and durability for small-scale specimens. The static and fatigue response was investigated on full-scale bridge deck panels (Gopalaratnam, Meyer, De Young, Belarbi, & Wang, 2006). Although the MoDOT planned to implement this bridge deck type on a bridge in 2007, the author is unaware of whether the project was carried out or not (MoDOT, 2006).

2.2 Durability

2.2.1 Durability of Steel

The corrosion of steel reinforcing is the primary catalyst for research in alternative bridge deck reinforcing strategies as a means of corrosion mitigation. As mentioned in the introduction of this document, as of 2002, steel corrosion in bridge decks accounted for $2 billion in annual costs (Koch et al., 2002). The expansion of the steel as it corrodes causes delamination and surface spalling. Bridge decks in cold climates are frequently exposed to deicing salts, which accelerates corrosion significantly.

Some research from the South Dakota Department of Transportation predicts an ultimate service life of 10 to 25 years for conventional bridge decks without any epoxy coating. The same study suggested that epoxy-coated rebar (ECR) will have a service life of 30 to 40 years (Darwin, Browning, Van Nguyen, & Locke Jr, 2002).

Other research suggests that bridge decks with ECR should expect service lives of around 50 years (A. A. Almusallam, Khan, Dulaijan, & Al-Amoudi, 2003; Fanous & Wu, 2000). Another study done in Florida suggests that in as little as 20 years, bridge decks with ECR can experience spalling and delamination, especially if the rebar has severe “coating distress” (Sagüés, Powers, & Kessler, 2001). This coating distress can be minimized by proper handling of the rebar prior to placement, but even small areas of damage can lead to a corrosion propagation phase.

An innovative new technology being investigated recently is bridge inspection through autonomous control of small unmanned aerial systems (sUAS). Bridge inspections are required for every bridge in the United States typically every 24 months. Using deep learning and image recognition, the spalling, cracking, and delamination of steel-reinforced concrete bridge decks can be identified. Using the information obtained through this process, service life can be predicted (Dorafshan & Maguire, 2018; Dorafshan, Thomas, Coopmans, & Maguire, 2019; Dorafshan, Thomas, & Maguire, 2019).

There seems to be a wide range of estimated service lives for ECR bridge decks in the literature. Part of the reason is the large range of parameters involved. The regional climate, moisture content, size of cracking at placement and over the lifespan of the bridge deck, use of deicing salts, coating damage at placement, and many other factors affect the service life of ECR bridge decks. While some of these factors can be controlled through proper deck design and handling of the reinforcement, there are still some parameters that are out of the control of the owner, designer, and contractor.

2.2.2 Durability of GFRP

According to ACI (2015), GFRP bars are not impervious to concerns regarding durability. Although GFRP is highly resistant to electrochemical corrosion, research has shown that moisture, alkaline or acidic environments, saline solutions, elevated temperature, water, and ultraviolet (UV) radiation can all cause changes in both strength and stiffness of GFRP. Laboratory experiments can create “accelerated exposure” conditions that simulate environmental conditions encountered in the field over long periods. Several of the attempts to qualify long-term behavior of GFRP under various conditions are summarized in this section.

Portland Cement has a pH level of between 12.5 and 13.0 (Behnood, Van Tittelboom, & De Belie, 2016). It has been shown this extremely alkaline environment can adversely affect the tensile strength and stiffness of GFRP. Tannous (1997) exposed GFRP comprised of E-glass fibers as well as alkali-resistant (AR) fibers to seven different solutions mimicking different field conditions. After six months of direct exposure, the specimens were tested in tension and the ultimate tensile strength, elastic modulus, and failure strain were recorded. He concluded that E-glass and AR-glass fibers exhibit poor behavior after exposure to alkaline solutions, marine environments, and deicing salt solutions.

Micelli et al. (2001) tested GFRP bars with a thermoplastic resin and bars with a polyester resin, and found that the thermoplastic matrix resulted in almost no residual tensile strength loss after accelerated exposure to an alkaline environment. The bars with a polyester matrix experienced a significant strength reduction. Sen et al. (2002) conducted a nine-month experiment on No. 3 E-Glass GFRP bars with a vinyl ester resin in an alkaline exposure that mimicked the MRI Pier construction project completed by the U.S. Navy in San Diego, California. At constant stress levels above 15%, the bars showed very limited durability. With no long-term load applied, tensile strength reductions of 63% were reported after nine months of exposure time.

Benmokrane et al. (2002) performed over 400 accelerated aging tests on different GFRP bars. The bars were subjected to sustained loads varying from 25% to 68% of the ultimate tensile capacity while experiencing simulated alkaline environments. They found, like other researchers, that polyester resins are inferior to vinyl ester resins, and that alkali-resistant (AR) glass fibers are superior to regular E-glass with regard to alkaline environments. They recommend that GFRP should be maintained at a level less than 25% of the guaranteed design strength.

Gaona (2004) showed that the tensile strength of GFRP reinforcing bars strength degraded by up to 24% strength loss after 50 weeks in an alkaline environment that simulated concrete. Surprisingly, the elastic modulus increased by 9% after 50 weeks of exposure time. In 2005, Abdel-Magid et al. (2005) conducted durability tests of GFRP bars with E-glass fibers in an epoxy resin. They subjected the bars to a sustained load of 20% of the tensile capacity of the bars while they were submerged in distilled water at different temperatures and durations. After 1,000 hours of sustained stress and a 65° C temperature, the specimens had an 18% strength reduction and a 28% decrease in the elastic modulus. They attributed this softening effect to "matrix plasticization."

Robert et al. (2013) investigated GFRP bars embedded in concrete while being exposed to a saline solution at different temperatures for 365 days. They concluded that the tensile strength reduction was very small, including at 50° C and 70° C. Therefore, by extrapolating their data based on the Arrhenius theory, they found that after 100 years, the GFRP bars would only lose 30% or 23% in mean annual temperatures of 50° C and 10° C, respectively.

According to Benmokrane et al. (2016), in 2004, ISIS Canada, a Canadian Network of Centres of Excellence, started a field study to examine the long-term effects of actual in-field conditions on GFRP-reinforced bridge decks that were already in service. Five pilot bridge decks reinforced with GFRP, chosen from a large range of field conditions, were selected for the microanalysis study. By comparing the samples pulled from the actual bridge decks to samples that were saved from the projects in laboratory conditions, they were able to conclude that no amount of chemical degradation had occurred due to alkalinity.

A follow up study in 2009 examined GFRP-reinforced cores from three of the five initial bridge decks. Scanning electron microscopy (SEM), energy dispersive X-ray (EDX), optical microscopy (OM), differential scanning calorimetry (DSC), and Fourier transform infrared spectroscopy (FTIS) were the tests used to examine the condition of GFRP after 10 to 13 years of actual environmental exposure. Although the 10 to 13 years of exposure is nowhere close to the target service life of 75 years or greater, it was once again confirmed that the GFRP did not show any signs of degradation due to its exposure to alkaline environments (Brahim Benmokrane & Ali, 2016).

There is often conflicting literature regarding the durability of GFRP in concrete. While some experiments demonstrate enormous reductions in strength, others state that the strength and stiffness reductions are very small. ACI (2015) reported a tensile strength reduction of 0% to 75% in the literature and a stiffness reduction between 0% and 20%. This is in part due to the wide range of exposure times and exposure conditions used for the accelerated aging experiments. As the research in GFRP for civil applications has increased, the number of available products has also increased, making direct comparisons difficult.

ACI Committee 440 came to the consensus that a sweeping environmental reduction factor, C_E, was required to account for material degradation and reduce the tensile strength of FRPs based on the environment to which they are subjected.

Table 2.2.1 contains the reduction factors for CFRP, GFRP, and AFRP. A comparison of safety and environmental reduction factors is provided in Rossini et al. (2019). This is an ever-evolving field of study, and one recent report demonstrated that a reduction of tensile strength of only 2.13% was exhibited by GFRP bars that were cast in a bridge deck after 17 years in service Benzecry et al. (2019).

Table 2.2.1 FRP Environmental Reduction Factors (ACI Committee 440, 2015)

Exposure Condition	Fiber Type	Environmental Reduction Factor C_E
Concrete not exposed to earth and weather	Carbon	1.0
	Glass	0.8
	Aramid	0.9
Concrete exposed to earth and weather	Carbon	0.9
	Glass	0.7
	Aramid	0.8

To account for the creep rupture phenomena due to sustained loading or fatigue loading, a reduction factor is similarly applied to the nominal tensile strength as shown in Table 2.2.2, resulting in a creep rupture stress limit, $f_{fs,sus}$ (ACI Committee 440, 2015).

Table 2.2.2 FRP Long-Term Stress Reductions (ACI Committee 440, 2015)

Fiber Type	GFRP	AFRP	CFRP
Creep Rupture Stress Limit, $f_{fs,sus}$	$0.2f_{fu}$	$0.3f_{fu}$	$0.55f_{fu}$

Byars et al. (2003) summarize the different treatments the FRP durability concern receives from five different codes, including: ACI, NS3473, CHBDC, JSCE, and BISE. They also propose a more refined solution to account for variability in moisture condition, mean annual temperature (MAT), and requested service life. They clearly state that international agreement and FRP acceptance will only be accomplished when producers, engineers, and academics can agree on a durability test method and specification.

2.3 Flexural Response

2.3.1 Flexural Design of Bridge Decks

The traditional bridge deck design for steel-reinforced concrete bridge decks outlined in the AASHTO LRFD Bridge Design Specifications divides the total load on one traffic lane into “equivalent strips” (AASHTO, 2018c). These strips account for the distribution of the wheel loads through the deck in the transverse direction perpendicular to the bridge deck span.

This approximate method of analysis assumes that the deck is a flexural element, and the positive and negative moments are calculated by positioning the HL-93 design truck or the design tandem to cause the maximum positive or negative moment. This moment is divided by the width of the equivalent strip as defined in Table 4.6.2.1.3-1 of the LRFD specifications shown in Table 2.3.1 where:

- S = the spacing of the supporting components (ft)
- $+M$ = the positive moment
- $-M$ = the negative moment
- X = the distance from load to point of support (ft)

Table 2.3.1 Equivalent Strips – Adapted from Table 4.6.2.1.3-1 (AASHTO, 2018c)

*Type of Deck	Direction of Primary Strip Relative to Traffic	Width of Primary Strip (in.)
Cast-in-place	Overhang	45.0 + 10.0*X*
	Either Parallel or Perpendicular	+*M*: 26.0 + 6.6*S*
		-*M*: 48.0 + 3.0*S*
Cast-in-place with stay-in-place concrete formwork	Either Parallel or Perpendicular	+*M*: 26.0 + 6.6*S*
		-*M*: 48.0 + 3.0*S*
Precast, post-tensioned	Either Parallel or Perpendicular	+*M*: 26.0 + 6.6*S*
		-*M*: 48.0 + 3.0*S*
* The AASHTO Table 4.6.2.1-3 also includes strip widths for steel and wood decks. This paper includes only concrete bridge deck types.		

Design moments are also tabulated for the design engineer in Appendix Table A4-1, with the assumptions and limitations included in the analysis listed in Appendix A4. After a moment per-foot width is obtained, the design engineer uses conventional flexural theory to design the concrete slab. The following sections describe the flexural design requirements and theory of GFRP-reinforced concrete members as well as FRC with discrete GFRP rebar.

2.3.2 GFRP Flexure

Unlike steel-reinforced concrete, the desirable limit state for a GFRP-reinforced beam is the crushing of the concrete. Although brittle, the crushing of the concrete displays slightly more post-peak behavior than rupture of the GFRP rebar, which results in a sudden and catastrophic failure (Nanni, 1993). Even though the concrete crushing is recommended, both compression- and tension-controlled beams are allowed per the ACI 440 design recommendations (ACI Committee 440, 2015).

Several of the design assumptions made to design FRP-reinforced beams are as follows:

- Plane-sections remain plane after loading
- The maximum usable concrete strain is 0.003
- The tensile strength of concrete is negligible
- FRP is linear-elastic
- FRP exhibits a perfect bond with the concrete throughout the loading

Using strain compatibility, equilibrium of forces, and the material constitutive relationships, the moment capacity of the FRP-reinforced beam can be attained. The balanced failure reinforcement ratio is shown in Equation 2.3.1 (ACI Committee 440, 2015).

$$\rho_{fb} = 0.85\beta_1 * \frac{f_c{}'}{f_{fu}} * \frac{E_f \epsilon_{cu}}{E_f \epsilon_{cu} + f_{fu}} \tag{2.3.1}$$

Where

- ρ_{fb} = Balanced reinforcement ratio
- β_1 = Whitney stress block factor
- f_c' = Compressive strength of concrete
- f_{fu} = Design tensile strength of FRP
- E_f = Design modulus of elasticity of FRP
- ϵ_{cu} = Ultimate concrete strain = 0.003

If the reinforcement ratio, $\rho_f > \rho_{fb}$, where ρ_f is the FRP reinforcement ratio of the section, then the member is compression-controlled and the concrete will crush prior to the rupture of the GFRP. This case has a simple closed-form solution shown in Equations 2.3.2, 2.3.3, and 2.3.4:

$$f_f = \left(\sqrt{\frac{\left(E_f \epsilon_{cu}\right)^2}{4} + \frac{0.85\beta_1 f_c'}{\rho_f} E_f \epsilon_{cu}} - 0.5 E_f \epsilon_{cu} \right) \leq f_{fu} \tag{2.3.2}$$

$$a = \frac{A_f f_f}{0.85 f_c' b} \tag{2.3.3}$$

$$M_n = A_f f_f \left(d - \frac{a}{2}\right) \tag{2.3.4}$$

Where

- f_f = FRP tensile stress
- ρ_f = FRP reinforcement ratio
- a = Depth of compression block
- A_f = Area of FRP reinforcement
- b = Width of beam
- M_n = Nominal moment capacity of the section
- d = Depth of FRP from top of compression block

Equations 2.3.2 and 2.3.3 are substituted into Equation 2.3.4 to solve for the moment capacity. The tension-controlled case where $\rho_f < \rho_{fb}$ does not have a simple closed-form solution, but ACI 440.1R-15 allows a lower bound simplification shown in Equations 2.3.5 and 2.3.6:

$$c_b = \left(\frac{\epsilon_{cu}}{\epsilon_{cu} + \epsilon_{fu}}\right) d \tag{2.3.5}$$

$$M_n = A_f f_{fu} \left(d - \frac{\beta_1 c_b}{2}\right) \tag{2.3.6}$$

Where

- ϵ_{fu}= FRP rupture strain
- c_b = Depth to neutral axis at balanced condition

The factored nominal resistance is obtained by multiplying the nominal moment capacity, M_n, by the resistance factor, ϕ. Equation 2.3.7 shows the resistance factor for tension-controlled sections and compression controlled sections. For ρ_{fb} to $1.4\rho_{fb}$, the section is in a transition zone. This is shown in Figure 2.3.1.

$$\phi = \begin{cases} 0.55 \; for \; \rho_f \leq \rho_{fb} \\ 0.3 + 0.25 \dfrac{\rho_f}{\rho_{fb}} \; for \; \rho_{fb} < \rho_f < 1.4\rho_{fb} \\ 0.65 \; for \; \rho_f \geq 1.4\rho_{fb} \end{cases} \tag{2.3.7}$$

Where

- ϕ = Strength reduction factor

A number of researchers agree that prior to cracking, the FRP decks and steel-reinforced decks behave almost identically. After cracking, large cracks and deflections are seen as compared to the steel decks. According to the research, this can be attributed to the low modulus of the FRP (Abdelkarim, Ahmed, Mohamed, & Benmokrane, 2019; T. H. Almusallam, 1997; B. Benmokrane, Masmoudi, & Chaallal, 1996; Michaluk, Tadros, Benmokrane, & Rizkalla, 1998).

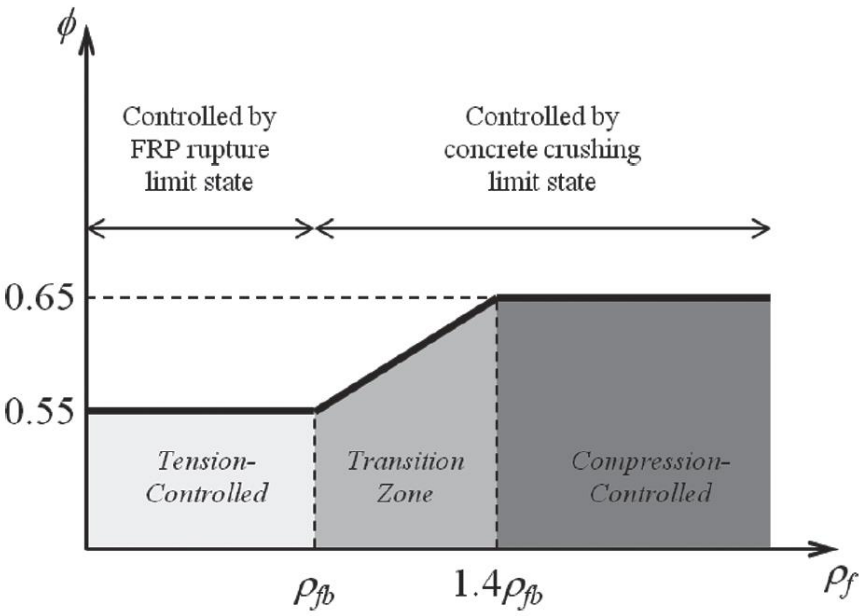

Figure 2.3.1 Resistance factor of FRP-reinforced concrete (ACI Committee 440, 2015)

AASHTO takes an identical approach to ACI for the flexural design of GFRP-reinforced members with a slight modification of the resistance factor (AASHTO, 2018a). The upper limit of 0.65 has been increased to 0.75 in compression-controlled sections as the result of a recent reliability analysis of steel- and GFRP-reinforced beams (Zadeh & Nanni, 2013).

2.3.3 Fiber-Reinforced Concrete Flexure

In a sectional analysis of a conventional reinforced concrete beam, the tensile capacity at the strength limit state is assumed to be negligible, and all the tension force in the section is assumed to be carried by the bonded reinforcement. In structural FRC, there is some post-peak residual tensile capacity in the concrete due to crack bridging behavior by the fibers. Developing a standardized test to describe the constitutive relationship of the FRC in tension has been difficult, and many attempts have been made with some success.

ACI 544.4R-18, the *Guide to Design with Fiber-Reinforced Concrete*, discusses some of the challenges to developing a direct tension test for FRC. Among the issues mentioned are concrete crushing at the grips, stiffness of the testing machine, gauge length, mode of test control (open or closed loop), and number of cracks observed. Due to these issues, most of the accepted tests require back-calculation of the tensile properties of FRC from flexural tests (ACI Committee 544, 2018).

In the United States, the adopted test for determining the residual tensile capacity of FRC is ASTM C1609/C1609M. In this test, a 6 x 6 x 20 in. (150 x 150 x 500 mm) FRC beam with an 18 in. (450 mm) span is subjected to four-point bending until the beam reaches a midpoint deflection of L/150, or 0.12 in. (3 mm). Loads P_p, P_{600}^D, and P_{150}^D are recorded at the peak and at deflections values of L/600 and L/150, respectively. Figure 2.3.2 shows the test setup and beam configuration.

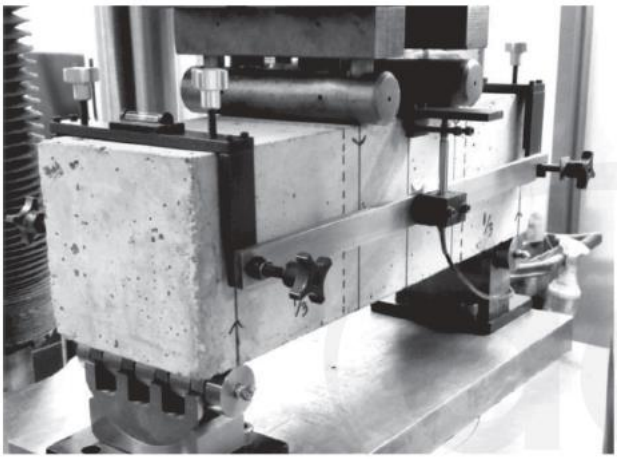

Figure 2.3.2 ASTM C1609 test setup (ACI Committee 544, 2018)

The European test for determining the residual properties of FRC is the EN 14651 test. This test calls for a notched beam that is 6 x 6 x 22 in. (150 x 150 x 550 mm) and spans 20 in. (500 mm) to be tested under three-point bending. A crack displacement transducer spans the 1-in. (25 mm) crack and the load is taken at the peak, as well as when the crack-mouth opening displacement (CMOD) is equal to 0.02, 0.06, 0.1, and 0.14 in. (0.5, 1.5, 2.5, and 3.5 mm). These force values are labeled F_1, F_2, F_3, and F_4 for the CMOD values listed. The force F_L is the load at the peak. The test allows for control of either the rate of CMOD opening, or a displacement rate that is related to the CMOD. The EN 14651 test configuration is shown in Figure2.3.3.

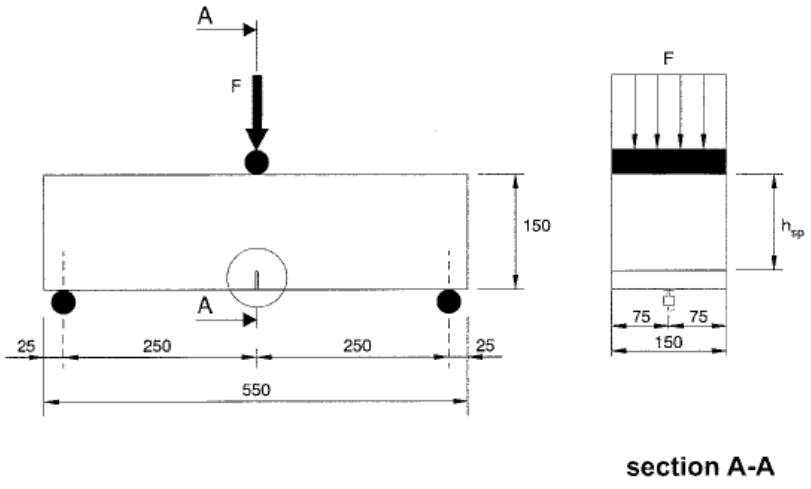

Figure 2.3.3 EN 14651 beam setup (EN 14651, 2005)

For both tests, the flexural residual loads are then converted into residual flexural stresses by assuming a linear stress distribution. In order to obtain the residual tensile capacity of the FRC, a conversion must be performed. The residual flexural strength is approximately 2.5 to 3 times greater than its residual tensile strength (ACI Committee 544, 2018). Table 2.3.2 contains some comparisons of the tests as well as the nomenclature for the residual flexural stress

Table 2.3.2 Comparison of FRC test procedures

Test Parameter	ASTM C1609/C1609M	EN 14651
Geometry	6 x 6 x 20 in. (150 x 150 x 500 mm)	6 x 6 x 22 in. (150 x 150 x 550 mm)
Span	18 in. (450 mm)	20 in. (500 mm)
Notch?	No	Yes
Loading pattern	Four-point bending	Three-point bending
Load control	Deflection	CMOD or deflection
Force parameters	$P_p, P_{600}^D, P_{150}^D$	F_L, F_1, F_2, F_3, F_4
Residual flexural parameters	$f_p, f_{600}^D, f_{150}^D$	$f_{ct,L}^f, f_{R1}, f_{R2}, f_{R3}, f_{R4}$

The fib Model Code adopts two general FRC stress-crack opening models. The first model describes the residual tensile behavior of FRC as rigid-plastic. A constant stress is assumed for the ultimate residual tensile strength (CEB-FIB, 2013). This stress is calculated in accordance with Equation 2.3.8:

$$f_{Ftu} = \frac{f_{R3}}{3} \tag{2.3.8}$$

Where

- f_{Ftu} = Ultimate residual strength of FRC
- f_{R3} = Residual flexural tensile strength at $CMOD = CMOD_3$

The second constitutive FRC model accepted by the fib Model Code assumes linear-elastic behavior starting at a crack opening corresponding to the service limit state (SLS). The residual capacity either decreases or increases from the SLS capacity down to an ultimate residual strength for the ultimate limit state (ULS) depending on whether or not the FRC exhibits strain-softening or strain-hardening behavior (CEB-FIB, 2013).

For the rigid plastic model, the maximum considered crack, w_u, is 0.1 in. (2.5 mm), whereas the linear-elastic model depends on the ductility required (Blanco, Pujadas, de la Fuente, Cavalaro, & Aguado, 2013). Equation 2.3.9 and 2.3.10 describe the residual capacities of the linear-elastic model, and Figure2.3.4 shows the two models side-by-side.

$$f_{Fts} = 0.45 f_{R1} \tag{2.3.9}$$

$$f_{Ftu} = f_{Fts} - \frac{w_u}{CMOD_3}(f_{Fts} - 0.5 f_{R3} + 0.2 f_{R1}) \geq 0 \tag{2.3.10}$$

Where

- f_{Fts} = Serviceability residual strength of FRC
- f_{R1} = Residual flexural tensile strength at $CMOD = CMOD_1$
- w_u = Maximum crack opening accepted in structural design

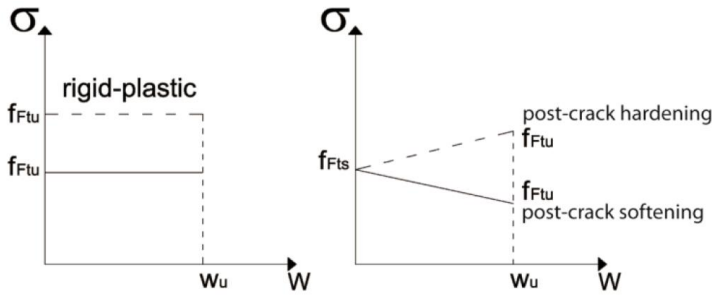

Figure 2.3.4 FRC constitutive models from fib Model Code (CEB-FIB, 2013)

For the ASTM C1609/C1609M standard, the residual strength of the FRC can be determined by Equation 2.3.11:

$$f_{Ftu} = 0.37 f_{150}^{D} \tag{2.3.11}$$

Where

- f_{150}^{D}= Residual strength at net deflection of L/150

ACI states that if SLS criteria must be met, f_{150}^{D} can be substituted by the residual strength at a smaller crack width, f_{600}^{D}.

Once the FRC constitutive models are determined, analogies can be made to the regular design of reinforced concrete sections prior to cracking. Before a steel-reinforced concrete beam ruptures, the moment is less than the cracking moment, and the compressive force is balanced by the small tensile capacity of the concrete. Because FRC has residual capacity post-cracking, the tension force from the fibers balances with the compressive force; therefore, the ULS design capacity for a rectangular section is shown in Equation 2.3.12 or Equation 2.3.13 for the ASTM C1609/C1609M test and EN 14651 tests, respectively:

$$M_{n-FRC} = f_{150}^{D} \frac{bh^2}{6} \tag{2.3.12}$$

$$M_{n-FRC} = f_{R3} \frac{bh^2}{6} \tag{2.3.13}$$

Where

- M_{n-FRC} = Nominal moment capacity of FRC section

2.3.4 Combined GFRP and FRC Considerations

There is limited research available on the behavior of hybrid concrete sections reinforced with both macrofibers as well as discrete GFRP rebar. Some researchers refer to the combination of rebar and FRC as hybrid reinforced concrete (HRC) (Mobasher, Yao, & Soranakom, 2015). Some of the pioneering research in FRP composite rebar in FRC concrete was performed in 1999 by Alsayed et al. They tested 18 beams in flexure, and the GFRP-reinforced HRC beams were compared with steel-reinforced HRC beams. They showed that ductility was improved as the fiber dosage increases (Alsayed & Alhozaimy, 1999).

In 2005, MoDOT and the University of Missouri commenced a project to investigate the addition of synthetic fibers to GFRP-reinforced bridge decks to determine the behavior of these hybrid reinforced decks. The static and fatigue bond behavior, flexural ductility, accelerated durability, and static and fatigue behavior of full-scale bridge deck panels were described during the experiments. Adding fibers improved the structural performance of the hybrid bridge decks, and better ductility and smaller crack widths were observed than for the plain concrete counterparts (Gopalaratnam et al., 2006; Wang, 2005).

Other researchers discussed the improved ductility exhibited by these HRC flexural elements. Wang et al. (2011) showed that GFRP- and CFRP-reinforced beams with added fibers showed improved post-peak behavior due to the residual capacity of FRC. The ductility of the FRC beams was better than similar plain concrete beams, as expected. Some research has shown similar enhanced beam ductility for high strength FRC at the ultimate load capacity (Issa, Metwally, & Elzeiny, 2011; J.-M. Yang, Min, Shin, & Yoon, 2012).

Analytical models developed by researchers have been created to predict moment-curvature behavior of FRC with discrete FRP bars. Some models use the stress-strain constitutive models of the different materials to predict behavior, while others use the stress-crack width relationship of FRC to describe the response. Most of the models predict the response with good agreement (Barros, Taheri, & Salehian, 2015; Mobasher et al., 2015; Taheri, Barros, & Salehian, 2011).

2.4 Fatigue Response

2.4.1 Concrete Fatigue Background

Since as early as 1829, the fatigue behavior of metals has been studied and documented rigorously (Suresh, 1998). Schütz, in a critical review of fatigue literature, cited over 500 resources and mentioned that researchers such as Thum co-authored 574 papers and reports regarding fatigue of metallic materials (Schütz, 1996). In comparison, research and publications on the fatigue behavior of concrete are scarce.

The earliest reported study on fatigue of cement was conducted by De Joly in 1898, nearly 60 years after the pioneering research on the fatigue of metals (Falk, 1904). De Joly created tension briquettes and performed cyclic loading at a percentage of their ultimate tensile capacity and at varying ages. He found that not only was the age of the specimen a major factor in the number of cycles to failure, but the rate of cycle application affected the number of cycles to failure.

Professor J. L. Van Ornum performed the first compressive fatigue tests on Portland cement cubes as early as 1903. He recognized, just like De Joly, that concrete can fail at a percentage of its ultimate capacity when subjected to repeated loadings. He also recognized that the concrete specimens experienced a stiffness degradation under cyclic loading as shown in Figure 2.4.1 (Van Ornum, 1903).

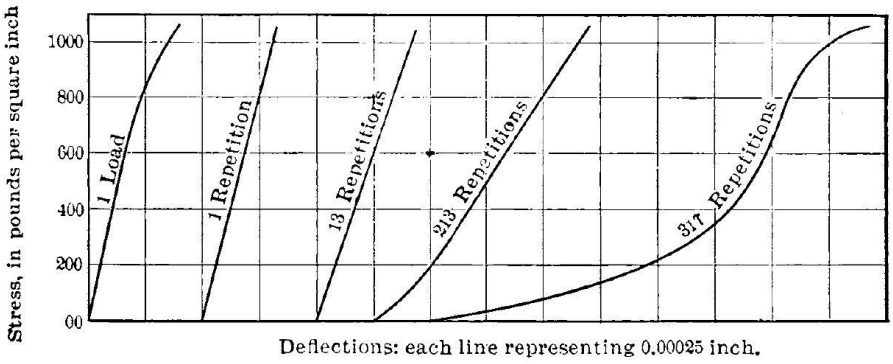

Figure 2.4.1 Stiffness degradation under cyclic compression, (Van Ornum, 1903)

Féret (1906) performed the first flexural fatigue tests on plain and reinforced beams. Féret presented this work as a portion of a larger study on behavior of beams, cubes, and cylinders. Nordby, in a review of research on concrete fatigue in 1958, asserts that the work done by Féret in this area is of historical interest only, even though the specimens contained in his research were similar to those of subsequent researchers (Nordby, 1958).

A number of researchers followed this pioneering work of De Joly, Van Ornum, and Féret, and several notable relationships and mechanisms were summarized by Nordby with regard to fatigue of plain and reinforced concrete. For plain concrete, all of the researchers agreed that the fatigue limit, or the point at which subsequent cycles do not cause a substantial decrease in the residual strength, was approximately 50% to 55% of the initial static strength. This value was the same for flexure and tension but with a higher variance for specimens with various ages, moisture contents, curing, and aggregate type (Clemmer, 1922; Hatt, 1922; Probst & Treiber, 1932; Williams, 1943).

Murdock, in another review of fatigue literature, noted that there is no fatigue limit for plain concrete up to 10 million cycles. (Murdock, 1965) This observation is substantiated in Murdock and Kesler's work that tried to relate rate of testing to fatigue strength. They concluded that the rate of testing between 70 and 440 cycles per minute appeared to have no significant effect on the fatigue strength of their plain concrete specimens. They observed that up to 10 million cycles there did not appear to be an endurance limit, as shown in Figure 2.4.2 (Murdock & Kesler, 1958). Murdock, however, stated that the fatigue strength at 10 million cycles can be conservatively taken as 55% of the ultimate strength.

In a later review of fatigue research, Raithby and Whiffin (1968) stated that no evidence shows a fatigue limit for plain concrete, and even cautioned readers of older research on concrete fatigue to not give too much significance to the term "fatigue strength." For many of the tests, fatigue strength was only given to describe a particular loading scenario and cycle count, which does not truly describe the endurance or fatigue limit.

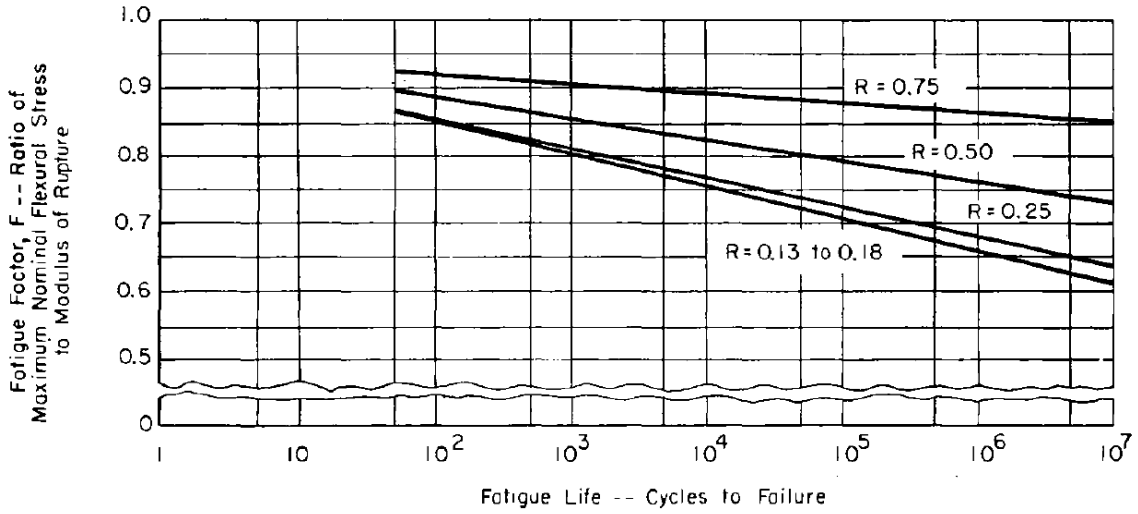

Figure 2.4.2 S-N curve for varying stress ranges (John W Murdock & Kesler, 1958)

Nordby (1958) noted that among the previous research, the rate of testing seemed to have little effect on fatigue strength of concrete in spite of De Joly's initial observations. He also found that several researchers, such as De Joly, Probst, Hatt, and Crepps, stated that rest periods seemed to allow for a fatigue recovery and increased the fatigue resistance of the specimens (Crepps, 1923; Hatt, 1925; Probst & Treiber, 1932). In fact, one of the tests performed by Hatt had an accidental shutdown that gave a rest period of five weeks to a specimen. The specimen, which was near failure, had an almost complete recovery (Hatt, 1925).

Most of the permanent deformation occurs in the first cycles of the fatigue tests. Following this stage of permanent deformation, the total deformation will slowly increase until failure (Nordby, 1958). The stress range also tends to have an influence on the strength of concrete in fatigue. Nordby asserts that, per the research, a decrease in the stress range correlates to an increase in the upper limit of stress.

With regards to reinforced concrete beams, Nordby (1958) summarized that the majority of failures of the beams came from rupture of the reinforcing steel. For reinforced beams designed to fail in flexure, the fatigue limit reported was 60% to70% of the static strength after 1,000,000 cycles. Only Le Camus (1945) reported a fatigue compression failure of the compression zone. Beams that failed in shear were reported to have failed at cyclic loads of 40% of their ultimate strength (Nordby, 1958).

In his critical review of fatigue literature, Murdock (1965) stated that perhaps the most elusive, yet important, part of fatigue testing that had not been extensively treated or examined was the internal mechanism of concrete fatigue and crack propagation. Probst and his research associates initiated studies that aided in understanding the fatigue mechanism by measuring progressive deformation and crack widths during cyclic behavior (Probst & Treiber, 1932).

Raithby and Whiffin (1968), in reviewing fatigue literature, discussed two "characteristics" that can aid in understanding the mechanism of fatigue failure. These are changes in stress-strain relationships and measuring crack growth propagation. He surmised that fatigue initiates bond failure between the aggregate and the cement matrix. These cracks then progress along the matrix until they are stopped at a discontinuity, such as an aggregate. The bond failure mechanism then repeats and the process continues until complete fracture.

Shah and Chandra (1970) used ultrasonic pulses to measure internal changes in the cement matrix and examined microcrack propagation to understand the fatigue mechanism of concrete. They recognized that there was an initial deceleration of crack growth, Stage I, where strains increased slowly, and then an acceleration phase, Stage II, where the rate of change of the strains and cracks in the concrete increased drastically. Also, more microcracking was observed in the fatigue specimens than in the static specimens.

Following Shah and Chandra's research, several researchers began to create analytical and numerical models to correlate experimental research. Diaz and Hilsdorf (1971) used fracture mechanics models to understand crack propagation at a micro-level. They used a simplistic model that qualitatively described the crack growth process on linear microcracks. Whaley and Neville (1973) developed an empirical equation to describe the cyclic creep of concrete. Their study measured non-elastic deformations under varying mean concrete stress and stress ranges.

Zhaodong and Jie (2018) summarized three types of attempts that have been made to capture the fatigue behavior of concrete. They said the first types are experimental approaches at the macro-level that can be used to attempt to describe micro-scale behavior (Aas-Jakobsen & Lenschow, 1973; Breitenbücher & Ibuk, 2006; Cornelissen, 1984; Oh, 1991; Tepfers & Kutti, 1979). According to Zhaodong and Jie, these phenomenological studies provide intuitional information, but they do not entirely capture the microscopic nature of fatigue.

The next type of study that attempts to qualify fatigue behavior is fracture mechanics and crack growth modeling (Kessler-Kramer, Mechtcherine, & Müller, 2004; Nguyen, Repetto, Ortiz, & Radovitzky, 2001; B. Yang, Mall, & Ravi-Chandar, 2001). These studies model a single crack, which also does not fully describe the fatigue mechanism, as there is a multitude of microcracks prior to failure in a concrete specimen experiencing fatigue.

The final type of fatigue study described by Zhaodong and Jie (2018) is damage mechanics. Damage mechanics concerning concrete fatigue attempts to model material degradation that occurs due to the propagation of a microcrack group. Researchers in this area introduced the idea of a damage surface, which is similar to a yielding surface in plastic mechanics (Alliche, 2004; Mai, Le-Corre, Foret, & Nedjar, 2012; Papa & Taliercio, 1996). Other researchers used rate process theory to describe microcrack propagation (Krausz, 1988; Le & Bažant, 2014).

One pioneering research project of particular interest in the context of reinforced concrete bridge decks came from Valette, who researched bridge components for railroads in France. The decks were tested at 500 cycles per minute with two point loads, and two of the three specimens had a fatigue failure of the steel. Valette concluded that mild steel is adequate for various types of moving or stationary loads (Valette, 1947).

Tilly (1979) gives a brief overview on the fatigue behavior of reinforcing bars for reinforced concrete. He noted that larger diameter bars have reduced fatigue strength. He also noted that from the research, corrosion can cause a 35% reduction in fatigue strength. According to Tilly, there is a need for long-term testing to assess corrosion fatigue that more closely models typical service life.

Raithby (1979) made the interesting observation, after testing a multitude of static and fatigue specimens at varying ages and moisture contents, that fatigue behavior imitates static behavior. He observed that concrete specimens with a higher flexural capacity will have proportionately larger fatigue strength. He suggests that this relationship will permit some extrapolation when trying to determine fatigue strengths of different concrete mixes and conditions. This relationship can be utilized to some extent to understand service and ultimate load behavior of bridge decks subjected to a variety of conditions.

Hsu (1981) stated that railroad bridges, highway bridges, and pavements will experience anywhere between 100,000 to 10,000,000 cycles of loading over the course of their service life. This number surely increases as the population increases, but because these values were the "target" of most of the research, cycle repetitions within this range are accepted as high cycle fatigue. Hsu also related the fatigue strength, number of cycles, stress range, and period of repetitive loads, thus creating a "four-variable" fatigue relationship.

Sonoda and Horikawa performed a series of fatigue tests on twenty 1/3-scale reinforced concrete bridge deck models and found moving loads to be much more detrimental to the fatigue strength of a deck than a stationary pulsating load. Figure 2.4.3 shows typical grid-like cracking patterns demonstrated after cycles of moving loads (Sonoda & Horikawa, 1982). They also concluded that transverse reinforcement is much more important in the case of moving loads than fixed-point cyclic loading. Perikardis and Beim (1988) arrived at a similar conclusion for moving fatigue loads on a bridge deck.

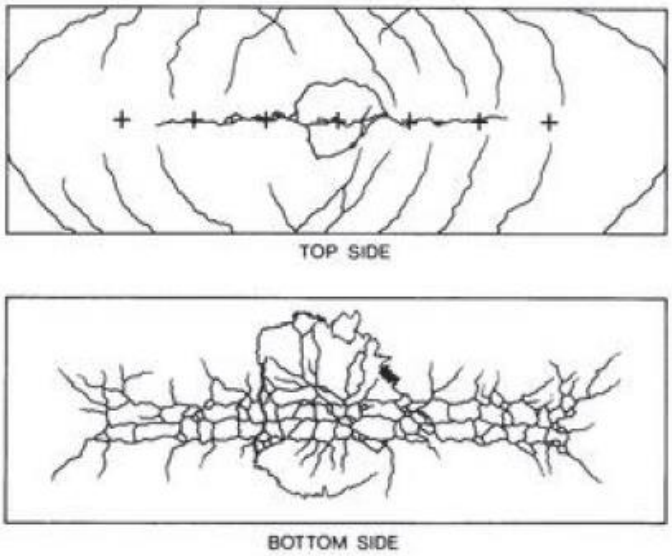

Figure 2.4.3 Cracking developed due to moving load, (Sonoda & Horikawa, 1982)

Researchers agree that the governing limit state for the majority of bridge decks is punching shear (Batchelor, Hewitt, & Csagoly, 1978; Graddy, Kim, Whitt, Burns, & Klingner, 2002; Natário, Fernández Ruiz, & Muttoni, 2015; Okada, Okamura, & Sonoda, 1978; Perdikaris, Beim, & Bousias, 1989; Youn & Chang, 1998). Therefore, an understanding of the shear fatigue mechanism is paramount to understanding bridge deck behavior.

Kesler and Chang (1958), while performing fatigue experiments on beam specimens, recognized that some of their specimens were failing in shear. The two types of shear fatigue failures they defined were "diagonal cracking" and "shear-compression." Diagonal cracking was characterized by the sudden development of a 45° shear crack that traveled from the tension region through the compression zone and resulted in a sudden failure. Shear compression failures also demonstrated a shear crack that propagated from the tension region into the compression region, but the diagonal crack did not develop as quickly, and the beam still sustained load cycles prior to failure. Gallego et al. (2014) developed a mechanical model that describes the shear crack propagation described by Kesler and Chang.

Many researchers have made experimental and analytical attempts at qualifying the shear fatigue mechanism in bridge decks without any shear reinforcement (Batchelor et al., 1978; Fang, Tsui, & Burns, 1990; Graddy et al., 2002; Youn & Chang, 1998). Batchelor et al. (1978) found that steel-reinforced

bridge decks that have not experienced a failure in less than 2 million cycles are not likely to experience a failure at the subjected load level.

2.4.2 FRP Fatigue

In 1991, the National Research Council advised that there is an "urgent national need" to use composites in load-bearing scenarios. They cited improved fatigue resistance as one of the primary bases for this statement. They described the fatigue of unidirectional fiber composites as always being in the damage initiation phase, whereas metallic materials experience both damage initiation and damage propagation phases. This lack of damage propagation in composite materials is due to the rapid convergence of microcracks in the resin at discrete fiber ruptures at failure. Due to stress redistribution among the matrix and fibers after microcracking of the FRP, there is an increase in residual strength (National Research Council, 1991).

Fatigue testing of FRP bars is complicated by the difficulty of gripping the specimen without introducing local breakdown of the resin matrix at the grips. Demers (1998) reviewed tension-tension fatigue tests for FRP specimens subjected to cyclic loading of 5 Hz or less and without any environmental parameters. She established a linear lower bound 95% confidence level, shown in Equation 2.4.1 for different stress ranges based on the prior research.

$$\frac{S_{max}}{S_{min}} = -0.078 \log N + 0.790 \qquad (2.4.1)$$

Where

- S_{max} = Maximum tensile fatigue stress in fatigue load cycle
- S_{min} = Minimum tensile fatigue stress
- N = Fatigue life measured in cycles

Chaallal and Benmokrane (1993) investigated FRP rods under cyclic loading, but they had to fabricate special rectangular coupons due to the repeated failure of the bars in the anchorage zones. Adimi et al. (2000) recognized that FRP bars are embedded in concrete in service conditions for reinforced concrete members and developed a test method that simulated FRP fatigue in service conditions. Their test setup consisted of two large top and bottom concrete blocks that serve as grips and a smaller concrete block in the middle that is separated from the anchor blocks by cardboard. The bars showed surface degradation and matrix cracking due to the friction between the concrete and the FRP bars. Figure 2.4.4 shows a typical test specimen.

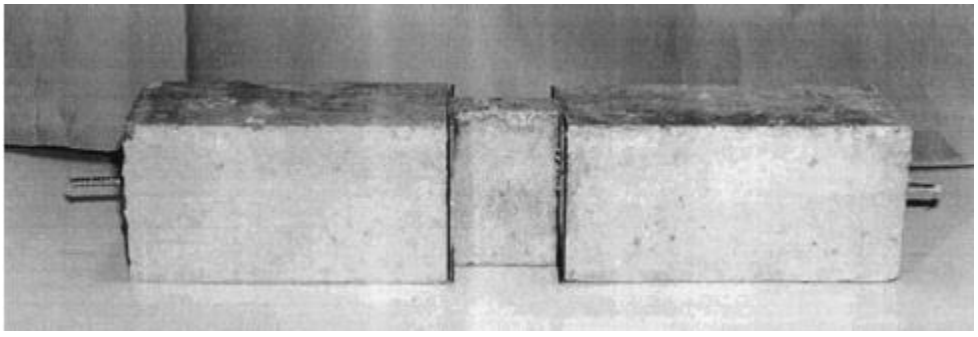

Figure 2.4.4 FRP fatigue specimen to prevent gripping damage, (Adimi et al., 2000)

Noël and Soudki (2014) performed fatigue experiments, on both FRP bars subjected to air and loaded axially, as well as concrete beam-hinge specimens. The axial specimens had to be machined between the supports to ensure that the stress concentrations at the wedge anchors were less than the stress concentration at the reduced critical cross-section. The FRP beam-hinge specimens had a lower fatigue life than the axial specimens. They suggested that the friction between the FRP bar and the concrete accounted for the decrease in fatigue life at similar loadings.

With the results of this experiment, Noël and Soudki related the effect of concrete on the cyclic behavior of GFRP-reinforcement by introducing a stress concentration factor K_{te}. This parameter modifies the nominal stress in the bar as shown in Equation 2.4.2. Equation 2.4.3 gives a power law function that was calibrated to the data in the experiment using a least-squares regression and quantifying the fatigue life as the dependent variable.

$$\sigma_e = K_{te}\sigma_n \tag{2.4.2}$$

$$\sigma_e = 1{,}793.2N^{-0.147} \tag{2.4.3}$$

Where

- σ_e = Effective stress value for fatigue calculations
- K_{te} = Effective fatigue stress factor accounting for the presence of concrete
- σ_n = Nominal stress in the FRP bar calculated using elastic cracked section analysis
- N = Number of load cycles

It is important to note that a similar procedure must be effectuated for different loading scenarios and environmental conditions to obtain the applicable stress concentration factor value, but Noël and Soudki suggest a value of 1.6 be used for K_{te} for regular design scenarios.

Porter et al. (1993) performed field and laboratory studies on FRP tie rods in pavements at joints to understand fatigue, static, and dynamic behavior of these bars. Despite the fact that FRP is weaker in shear than steel, they found that when subjected to cyclic loading, the FRP dowels performed comparably to the steel rods in shear fatigue up to 10 million cycles.

Kumar et al. (1998) performed some of the first fatigue testing on bridge decks reinforced with GFRP rebar. They cast four concrete decks with varying deck to girder connection details and subjected one of the decks to posttensioning. The decks were tested at a frequency of 1 Hz to 2,500,000 cycles. After each 100,000 cycles, a static test was performed to measure deck and stringer deflections. Following the fatigue testing, the decks were subjected to a final static loading up to 90 kips.

Kumar et al. noted that during the fatigue loading, several major cracks propagated parallel to the steel girders, and transverse fatigue cracks developed near the midspan and loaded area, and together the cracks formed a grid-like pattern. The majority of these cracks formed in the first 500,000 cycles. The degradation rates (slope of the deflection versus number of cycles) of the FRP decks were comparable to steel decks. They determined that 2,000,000 cycles could be "conservatively assumed" as 80% of the fatigue life of the deck.

Klowak et al. (2006) described the static and fatigue behavior of "second generation steel-free bridge decks." They conceptually divided one monolithically cast deck into three segments. Segment A was a control steel-reinforced deck, segment B was a steel free/CFRP hybrid design with a CFRP crack control

grid, and segment C was a steel free/GFRP hybrid design with a GFRP crack control grid. Both segments B and C had external steel straps on the bottom of the deck segments.

Klowak et al. subjected the decks to 25-ton fatigue loading for 1 million cycles, and then increased the fatigue load to 60 tons for subsequent cycles until failure. The maximum crack after the 25-ton fatigue loading for all three deck segments was reported as 0.4 mm. They concluded that the steel-free system with an internal FRP crack control grid and external steel strap precludes the development of cracks and mitigates corrosion. Of all three segments, the second-generation steel-free bridge deck segment with the GFRP reinforcement demonstrated the best fatigue performance.

El-Ragaby et al. (2007) performed full-scale bridge deck testing to describe the fatigue behavior of GFRP-reinforced bridge deck panels with varying top reinforcement ratios. Four GFRP-reinforced slabs (S1, S2, S3, and S4) and one steel-reinforced slab (S0) were cast and tested under differing fatigue schemes. The decks were instrumented with 26 strain gauges to measure strains in the reinforcing bars and upper concrete surface; six LVDTs were placed underneath the slabs to measure deflection, and one LVDT was installed at the first crack location to observe crack widths during fatigue.

Four of the slabs were subjected to variable amplitude fatigue loads that were multiples of the Canada Highway Bridge Design Code (CHBDC) fatigue limit state. Each fatigue step in the variable amplitude loading consisted of 100,000 cycles at a frequency of 2 Hz with a minimum load of 15 kN and a maximum load of 1.5, 2, 3, and 4 times the fatigue limit state. If failure occurred during the fatigue step, then testing was stopped. If failure did not occur, then a monotonic test with a load of 1.5 times the fatigue limit state load was applied, and the next level of variable loading would be applied for 100,000 cycles following the static load.

Slab S2, which was reinforced exactly the same as slab S1, was subjected to constant amplitude fatigue loading, with a minimum load of 15 kN and a maximum load equal to the fatigue limit state for 4 million cycles at 4 Hz. Based on their data, El-Ragaby et al. concluded that under variable amplitude loading, the steel bridge deck failed under fewer cycles than the GFRP-reinforced bridge decks. The results from the GFRP-reinforced decks showed similar results regardless of the top reinforcement for lower load levels; however, dissimilarities became apparent at higher loads. Even after the 4 million cycles, the GFRP bridge deck did not fail. They concluded that GFRP-reinforced concrete decks perform better in fatigue and have a longer fatigue life than steel decks. They attributed the improved performance to the close modulus of elasticity for GFRP and concrete.

Sivagamasundari and Kumaran (2008) investigated the flexural behavior of GFRP-reinforced slabs under fatigue loads. The slabs cast were simply supported and failed in flexure. Seven of the 21 one-way slabs were subjected to a monotonic loading until failure. Another seven slabs were subjected to constant amplitude fatigue loading and had a minimum and maximum fatigue load of 10 and 80 percent of the ultimate static load, respectively. The cycles were applied at a frequency of 4 Hz. The final seven slabs experienced variable amplitude fatigue loading at steps of 20%, 40%, 60%, and 80% of the ultimate load for 10,000 cycles each step.

Sivagamasundari and Kumaran found that the damage accumulation of the steel-reinforced slabs was greater than for the GFRP slabs. They also determined that their decks reinforced with sand-coated GFRP experienced the smallest residual deflection and the highest stiffness under cyclic loading. The cracks measured during testing satisfied the code recommendations at the service limit state.

Carvelli et al. (2010) investigated the fatigue performance of four full-scale bridge decks designed with GFRP to the Eurocode specification. Fatigue loading was applied at a frequency of 0.2-1.25 Hz depending on the system capacity at varying deflections. Two hydraulic actuators provided alternating

pulsating loads to mimic a moving load. The load was conservatively applied to an area of 200 x 300 mm, which is smaller than the design area, and the edges of the deck were simply supported. Carvelli et al. justified the simple supports by citing Kirchhoff's plate theory and asserting that, due to the thin nature of the deck, the free edges of the deck have little influence on the deck's behavior. The first deck was tested at 1.5 times the design fatigue load; the second slab was tested at 2 times the load on the first slab; the third slab was tested at 3 times the load on the first slab; and the fourth deck was tested monotonically.

No debonding of the GFRP was seen in any of the static or cyclic testing. Displacement increased very quickly during the first 100,000 and 10,000 cycles for the first and second decks, respectively. This rapid increase in deflection then was followed by a stabilization period with minimal deflection increase. The third deck failed quickly after 403 cycles of a load 4.5 times greater than the required fatigue load. The slabs performed very well compared with the Eurocode serviceability limit states, even with conservative loading and contact areas.

Yost et al. (2015) investigated the structural response of steel and GFRP-reinforced bridge decks when subjected to AASHTO's prescribed service and fatigue loading. Two full-scale decks were designed using the traditional method and the empirical method. The empirical design method accounts for the compressive membrane forces that resist wheel loads in composite bridge decks. As shown in Figure 2.4.5, the steel and GFRP decks were conceptually divided into two sides according to the design methodology. The loading was then applied at several locations to induce a maximum negative and positive moment, respectively.

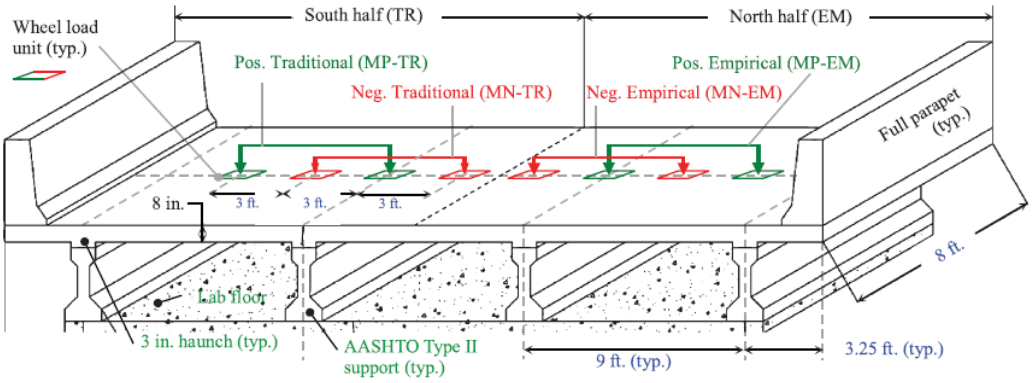

Figure 2.4.5 Typical geometry and load cases, (Yost et al., 2015)

Each deck load case was subjected to 2 cycles at 60 kips to induce cracking. Following this cracking load, 100 cycles at 80 kips was applied to achieve a "steady state stiffness" before the fatigue loading. The fatigue load was applied for 1 million cycles at 36 kips and was followed by 1 million cycles at the service limit state of 64 kips. The frequency of the fatigue loading was held constant at 2 Hz for the duration of the experiment. Three LVDTs measured deflections, strain gauges were placed at 18 inches on center on the top surface centerline to measure concrete strains; three pi gauges measured crack openings during fatigue testing.

Yost et al. determined that the crack widths, deflections, and concrete strain were more severe in the decks designed using the empirical method. The steel deck violated the allowable deflection, crack width, and concrete strain when designed with the empirical method. The GFRP-reinforced deck satisfied all of the criteria for both design methodologies.

You et al. (2015) tested eight full-scale bridge decks to evaluate the performance of GFRP-reinforced bridge decks subjected to different fatigue load magnitudes. Three different load magnitudes were applied for a minimum of 2 million cycles on each deck at a frequency of 3 Hz. Shear studs were included to provide composite action within the slabs. Strain gauges were placed on the rebar to measure rebar strain, five LVDTs measured the deformation at different locations under the deck around the loaded area and supports, and Omega-shaped crack gauges measured crack openings. A monotonic load was applied to each slab following the fatigue loading.

You et al. concluded that increasing the reinforcement ratio on the bottom of the deck did not significantly improve fatigue performance. All the failures in both GFRP and steel decks observed were punching shear failure. The GFRP decks had an increased residual deflection compared with the steel decks. They also concluded that the peak load applied under fatigue loading should be less than 58% of the maximum static load.

2.4.3 FRC Fatigue

In the early 1970s, researchers were beginning to examine the flexural fatigue mechanism for fiber reinforced concrete beams. Batson et al. (1972) cast 4 x 6 x 102-inch beams with differing steel fiber lengths and tested them under third-point loading on a 96-inch span. All the tests experienced a cyclic rate of 3 Hz and demonstrated fatigue strengths at 2 million cycles between 74% and 83% of the static flexure strength after first crack. Batson et al. observed, counterintuitively, that the beams that did not fail after 2 million cycles had a higher modulus of rupture than the pre-fatigue beams. The fibers in the beams failed by pulling out rather than by breaking.

O'Neil (1978) performed a similar study on steel fiber reinforced beams in flexural fatigue, but he cast 6 x 6 x 36-inch beams. His beams also experienced 2 million cycles at 3 Hz, but he reported lower residual strengths of just over 50%. It was also observed by O'Neil that the beams that survived the 2 million cycles failed at a greater modulus of rupture than the pre-fatigue specimens.

Ramakrishnan et al. (1989) included three different fiber types, including polypropylene, and tested 6 x 6 x 21-inch beams for 2 million cycles at 20 Hz. They found that the endurance limit and fatigue strength both increased with increasing fiber content. The beams that survived the 2 million cycles were subjected to 2 million more cycles. They reported that the static flexural strength of the surviving beams, even after experiencing 4 million cycles, showed a higher static flexural strength than the initial static testing of the corresponding batch. The hooked-end steel fibers showed better fatigue strength than the straight steel fibers and polypropylene fibers.

Johnston et al. (1991) performed fatigue testing on 194 specimens with varying fiber volume fractions, fiber types, and fiber aspect ratios. The samples experienced 500,000 cycles at 15 Hz. Of all the variables, he determined that fiber dosage was the most critical to the flexural behavior of the beams. Wei et al. (1996) performed fatigue testing on fiber reinforced concrete beams that also included silica fume. They surmised that a "double composite behavior" was created by adding fibers to silica fume concrete. Under fatigue loading, the silica fume improved the interfacial zone bonding, and the fibers provided crack control and mitigation for the beams.

By the late 1990s, mechanical models and analyses were being prepared to predict fatigue behavior of FRC materials. Spadea and Bencardino (1997) prepared a moment curvature model for a concrete section reinforced by both conventional, discrete reinforcement as well as fiber reinforcing dispersed throughout the mix. Their model predicts increases in both yield and ultimate moment as well as more energy absorption during cyclic loading in these hybrid FRC and steel rebar reinforced beams. Li and Matsumoto (1998) developed a crack growth model that also predicted fatigue life of FRC materials in flexure.

Zhang et al. (1998) used fatigue loading at a frequency of 2 Hz and a stress ratio of 0.2. They found that at failure in fatigue, the max deflection is very close to the same deflection on the descending portion of the static testing load-deflection curve at the corresponding load. Singh and Kaushik (2003) found after 67 flexural fatigue tests and 54 static tests that the fatigue behavior of fiber reinforced concrete follows a two-parameter Weibull Distribution.

Lee and Barr (2004), in an overview of the available fatigue literature for plain and fiber reinforced concrete, summarized that while plain concrete shows no fatigue limit, fiber reinforced concrete appears to have an endurance limit at 2 million cycles. They also talked about some of the discrepancies in concrete fatigue literature and stated that more research is needed to completely understand fatigue behavior of plain concrete and FRC. Fatigue behavior of FRC in compression shows no improvement over plain concrete, but FRC shows greater fatigue behavior in flexural specimens than plain concrete specimens.

Some of the "Steel-Free Bridge Decks" in Canada have fiber reinforcing, but this reinforcing is required for these types of bridges as a method of crack control by the Canadian bridge design code. Although fatigue experiments have been conducted on these bridge decks, as far as this author is aware, the additional flexural or punching shear capacity under fatigue loading was not quantified for the additional fibers (Klowak et al., 2006; Memon, 2005; Scaletta, 2015).

An experimental study performed in 2006 by Gopalaratnam et al. (2006) investigated the fatigue behavior of a "hybrid steel-free reinforcing system" that had continuous FRP bars with short discrete polypropylene fibers. Three different types of full-scale slabs (14'6" parallel to span by 5'0" perpendicular to span) were tested.

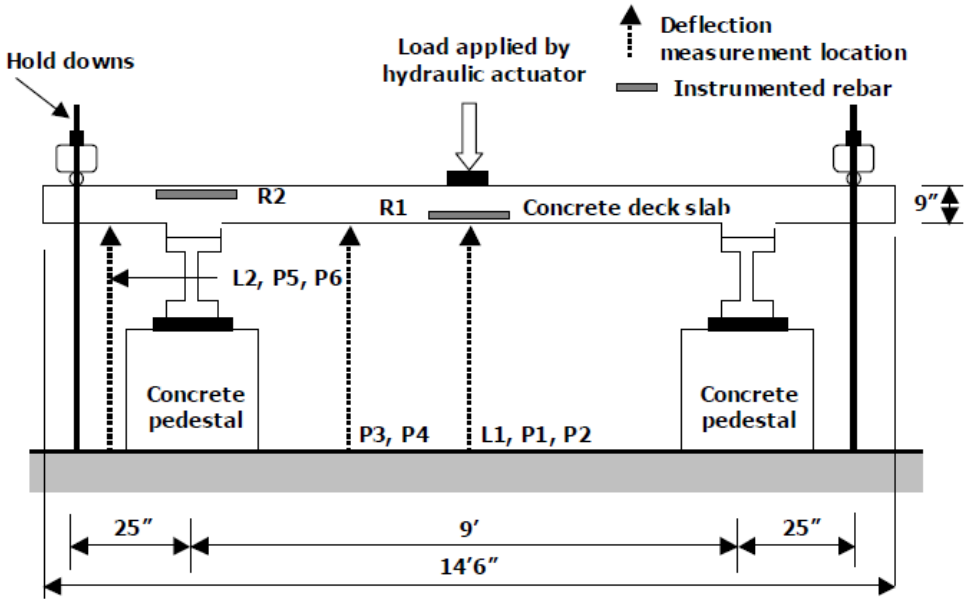

Figure 2.4.6 Static and fatigue setup, (Gopalaratnam et al., 2006)

The control deck had epoxy coated rebar in a plain concrete mix, the second type had GFRP bars in a fiber reinforced concrete mix, and the third type had alternating GFRP and CFRP with the same fiber mix as the second type. The fatigue tests were performed using a 3 Hz sinusoidal loading up with an upper load limit of 20 kips and a lower limit of 10 kips to 1 million cycles. The span between girder supports

was 9 feet and hold-downs were used to place a negative moment region over the supports as shown in Figure2.4.6.

They found that the stiffness degradation of the hybrid GFRP and hybrid GFRP/CFRP was similar to that of the epoxy coated steel rebar decks. They also concluded that, although the fibers affect the near surface crack widths, they are insignificant for "global properties." The crack widths of the hybrid GFRP/CFRP slab were comparable to the steel control deck, while the GFRP deck had larger cracks. Under service loading, Gopalaratnam et al. concluded that the fatigue performance of cracked FRP reinforced slabs is comparable to the steel slabs during the 1 million cycles.

2.5 Punching Shear Behavior

2.5.1 Steel Reinforced Punching Shear

It has been well documented that an *in situ* bridge deck will experience punching shear at the ultimate limit state (Batchelor et al., 1978; Graddy et al., 2002; Natário et al., 2015; Okada et al., 1978; Perdikaris et al., 1989; Youn & Chang, 1998). The AASHTO empirical method is a prescriptive reinforcement method and is an attempt at quantifying the compressive membrane action (CMA) in a bridge deck with sufficient transverse stiffness at the composite deck-girder connections.

Amir et al. (2015) tested 1:2 scale bridge deck specimens cast integral with girder supports. Their results showed good agreement with the predictive behavior of a finite element analysis that accounted for the girder effects. They also compared ACI, EN, fib Model Code, and other standards to see how the punching shear behavior was predicted by each. They found that none of the codes makes use of the beneficial compressive membrane action.

Graddy et al. (2002) performed tests on full-scale, cast-in-place bridge deck specimens and observed that the punching shear in the deck sections is significantly higher than the AASHTO or ACI predictions. They also concluded that arching action is achievable with simple supports but does not significantly increase the flexural capacity of the members.

The ACI code provisions for punching shear in steel-reinforced decks were developed in the early 1970s and are still in use today. Equations 2.5.1, 2.5.2, and 2.5.3 show the three punching shear equations for two-way shear in concrete members (ACI Committee 318, 2014):

$$v_c = 4\lambda\sqrt{f_c'} \tag{2.5.1}$$

$$v_c = \left(2 + \frac{4}{\beta}\right)\lambda\sqrt{f_c'} \tag{2.5.2}$$

$$v_c = \left(2 + \frac{\alpha_s d}{b_0}\right)\lambda\sqrt{f_c'} \tag{2.5.3}$$

Where

- v_c = Stress corresponding to nominal two-way shear strength, psi
- λ = Lightweight concrete modification factor (1.0 for normal-weight concrete)
- f_c' = Compressive strength of concrete, psi
- β = Ratio of long to short dimensions of concentrated load
- α_s = Constant to account for location of load on slab (40 for interior, 30 for edge, and 20 for corner loads)
- d = Distance from top of compression block to centroid of tensile reinforcement, in.
- b_0 = Perimeter of the critical section for two-way shear, in.

Equation 2.5.2 accounts for the aspect ratio of the loaded area. For ratios larger than two, Equation 2.5.1 yields non-conservative stresses on the long sides of the loaded area. Equation 2.5.3 accounts for the depth of the section relative to the loaded perimeter. For thin slabs with large loaded areas, the stresses in the section decrease. The AASHTO provisions for punching shear are identical to Equation 2.5.1 for the simple case. However, the units are input in ksi, rather than psi.

2.5.2 GFRP Reinforced Punching Shear

Many researchers have developed equations and models to accurately predict punching shear behavior. Including all of the efforts at quantifying this mechanical behavior is outside of the scope of this report. Therefore, only a few of the most relevant experiments, equations, and models are included in this paper.

In 2000, Matthys et al. (2000) conducted 17 punching shear tests on square slabs with sides of 3.28' (1 m) and slab depths of 4.7" or 6" (120 mm or 150 mm). The slabs had either FRP reinforcement (CFRP or GFRP) or steel reinforcement. For the FRP-reinforced slabs, there was significant slip prior to failure, resulting in larger deflections than the steel counterpart decks. They also determined that a lower stiffness deck reinforcement results in a decrease in the punching shear cone angle. They also found that the FRP decks with similar flexural strengths saw a decrease in punching shear load and an increase in deflection.

Other researchers also found that the decrease in the stiffness of the FRP composites results in reduced capacity and increased deflections at the ultimate limit state. Therefore, a reduction is required to account for this discrepancy in stiffness. Multiple researchers have studied this and performed experiments to quantify this behavior (Bouguerra, Ahmed, El-Gamal, & Benmokrane, 2011; Carrette & El-Salakawy, 2018; S El-Gamal, El-Salakawy, & Benmokrane, 2005; Hassan, Fam, & Benmokrane, 2016; Hussein & El-Salakawy, 2018; Ju, Park, & Park, 2018; J.-H. Lee, Yoon, Cook, & Mitchell, 2009; Metwally, 2013; Ospina, Alexander, & Cheng, 2003; Zaghloul, Mahmoud, & Salama, 2008).

The ACI code equations developed in ACI 440.1R-15 attempt to account for the stiffness of the FRP. Equations 2.5.4 and 2.5.5 contain these modified equations.

$$V_c = 10\sqrt{f_c'}\, b_0 (kd) \tag{2.5.4}$$

$$k = \sqrt{2\rho_f n_f + \left(\rho_f n_f\right)^2} - \rho_f n_f \tag{2.5.5}$$

Where

- V_c = Nominal two-way shear strength of GFRP-reinforced slabs, lbs
- f_c' = Compressive strength of concrete, psi
- b_0 = punching shear perimeter, in.
- ρ_f = Fiber-reinforced polymer reinforcement ratio
- n_f = Ratio of modulus of elasticity of FRP bars to modulus of elasticity of concrete

This equation provided by the ACI tends to be over-conservative (Grimaldi, Meda, & Rinaldi, 2013); therefore, in the following paragraphs, a few different punching shear models for FRP composite reinforcements will be summarized.

The Canadian Code CSA S806-12 developed an equation for punching shear in FRP-reinforced concrete members. The minimum stress from Equation 2.5.6, Equation 2.5.7, and Equation 2.5.8 is taken

(Canadian Standards Association, 2012). This stress is then multiplied by d and b_0 to get a punching shear force.

$$v_c = 0.028\left(1 + \frac{2}{\beta_c}\right)\lambda\phi_c\left(E_f\rho_f f_c'\right)^{\frac{1}{3}} \quad (2.5.6)$$

$$v_c = 0.147\left(0.19 + \alpha_s\frac{d}{b_0}\right)\lambda\phi_c\left(E_f\rho_f f_c'\right)^{\frac{1}{3}} \quad (2.5.7)$$

$$v_c = 0.056\lambda\phi_c\left(E_f\rho_f f_c'\right)^{\frac{1}{3}} \quad (2.5.8)$$

Where

- v_c = Shear stress in concrete on punching shear surface
- β_c = Ratio of long to short side of loading area
- λ = Concrete density modification factor, 1.0 for normal-weight concrete
- ϕ_c = Resistance factor for concrete
- E_f = Modulus of elasticity of GFRP, MPa
- f_c' = Concrete compressive strength, MPa
- α_s = Parameter to account for location of load on slab (4 for interior, 3 for edge, and 2 for corner columns)

The Japanese Code JSCE-97 (1997) also contained provisions for the punching shear prediction for panels containing discrete FRP reinforcement. The equations were based on slab size, reinforcement ratio and type, and punching area compared to the depth of the section. Equation 2.5.9, 2.5.10, 2.5.11, 2.5.12, and 2.5.13 contain the equations used to evaluate the punching shear strength according to this method.

$$v_c = \beta_d\beta_p\beta_r\left(\frac{f_{pcd}}{\gamma_b}\right) \quad (2.5.9)$$

$$\beta_d = \sqrt[4]{\frac{1000}{d}} \leq 1.5 \quad (2.5.10)$$

$$\beta_p = \sqrt[3]{100\rho_f\frac{E_f}{E_s}} \leq 1.5 \quad (2.5.11)$$

$$\beta_r = 1 + \frac{1}{1 + 0.25\frac{u}{d}} \quad (2.5.12)$$

$$f_{pcd} = 0.2\sqrt{f_c'} \leq 1.2 \quad (2.5.13)$$

Where

- v_c = Shear along punching surface, MPa
- β_d = Slab depth factor
- β_p = Reinforcement ratio and type factor
- β_r = Load perimeter factor
- f_{pcd} = Design shear stress along loaded failure plane, MPa
- f_c' = Design compressive strength of concrete, MPa
- γ_b = Safety factor, typically 1.3
- u = Perimeter of loaded area

Modifications were proposed to the British Standard BS 8110-97 (British Standards Institution, 1997) by the Institute of Structural Engineers (IStructE, 1999). The change involved including a method for adjusting the equation for the lower modulus FRP reinforcement. The original BS 8110-97 equation is shown in Equation 2.5.14, and the adjusted equation is shown in Equation 2.5.15.

$$V_c = 0.79(100\rho_s)^{\frac{1}{3}}\left(\frac{400}{d}\right)^{\frac{1}{4}}\left(\frac{f_{ck}}{25}\right)^{\frac{1}{3}} b_{1.5}d \tag{2.5.14}$$

$$V_c = 0.79\left(100\rho_f \frac{E_f}{E_s}\right)^{\frac{1}{3}}\left(\frac{400}{d}\right)^{\frac{1}{4}}\left(\frac{f_{ck}}{25}\right)^{\frac{1}{3}} b_{1.5}d \tag{2.5.15}$$

Where

- V_c = Punching shear force, N
- ρ_s = Steel reinforcement ratio
- ρ_f = FRP reinforcement ratio
- E_f = FRP modulus of elasticity, MPa
- E_s = Steel modulus of elasticity, 200,000 MPa
- f_{ck} = Cube concrete compressive strength $\left(\frac{f_c'}{0.8}\right)$, MPa
- $b_{1.5}$ = Perimeter measured at a distance of 1.5d from column face, mm

Apart from codified predictive equations, several researchers have developed modifications based on their own experimental data and curve fits. Only a few of these will be included in this report. El-Ghandour modified the ACI code by taking the cubic root of n_f as shown in Equation 2.5.16 (El-Ghandour, Pilakoutas, & Waldron, 1999). El-Ghandour et al. (2000) also developed an adjustment to the British code equation in Equation 2.5.14 by adding an additional adjustment based on the strain of the GFRP as shown in Equation 2.5.17. Matthys and Taerwe (2000) also adjusted the British Code equation by grouping factors and changing the f_{ck} factor to f_c'. Carrette et al. (2018), in an overview of available FRP punching shear equations, stated that the Matthys and Taerwe equation also accounts for the low modulus FRP. The Matthys and Taerwe equation is shown in Equation 2.5.18.

$$V_c = 0.33\sqrt{f_c'}\left(\frac{E_f}{E_s}\right)^{\frac{1}{3}} b_0 d \tag{2.5.16}$$

$$V_c = 0.79\left(100\rho_f \frac{E_f}{E_s}\frac{0.0045}{\epsilon_y}\right)^{\frac{1}{3}}\left(\frac{400}{d}\right)^{\frac{1}{4}}\left(\frac{f_{ck}}{25}\right)^{\frac{1}{3}} b_{1.5}d \tag{2.5.17}$$

$$V_c = 1.36\frac{\left(100\rho_f \frac{E_f}{E_s} f_c'\right)^{\frac{1}{3}}}{d^{\frac{1}{4}}} b_{1.5}d \tag{2.5.18}$$

Where

- ϵ_y = Yield strain in steel, mm/mm

Ospina et al. (2003) found they could neglect the size effect factor term from the British code, and they also determined that the square root of the modular ratio yielded more accurate results as shown in Equation 2.5.19. To account for the continuity of rigid edge supports, El-Gamal et al. (2005) developed

Equations 2.5.20 and 2.5.21. By adjusting the value for N based on the boundary conditions, the equations will adjust accordingly.

$$2.77\left(\rho_f f_c'\right)^{\frac{1}{3}}\sqrt{\frac{E_f}{E_s}}b_{1.5}d \tag{2.5.19}$$

$$V_c = 0.33\sqrt{f_c'}b_0 d\alpha(1.2)^N \tag{2.5.20}$$

$$\alpha = 0.62\left(\frac{\rho_f E_f}{1000}\right)^{\frac{1}{3}}\left(1+\frac{8d}{b_0}\right) \tag{2.5.21}$$

Where

- α = Factor to account for the flexural stiffness of the bottom reinforcement, the area of the load, and the effective depth of the slab
- E_f = Modulus of elasticity of FRP in MPa

2.5.3 FRC Punching Shear

There are no code provisions the author is aware of that describes the punching shear behavior of FRC slabs. Several attempts have been made by researchers to describe this mechanism (Alexander & Simmonds, 1992; Cheng & Parra-Montesinos, 2010; Choi, Reda Taha, Park, & Maji, 2007; Grimaldi et al., 2013; Harajli, Maalouf, & Khatib, 1995; Higashiyama, Ota, & Mizukoshi, 2011; Maya, Ruiz, Muttoni, & Foster, 2012; Mufti et al., 1993; Nguyen-Minh, Rovňák, Tran-Quoc, & Nguyenkim, 2011; Swamy & Ali, 1982; K.-H. Tan & Paramasivam, 1994; K. H. Tan & Venkateshwaran, 2019).

Grimaldi et al. (2013) developed a simple method to treat the additional capacity of FRC slabs. They added the contributions of the concrete and the fibers as shown in Equation 2.5.22:

$$V_{Total} = V_C + V_F \tag{2.5.22}$$

Where

- V_{Total} = Combined two-way shear strength of the concrete and fibers, lbs
- V_c = Nominal two-way shear strength contribution of concrete, lbs
- V_f = Nominal two-way shear strength contribution of the fibers, lbs

The contribution of the concrete is calculated for either steel- or GFRP-reinforced slabs as given in Equations 2.5.1 – 2.5.21. To find the additional contribution of the fibers, the vertical resultant stress from the fibers is multiplied by the surface area of the punching cone, or frustum. Equation 2.5.23 gives the fiber contribution from fibers at an ultimate crack width, taken to be 0.1 in. (2.5 mm).

$$f_{fTu} = \frac{f_{R3}}{3} \tag{2.5.23}$$

Where

- f_{fTu} = Residual tensile fiber stress from FRC at ultimate limit state
- f_{R3} = Residual flexural tensile fiber stress from FRC at CMOD 0.1 in. (2.5 mm)

The area of the punching shear surface can be calculated using Equation 2.5.24:

$$S = \frac{1}{2}(p_1 + p_2)a \tag{2.5.24}$$

Where

- S = Surface area of punching shear surface of the truncated pyramid
- p_1 = Perimeter of the top of the punching cone
- p_2 = Perimeter of the bottom of the punching cone
- a = Apothem of the punching surface, or "slant height"

To find the slant height, the distance to the centroid of the reinforcement bars from the compression surface, d, must be multiplied by the cosine of the angle, θ, measured from the top surface of the deck to the punching shear cone, or $a = d/sin(\theta)$. Once the punching surface area is calculated by Equation 2.5.9, the vertical component of the fiber stress can be found using Equation 2.5.25:

$$V_F = S * f_{fTu} * \cos(\theta) \tag{2.5.25}$$

Where

- θ = Angle of punching, measured from top surface of deck to punching surface

Although f_{fTu} was back-calculated from a flexural beam test, and the stress in the FRC along the punching shear surface may be less or more than f_{fTu}, without directly developing a model to accurately predict the exact stress in the section or creating a new test procedure to evaluate this stress, f_{fTu} will be used in this report to estimate the stress in the punching shear plane that are contributed from the FRC. This has shown good agreement for several tests performed on full-scale steel-reinforced SFRC slabs (Grimaldi et al., 2013).

2.6 Literature Summary

The historical and contemporary use of FRP and FRC materials in bridge deck applications has been discussed above. There is a clear trend of increased use of composites in concrete structures, and the corrosion resistance of FRP is especially popular in elements that experience severe weather conditions, such as bridge decks. Money has been poured into alternative reinforcing schemes, including FRP composites, by various organizations since the early 2000s.

The durability of steel and GFRP was compared, and research projects attempting to predict the service life of both steel and GFRP *in situ* were summarized. Concrete spalling and delamination is caused by the expansive stresses induced by steel corrosion, and this corrosion has resulted in costly bridge deck repairs and replacements for many years. GFRP is affected by durability concerns as well, and highly alkaline environments, such as concrete, can result in fiber deterioration. Certain resins can protect the glass fibers, and alkali-resistant fibers also help prevent strength loss from alkali exposure.

The basis for flexural design of steel-reinforced concrete bridge decks and the equivalent strip method was summarized. The flexural response of GFRP was then examined, and research suggests that a compression-controlled member is desirable for a GFRP-reinforced concrete flexural member. The design of FRC beams according to current design standards was also qualified, and an attempt was made to succinctly discuss the flexural behavior of HRC beams consisting of GFRP bars in a fiber matrix.

The fatigue behavior of concrete was discussed, starting with the very earliest attempts to describe the fatigue mechanics of RC, to contemporary experiments on full-scale bridge decks. The effect of the rate of loading on concrete specimens was discussed and shown to be mostly negligible for ranges of 1-5 Hz. Experiments discussing the effect of moving loads versus stationary pulsating loads were detailed, and moving loads were found to be more critical to fatigue behavior.

The fatigue mechanism was examined from a microscopic level to a macro-scale, and different attempts to describe fatigue of concrete were discussed. Most bridge decks experience a punching shear load at failure, and the shear fatigue mechanism was discussed as observed in numerous experiments on steel- and GFRP- reinforced bridge deck panels. Overall, the researchers agree that a bridge deck experiencing service level loads will be safe for millions of cycles of loading without any significant detrimental effects.

Finally, the punching shear behavior of each deck type was analyzed. Code provisions and methods developed by research were provided for each deck type. Although there has been a lot of research done in the field of punching shear for steel, GFRP, and FRC, there is no general consensus as to which equations or prediction models are best. The punching shear mechanics are very complicated and depend on slab measurements, aspect ratio, bar stiffness, concrete strength, boundary conditions, loading area, and other parameters.

3. EXPERIMENTAL PROGRAM – FLEXURE

3.1 Introduction

This chapter contains a summary of the experiment that was designed and performed to ascertain flexural properties of bridge deck panels with different reinforcing schemes. The experiment consisted of examining the monotonic and cyclic behavior of the members. The applicable testing standards and materials designated by both the American Society for Testing and Materials (ASTM) and the European standards (EN) are described in this chapter.

The tests described below are designed to isolate the resultant effect of a corrosion-resistant hybrid reinforced concrete (HRC) bridge deck panel, which contains both discrete GFRP bars as well as discrete alkali-resistant fiberglass composite macrofibers. The experimental data from the HRC panels will be compared to panels with conventional steel reinforcing and panels with discrete GFRP bars.

The first section of this chapter details the standard tests used during the experiment as well as the material properties. The second portion of this chapter outlines the full-scale flexural deck fabrication and test setup and assumptions used to design the test. Although real bridge decks experience arching action through the rigid, composite slab-to-girder connection, justification is given below to validate the flexural specimens with simple supports.

3.2 Material Information and Testing Standards

3.2.1 Steel Rebar

The steel rebar used throughout this experiment was #5 ASTM A615 Grade 60 deformed carbon-steel rebar (ASTM A615, 2018). The steel rebar was tested according to ASTM E8 to determine its tensile properties (ASTM E8, 2016). Figure 3.2.1 shows the test setup for a typical bar with a 2-inch (50 mm) extensometer. Figure 3.2.2 shows the failed specimen with the necked region at the rupture.

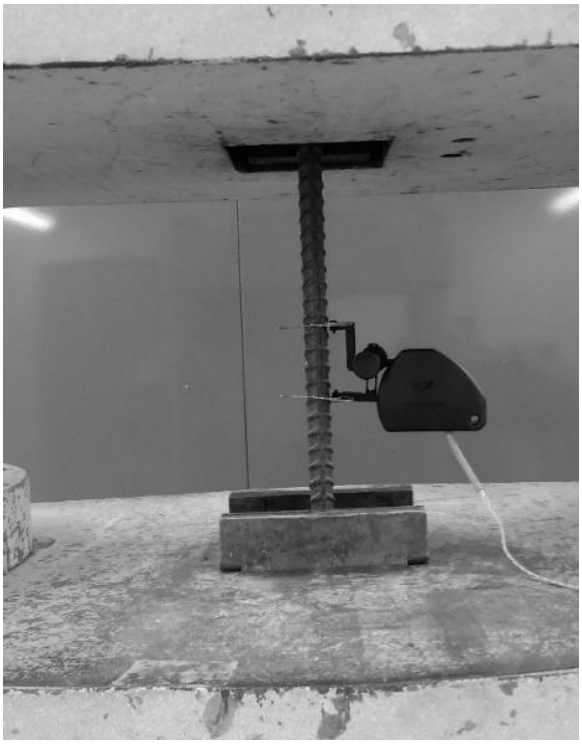

Figure 3.2.1 Steel rebar tensile test setup

Figure 3.2.2 Necked region

3.2.2 GFRP Rebar

The GFRP used in this project was Aslan 100 #6 (19 mm) rebar. The bars used are provided with surface undulations and a sand coating to provide a better bond to the concrete. The matrix of the rebar consists of vinyl ester resin, which has shown improved alkaline resistance compared with other resins (Brahim Benmokrane et al., 2002). The continuous fiber reinforcement of the bars is electrical grade glass fibers (E-glass) at a volume fraction of 70% minimum.

Per the ASTM D 7205 standard, anchors are recommended, to prevent stress concentrations at the grips (ASTM D7205, 2016). To obtain the tensile properties of the GFRP for this experiment, the specimens were potted in schedule 40 steel pipe as shown in Figure 3.2.3. To ensure that the GFRP would rupture prior to the pullout of the specimens from the grips, Dexpan Expansive Demolition Grout was used to confine the bars in the anchors. A simple jig was utilized to keep the anchors straight on the bar. This prevented eccentric loading and guaranteed that the load applied to the bar by the machine acted coincident to the longitudinal axis of the bar. The test setup is shown in Figure 3.2.4, and Figure 3.2.5 shows the beginning of a failure. Figure 3.2.6 shows a specimen that is completely failed.

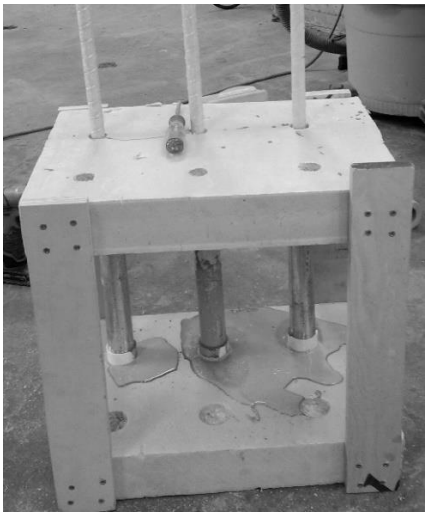

Figure 3.2.3 Using a jig to keep GFRP bars vertical

Figure 3.2.4 **GFRP tensile test setup**

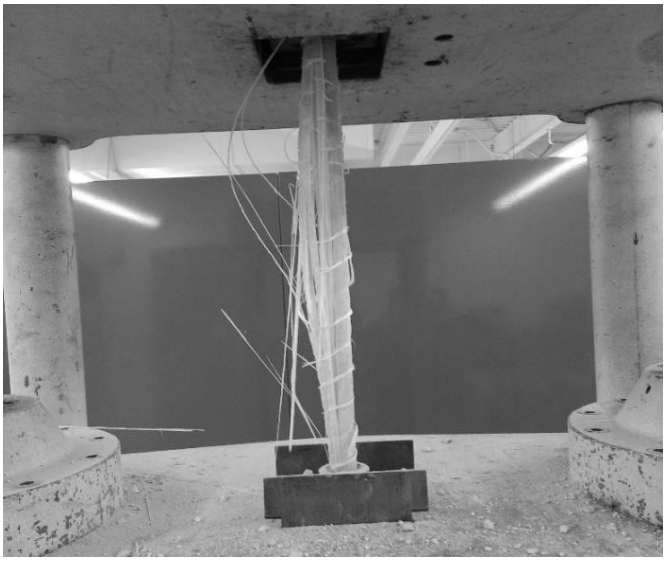

Figure 3.2.5 GFRP at rupture initiation

Figure 3.2.6 Fully ruptured GFRP specimen

3.2.3 Concrete Mix Properties

Both the steel-reinforced decks as well as the GFRP-reinforced decks used plain concrete from a local batch plant with no fiber addition. The HRC decks contained the same mix design; however, fibers were added according to the design dosage in the lab. The fibers used in this project for the FRC consisted of 1.70 in. (43 mm) Cem-FIL Minibars™ as shown in Figure 3.2.7. These AR-glass FRP composite macrofibers contain alkali-resistant (AR) glass fibers in a vinyl ester resin. Table 3.2.1 lists additional geometric and mechanical properties of the fibers.

Figure 3.2.7 Macrofibers used in this experiment

Table 3.2.1 Cem-FIL MiniBars™ properties and behavior

Property	Value
Diameter	0.03 in. (0.70 mm)
Length	1.70 in. (43 mm)
Specific Gravity	2.0
Modulus of Elasticity	6,090 ksi (42 GPa)
Tensile Strength	145 ksi (1000 MPa)

Prior to pouring the HRC decks, the fibers were measured out by weight to achieve the design dosage of 15 lb./yd^3 (8.90 kg/m^3). When the truck arrived, fibers were added to the drum by using a steel grate to ensure minimal clumping as shown in Figure 3.2.8.

Figure 3.2.8 Adding fibers through a grate to prevent clumping

In accordance with ASTM C31, eighteen 4 x 8 in. (100 x 200 mm) cylinders were taken from each batch of concrete in accordance with ASTM C31 (ASTM C31, 2019). The concrete was ordered to obtain a 28-day compressive strength, f_c', of 5,000 psi (34.5 MPa). Table 3.2.2 shows the design specifications of the mix that was commissioned for each deck.

Table 3.2.2 Design mix specifications for 5 ksi (34.5 MPa) mix

Material	Batched Amount	Specific Gravity	% Volume
Coarse Aggregate (BRIG-#57)	1520 lb/cy (900 kg/m^3)	2.70 (SSD)	34.00%
Fine Aggregate (BRIG-#8)	200 lb/cy (120 kg/m^3)	2.70 (SSD)	4.50%
Sand	1240 lb/cy (735 kg/m^3)	2.65 (SSD)	27.80%
Type II/V Cement	560 lb/cy (330 kg/m^3)	3.15	10.60%
Bridger Fly Ash	100 lb/cy (60 kg/m^3)	2.30	2.60%
MasterAir AE 200 Air Entrainer	3 oz/cy (120 g/m^3)	1.01	0.01%
MasterPozzolith 200 Water Reducer	15 oz/cy (555 g/m^3)	1.13	0.05%
MasterGlenium 3030	31 oz/cy (1130 g/m^3)	1.05	0.11%
*Water	29 gal/cy (145 L/m^3)	1.0	14.40%
Design Air Volume	N/A	N/A	6.00%

* Note that the water includes the absorbed water in aggregates.

Table 3.2.3, Table 3.2.4, and Table 3.2.5 show the mix of the steel-reinforced, GFRP-reinforced, and hybrid FRC decks by batched weight or volume, as well as percent material by volume, respectively. Two sets of HRC decks were poured, and Table 3.2.6 shows the mix design of the second set of HRC panels.

Table 3.2.3 Steel-reinforced concrete mix design

Material	Batched Amount	Specific Gravity	% Volume
Coarse Aggregate (BRIG-#57)	1520 lb/cy (900 kg/m^3)	2.70 (SSD)	34.90%
Fine Aggregate (BRIG-#8)	210 lb/cy (125 kg/m^3)	2.70 (SSD)	4.80%
Sand	1230 lb/cy (730 kg/m^3)	2.65 (SSD)	28.30%
Type II/V Cement	560 lb/cy (330 kg/m^3)	3.15	10.80%
Bridger Fly Ash	100 lb/cy (60 kg/m^3)	2.30	2.60%
MasterAir AE 200 Air Entrainer	3 oz/cy (125 g/m^3)	1.01	0.01%
MasterPozzolith 200 Water Reducer	15 oz/cy (545 g/m^3)	1.13	0.05%
MasterGlenium 3030	31 oz/cy (1140 g/m^3)	1.05	0.11%
*Water	24 gal/cy (120 L/m^3)	1.0	12.20%
Fibers	0 lb/cy (0 kg/m^3)	2.0	0%
Design Air Volume	N/A	N/A	6%

* Note that the water includes the absorbed water in aggregates.

Table 3.2.4 GFRP-reinforced concrete mix design

Material	Batched Amount	Specific Gravity	% Volume
Coarse Aggregate (BRIG-#57)	1520 lb/cy (900 kg/m^3)	2.70 (SSD)	32.60%
Fine Aggregate (BRIG-#8)	200 lb/cy (120 kg/m^3)	2.70 (SSD)	4.30%
Sand	1280 lb/cy (760 kg/m^3)	2.65 (SSD)	27.60%
Type II/V Cement	530 lb/cy (310 kg/m^3)	3.15	9.50%
Bridger Fly Ash	130 lb/cy (80 kg/m^3)	2.30	3.30%
MasterAir AE 200 Air Entrainer	1.2 oz/cy (45 g/m^3)	1.01	0.004%
MasterPozzolith 200 Water Reducer	23 oz/cy (860 g/m^3)	1.13	0.07%
MasterGlenium 3030	0 oz/cy (0 g/m^3)	1.05	0%
*Water	35 gal/cy (175 L/m^3)	1.0	16.80%
Fibers	0 lb/cy (0 kg/m^3)	2.0	0%
Design Air Volume	N/A	N/A	6%

* Note that the water includes the absorbed water in aggregates.

Table 3.2.5 HRC mix design set #1

Material	Batched Amount	Specific Gravity	% Volume
Coarse Aggregate (BRIG-#57)	1520 lb/cy (900 kg/m^3)	2.70 (SSD)	33.80%
Fine Aggregate (BRIG-#8)	230 lb/cy (135 kg/m^3)	2.70 (SSD)	5.0%
Sand	1220 lb/cy (720 kg/m^3)	2.65 (SSD)	27.20%
Type II/V Cement	560 lb/cy (330 kg/m^3)	3.15	10.50%
Bridger Fly Ash	100 lb/cy (60 kg/m^3)	2.30	2.50%
MasterAir AE 200 Air Entrainer	2.2 oz/cy (80 g/m^3)	1.01	0.08%
MasterPozzolith 200 Water Reducer	15 oz/cy (545 g/m^3)	1.13	0.05%
MasterGlenium 3030	51 oz/cy (1880 g/m^3)	1.05	0.20%
*Water	29 gal/cy (143 L/m^3)	1.0	14.30%
Fibers	15 lb/cy (9 kg/m^3)	2.0	0.44%
Design Air Volume	N/A	N/A	6%

* Note that the water includes the absorbed water in aggregates.

Table 3.2.6 HRC mix design set #2

Material	Batched Amount	Specific Gravity	% Volume
Coarse Aggregate (BRIG-#57)	1520 lb/cy (900 kg/m^3)	2.70 (SSD)	34.50%
Fine Aggregate (BRIG-#8)	190 lb/cy (115 kg/m^3)	2.70 (SSD)	4.40%
Sand	1235 lb/cy (730 kg/m^3)	2.65 (SSD)	28.10%
Type II/V Cement	560 lb/cy (330 kg/m^3)	3.15	10.70%
Bridger Fly Ash	120 lb/cy (70 kg/m^3)	2.30	3.20%
MasterAir AE 200 Air Entrainer	3.0 oz/cy (110 g/m^3)	1.01	0.01%
MasterPozzolith 200 Water Reducer	15 oz/cy (535 g/m^3)	1.13	0.05%
MasterGlenium 3030	50 oz/cy (1840 g/m^3)	1.05	0.18%
*Water	24.5 gal/cy (121 L/m^3)	1.0	12.33%
Fibers	15 lb/cy (9 kg/m^3)	2.0	0.45%
Design Air Volume	N/A	N/A	6.00%

* Note that the water includes the absorbed water in aggregates.

Although the same mix was commissioned from the same batch plant, there was a noticeable variability in the mixes that were received. The GFRP-reinforced decks had a much higher w/c ratio as shown in Table 3.2.7. No additional water was added to the mix as it arrived at the lab. According to the mix design specification sheet, the design w/c ratio was 0.38, while the specified w/c ratio for the mix was 0.40. The target amount of water was 30.5 gallons/cy (151 L/m^3).

Table 3.2.7 Water/cement ratio of the different mixes

Deck Type	w/c Ratio
Steel	0.305
GFRP	0.448
HRC1	0.368
HRC2	0.301

3.2.4 Concrete Mechanical Properties

The cylinders taken were placed by the specimens underneath 0.31 mil plastic sheeting to retain moisture during the curing process. At certain time increments, the cylinders were tested to ensure that the panels would not crack when moved around the lab. In accordance with ASTM C39, at least three 4 x 8 in. (100 x 200 mm) cylinders were tested in compression at a rate of 440 lb/min (1960 N/min). The cylinders were capped with neoprene pads as described in ASTM C39 to ensure proper and uniform contact between the testing apparatus and the cylinder (ASTM C39, 2012). Figure 3.2.9 shows the compression testing machine with a failed FRC cylinder.

Figure 3.2.9 Compression test of an FRC cylinder

The static modulus of elasticity was obtained by following the specifications outlined in ASTM C469. Using an axial compressometer, stresses and strains were recorded at values of 10%, 20%, and 40% of the expected peak cylinder strength (ASTM C469, 2014). This process was repeated three times on three different cylinders.

The splitting tensile strength was ascertained in accordance with ASTM C496. Three 4 x 8 in. (100 x 200 mm) cylinders were placed on their side and loaded perpendicular to their longitudinal axis. Wooden shims were used to ensure proper and uniform contact between the testing apparatus and the loaded specimen. The splitting strengths were only taken for the steel- and GFRP-reinforced panels, since the tensile properties of FRC are obtained using a different standard test.

The European standard EN 14651 was used to obtain the residual flexural tensile capacity of the hybrid FRC bridge decks. As discussed above, the standard requires that a 6 x 6 x 22 in. (150 x 150 x 550 mm) specimen with a span of 20 in. (500 mm) is tested in 3-point bending and loaded at a specified crack opening or deflection rate (EN 14651, 2005). The force vs. CMOD curve is then used to obtain residual strengths of the FRC for different crack openings. A crack opening displacement transducer, as shown in Figure 3.2.1, with a 6 mm range was utilized in this project to record the CMOD.

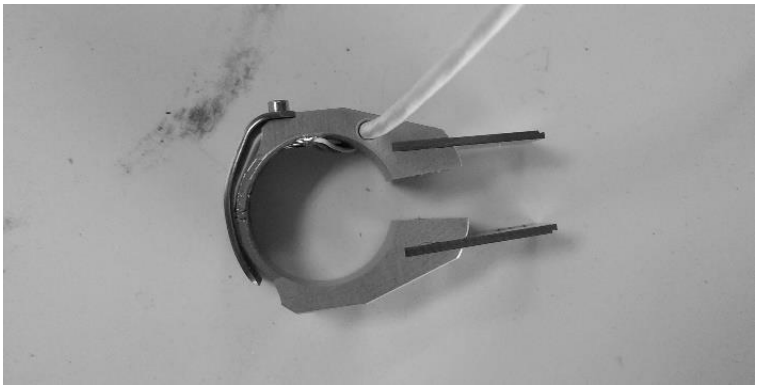

Figure 3.2.1 Crack opening displacement transducer

The specimens were taken from the large-scale batches by using three 6 x 6 x 22 in. steel molds. As required by the standard, 90% of the mold was filled by placing a large amount of FRC in the center, followed by two smaller portions on either side. The mold was then compacted by external vibration as the remaining 10% was filled. The surface was smoothed out and the beam was placed next to the bridge deck specimens until the test day. Figure 3.2.2 shows the required order for pouring the FRC molds, and Figure 3.2.3 shows two of the molds filled to roughly 90% prior to compaction.

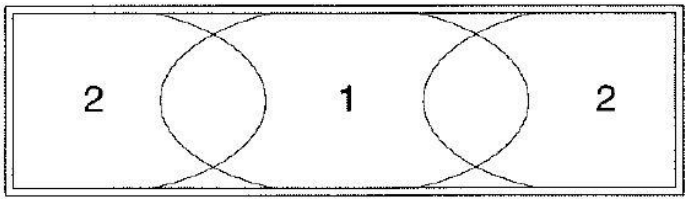

Figure 3.2.2 Specified pattern to fill up molds (EN 14651, 2005)

Figure 3.2.3 Filling up the mini beam molds

Before testing the FRC beams, they were rotated 90° on their longitudinal axis, and a 1-in. (25 mm) notch with a width of less than 0.2 in. (5 mm) was made using an MK Diamond Brick saw with a 0.015 in. (0.38 mm) segmented cutting blade as shown in Figure 3.2.4. The saw was set at the correct height for the notch, and the specimens were wet sawn at the midpoint.

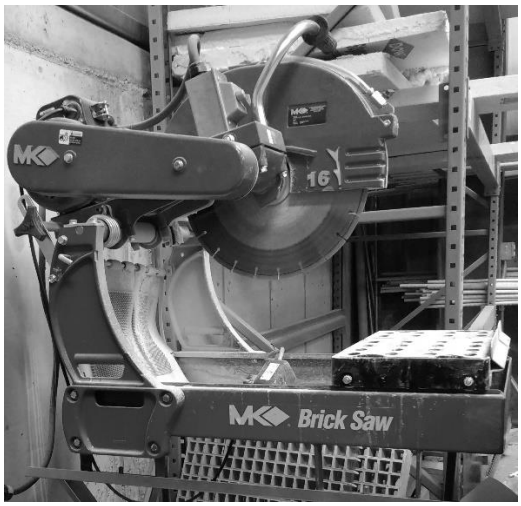

Figure 3.2.4 Saw used to notch FRC specimens

Initially, the test was attempted with CMOD control, but the Tinius Olsen electric feedback mechanism in the lab was not tuned sufficiently to control the CMOD. The rates outlined in the EN 14651 test standard are 0.002 in./min (0.05 mm/min) until the crack reaches 0.004 in. (0.1 mm), at which point the rate is increased to 0.008 in./min (0.2 mm/min). Due to these equipment limitations, deflection control was used for the rest of the experiment, as permitted by the standard. To achieve the required deflection control, the relationship shown in Equation 3.2.1 was used to obtain the necessary rates.

$$\delta = 0.85CMOD + 0.04 \quad (3.2.1)$$

Where

- δ = Deflection in mm
- $CMOD$ = Crack mouth opening displacement in mm

Therefore, the initial rate was 0.003 in./min (0.08 mm/min) until a crack width of 0.005 in. (0.13 mm) was reached. After a displacement of 0.005 in. (0.13 mm), the deflection rate was increased to 0.008 in./min (0.21 mm/min). The standard requires that the specimen achieve a crack width of 0.16 in. (4 mm) prior to stopping the test. This test procedure was executed for both sets of 6 x 6 x 22 in. (150 x 150 x 550 mm) mini beams that were cast with the respective HRC bridge deck panels. Figure 3.2.5 shows the test setup, and Figure 3.2.6 demonstrates a failed specimen. Small wood pieces were placed underneath the specimen to protect the CMOD transducer in the case of instability or collapse.

Figure 3.2.5 FRC mini beam test setup

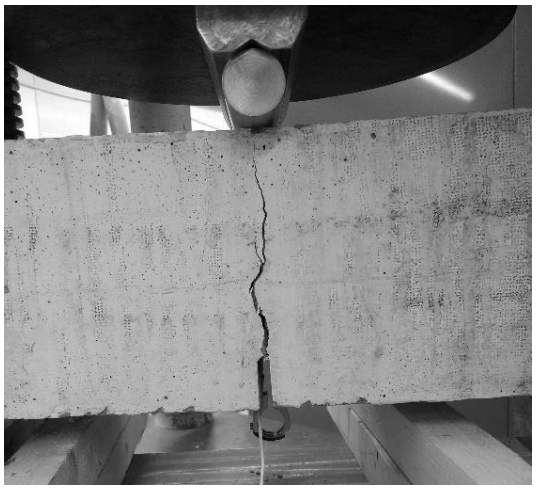

Figure 3.2.6 Failed FRC specimen

3.3 Flexural Bridge Deck Panels

The following sections will describe the design process used to detail the full-scale flexural bridge deck panels. Following the design process and deck details, the test setup for the static and fatigue experiments will be outlined. Changes to the setup partway through the experiment will be explained and justified. Any extended calculations performed will be placed in Appendix A and are based on designs performed by AASHTO and Eriksson Technologies.

3.3.1 Panel Design and Fabrication

All of the bridge panel design was done in accordance with the AASHTO LRFD specifications. The GFRP and HRC decks were designed using the guidance in the AASHTO GFRP 2018 guide (AASHTO, 2018b). An *in situ* bridge deck experiences compressive membrane action from the composite action and lateral stiffness that the bridge girders provide. The empirical bridge deck design method attempts to account for this "arching action" by providing prescriptive reinforcing requirements (AASHTO, 2018c).

Certain criteria must be met to utilize this method, and many design engineers opt for the traditional "equivalent strip method." As mentioned in Chapter 2 of this report, at its essence, the equivalent strip method is an approximate method that assumes the flexural loads imposed by the AASHTO HL-93 or tandem truck are spread out transversely over a codified distance. The designer can then find a unit moment per-foot width. Figure 3.3.1 shows how the loads are distributed in this method.

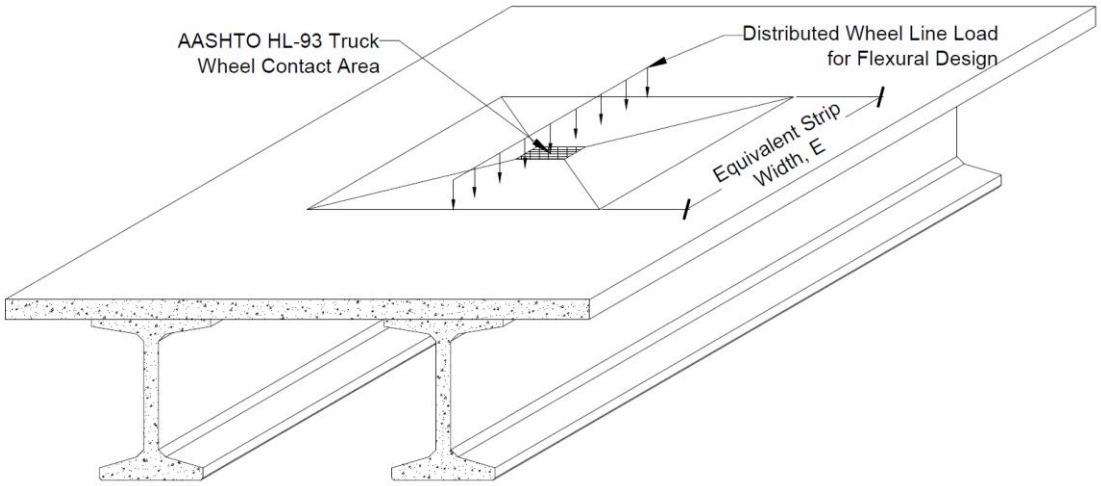

Figure 3.3.1 Equivalent strip method – wheel load distribution

Thus, even though a more complicated stress distribution is present in a bridge deck under loading, design engineers are still relating the capacity of a bridge deck to its moment capacity per-unit width. For this reason, the flexural behavior of a section of bridge deck must be understood. The simplest way to isolate flexural behavior to understand the micro- and macro-level behavior of a concrete specimen is to test a beam under four-point loading on simple supports. This ensures that no shear is present in the maximum moment region of the beam.

To simulate a real-life bridge design application, the "Prestressed Precast Concrete Beam Bridge Design" example provided by the Florida DOT was followed (Florida DOT, 2011). Section 2.06 of the report outlines the traditional bridge deck design methodology, and calculations were prepared for steel-reinforced, GFRP-reinforced, and HRC bridge deck sections using their same geometry and span.

The f_{R1} and f_{R3} values used for the fibers in the design were taken from a test report prepared by the manufacturers of the macrofibers. The bridge deck calculations are attached to this report in Appendix A. A 1.5-in. (38 mm) cover distance is provided for all bridge decks. Table 3.3.1 contains the reinforcing summary for each bridge deck type.

Table 3.3.1 Reinforcement summary

Deck Type	Transverse Reinforcement	Distribution Reinforcement
Steel	#5 (#16) Bars at 6" (150 mm) o/c	#5 (#16) Bars at 8" (200 mm) o/c
GFRP	#6 (#19) Bars at 6" (150 mm) o/c	#6 (#19) Bars at 9" (230 mm) o/c
HRC	#6 (#19) Bars at 8" (200 mm) o/c 15 lb/cy (8.90 kg/m^3) of fibers	#6 (#19) Bars at 13" (330 mm) o/c 15 lb/cy (8.90 kg/m^3) of fibers

Figure 3.3.2, Figure 3.3.3, and Figure 3.3.4 show the reinforcement layout of the steel, GFRP, and HRC bridge deck panels, respectively.

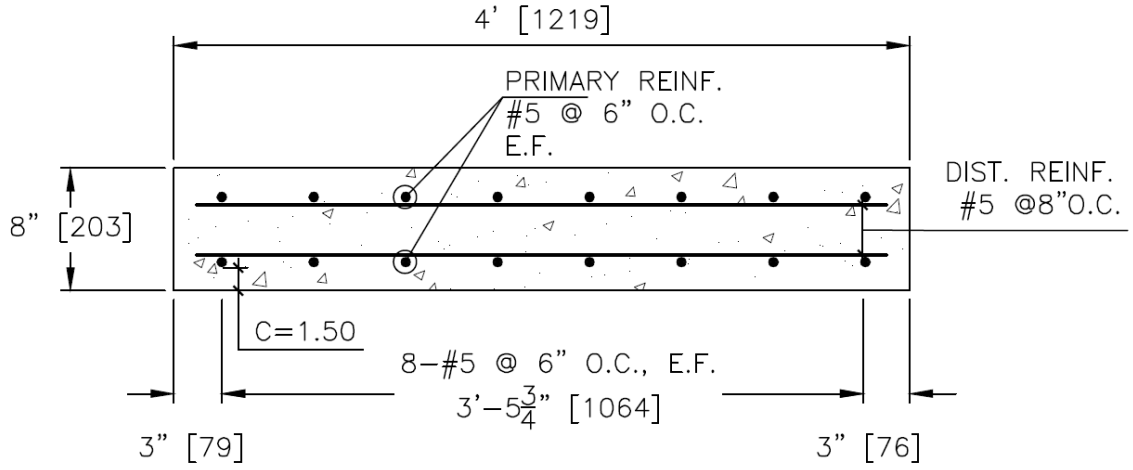

Figure 3.3.2 Steel reinforcement layout

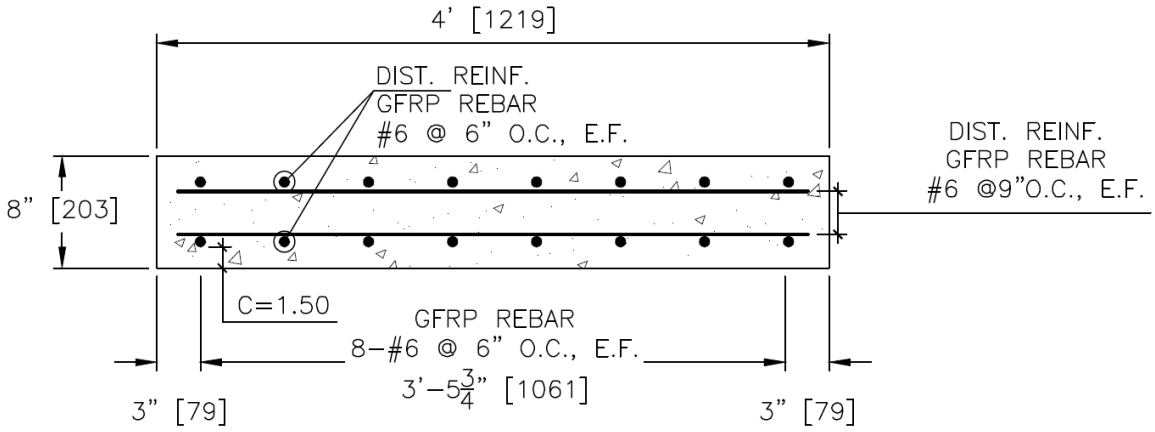

Figure 3.3.3 GFRP reinforcement layout

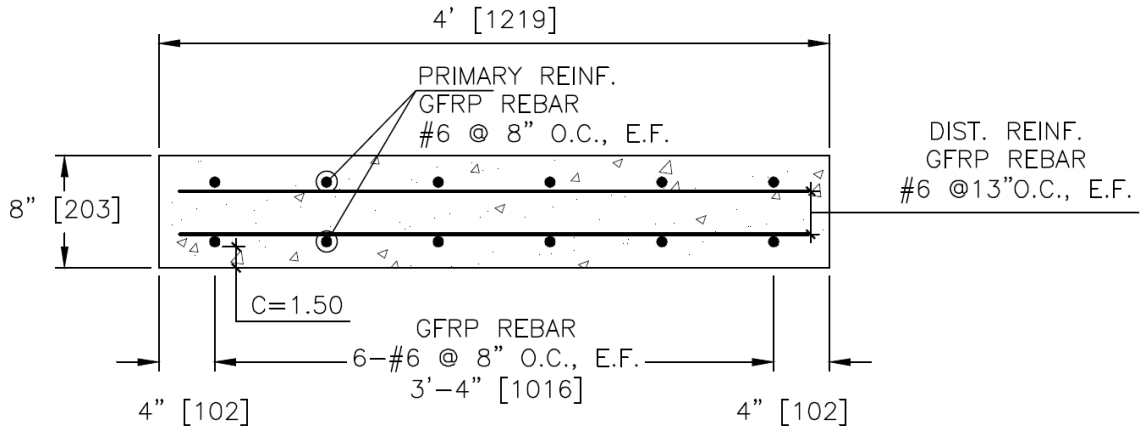

Figure 3.3.4 HRC reinforcement layout

It was determined that four 8-in. (200 mm) thick 4 x 12 ft (1.2 x 3.7 m) specimens of each reinforcing scheme would be fabricated. Two more 4 x 12 ft (1.2 x 3.7 m) HRC specimens were fabricated later for additional study of the HRC panels. Two of the specimens were tested in static flexure, while the other two of each type would experience fatigue cycles before a post-fatigue static test.

The rebar was tied according to the plans for each set of bridge deck panels, and high-density overlay (HDO) board was used to create the forms. The GFRP decks were tied using zip ties to create a completely steel-free deck system. After oiling the forms, placing the reinforcement, and ensuring the dimensions and rebar cover distance were correct, the decks were cast. Internal vibration was performed using a handheld electric concrete vibrator to guarantee proper consolidation of the concrete around the rebar as shown in Figure 3.35.

Figure 3.3.5 Internal vibration of deck panels

Care was taken to not over-vibrate the concrete. The decks were finished using a magnesium screed, bull float, and hand trowels. After casting, moist burlap was placed over the panels, and the deck panels were topped with 0.31 mil plastic sheeting to retain the moisture and provide adequate curing conditions. Figure 3.3.6 shows the steel-reinforced bridge decks prior to pouring and Figure 3.3.7 demonstrates the placement of the damp burlap on the specimens.

Figure 3.3.6 Steel-reinforced decks prior to pouring

Figure 3.3.7 Laying moist burlap on the panels

As mentioned, the fibers were added to the truck by boxes through a steel grate for the HRC panels. Due to the increased Glenium3030 in the mix, the FRC was very workable, and minimal clumping was observed during the pour. For each pour, 18 cylinders were taken and placed with the large-scale specimens to create identical curing conditions. Three 6 x 6 x 22-in. (150 x 150 x 550 mm) mini beams were taken during both of the HRC pours and left with the full-scale deck panels until it was time to notch and test them.

3.3.2 Static Loading

Static tests were performed on the bridge decks by monotonically increasing the load on the specimens. Because the design example used a girder spacing of 10 ft (3 m), the deck span was set at 10 ft (3 m). The panels were placed on pin and roller supports to create a simply supported, statically-determinate boundary condition.

The pin plates were made up of 1-in. (25 mm) thick hot rolled plates measuring 12 x 12 in (305 x 305 mm) with two small welded round bars offset sufficiently to prevent the rolling of a 2-in. (50 mm) diameter steel bar. This round bar was sandwiched between two of these pin plates. The roller plates were exactly the same as the pin plates, but without welded round bars. This enabled lateral movement of the roller with respect to the plates. Figure 3.3.8 shows the pin supports, and Figure 3.3.9 shows the roller supports. The spreader beam was also placed on pins and rollers to prevent undesired lateral restraint and thrust.

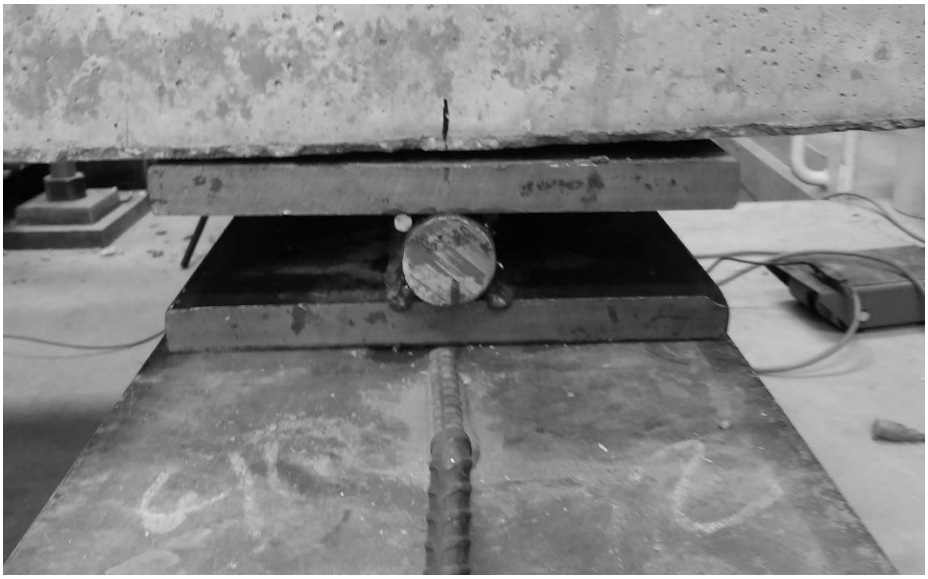

Figure 3.3.8 Pin support condition

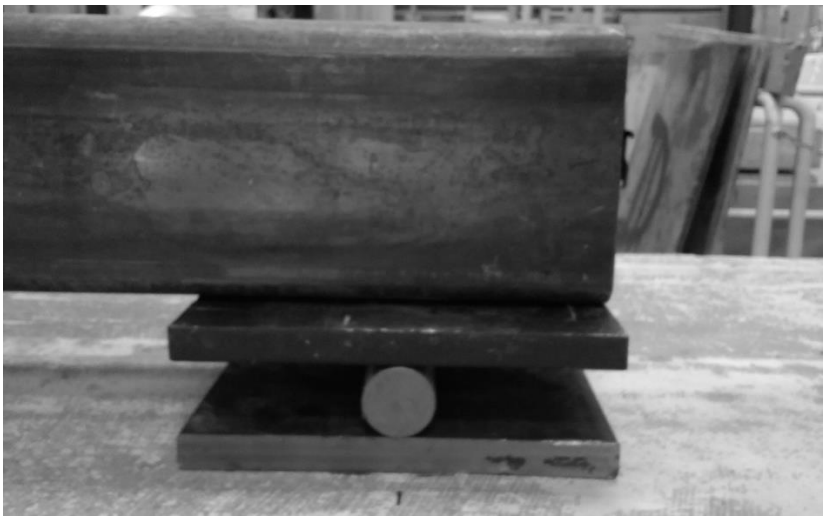

Figure 3.3.9 Roller support condition (Spreader Beam)

Two different loading schemes were utilized during the static testing portion of the experiment. Initially, a spreader beam was used to space the load by 4 ft (1.2 m). This created a 4-ft (1.2 m) section that had zero shear with a uniform maximum moment. The spreader beam was also placed on pin and roller plates as shown in Figure 3.3.. On one of the GFRP decks and GFRP decks with fibers, the spreader beam was taken out of the test setup and tested with a single point load at midspan. Figure 3.3.10, Figure 3.3.11,

and Figure 3.3.12 show the test design with a spreader beam, and Figure 3.3.13 shows a test without the spreader beam.

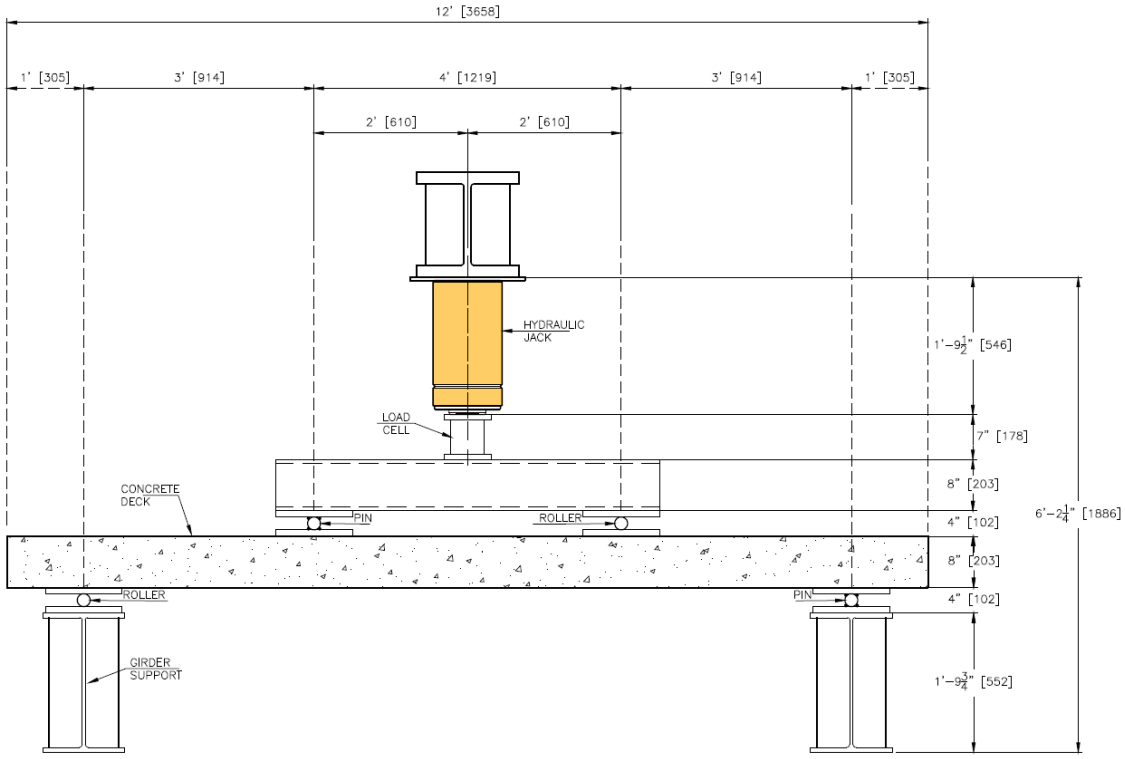

Figure 3.3.10 Static flexure test setup

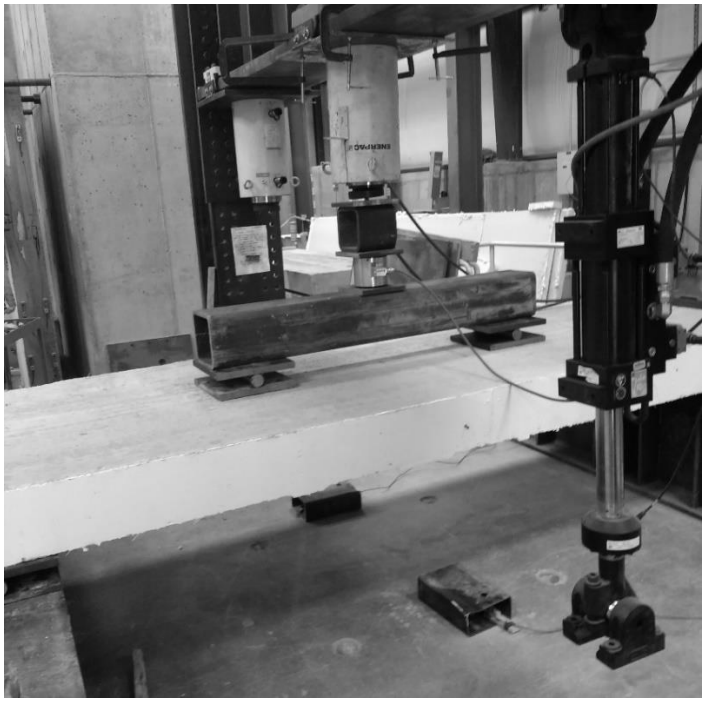

Figure 3.3.11 Static test setup (HRC deck)

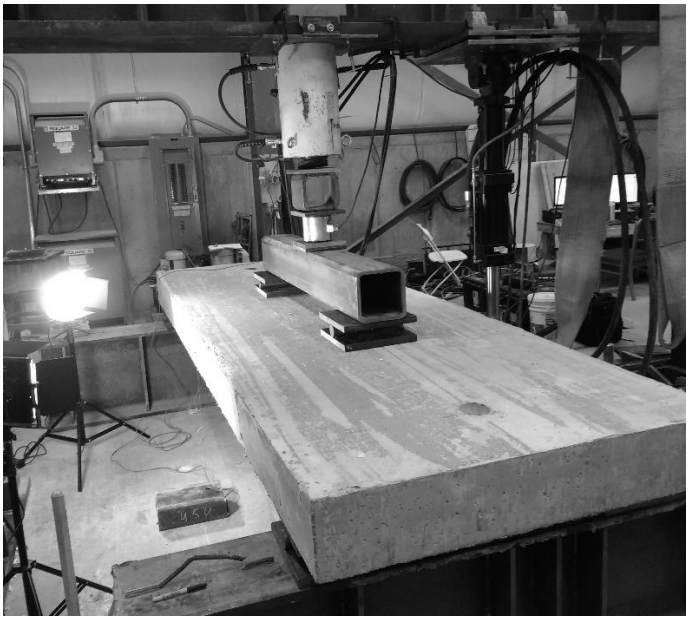

Figure 3.3.12 Static test setup (steel-reinforced deck)

Figure 3.3.13 Static test with centerline loading (GFRP deck)

Two potentiometers were placed at the centerline of the bridge deck to measure displacement, and one load cell was used underneath the hydraulic ram to measure force during testing. Steel plates and sections were used as shims to reach the required height for the test setup. The force was increased until the deck failed. The force and displacement were recorded for each deck panel and subsequently analyzed.

3.3.3 Fatigue Loading

Over the course of a design life, bridge decks will support millions of load cycles from large trucks that are similar or equivalent to the AASHTO HL-93 truck or tandem. The value of daily truck traffic on each bridge is highly variable and dependent on things such as number of lanes, road type, and overall number of vehicles passing over the bridge. To investigate fatigue on bridge deck panels, researchers typically subject their specimens from 1 to 2 million cycles of fatigue as mentioned in Chapter 2.

For this experiment, it was determined that to understand crack behavior in a uniform moment region, the spreader beam would once again be used at a 4-ft (1.3 m) spacing. Due to the simply supported boundary conditions, calculations were made to find a fatigue level live load moment for the 4-ft (1.3 m) wide bridge deck section. These calculations are provided in Appendix A. In order to maintain sufficient contact between the test setup and the hydraulic ram, a minimum fatigue load of 10% of the maximum was applied. The maximum fatigue load applied was 13.2 kip (59 kN), and the minimum fatigue load was 1.32 kip (5.9 kN). This fatigue load was applied with an MTS servo-hydraulic actuator.

Although a bridge deck in field conditions experiences these fatigue cycles over decades, a lab experiment is constrained by time. Therefore, a frequency of cycles must be selected within a reasonable range. The frequency of a number of fatigue experiments was listed in Chapter 2. For the current experiment, a frequency of 4 Hz was used for all cycles on the bridge deck panels.

The first set of bridge deck panels was subjected to 1 million cycles, and the subsequent set of panels experienced 2 million cycles. Prior to the fatigue loading, however, the decks were cracked with a monotonically increasing load to simulate a steady-state cracked bridge deck. Figure 3.3.14 and Figure 3.3.15 show the setup for the fatigue loading.

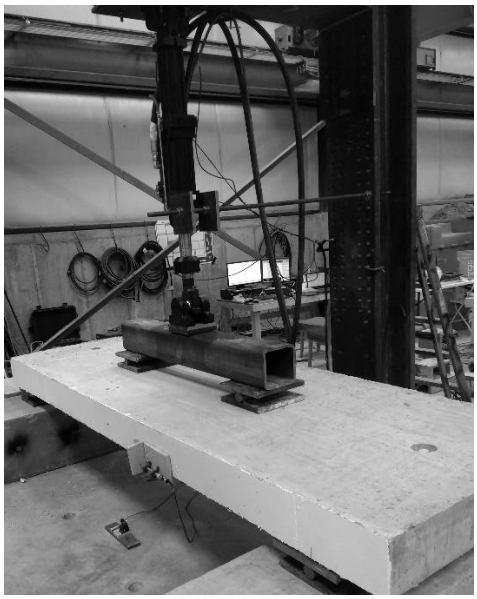

Figure 3.3.14 Fatigue test setup

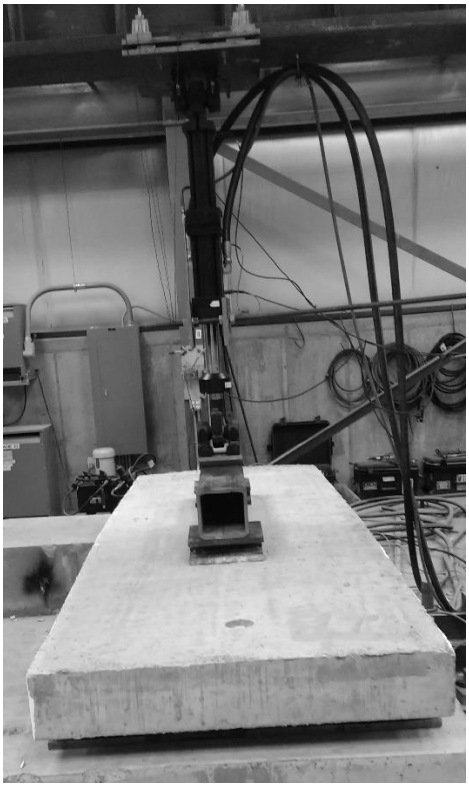

Figure 3.3.15 Fatigue test setup 2

During testing, the peak and valley deflection was monitored using two potentiometers on each side of the bridge deck panel at midspan as shown in Figure 3.3.16. The crack opening was monitored by locating the largest crack on each side prior to the fatigue loading and placing the plunger of the LVDT level with the bottom of the deck at that crack location. The LVDT spanned the crack and measured the peak and valley of the crack width during the fatigue cycles. Figure 3.3.17 shows a view from above the LVDT spanning the crack.

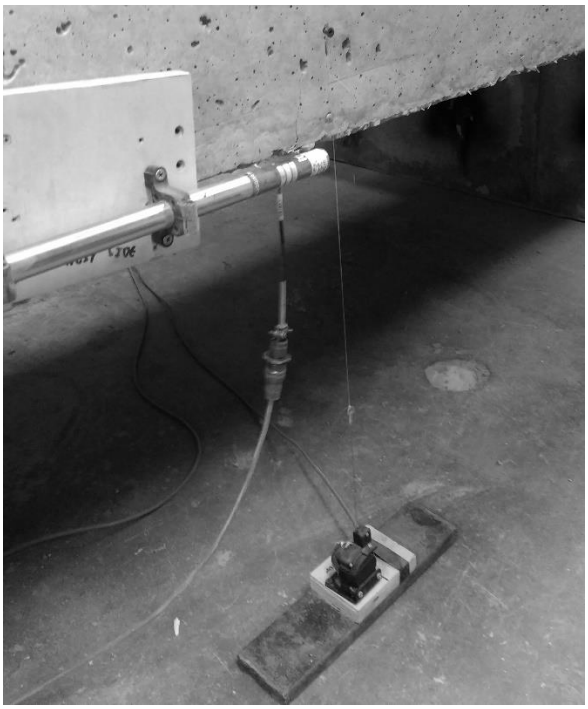

Figure 3.3.16 Measuring deflections with potentiometer

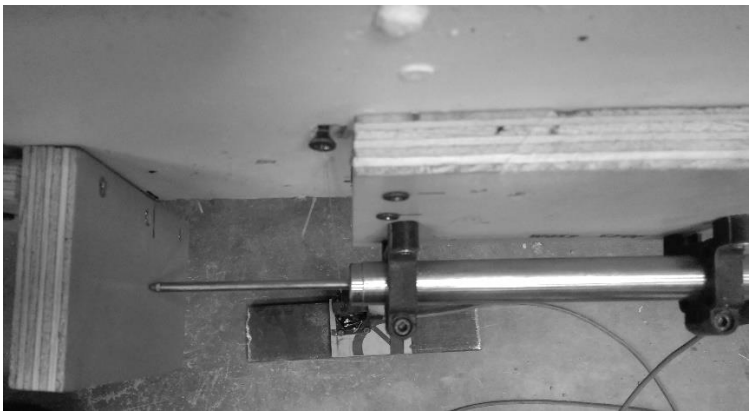

Figure 3.3.17 LVDT spanning crack at bottom level of deck

After experiencing all the cycles, the bridge decks were tested with a monotonically increasing load until failure. The test setup for the post fatigue flexure was identical to the static flexure test setup. A single line load at midspan was used for all the post-fatigue static testing to ensure a flexural failure. Figure 3.3.18 shows a post-fatigue static flexure test setup.

Figure 3.3.18 Static test after fatigue loading

4. EXPERIMENTAL PROGRAM – PUNCHING SHEAR

4.1 Introduction

This chapter discusses the design and execution of the punching shear phase of this experiment. Refer to Chapter 3 for a detailed explanation of the testing standards and specifications used to ascertain the constitutive relationships of the material components involved. The first section of this chapter gives the concrete mix properties for the punching shear deck panels.

The following section describes the pouring and fabrication of the 14'x12' punching shear deck panels. The static testing procedure is also outlined, including justifications for the design assumptions used. Finally, the fatigue and post-fatigue testing schemes are described.

4.2 Concrete Mix Properties

The same 5,000 psi (34.5 MPa) plain concrete mix was ordered for all three deck types. For the punching shear decks, the fibers were added at the batch plant to ensure proper mixing of the fibers. Once again, the fibers were passed through a grate to prevent clumping of the fibers. Table 4.2.1, Table 4.2.2, and Table 4.2.3 contain the mix specifications for the steel, GFRP, and HRC punching shear deck panels, respectively. Table 4.2.4 contains the design mix specifications as a reference.

Table 4.2.1 Mix design punching shear steel

Material	Batched Amount	Specific Gravity	% Volume
Coarse Aggregate (BRIG-#57)	1518 lb/cy (900 kg/m^3)	2.70 (SSD)	34.30%
Fine Aggregate (BRIG-#8)	198 lb/cy (117 kg/m^3)	2.70 (SSD)	4.50%
Sand	1233 lb/cy (731 kg/m^3)	2.65 (SSD)	28.00%
Type II/V Cement	559 lb/cy (332 kg/m^3)	3.15	10.70%
Bridger Fly Ash	107 lb/cy (63 kg/m^3)	2.30	2.80%
MasterAir AE 200 Air Entrainer	2 oz/cy (74 g/m^3)	1.01	0.01%
MasterPozzolith 200 Water Reducer	15 oz/cy (560 g/m^3)	1.13	0.10%
MasterGlenium 3030	31 oz/cy (1137 g/m^3)	1.05	0.10%
*Water	27 gal/cy (133 L/m^3)	1.0	13.50%
Fibers	0 lb/cy (0 kg/m^3)	2.0	0%
Design Air Volume	N/A	N/A	6.10%

* Note that the water includes the absorbed water in aggregates.

Table 4.2.2 Mix design punching shear GFRP

Material	Batched Amount	Specific Gravity	% Volume
Coarse Aggregate (BRIG-#57)	1513 lb/cy (898 kg/m^3)	2.70 (SSD)	34.60%
Fine Aggregate (BRIG-#8)	200 lb/cy (119 kg/m^3)	2.70 (SSD)	4.60%
Sand	1237 lb/cy (734 kg/m^3)	2.65 (SSD)	28.40%
Type II/V Cement	559 lb/cy (332 kg/m^3)	3.15	10.80%
Bridger Fly Ash	103 lb/cy (61 kg/m^3)	2.30	2.70%
MasterAir AE 200 Air Entrainer	2 oz/cy (74 g/m^3)	1.01	0.01%
MasterPozzolith 200 Water Reducer	15 oz/cy (544 g/m^3)	1.13	0.05%
MasterGlenium 3030	31 oz/cy (1137 g/m^3)	1.05	0.10%
*Water	25 gal/cy (124 L/m^3)	1.0	12.70%
Fibers	0 lb/cy (0 kg/m^3)	2.0	0%
Design Air Volume	N/A	N/A	6.10%

* Note that the water includes the absorbed water in aggregates.

Table 4.2.3 Mix design punching shear FRC

Material	Batched Amount	Specific Gravity	% Volume
Coarse Aggregate (BRIG-#57)	1513 lb/cy (898 kg/m^3)	2.70 (SSD)	34.10%
Fine Aggregate (BRIG-#8)	200 lb/cy (119 kg/m^3)	2.70 (SSD)	4.50%
Sand	1237 lb/cy (734 kg/m^3)	2.65 (SSD)	28.00%
Type II/V Cement	559 lb/cy (332 kg/m^3)	3.15	10.60%
Bridger Fly Ash	107 lb/cy (63 kg/m^3)	2.30	2.80%
MasterAir AE 200 Air Entrainer	3 oz/cy (122 g/m^3)	1.01	0.01%
MasterPozzolith 200 Water Reducer	15 oz/cy (552 g/m^3)	1.13	0.05%
MasterGlenium 3030	30 oz/cy (1121 g/m^3)	1.05	0.10%
*Water	27 gal/cy (132 L/m^3)	1.0	13.30%
Fibers	15 lb/cy (9 kg/m^3)	2.0	0.45%
Design Air Volume	N/A	N/A	6.10%

* Note that the water includes the absorbed water in aggregates.

Although the same mix was ordered for each deck type, there was a slight variability in the amount that was batched, similar to the flexural decks discussed in Chapter 3. Therefore, to show this mild variation in concrete mix, the water/cement ratio is reported in Table 4.2.4. Compared with the variability in mixes in the flexural deck panels, the difference was slight. The GFRP-only batch ticket did not show any superplasticizer, although the same mix was ordered. The reason for this is unclear, but due to the workability of the mix, it was assumed that a similar amount as the steel deck concrete was added and not reported.

Table 4.2.4 w/c Ratio punching shear mixes

Deck Type	w/c Ratio
Steel	0.338
GFRP	0.316
HRC	0.334

4.3 Punching Shear Deck Panels

The following sections contain information regarding the casting and fabrication of the full-scale 14'x12' punching shear panels. Following the fabrication summary, a description of the testing procedure used for both the static and cyclic testing is outlined. As mentioned in Chapter 3, any extended bridge deck design calculations performed will be placed in Appendix A.

4.3.1 Panel Design and Fabrication

Just like the flexural specimens, high density overlay (HDO) board was used to create the forms for the bridge deck panels. Two bridge decks of each type were cast. The same reinforcement spacing and details were used as in Chapter 3. They are once again shown in Table 4.3.1 for clarification.

Table 4.3.1 Reinforcement layout

Deck Type	Transverse Reinforcement	Distribution Reinforcement
Steel	#5 (#16) Bars at 6" (150 mm) o/c	#5 (#16) Bars at 8" (200 mm) o/c
GFRP	#6 (#19) Bars at 6" (150 mm) o/c	#6 (#19) Bars at 9" (230 mm) o/c
HRC	#6 (#19) Bars at 8" (200 mm) o/c 15 lb/cy (8.90 kg/m^3) of fibers	#6 (#19) Bars at 13" (330 mm) o/c 15 lb/cy (8.90 kg/m^3) of fibers

For these punching shear panels, the 12' (3.7 m) direction was the span direction and contained the transverse reinforcement as the primary reinforcement. The 14' (4.3 m) direction was the direction considered to be parallel with the supports; therefore, the distribution reinforcement was provided in this direction. Two mats of upper and lower reinforcement were cast in the decks as per the design with a constant cover of 1.5" (38 mm). The thickness of the panels was once again 8" (200 mm).

A concrete hopper was used to pour the panels since they were in lab locations that the truck chute could not reach, but a drop height of less than 3 ft (1 m) was enforced to ensure that the aggregate remained well mixed. Internal vibration was used once more to provide sufficient consolidation around the reinforcement joints. The fiber addition by the batch plant workers for the HRC is shown in Figure 4.3.1.

Figure 4.3.1 Adding the fibers at the batch plant

Figure 4.3.2 shows the steel-reinforced panels prior to pouring, and Figure 4.3.3 shows the steel decks as they were being cast. Figure 4.3.4 shows a close-up view of the GFRP on the concrete chairs prior to pouring. Figure 4.3.5 shows the GFRP decks being poured. Figure 4.3.5 shows the HRC decks prior to pouring, and Figure 4.3.6 shows the HRC decks being cast.

Figure 4.3.2 Steel punching shear deck prior to pouring

Figure 4.3.3 Pouring the steel punching shear deck with concrete hopper

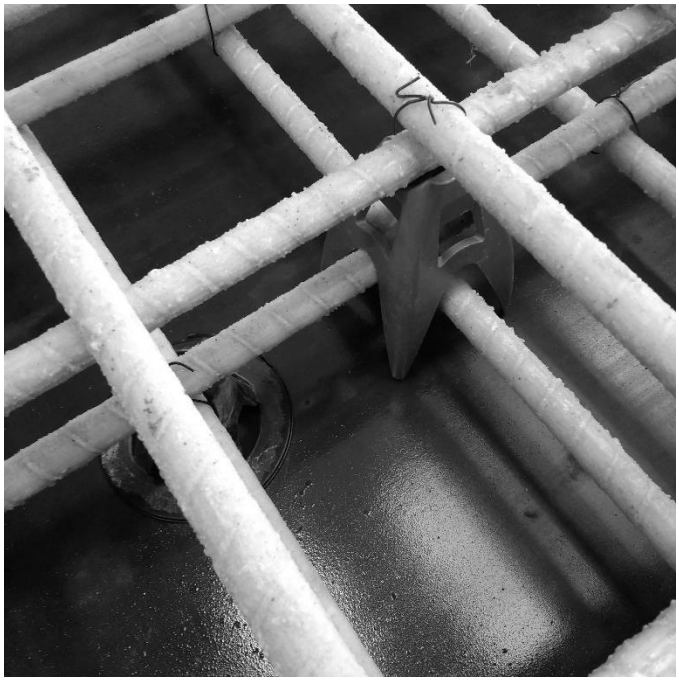

Figure 4.3.4 Close-up of GFRP reinforcement on chairs prior to pouring

Figure 4.3.5 Pouring the GFRP punching shear decks

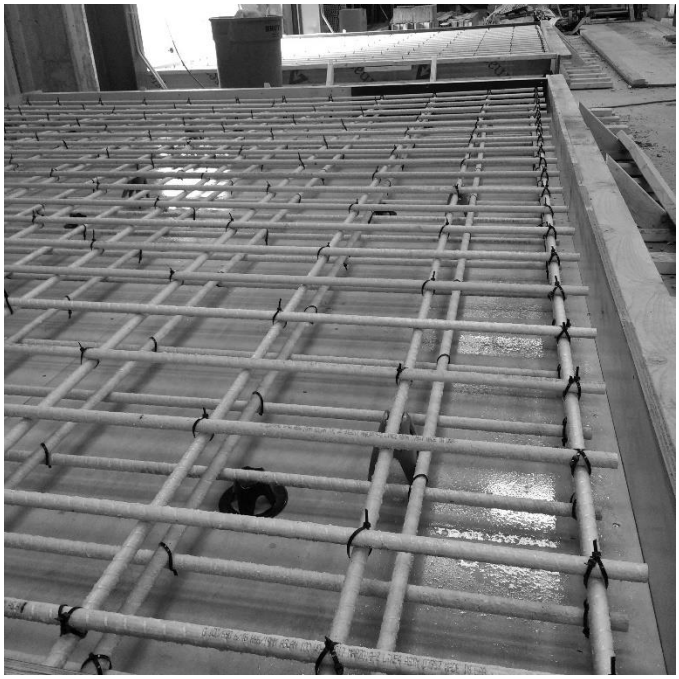

Figure 4.3.6 HRC punching shear decks before casting

Figure 4.3.7 HRC decks being poured with internal vibration

Similar to the flexural decks, moist burlap and plastic sheeting was placed over the deck panels to aid in the curing process. An uncovered, finished deck is shown in Figure 4.3.8. A deck with the plastic sheeting covering is shown in Figure 4.3.9.

Figure 4.3.8 Finished GFRP punching shear deck

Figure 4.3.9 Curing the punching shear decks

4.3.2 Static Testing

As mentioned in Chapter 2, bridge deck failures are characterized by a punching shear failure between girder supports. This is in part due to the lateral restraint provided by the composite girder sections as well as the "arching action" in the deck. Without casting the deck panels composite with the girders, this arching action cannot be achieved. Therefore, in order to create a pure punching shear failure, the decks were cast at an aspect ratio that was much closer to 1. The girder supports were also moved to within 6'

(1.8 m) of each other to ensure that the failure was a punching shear failure and not a flexural failure. This test setup is shown in Figure 4.3.10.

In order to simulate the AASHTO HL-93 truck, a 10” x 20” (255 x 510 mm) plate was used between the hydraulic ram and the bridge deck. This plate is the specified wheel area for the truck, and the same plate was used during the fatigue testing.

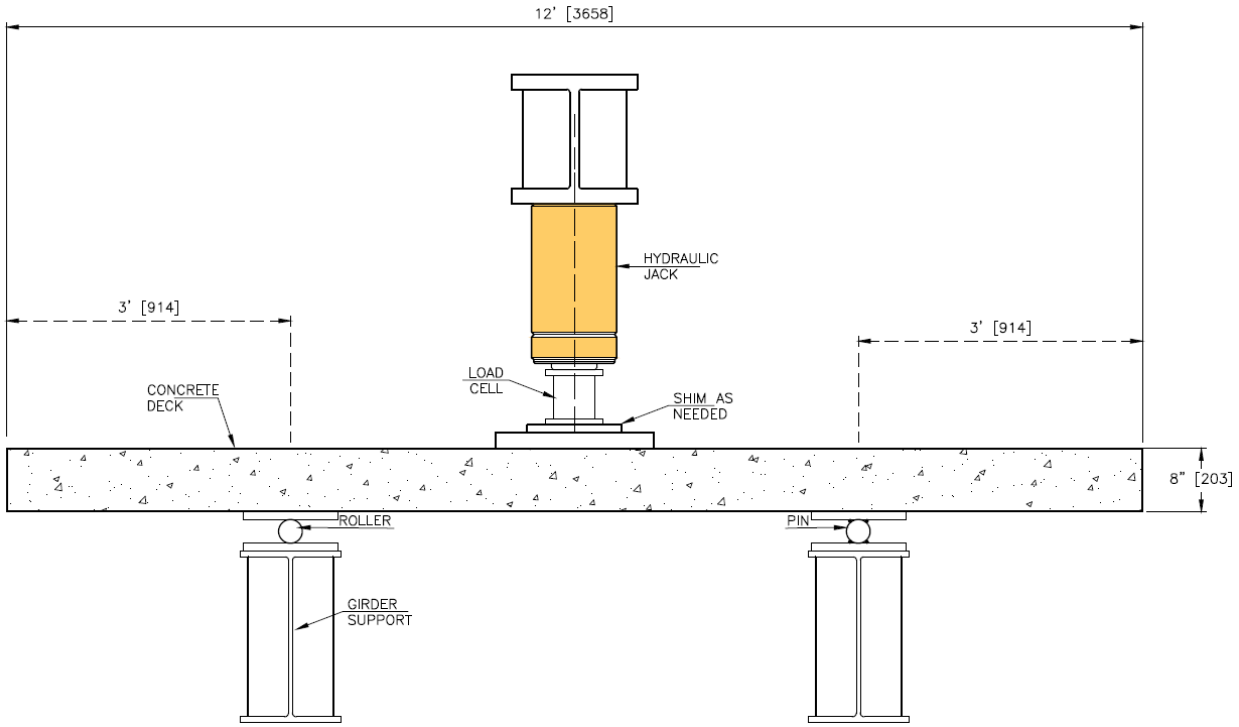

Figure 4.3.10 Punching shear static test setup

The actual location of the load was slightly off-center in both directions (parallel and perpendicular to the supports), but it was only off by 6” (150 mm) in the 14’ (4.3 m) and 5” (127 mm) in the 12’ (3.7 m) direction. This occurred due to the size of the loading frame and its location relative to the lab strong wall. Since the supports were held at the 6’ (1.8 m) spacing, and the load was centered over the span, only the difference in the distance to the free edge mattered. This was only a 5” (127 mm) distance over a distance close to 7’ (2.2 m); therefore, it was negligible.

Figure 4.3.11 shows the supports prior to placing a deck. It shows that 2x4s were used on the roller support side to make sure that the support was spaced uniformly and in a straight line prior to testing. Before running the test, the wood was removed to make sure there was no lateral restraint for the rollers. One load cell was placed under the hydraulic ram, and two potentiometers were measuring deflection from the deck to the frame. Figure 4.3.12, Figure 4.3.13, and Figure 4.3.14 demonstrate the static test setup for the steel, GFRP, and HRC decks, respectively. The load was increased monotonically until failure. Following the test, measurements were made on the bottom punching surface and the failure angle was determined.

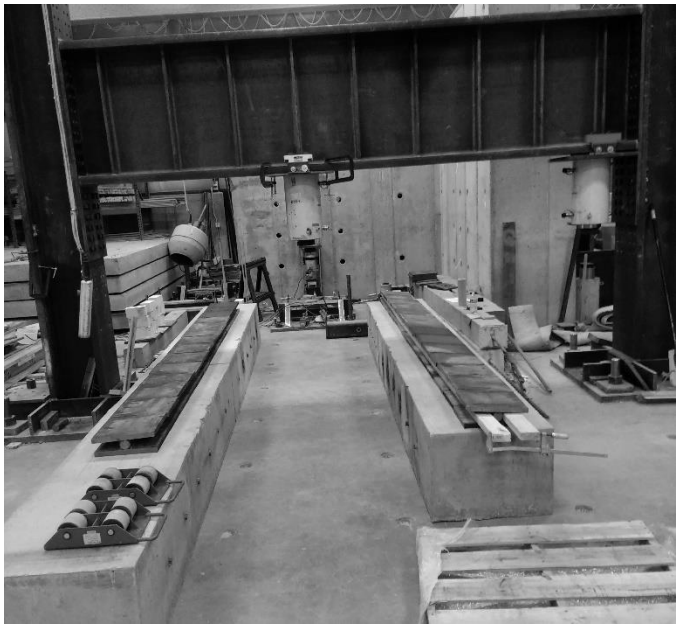

Figure 4.3.11 Punching shear deck supports

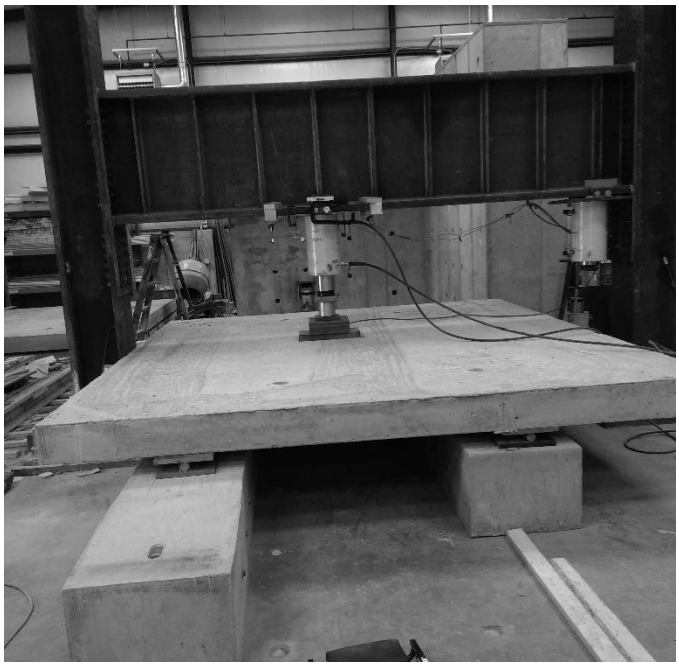

Figure 4.3.12 Steel punching shear deck static test setup

Figure 4.3.13 GFRP punching shear static test setup

Figure 4.3.14 HRC punching shear static test setup

4.3.3 Fatigue Testing

The fatigue loading scheme was identical to the flexural decks that experienced 1 million cycles with several minor exceptions. First, the load was increased to 16 kips (71.2 kN) to directly simulate a wheel on an HL-93 truck. Second, the LVDTs were not included to measure crack openings under fatigue since the decks were uncracked by the fatigue level load. Finally, although potentiometers were set up to monitor the deflection of the deck during the fatigue loading, the noise of the sensor, which was approximately 0.0009 in (0.02 mm), exceeded the deflection of the decks, which was measured at around 0.0004 in (0.01 mm) for the first few cycles.

The fatigue cycles were applied at a rate of 4 Hz for 1 million cycles. Shims were used beneath the deck and supports to attempt to mitigate bouncing or movement. Figure 4.3.15, Figure 4.3.16, and Figure 4.3.17 show the fatigue test setup for the punching shear decks. No flexural cracks were observed during the testing.

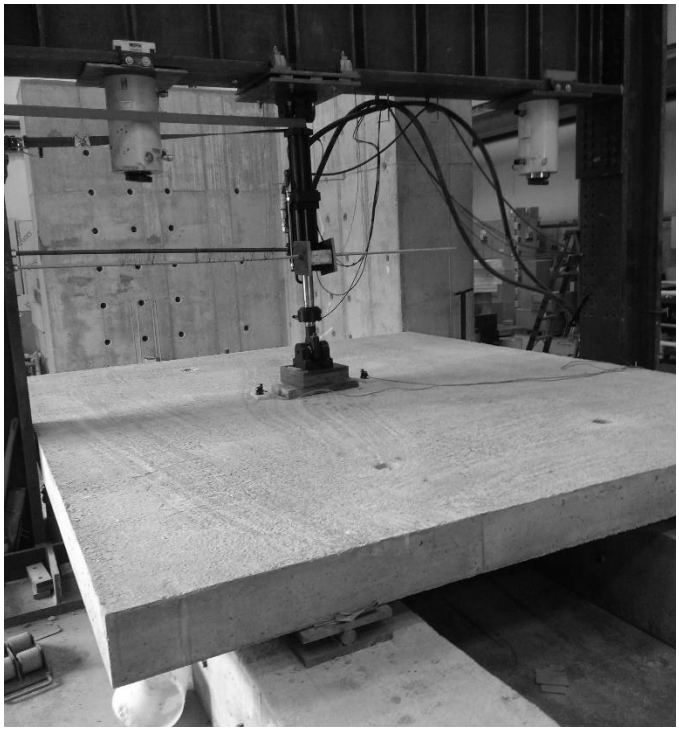

Figure 4.3.15 Fatigue test setup

Figure 4.3.16 Fatigue test setup 2

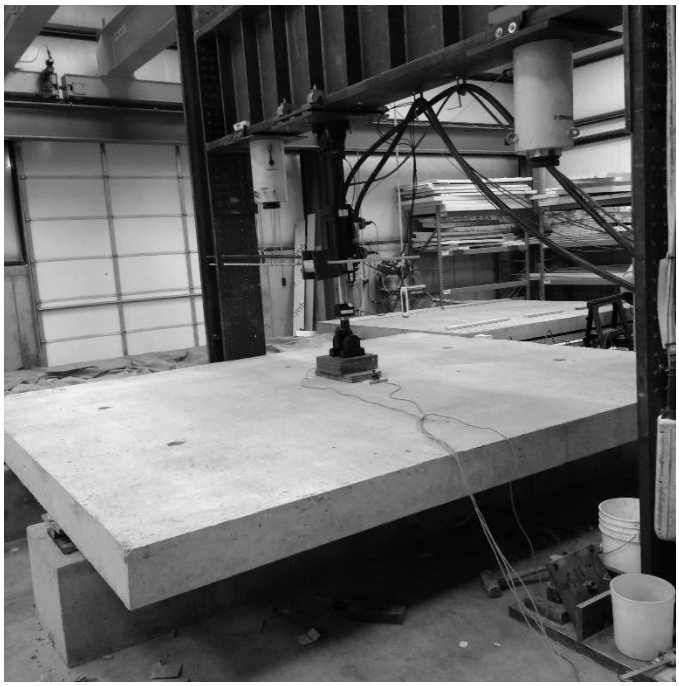

Figure 4.3.17 Fatigue test setup 3

Following the fatigue loading, the decks were tested until failure using the same testing protocol and design as the static testing that occurred prior to fatigue. The load and deflection were recorded, and measurements of the punching area were once again taken.

5. EXPERIMENTAL RESULTS – FLEXURE

5.1 Introduction

The following section presents the data obtained during the experiment described in Chapter 3. For each set of data, a figure will be provided in both imperial units as well as SI units. The first section presents all of the data associated with the small-scale material testing. The following section details the static flexure experimental results. After the static testing results, the fatigue data are presented. In the final section of this chapter the post-fatigue static testing results are detailed.

5.2 Materials Testing

The following section reports the results obtained from material testing on the steel rebar, the GFRP rebar, the plain concrete, and the FRC specimens. The results from the small-scale material testing are utilized in the discussion section of this report to create macro-scale analytical models and predictions. The inherent variability of the various materials necessitates multiple test specimens. Therefore, whenever possible, at least three specimens were tested, and the results were recorded.

There was very little variability in the steel reinforcing steel testing as shown in Figure 5.2.1 and Figure 5.2.2. As expected, for all four test specimens, the recorded yield stress and ultimate tensile stress exceeded the nominal values. The results from the steel rebar testing are given in Table 5.2.1.

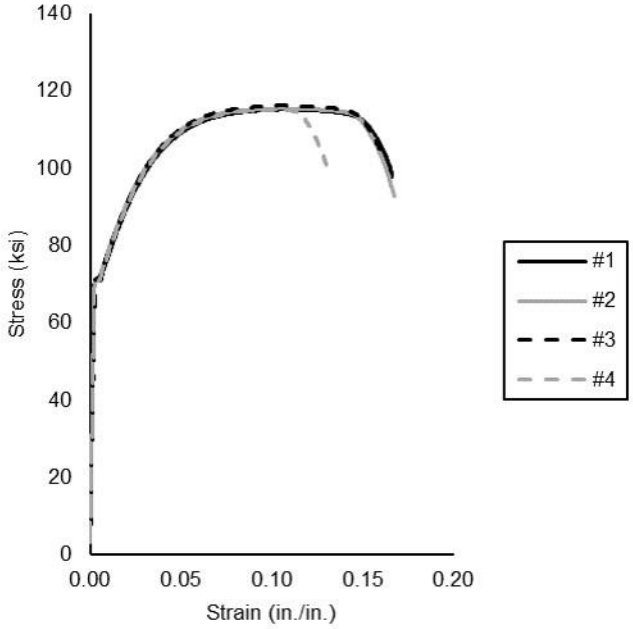

Figure 5.2.1 Stress-strain curve for steel rebar (Imperial)

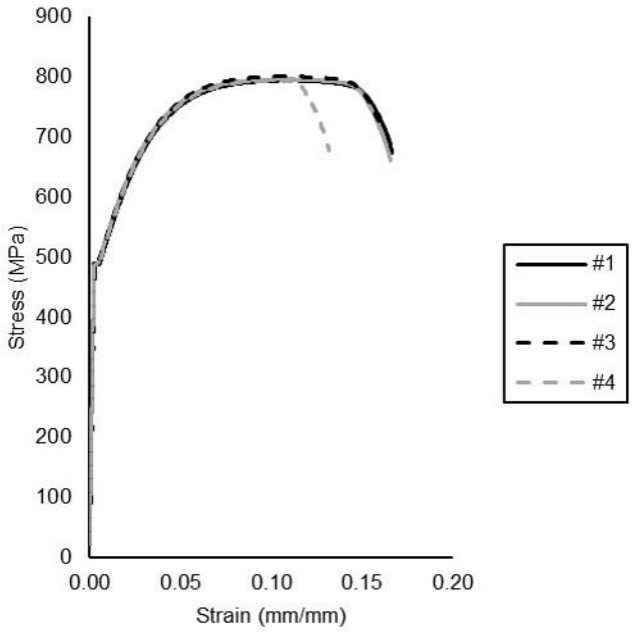

Figure 5.2.2 Stress-strain curve for steel rebar (SI)

Table 5.2.1 Steel rebar testing results

Property	**Mean Value**	**COV**
Modulus of Elasticity, E_s	32090 ksi (221.3 GPa)	0.088
Yield Stress, σ_y	71 ksi (489 MPa)	0.003
Tensile Strength σ_t	115.5 ksi (793 MPa)	0.004
Yield Strain, ϵ_y	0.29%	0.10
Strain Hardening Onset, ϵ_{sh}	0.44%	0.19
Peak Strain, ϵ_u	6.80%	0.07
Rupture Strain, ϵ_r	13.80%	0.10

Six GFRP rebar specimens were prepared and tested. Two of the bars experienced failures inside of the anchors, and so the four failures that occurred within the gauge length were recorded and compared. During testing, the extensometer was removed at a load of 50% of the predicted failure load to prevent damage to the sensor. Linear behavior was observed prior to the removal of the sensor, and therefore strain data were linearly extrapolated until failure. Figure 5.2.3 and Figure 5.2.4 show the stress-strain behavior of the GFRP, and Table 5.2.2 shows the tensile strength, elastic modulus, and the rupture strain of the GFRP.

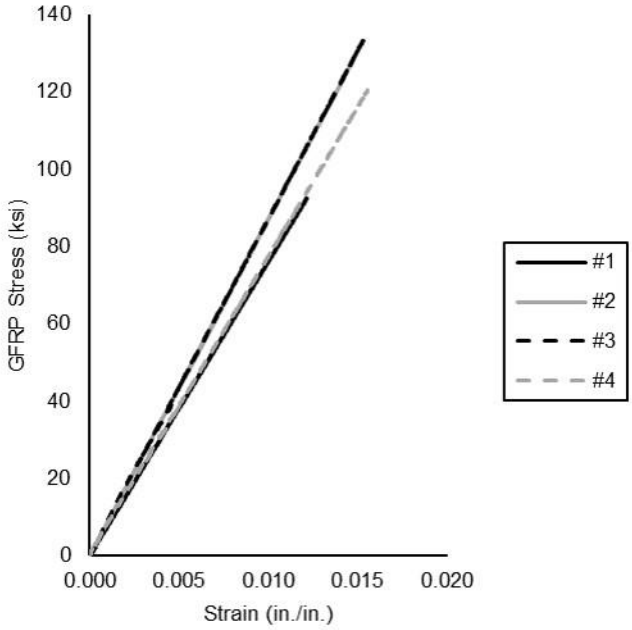

Figure 5.2.3 Stress-strain curve for GFRP (Imperial)

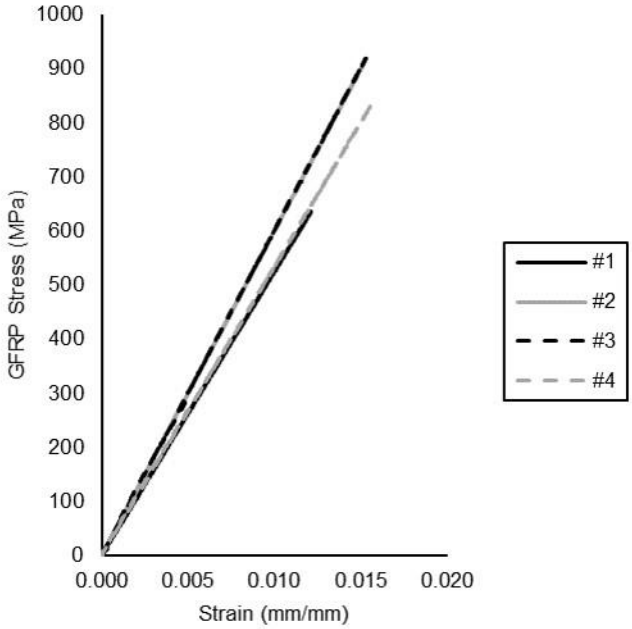

Figure 5.2.4 Stress-strain curve for GFRP (SI)

Table 5.2.2 GFRP rebar testing results

Property	**Mean Value**	**COV**
Tensile Strength, f_{fu}	119.7 ksi (825 MPa)	0.16
Modulus of Elasticity, E_f	8197 ksi (56.5 MPa)	0.07
Rupture Strain, ϵ_{fu}	1.45%	0.11

The compressive strength of the concrete was recorded at different times for each batch. Although attempts were made to test cylinders at 7 days, 14 days, and 28 days, as shown in Table 5.2.3, some days were postponed or skipped. Despite the increased w/c ratio in the GFRP mix, the GFRP decks hit almost 7.4 ksi (51 MPa) by the date of the fatigue test, while the steel decks achieved a strength of 5.4 ksi (37.5 MPa). For the second set of GFRP decks with fibers (HRC2), the fatigue test and static test occurred on the same day. The compressive strength for the different deck types at different days is shown in Table 5.2.3.

Table 5.2.3 Concrete compression testing results

Deck Type	**Compressive Strength f'_c, psi (MPa)**				
Steel	*7 Days*	*14 Days*	*28 Days*	*Static Test*	*Fatigue Test*
	3,190 (22)	3,920 (27)	4,400 (30)	5,410 (37)	5,430 (37.5)
GFRP	*7 Days*	*15 Days*	*28 Days*	*Static Test*	*Fatigue Test*
	Not Tested	5,065 (35)	6,095 (42)	6,755 (46.5)	7,390 (51)
HRC	*7 Days*	*14 Days*	*36 Days*	*Static Test*	*Fatigue Test*
	3,870 (26.7)	5,100 (35)	6,180 (42.5)	6,340 (43.7)	7,050 (48.5)
HRC2	*7 Days*	*14 Days*	*32 Days*	*Static Test*	*Fatigue Test*
	Not Tested	Not Tested	5,200 (36)	5,890 (40.5)	5,890 (40.5)

The static modulus of elasticity was obtained by compressing the cylinders to 10%, 20%, and 40% of their peak strength and recording the chord modulus. This process was repeated three times for the three different cylinders of each batch type on the static or fatigue testing days. The results for the modulus testing are shown in Table 4.2.4. The results for the splitting tensile strength testing are recorded in Table 5.2.5. Note that no splitting tensile test was performed on the HRC decks since the tensile capacity of the concrete is obtained according to a different standard, as described below.

Table 5.2.4 Concrete static modulus testing results

Deck Type	**Modulus of Elasticity, E_c, ksi (MPa)**	
	Static Test	*Fatigue Test*
Steel	4,765 (32,850)	5,260 (36,290)
GFRP	6,380 (44,000)	6,500 (44,815)
HRC	5,415 (37,335)	5,400 (37,230)
HRC2	5,175 (35,680)	5,175 (35,680)

Table 5.2.5 Concrete splitting tensile strength results

Deck Type	**Splitting Tensile Strength, f_t, psi (MPa)**	
	Static Test	*Fatigue Test*
Steel	592 (4.1)	654 (4.5)
GFRP	751 (5.2)	766 (5.3)

Three mini beams were tested in accordance with EN 14651. The force vs. CMOD curve for the first set of HRC panels is shown in Figure 5.2.5 and Figure 5.2.6. The residual flexural tensile strength vs. CMOD is shown in Figure 5.2.7 and Figure 5.2.8. Figure 5.2.9 and Figure 5.2.10 show the average flexural tensile strength corresponding with each design crack width.

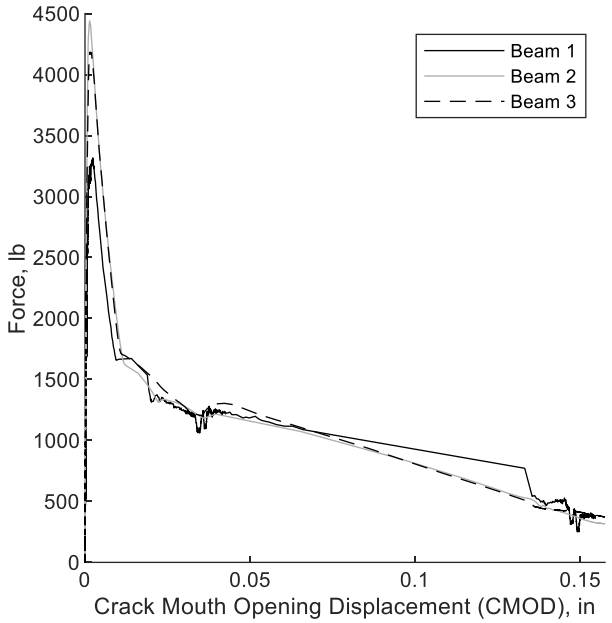

Figure 5.2.5 Force-CMOD curve HRC set #1 (Imperial)

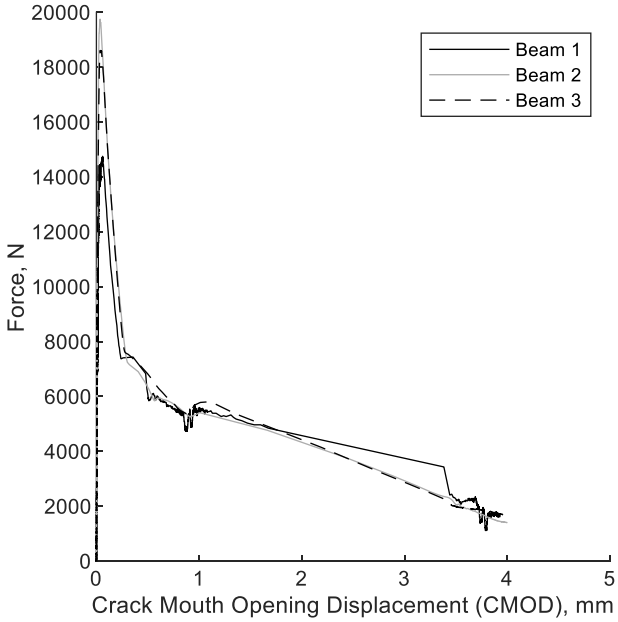

Figure 5.2.6 Force-CMOD curve HRC set #2 (SI)

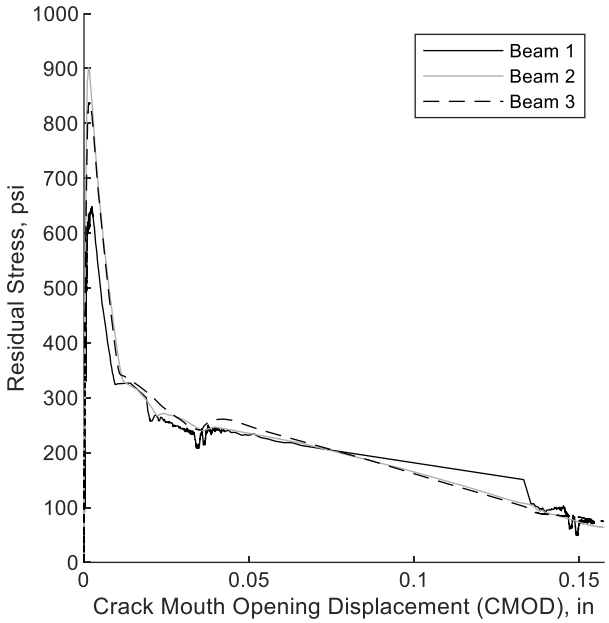

Figure 5.2.7 Stress-CMOD curve HRC set #1 (Imperial)

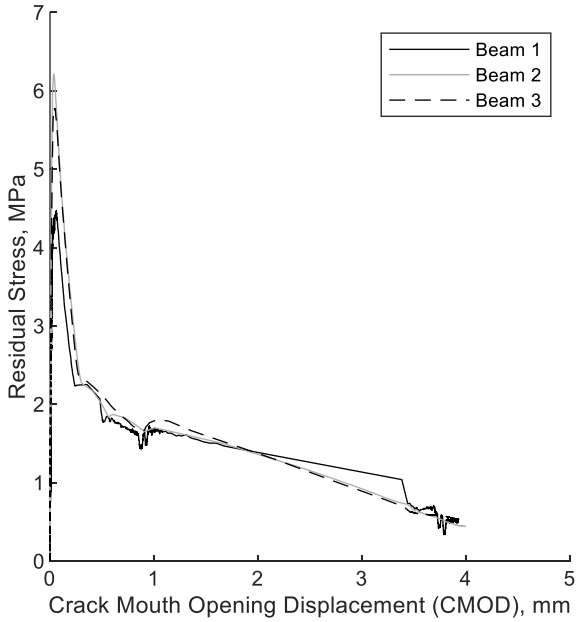

Figure 5.2.8 Stress-CMOD curve HRC Set #1 (SI)

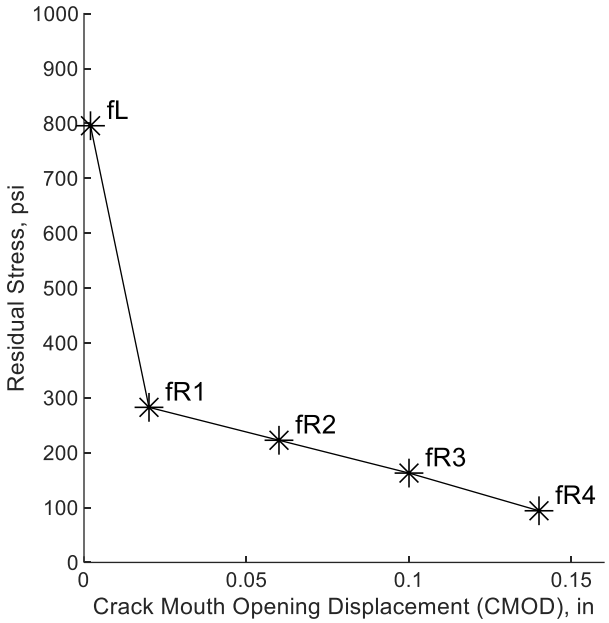

Figure 5.2.9 Average flexural tensile strength HRC set #1 (Imperial)

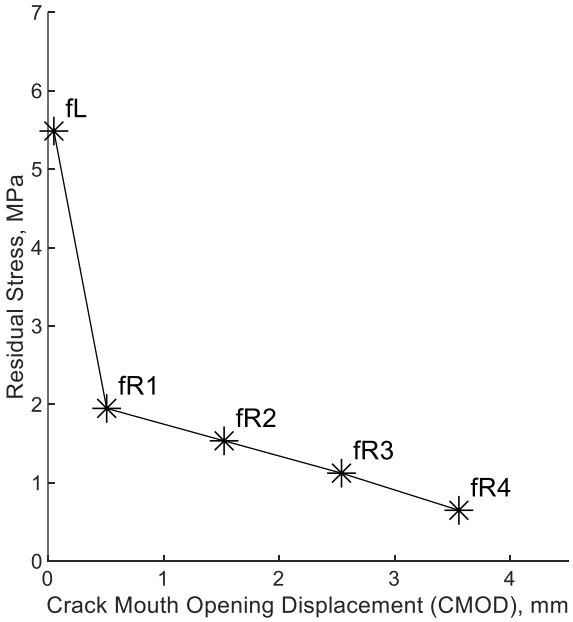

Figure 5.2.10 Average flexural tensile strength HRC set #1 (SI)

Three mini beams were also tested for the second set of HRC panels. The force vs. CMOD curve for the second set of HRC panels is shown in Figure 5.2.11 and Figure 5.2.12. The residual flexural tensile strength vs. CMOD is shown in Figure 5.2.13 and Figure 5.2.14. Figure 5.2.15 and Figure 5.2.16 show the average flexural tensile strength corresponding with each design crack width.

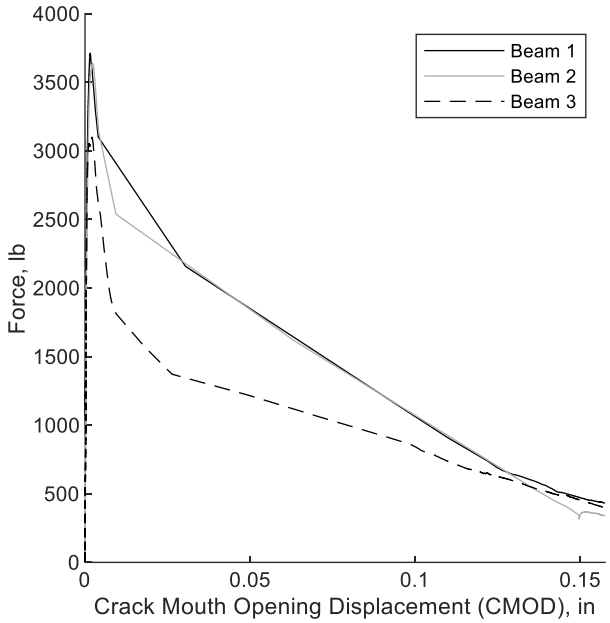

Figure 5.2.11 Force-CMOD curve HRC set #2 (Imperial)

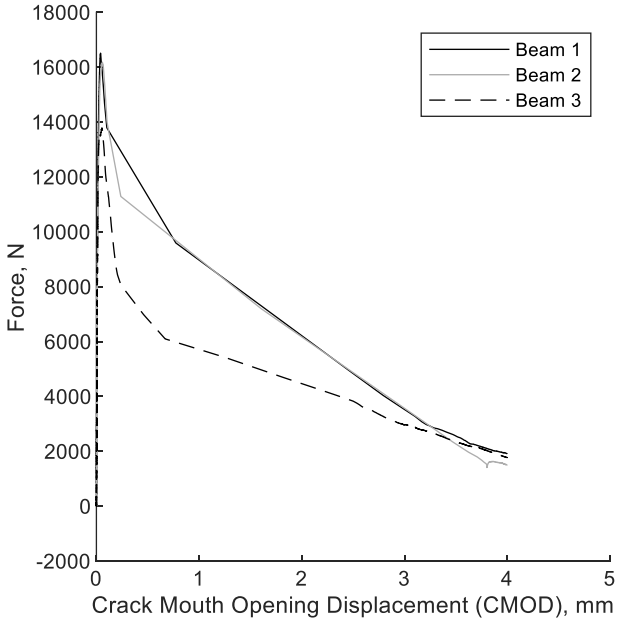

Figure 5.2.12 Force-CMOD curve HRC set #2 (SI)

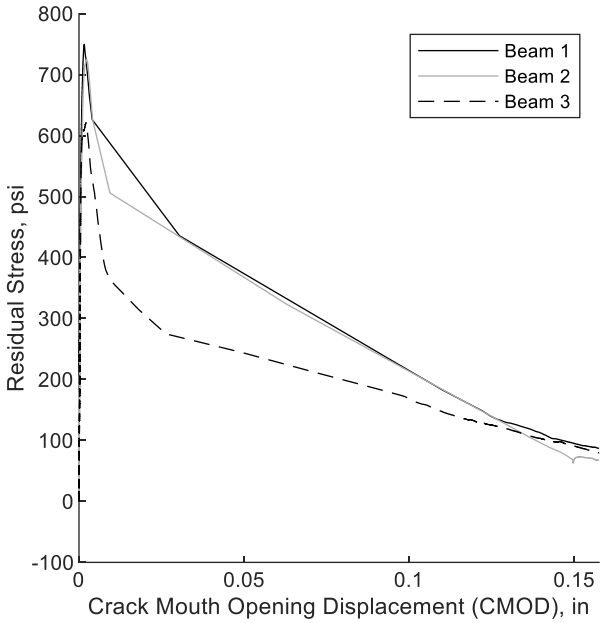

Figure 5.2.13 Stress-CMOD curve HRC set #2 (Imperial)

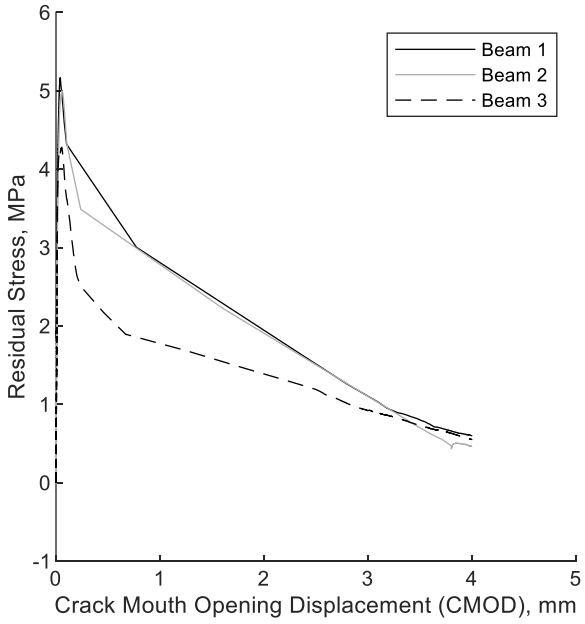

Figure 5.2.14 Stress-CMOD curve HRC set #2 (SI)

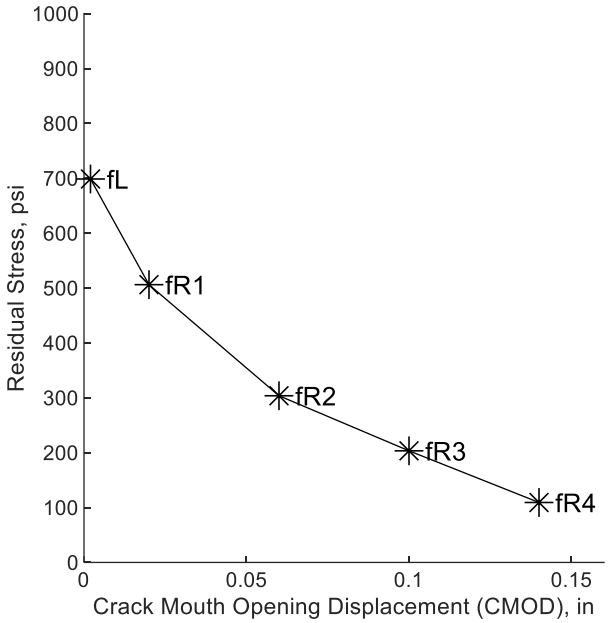

Figure 5.2.15 Average flexural tensile strength HRC set #2 (Imperial)

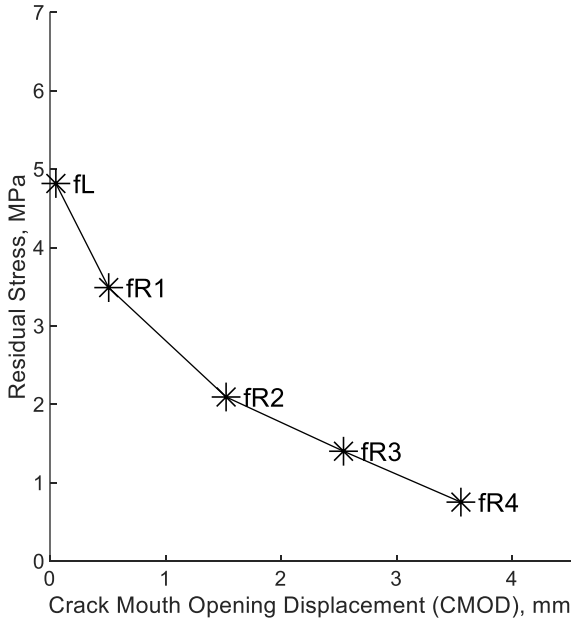

Figure 5.2.16 Average flexural tensile strength HRC Set #2 (SI)

As shown above, at a relatively small dosage of 15 lb/ft^3 (8.90 kg/m^3), there is little to no strain hardening behavior in the FRC. Almost every mini beam experienced significant strain softening post-cracking. The residual flexural tensile stresses are recorded for both sets of HRC concrete in Table 5.2.6.

.

Table 5.2.6 HRC residual flexural tensile stress results

Residual Stress	Deck Type	
	HRC Set #1	*HRC Set #2*
Limit of Proportionality, f_{Lk}	795.7 psi (5.50 MPa)	698.7 psi (4.80 MPa)
f_{R1}	282.6 psi (1.95 MPa)	506.1 psi (3.50 MPa)
f_{R2}	222.6 psi (1.53 MPa)	303.7 psi (2.09 MPa)
f_{R3}	162.8 psi (1.12 MPa)	203.4 psi (1.40 MPa)
f_{R4}	94.2 psi (0.65 MPa)	109.2 psi (0.75 MPa)

According to the fib Model Code 2010, in order to be suitable to replace conventional discrete reinforcement, the f_{R1}/f_{Lk} ratio must exceed 0.4, and the f_{R3}/f_{R1} ratio must exceed 0.5 (CEB-FIB, 2013).

For the first set of HRC decks, the f_{R1}/f_{Lk} ratio is equal to 0.36, and the f_{R3}/f_{R1} ratio is equal to 0.58. Therefore, the second check is okay, but the first check is not. The f_{R1}/f_{Lk} ratio for the second set of HRC decks is 0.72, and the f_{R3}/f_{R1} ratio is 0.65. Therefore, the second set of HRC decks passed both criteria. The behavior of the HRC decks performed similarly to decks with only discrete reinforcement. Therefore, the FRC ratios are arbitrary when FRC is used in combination with discrete reinforcing bars (HRC).

5.3 Static Testing Results

To account for the additional load from the spreader beam and plates used during the testing setup, a 540-lb (2.4 kN) force was used to account for this self-weight of the setup. By imposing static equilibrium, moments were calculated for each time increment from the load cell reading. Figure 5.3.17 and Figure 5.3.18 show the moment-deflection relationship of the steel-reinforced deck panels. The moment-deflection response of the GFRP panels is shown in Figure 5.3.19 and Figure 5.3.20. Finally, Figure 5.3.21 and Figure 5.3.22 contain the HRC testing results for static flexure.

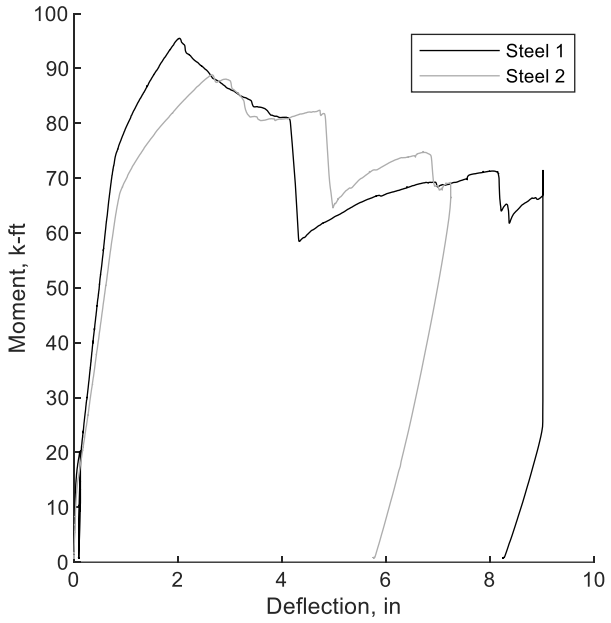

Figure 5.3.17 Moment-deflection curves for steel-reinforced decks (Imperial)

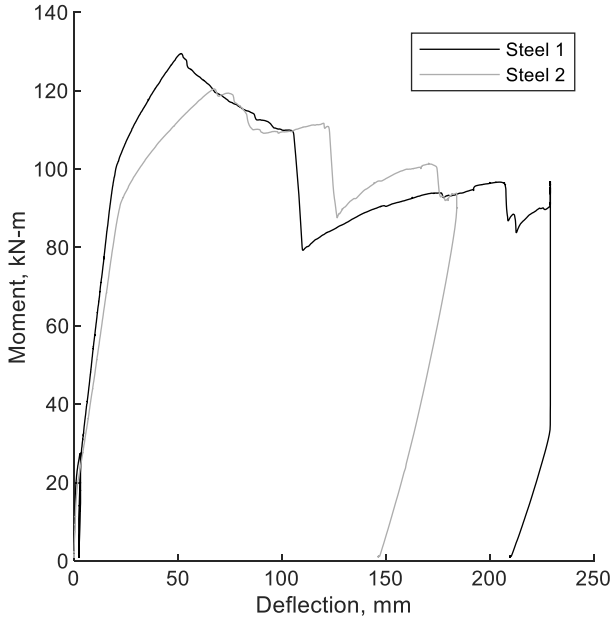

Figure 5.3.18 Moment-deflection curves for steel-reinforced decks (SI)

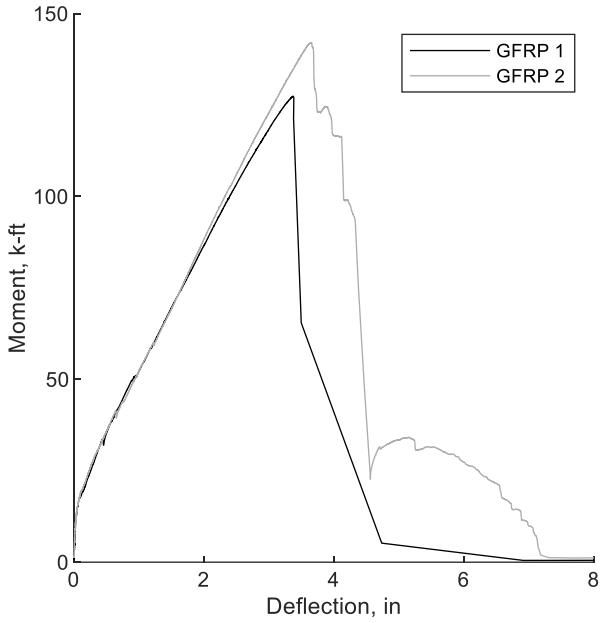

Figure 5.3.19 Moment-deflection curves for GFRP-reinforced decks (Imperial)

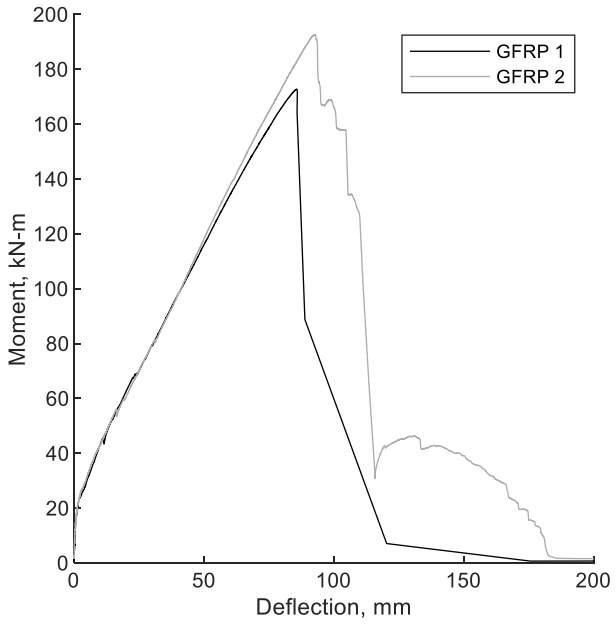

Figure 5.3.20 Moment-deflection curves for GFRP-reinforced decks (SI)

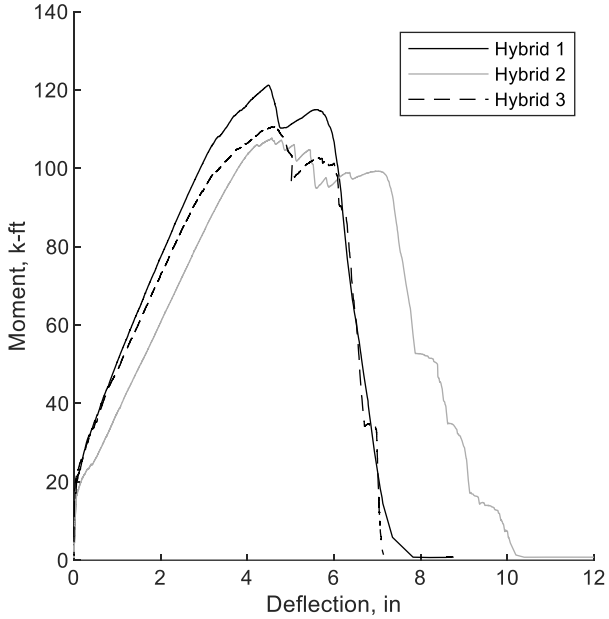

Figure 5.3.21 Moment-deflection curves for HRC decks (Imperial)

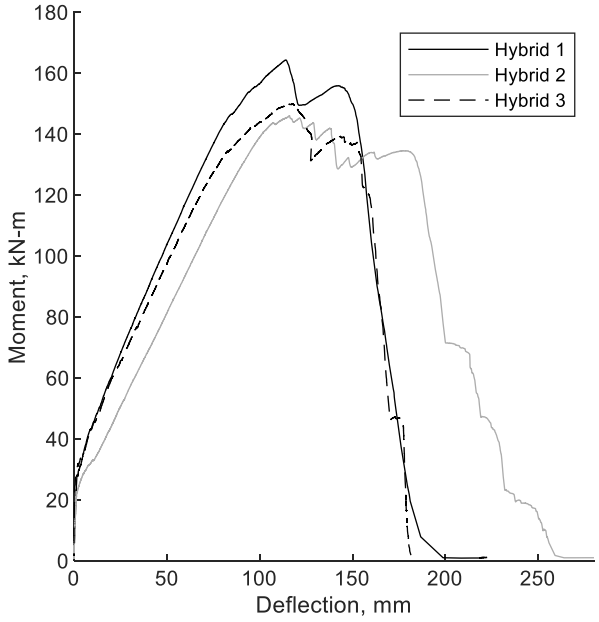

Figure 5.3.22 Moment-deflection curves for HRC decks (SI)

The steel decks could have deflected further, but the rams reached the end of their stroke, and the concrete had crushed. Therefore, the decks were considered failed for relevant strength and serviceability limit states. All of the figures for the three types of bridge decks were superimposed in Figure 5.3.23 and Figure 5.3.24.

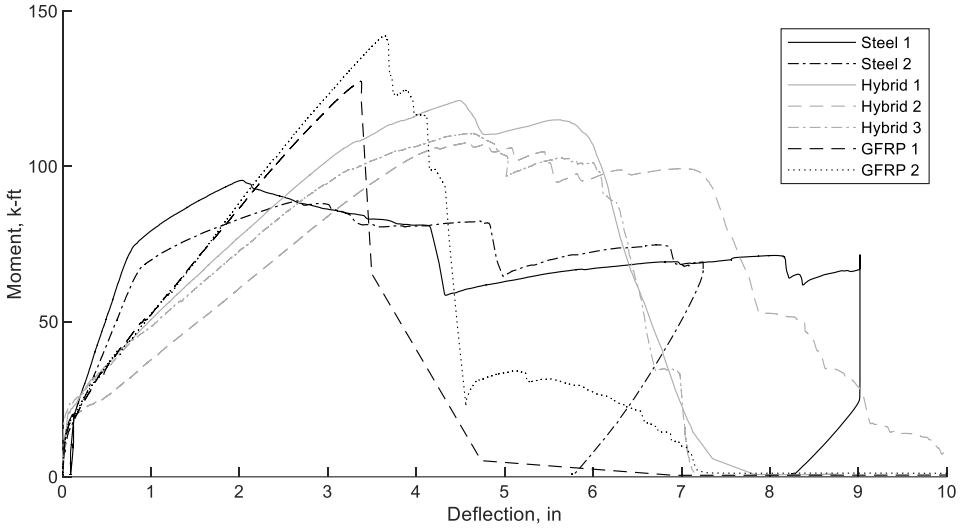

Figure 5.3.23 Moment-deflection curves for all bridge decks (Imperial)

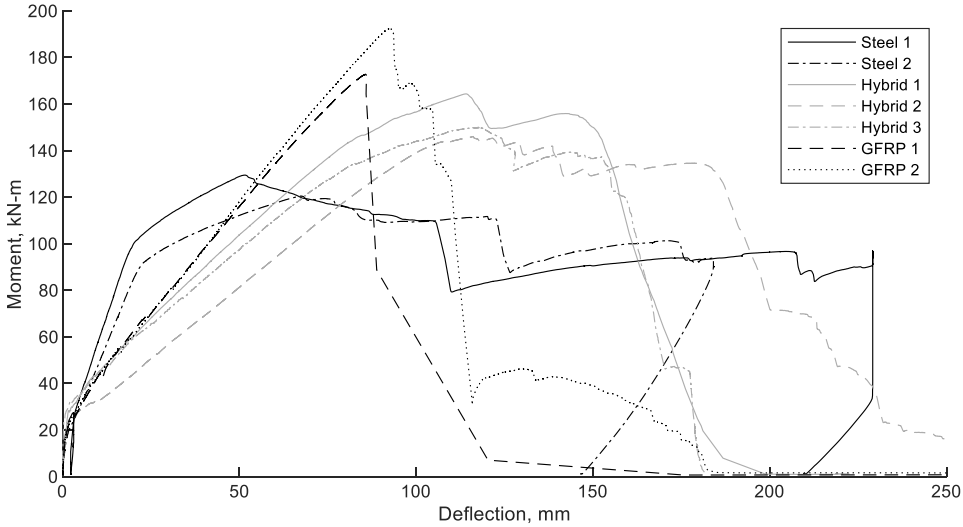

Figure 5.3.24 Moment-deflection curves for all bridge decks (SI)

The maximum moment was recorded at failure for each panel, and the deflection at this peak moment was noted as well. For both the GFRP-reinforced and HRC bridge decks, the concrete crushed before the rupture of the GFRP. The steel rebar yielded prior to the concrete crushing for the steel-reinforced decks. The maximum moments and deflections at failure are shown in Table 5.3.7.

.

Table 5.3.7 Maximum moments and deflections at failure for static flexure decks

Deck Type	Maximum Moment, kip-ft (kN-m)	Deflection at Failure, in (mm)
Steel 1	95.5 (129.5)	2.03 (51.6)
Steel 2	88.8 (120.4)	2.66 (67.6)
GFRP 1	127.4 (172.7)	3.37 (85.6)
GFRP 2	142.0 (192.5)	3.64 (92.5)
HRC 1	121.2 (164.3)	4.49 (114.0)
HRC 2	107.7 (146.0)	4.57 (116.1)
HRC 3	110.8 (150.2)	4.63 (117.6)

5.4 Fatigue Testing Results

The first set of flexural fatigue decks underwent 1 million fatigue level cycles at a frequency of 4 Hz. The second set of decks experienced 2 million cycles at the same frequency. All of the decks that were tested were already more than 100 days old; therefore, the increase in compressive strength of the concrete over the few days of fatiguing was assumed to be negligible.

Four variables were considered during the testing: the peak deflection, peak crack width, live load deflection, and live load crack opening. The peak deflection was defined as the absolute deflection of the deck from the initial resting datum. The peak crack opening was defined as the maximum opening that the crack saw during the fatigue testing.

Due to sensor drift from thermal and mechanical changes in the laboratory, there is some inherent error in these absolute readings from the potentiometer and LVDT. More accurate and useful is the change from peak to valley of both the deflection and crack width. This was considered to be the change due to the live load. The live load deflection was the distance the deck deflected from peak to valley of each cycle. The live load crack opening was the amount the crack opened and closed during one cycle of fatigue loading.

Figure 5.4.1 and Figure 5.4.2 show the peak deflection for 1 million cycles. Figure 5.4.3 and Figure 5.4.4 show the peak crack width for 1 million cycles. Figure 5.4.5 and Figure 5.4.6 show the live load deflection of the decks for 1 million cycles, and Figure 5.4.7 and Figure 5.4.7 show the live load crack opening for 1 million cycles.

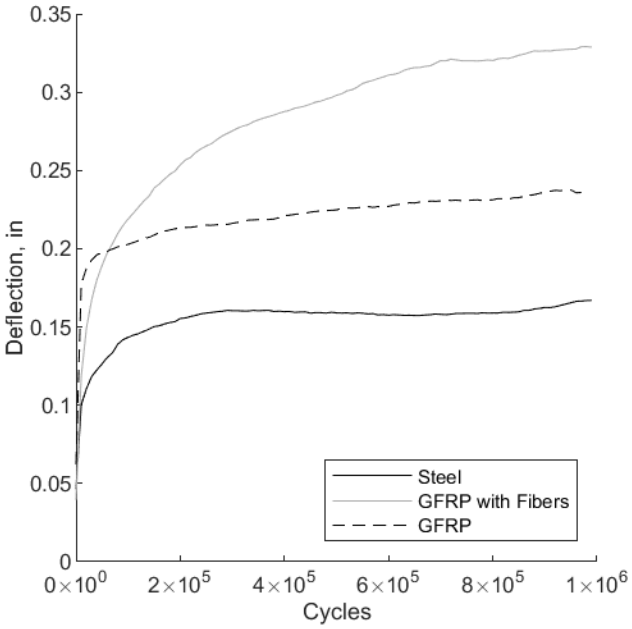

Figure 5.4.1 Peak deflection vs. No. of cycles for 1 million cycles (Imperial)

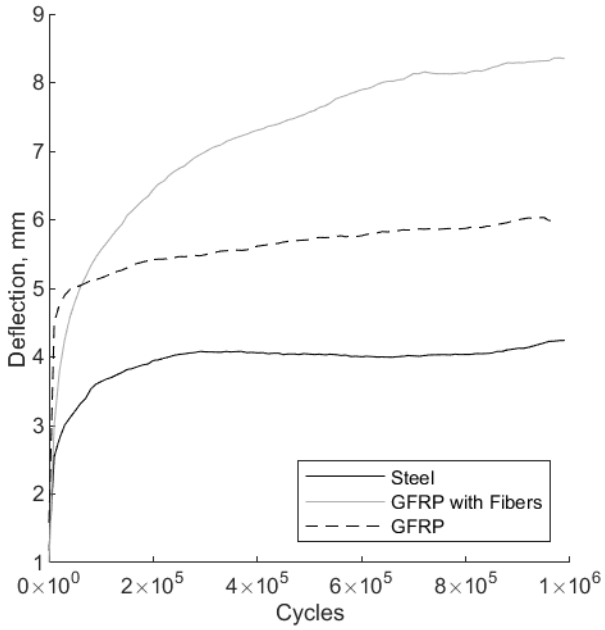

Figure 5.4.2 Peak deflection vs. No. of cycles for 1 million cycles (SI)

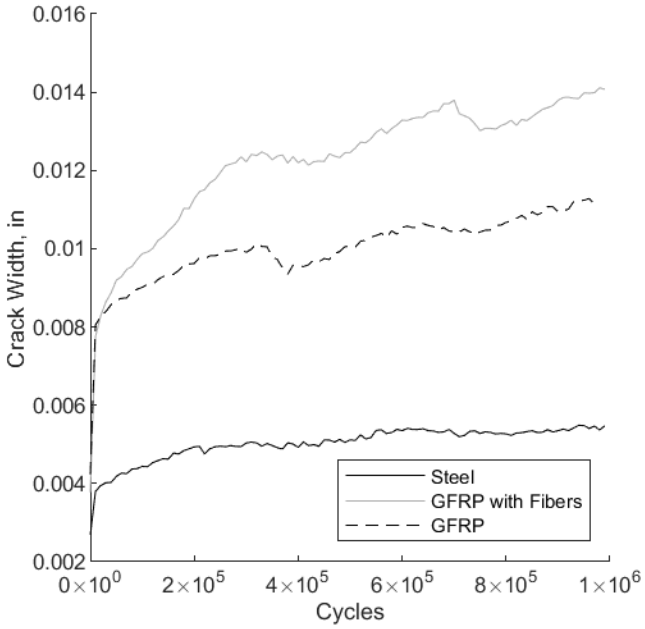

Figure 5.4.3 Peak crack width vs. No. of cycles for 1 million cycles (Imperial)

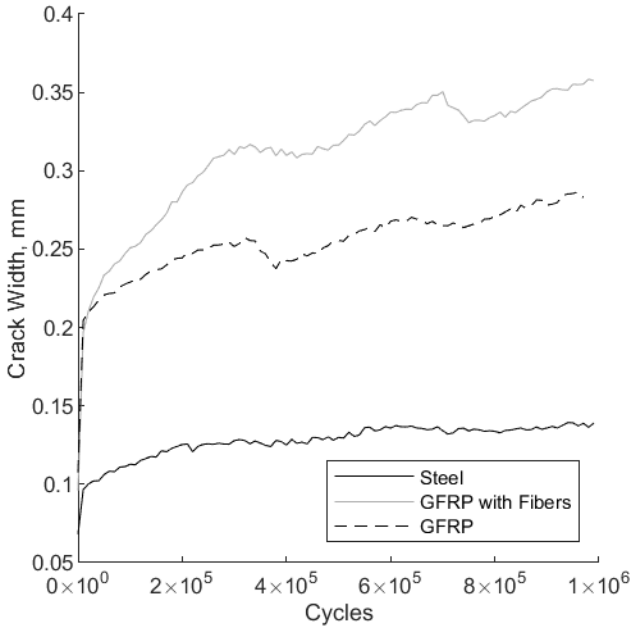

Figure 5.4.4 Peak crack width vs. No. of cycles for 1 million cycles (SI)

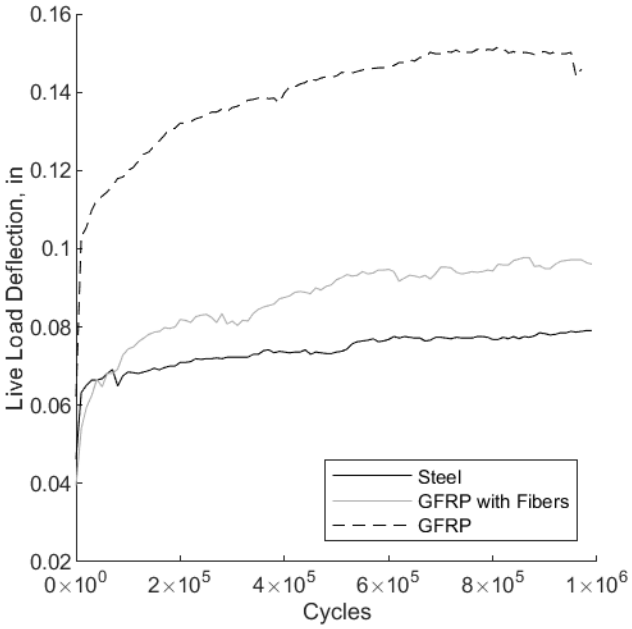

Figure 5.4.5 Live load deflection vs. No. of cycles for 1 million cycles (Imperial)

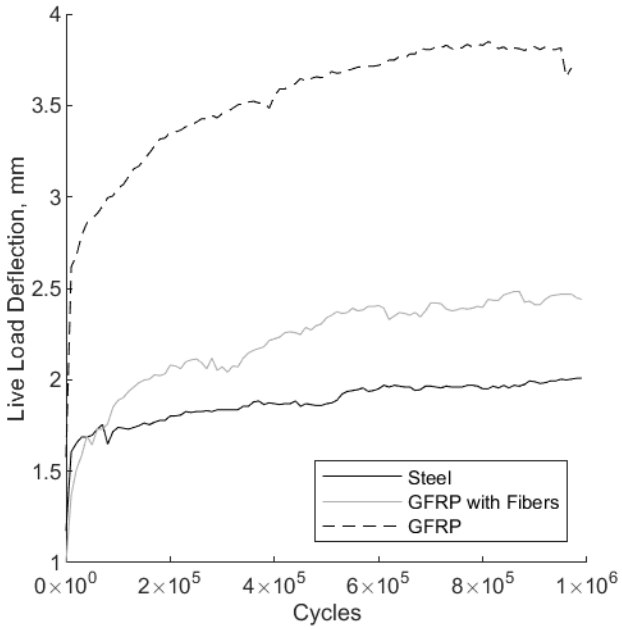

Figure 5.4.6 Live load crack opening vs. No. of cycles for 1 million cycles (SI)

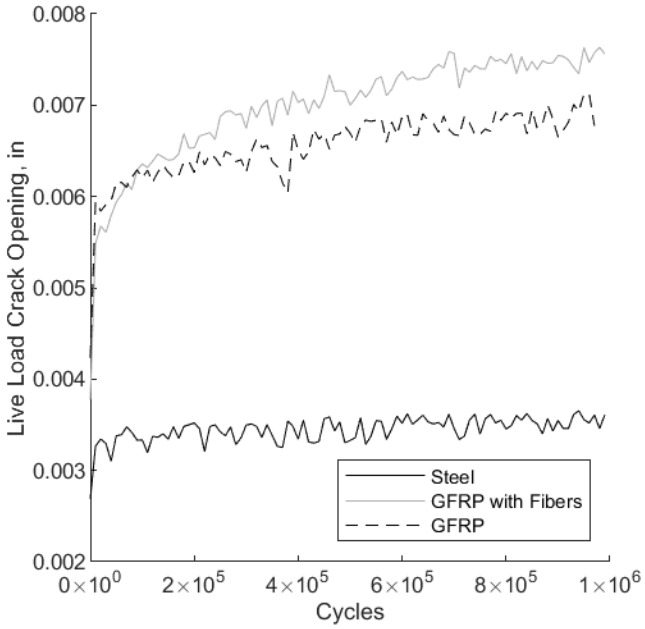

Figure 5.4.7 Live load crack opening vs. No. of cycles for 1 million cycles (Imperial)

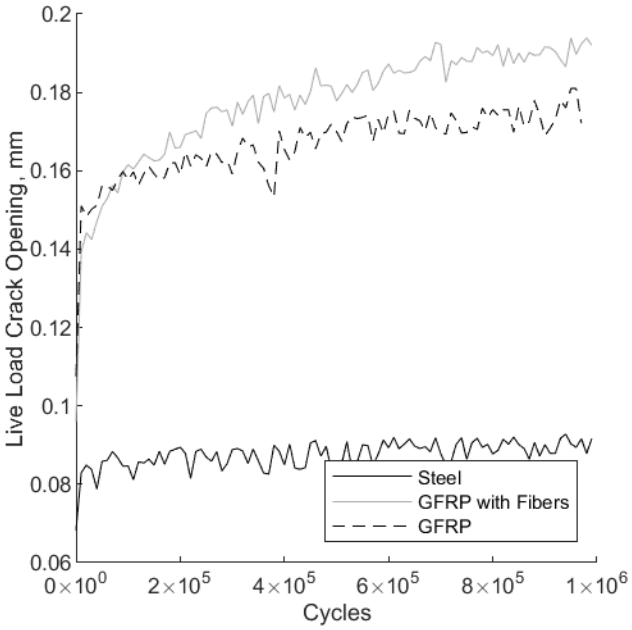

Figure 5.4.8 Live load crack opening vs. No. of cycles for 1 million cycles (SI)

Figure 5.4.9 and Figure 5.4.10 show the peak deflection for 2 million cycles. Figure 5.411 and Figure 5.4.12 show the peak crack width for 2 million cycles. Figure 5.4.13 and Figure 5.4.14 show the live load deflection of the decks for 2 million cycles, and Figure 5.4. and Figure 5.4. show the live load crack opening for 2 million cycles.

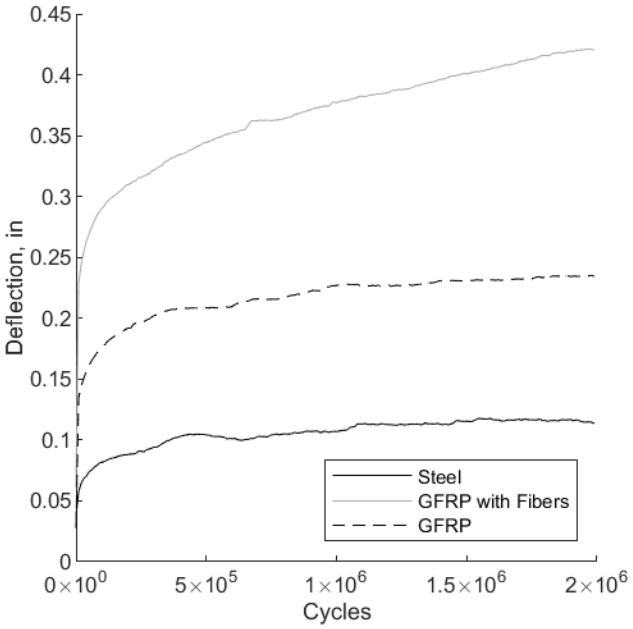

Figure 5.4.9 Peak deflection vs. No. of cycles for 2 million cycles (Imperial)

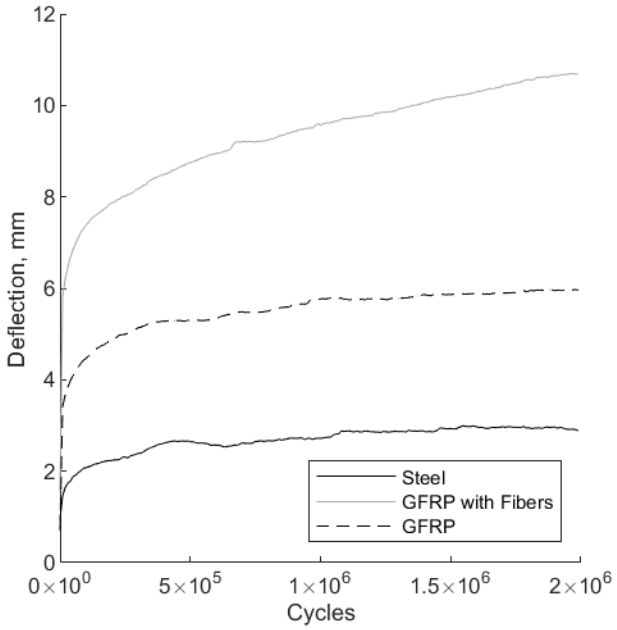

Figure 5.4.10 **P**eak deflection vs. No. of cycles for 2 million cycles (SI)

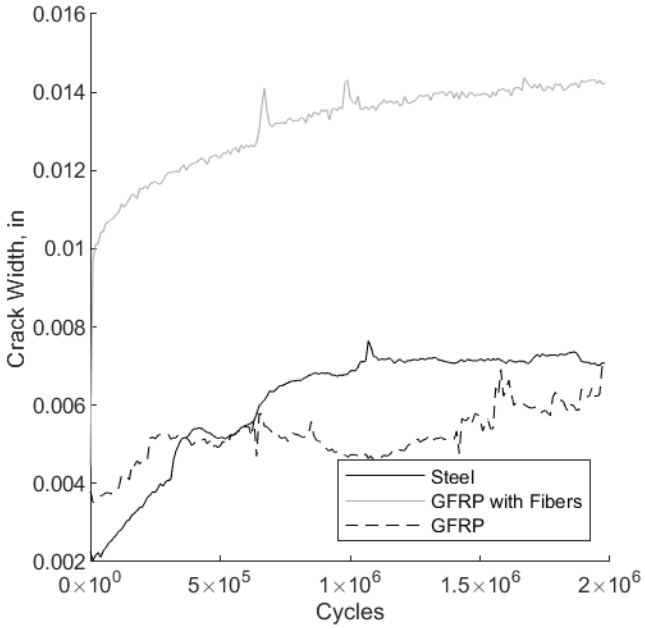

Figure 5.4.11 Peak crack width vs. No. of cycles for 2 million cycles (Imperial)

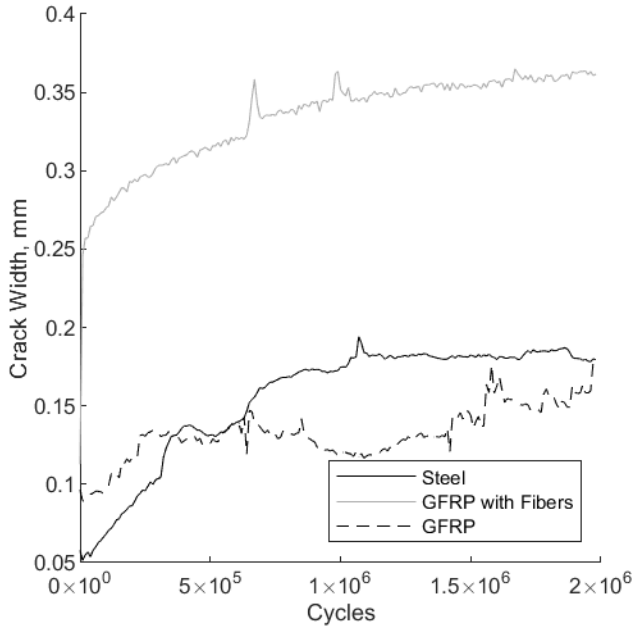

Figure 5.4.12 Peak crack width vs. No. of cycles for 2 million cycles (SI)

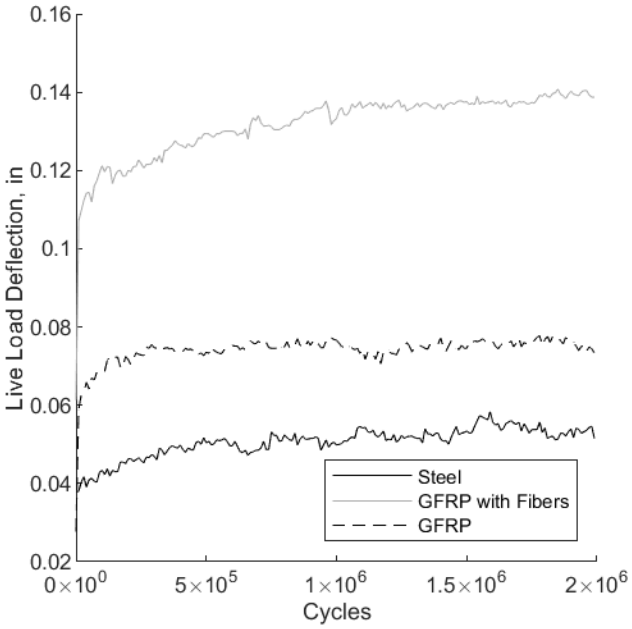

Figure 5.4.13 Live load deflection vs. No. of cycles for 2 million cycles (Imperial)

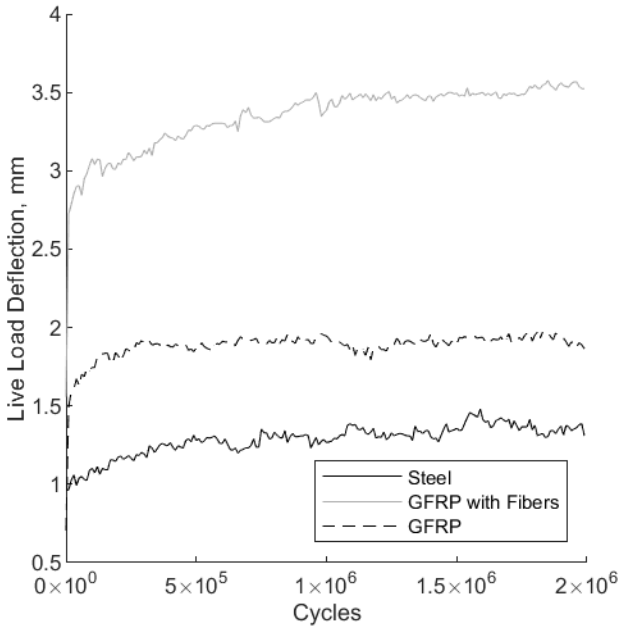

Figure 5.4.14 Live load deflection vs. No. of cycles for 2 million cycles (SI)

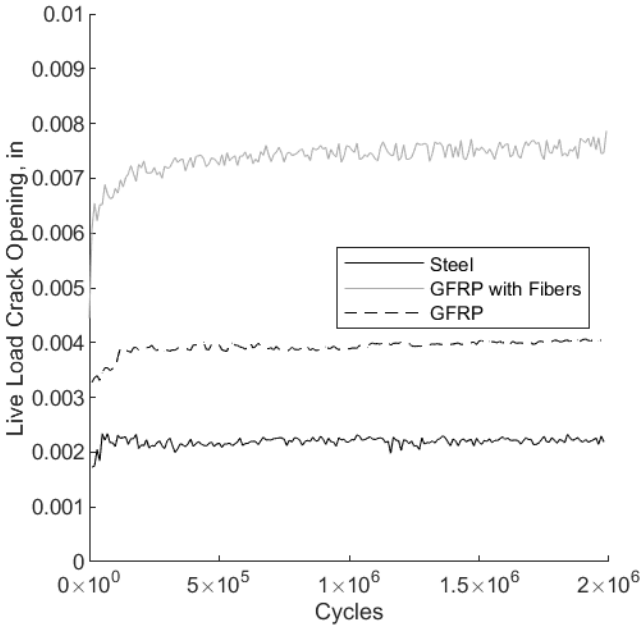

Figure 5.4.15 Live load crack opening vs. No. of cycles for 2 million cycles (Imperial)

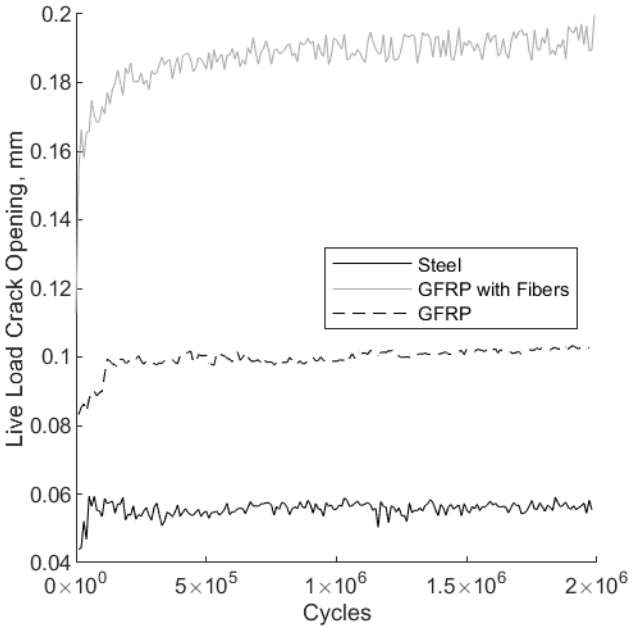

Figure 5.4.16 Live load crack opening vs. No. of cycles for 2 million cycles (SI)

The combined 1 and 2 million cycles are shown in the following figures. Figure 5.4.17 and Figure 5.4.18 contain the combined peak deflection, Figure 5.4.19 and Figure 5.4.20 show the combined peak crack width, Figure 5.4.21 and Figure 5.4.22 show the combined live load deflection, and Figure 5.4.23 and Figure 5.4.24 show the live load crack opening.

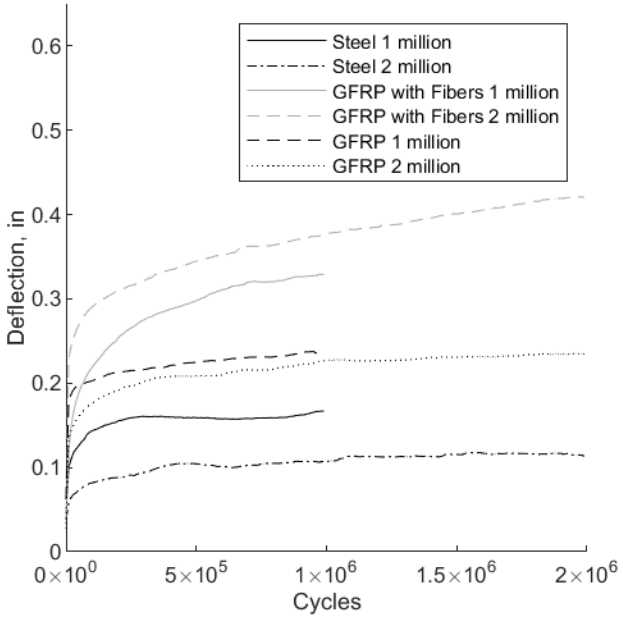

Figure 5.4.17 Peak deflection vs. No. of cycles – combined (Imperial)

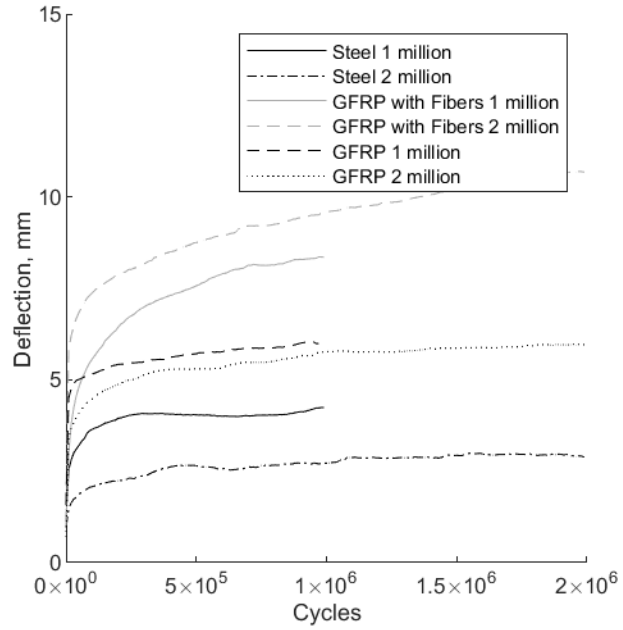

Figure 5.4.18 Peak deflection vs. No. of cycles – combined (SI)

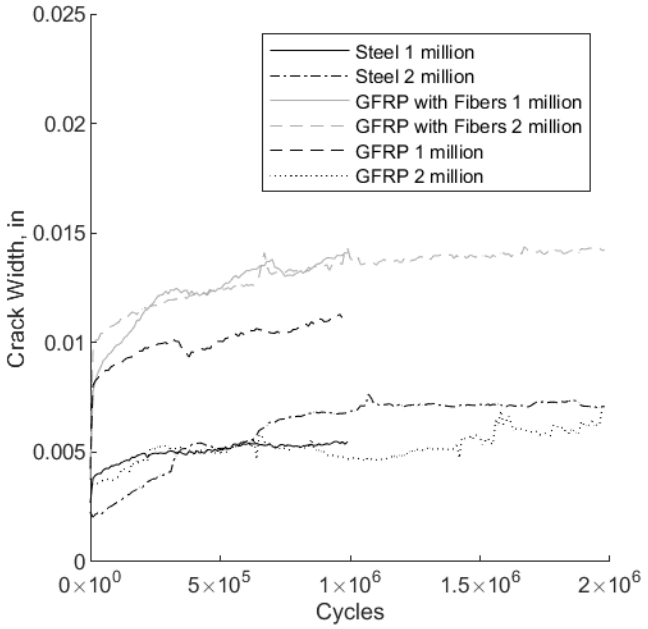

Figure 5.4.19 Peak crack opening vs. No. of cycles – combined (Imperial)

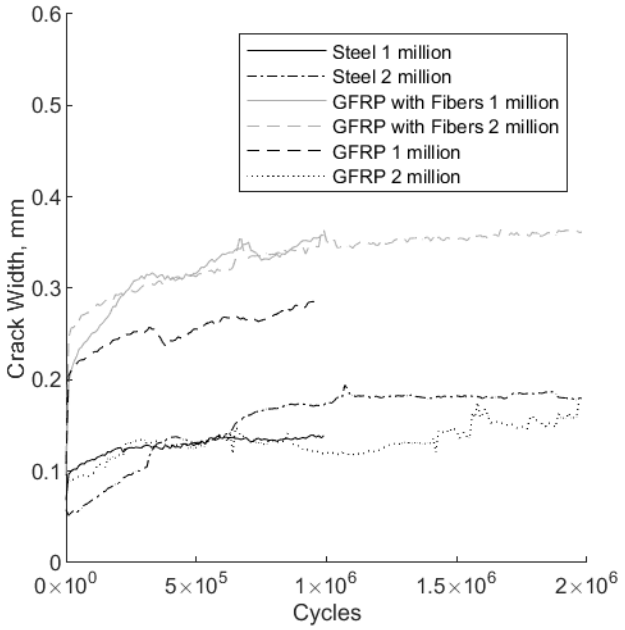

Figure 5.4.20 Peak crack opening vs. No. of cycles – combined (SI)

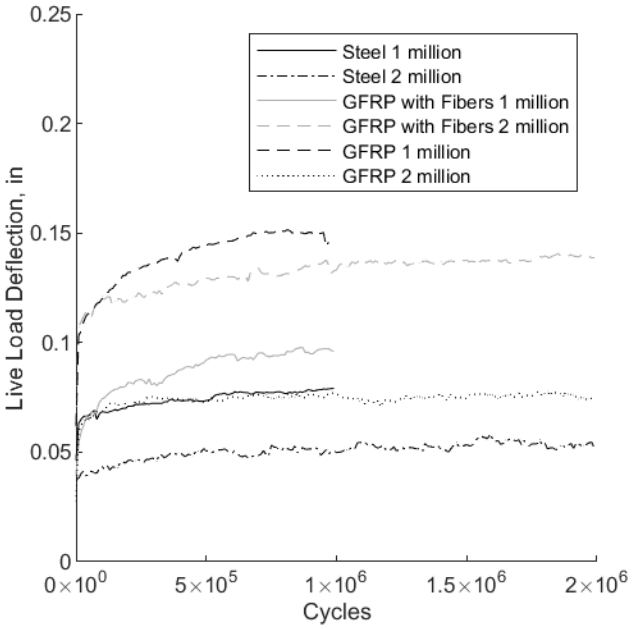

Figure 5.4.21 Live load deflection vs. No. of cycles – combined (Imperial)

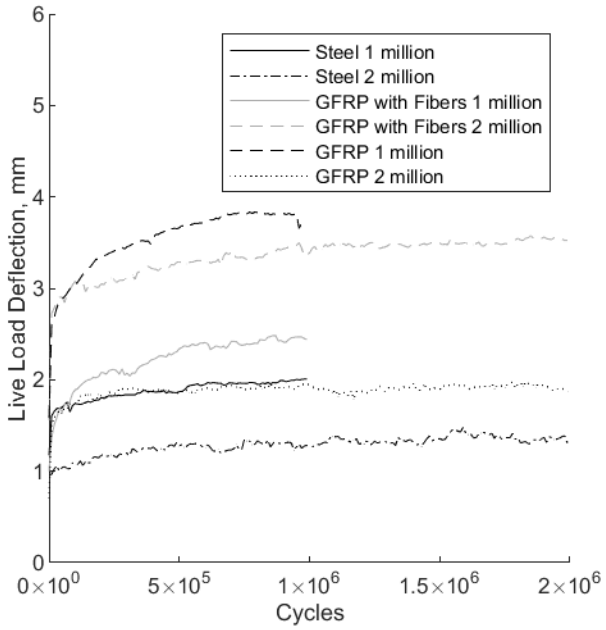

Figure 5.4.22 Live load deflection vs. No. of cycles – combined (SI)

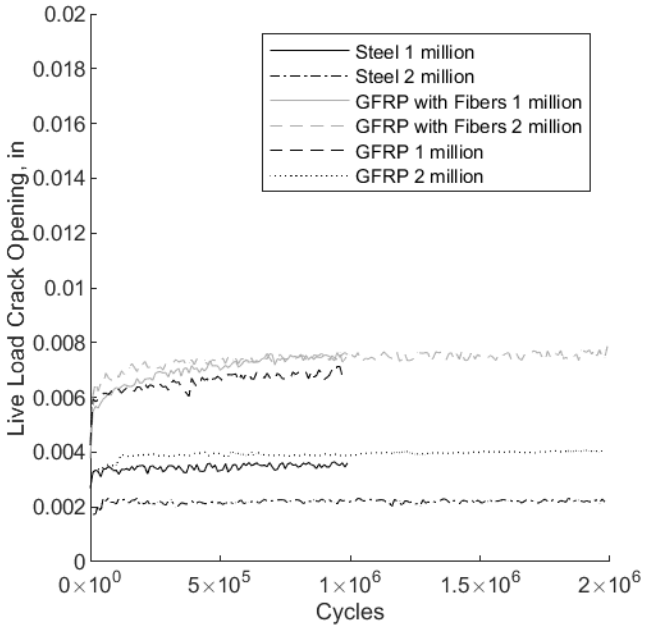

Figure 5.4.23 Live load crack opening vs. No. of cycles – Combined (Imperial)

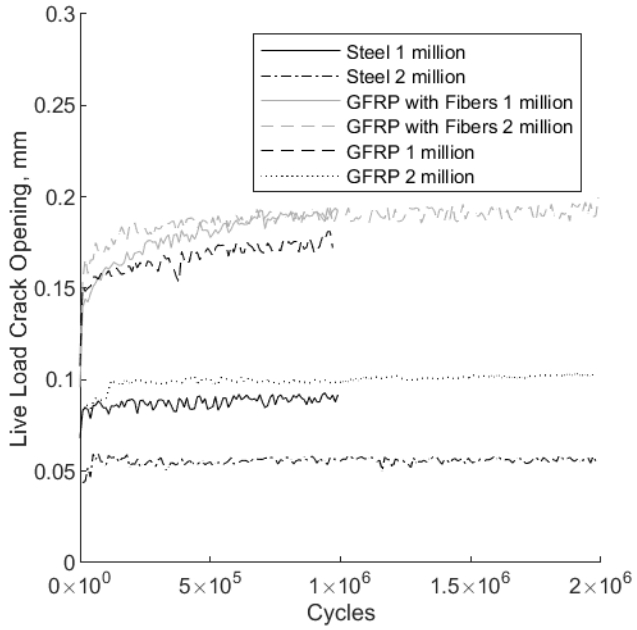

Figure 5.4.24 Live load crack opening vs. No. of cycles – Combined (SI)

Table 5.4.1 contains the maximum values for the peak deflection, Table 5.4.2 contains the maximum values for the peak crack width, Table 5.4.3 contains the maximum values for the live load deflection, and Table 5.4.4 contains the maximum values for the live load crack opening.

Table 5.4.1 Peak deflection values

Deck Type	Cycle Count	Peak Deflection, in. (mm)
Steel	1 Million	0.17 (4.3)
	2 Million	0.12 (3.0)
GFRP	1 Million	0.24 (6.1)
	2 Million	0.24 (6.1)
HRC	1 Million	0.33 (8.4)
	2 Million	0.42 (10.7)

Table 5.4.2 Peak crack width values

Deck Type	Cycle Count	Peak Crack Width, in. (mm)
Steel	1 Million	0.006 (0.14)
	2 Million	0.008 (0.20)
GFRP	1 Million	0.011 (0.29)
	2 Million	0.0073 (0.19)
HRC	1 Million	0.014 (0.36)
	2 Million	0.015 (0.37)

Table 5.4.3 Live load deflection values

Deck Type	Cycle Count	Live Load Deflection, in. (mm)
Steel	1 Million	0.080 (2.0)
	2 Million	0.059 (1.5)
GFRP	1 Million	0.15 (3.9)
	2 Million	0.079 (2.0)
HRC	1 Million	0.10 (2.5)
	2 Million	0.14 (3.6)

Table 5.4.4 Live load crack opening values

Deck Type	Cycle Count	Live Load Crack Opening, in. (mm)
Steel	1 Million	0.0038 (0.10)
	2 Million	0.0026 (0.07)
GFRP	1 Million	0.0072 (0.18)
	2 Million	0.0041 (0.10)
HRC	1 Million	0.0080 (0.20)
	2 Million	0.0079 (0.20)

5.5 Post-Fatigue Static Testing Results

After the fatigue cycles were completed, a post-fatigue static test was performed for each of the decks. To ensure a flexural failure, the decks were loaded under 3-point flexure with a line load at midspan. The same loading strategy as the static tests was executed, and the load and displacement was recorded with a load cell and potentiometer, respectively. The moment-deflection response of the steel, HRC, and GFRP bridge decks are contained in Figure 5.5.1 and Figure 5.5.2, Figure 5.5.3 and Figure 5.5.4, and Figure 5.5.6 and Figure 5.5.7, respectively. Figure 5.5.8 and Figure 5.5.9 contain the moment-deflection response of all the decks combined.

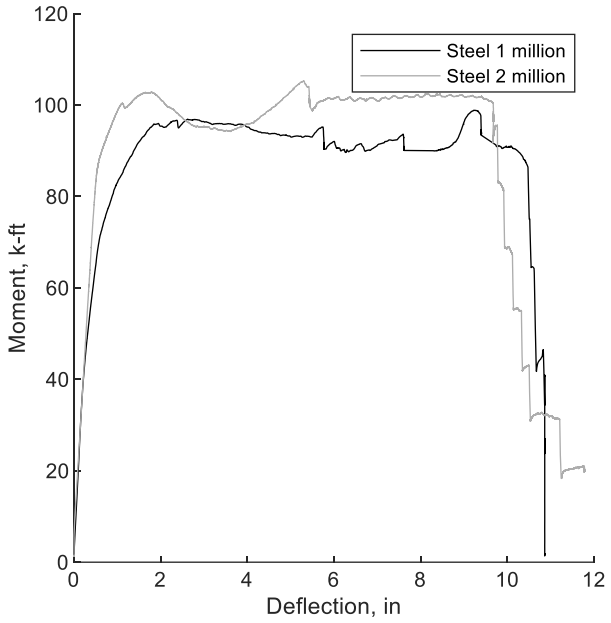

Figure 5.5.1 Moment-deflection response for post-fatigue steel decks (Imperial)

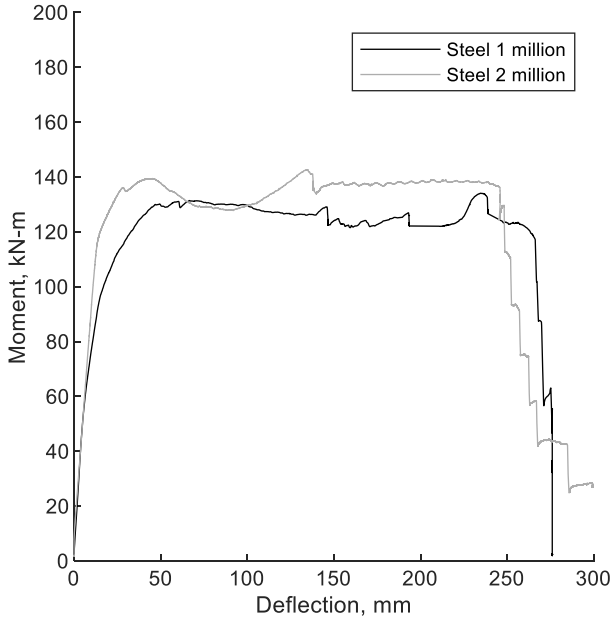

Figure 5.5.2 Moment-deflection response for post-fatigue steel decks (SI)

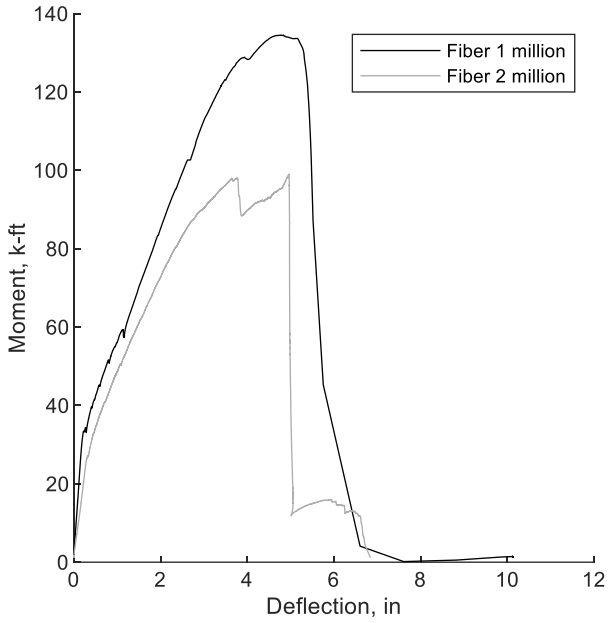

Figure 5.5.3 Moment-deflection response for post-fatigue HRC decks (Imperial)

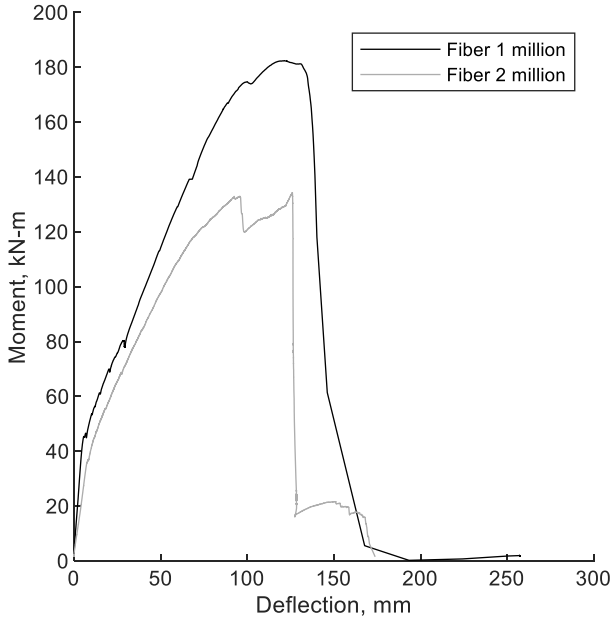

Figure 5.5.4 Moment-deflection response for post-fatigue HRC decks (SI)

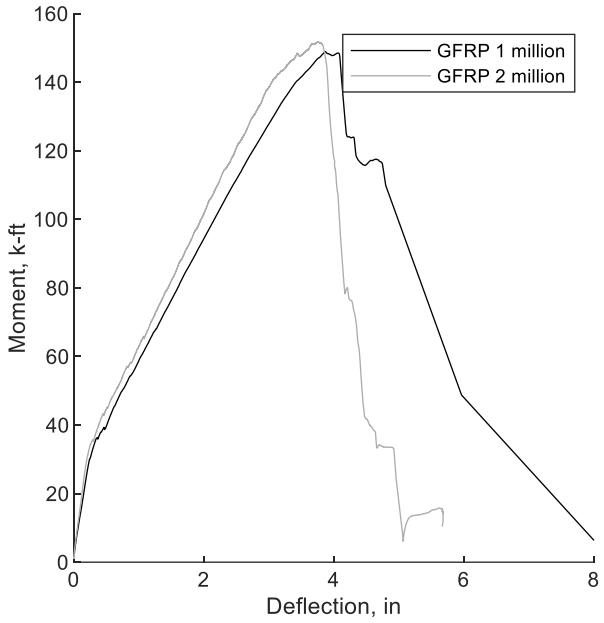

Figure 5.5.5 Moment-deflection response for post-fatigue GFRP decks (Imperial)

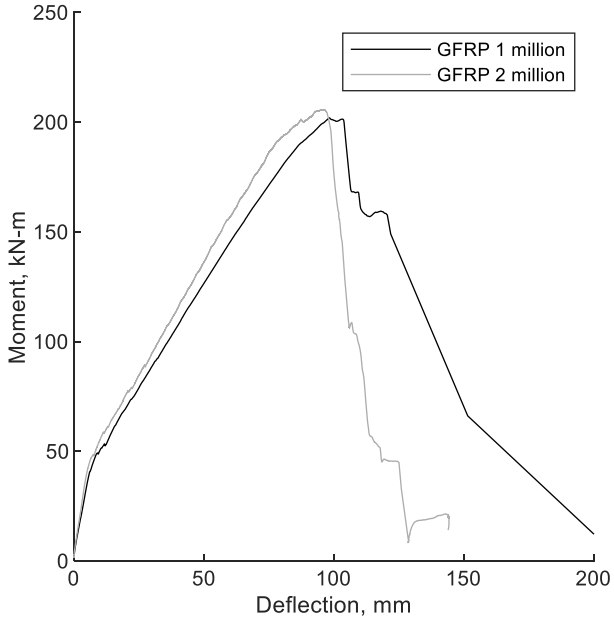

Figure 5.5.6 Moment-deflection response for post-fatigue GFRP decks (SI)

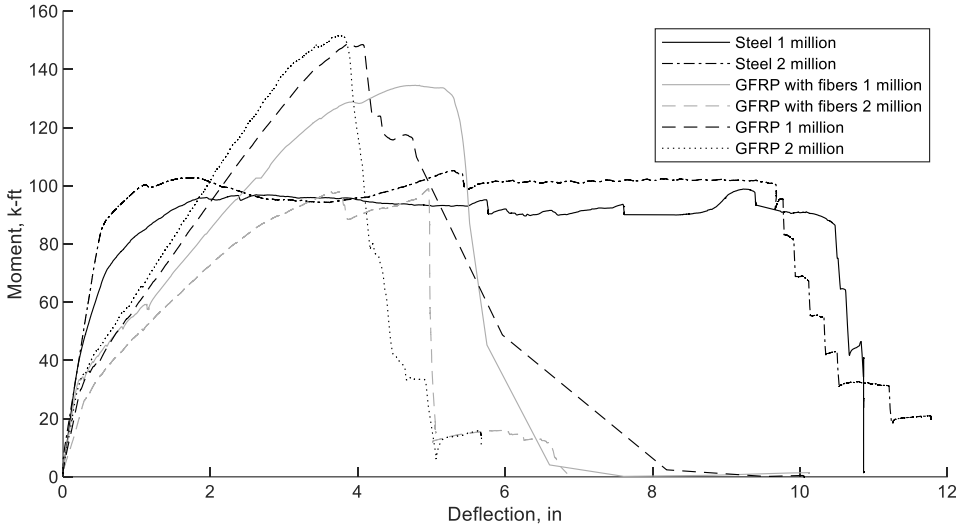

Figure 5.5.7 Moment-deflection response for post-fatigue decks (Imperial)

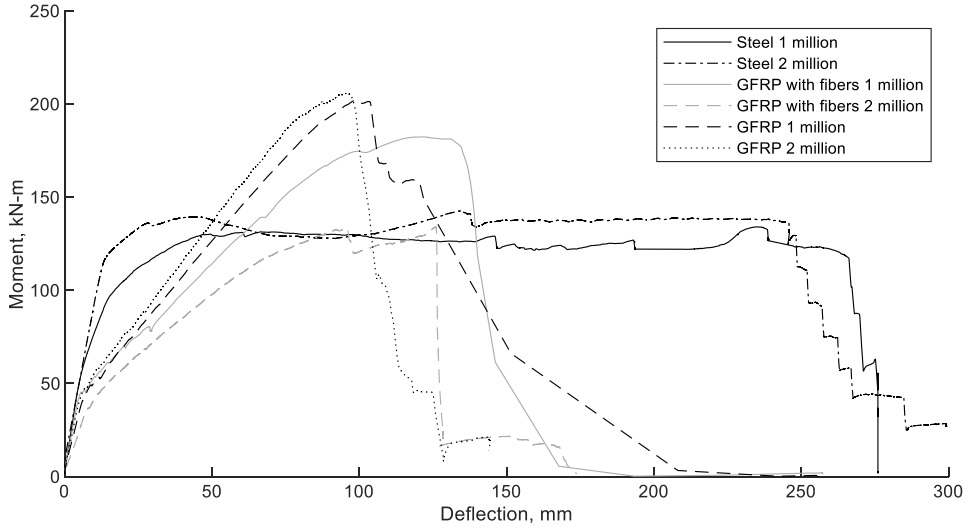

Figure 5.5.8 Moment-deflection response for post-fatigue decks (SI)

As in the static flexure testing, failure was defined as the moment that induced the crushing strain of the concrete. This failure moment and deflection at failure is recorded in Table 5.5.1.

.

Table 5.5.1 Maximum moments and deflections at failure for post-fatigue flexure

Deck Type	Cycle Count	Maximum Moment, kip-ft (kN-m)	Deflection at Failure, in. (mm)
Steel	1 Million	96.9 (131.4)	2.62 (66.5)
	2 Million	102.8 (139.4)	1.79 (45.5)
GFRP	1 Million	148.9 (201.9)	3.87 (98.3)
	2 Million	151.7 (205.7)	3.75 (95.3)
HRC	1 Million	134.5 (182.4)	4.84 (122.9)
	2 Million	99.0 (134.2)	4.96 (126.0)

In order to make a direct comparison of the capacity before and after the fatigue cycles, the moment-deflection response was plotted for both the pre- and post-fatigue behavior. Figure 5.5.9 and Figure 5.5.10 contain the compared steel deck moment-deflection response before and after fatigue. Figure 5.5.11 and Figure 5.5.12 show this comparison for the GFRP decks, and Figure 5.5.13 and Figure 5.5.14 demonstrate the change in the HRC deck capacity.

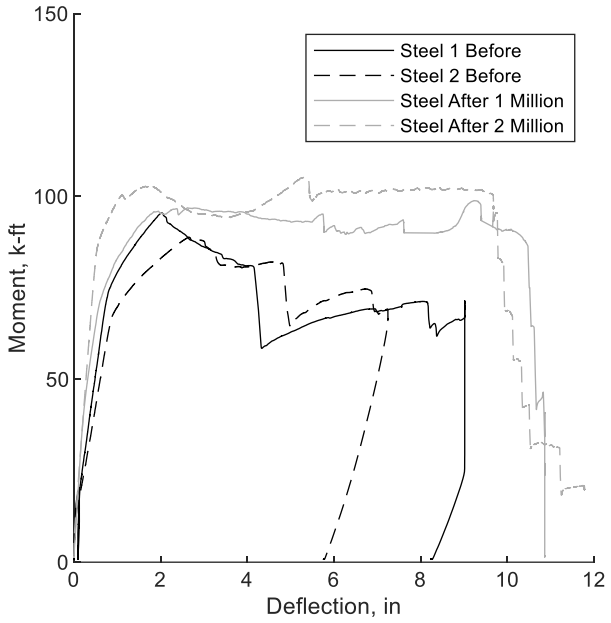

Figure 5.5.9 Moment-deflection before and after fatigue – steel (Imperial)

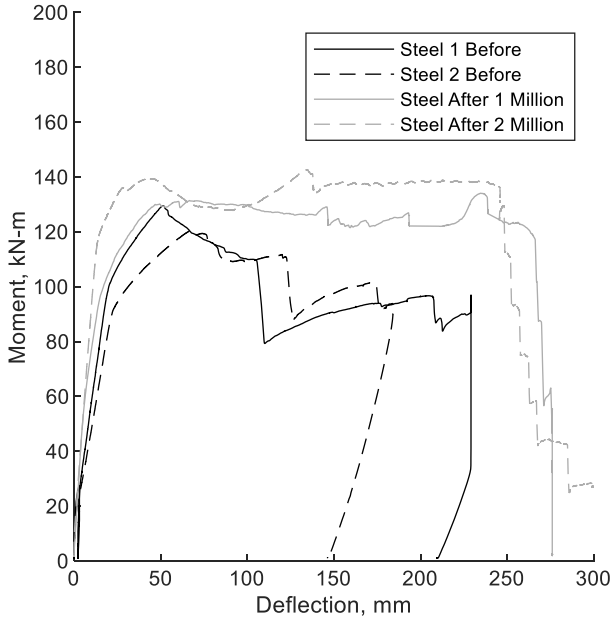

Figure 5.5.10 Moment-deflection before and after fatigue – steel (SI)

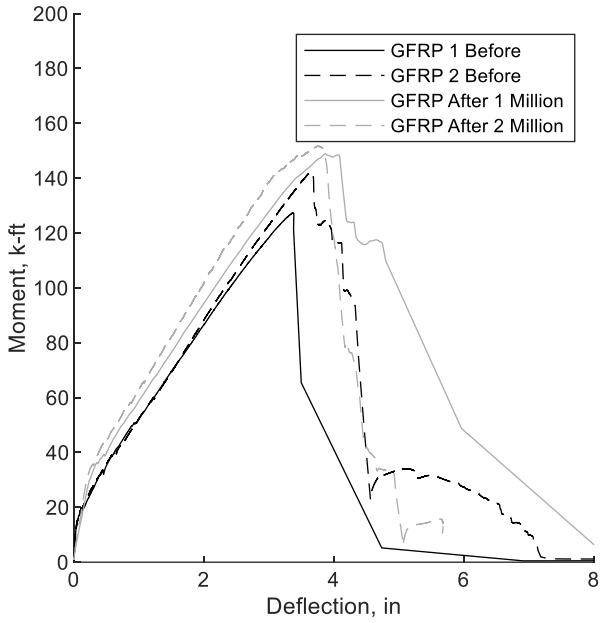

Figure 5.5.11 Moment-deflection before and after fatigue – GFRP (Imperial)

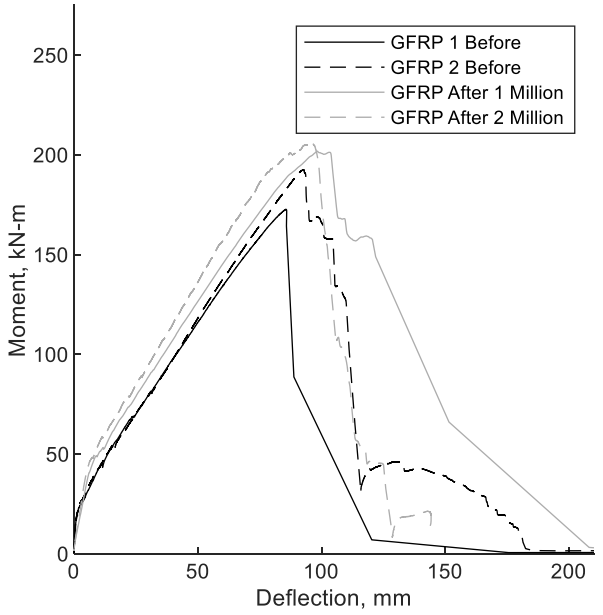

Figure 5.5.12 Moment-deflection before and after fatigue – GFRP (SI)

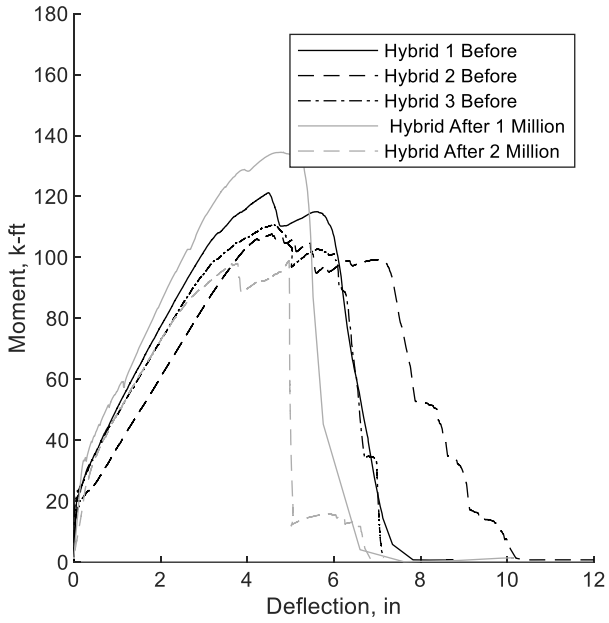

Figure 5.5.13 Moment-deflection before and after fatigue – HRC (Imperial)

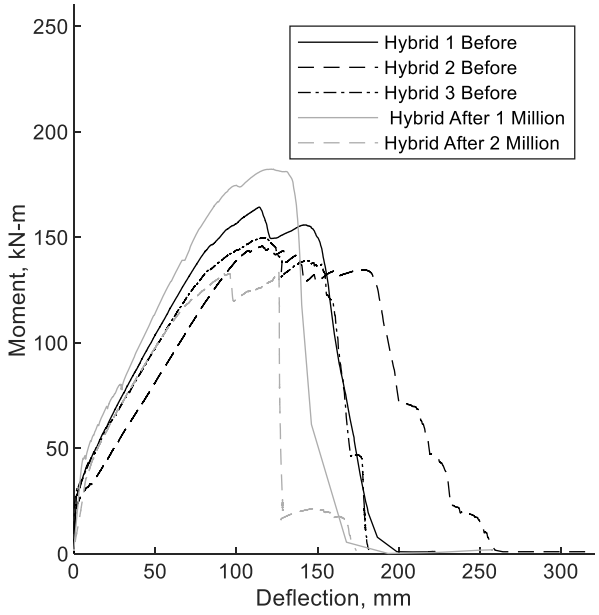

Figure 5.5.14 Moment-deflection before and after fatigue – HRC (SI)

6. EXPERIMENTAL RESULTS – PUNCHING SHEAR

6.1 Introduction

In the following section, the concrete testing data and punching shear data are presented. The rebar testing results from Chapter 5 are used for the entirety of the experiment; therefore, no additional rebar testing results are presented in this chapter. This section presents the pre-fatigue static punching shear data, as well as the post-fatigue static testing results. For each plot in Imperial units, a plot is also given in SI units.

6.2 Materials Testing

The compressive strength of the concrete was recorded at different times for each batch. The cylinders were tested at various days throughout the curing process. Although an attempt was made to test at 7, 14, and 28 days, some days were postponed or skipped. The target compressive strength of the concrete was 5 ksi (34.5 MPa). The compressive strength for the different deck types at different days is shown in Table 6.2.1.

Table 6.2.1 Compressive strengths of punching shear concrete

Deck Type	**Compressive Strength f'_c, psi (MPa)**				
Steel	*7 Days*	*14 Days*	*28 Days*	*Static Test*	*Fatigue Test*
	Not Tested	4,450 (30.7)	5,680 (39.2)	6,070 (41.9)	6,220 (42.9)
GFRP	*7 Days*	*14 Days*	*28 Days*	*Static Test*	*Fatigue Test*
	5,180 (35.7)	Not Tested	Not Tested	6,840 (47.2)	7,600 (52.4)
HRC	*7 Days*	*15 Days*	*28 Days*	*Static Test*	*Fatigue Test*
	2,640 (18.2)	3,550 (24.5)	3,790 (26.1)	4,250 (29.3)	4,250 (29.3)

The static modulus of elasticity was obtained by compressing the cylinders to 10%, 20%, and 40% of their peak strength and recording the chord modulus. This process was repeated three times for the three different cylinders of each batch type on the static large-scale testing days. The results for the modulus testing are shown in Table 6.2.2. Since the static and fatigue testing was performed within a window of, at most, 30 days, the modulus testing was performed for the static tests only.

The results for the splitting tensile strength testing is recorded in Table 6.2.3. Note that no splitting tensile test was performed on the HRC decks since the tensile capacity of the concrete is obtained according to a different standard, as described. Tensile splitting tests were performed on the day of the static testing.

Table 6.2.2 Modulus of elasticity of punching shear concrete

Deck Type	**Modulus of Elasticity, E_c, ksi (MPa)**
Steel	5,220 (36,000)
GFRP	5,920 (40,820)
HRC	5,415 (37,340)

Table 6.2.3 Splitting tensile strength of punching shear concrete

Deck Type	**Splitting Tensile Strength, f_t, psi (MPa)**
Steel	405 (2.8)
GFRP	416 (2.9)

Three mini beams were tested in accordance with EN 14651. The force vs. CMOD curve for the first set of HRC panels is shown in Figure 6.2.1. and Figure 6.2.2. The residual flexural tensile strength vs. CMOD is shown in Figure 6.2.3 and Figure 6.2.4. Figure 6.2.5 and Figure 6.2.6 show the average flexural tensile strength corresponding with each design crack width.

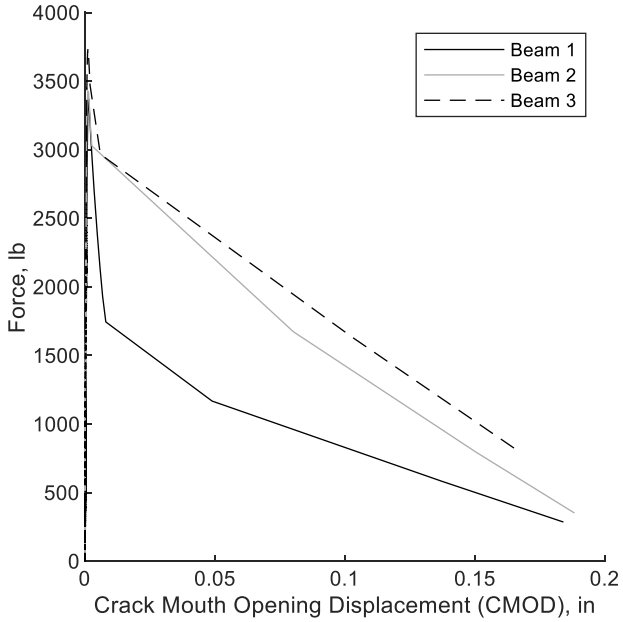

Figure 6.2.1 Force-CMOD curve HRC punching shear (Imperial)

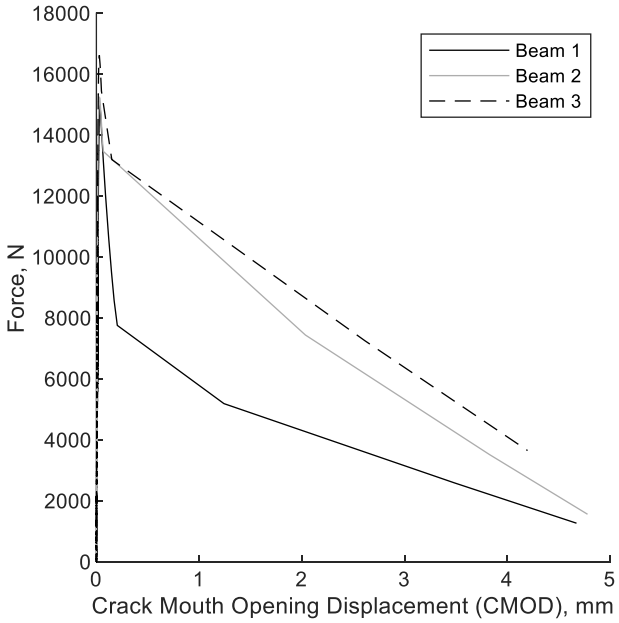

Figure 6.2.2 Force-CMOD curve HRC punching shear (SI)

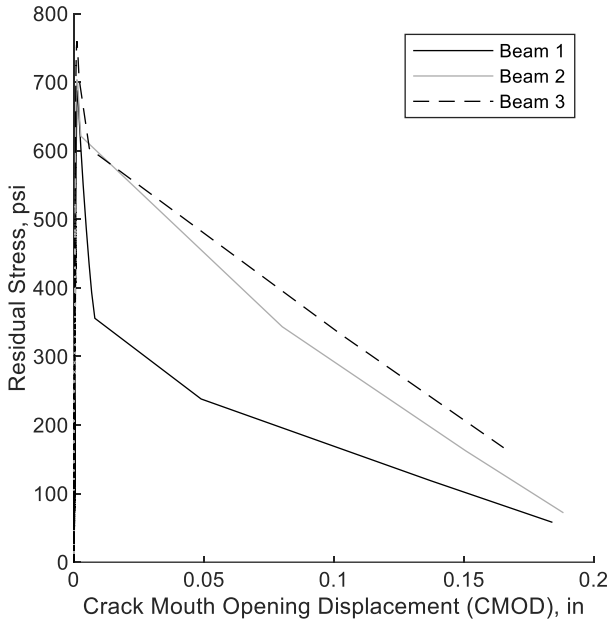

Figure 6.2.3 Stress-CMOD curve HRC punching shear (Imperial)

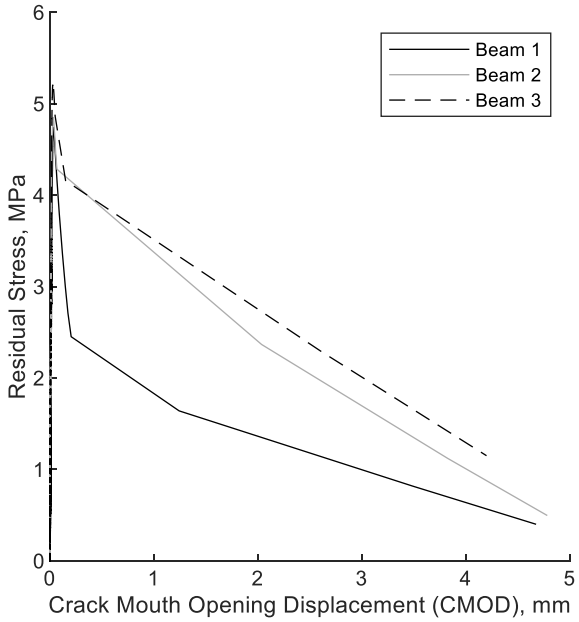

Figure 6.2.4 Stress-CMOD curve HRC punching shear (SI)

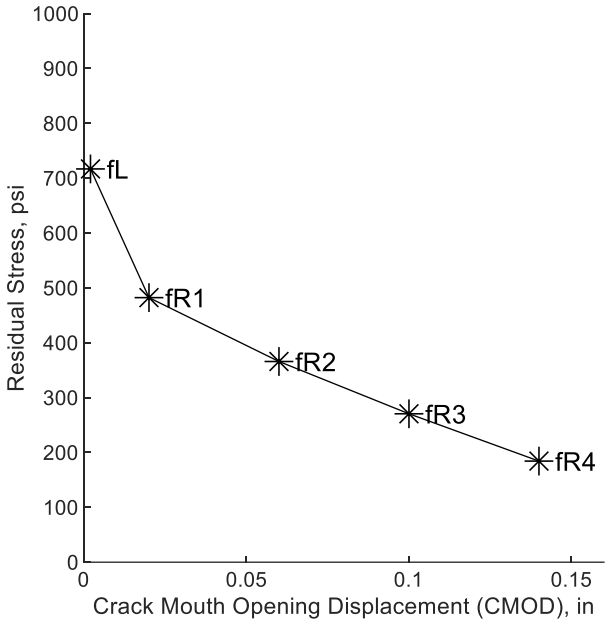

Figure 6.2.5 Average flexural tensile strength HRC punching shear (Imperial)

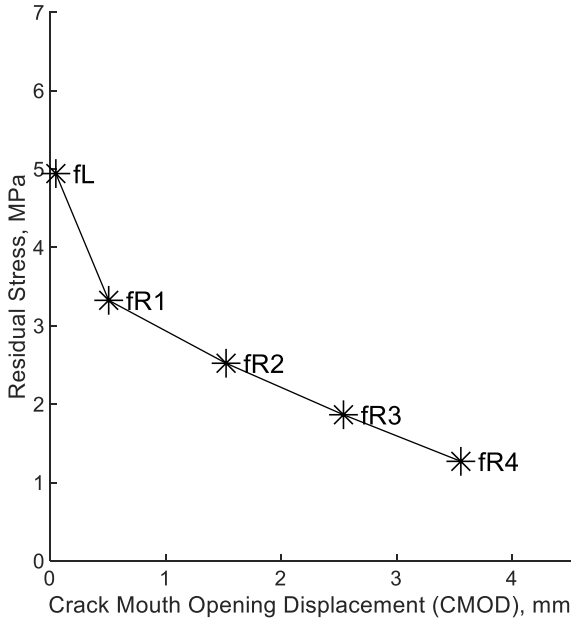

Figure 6.2.6 Average flexural tensile strength HRC punching shear (SI)

As shown above, at a relatively small dosage of 15 lb/ft^3 (8.90 kg/m^3), there is minimal strain hardening behavior post-cracking. The low compressive strength of the HRC also decreased the amount of post-cracking stress. The residual flexural tensile stresses are recorded for both sets of HRC concrete in Table 6.2.4.

Table 6.2.4 Residual flexural tensile stresses in punching shear FRC

Property	Residual Stress Value, psi (MPa)
Limit of Proportionality, f_{Lk}	716.9 psi (4.94)
f_{R1}	482.3 psi (3.33)
f_{R2}	365.8 psi (2.52)
f_{R3}	270.5 psi (1.87)
f_{R4}	184.3 psi (1.27)

According to the fib Model Code 2010, in order to be suitable to replace conventional discrete reinforcement, the f_{R1}/f_{Lk} ratio must exceed 0.4, and the f_{R3}/f_{R1} ratio must exceed 0.5 (CEB-FIB, 2013). For this set of HRC decks, the f_{R1}/f_{Lk} ratio is equal to 0.67, and the f_{R3}/f_{R1} ratio is equal to 0.56. Therefore, both checks are okay, and the decks are suitable according to the requirements for FRC. Once again, this check is only somewhat applicable to the HRC decks since they also have discrete bars.

6.3 Static Testing Results

While monotonically increasing the load, the force and deflection of the decks at the punching shear location were measured. Figure 6.3.7 and Figure 6.3.8 show the force-deflection relationship of the punching shear deck panels.

The maximum moment was recorded at failure for each panel, and the deflection at this peak moment was noted as well. For both the GFRP-reinforced and HRC bridge decks, the concrete crushed before the rupture of the GFRP. The steel rebar yielded prior to the concrete crushing for the steel-reinforced decks. The maximum moments and deflections at failure are shown in Table 6.3.5.

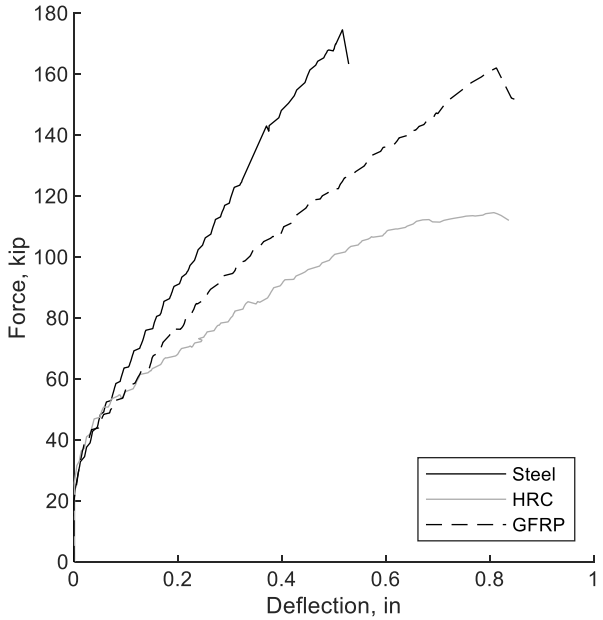

Figure 6.3.7 Force-deflection curves for punching shear decks (Imperial)

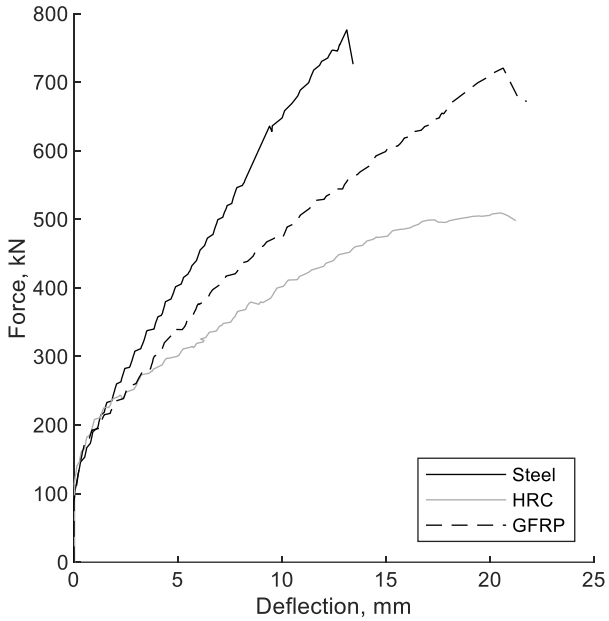

Figure 6.3.8 Force-deflection curves for punching shear decks (SI)

Table 6.3.5 Maximum force and deflections for punching shear decks

Deck Type	Maximum Force, kip (kN)	Deflection at Failure, in (mm)
Steel	176.8 (786.4)	0.52 (13.2)
GFRP	162.4 (722.4)	0.82 (20.8)
HRC	114.6 (509.8)	0.81 (20.6)

6.4 Fatigue Testing Results

Although the bridge deck sections were monitored for deflections throughout the testing, the deflections in the decks never reached a high enough threshold to exceed the noise in the sensor. The noise threshold was set at 0.0009" (0.023 mm). Therefore, the deflection data from the MTS actuator for the 1 million cycles were exported. These data were only relatively useful since the actuator saw deflections in the connection plates to the frame, bolts, plates at the swivel head, loading frame, and any other minor deflection in the setup. Figure 6.4.1 and Figure 6.4 2 show this actuator live load deflection compared with the AASHTO live load deflection limit.

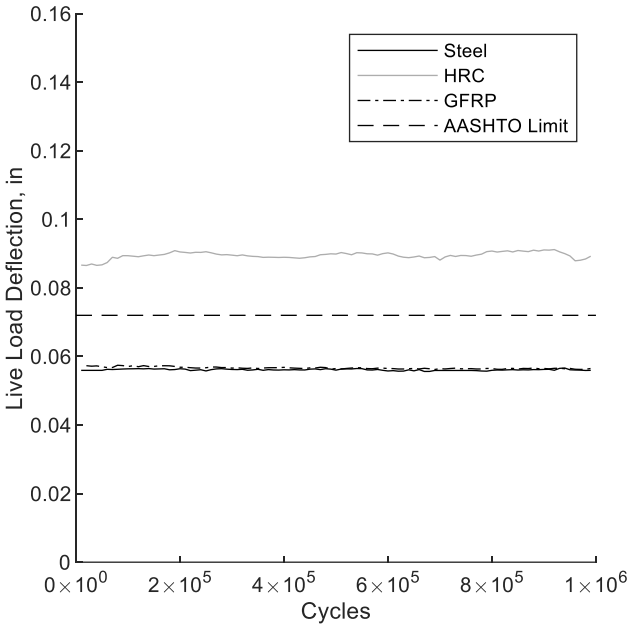

Figure 6.4.1 Actuator deflection for punching shear fatigue decks (Imperial)

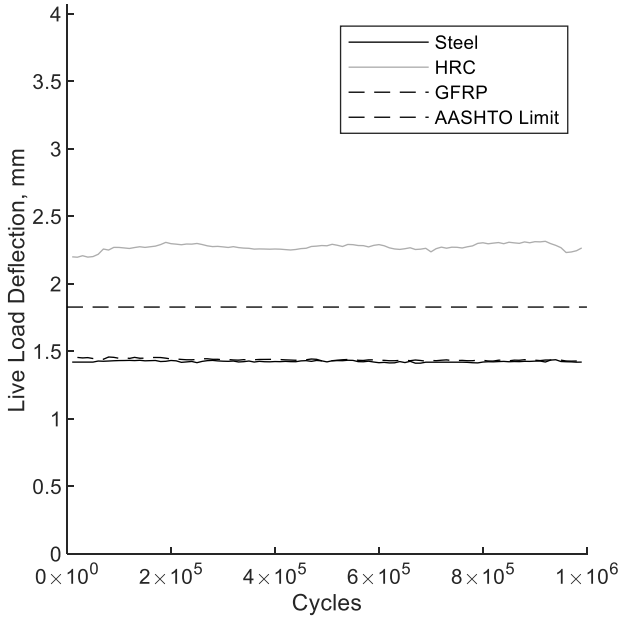

Figure 6.4.2 Actuator deflection for punching shear fatigue decks (SI)

6.5 Post-Fatigue Static Testing Results

After performing the 1 million cycles of fatigue, the decks were once again loaded until failure, and the deflection and load were recorded. Figure 6.5.1 and Figure 6.5.2 show the post-fatigue static testing results for each punching shear deck type. The load and deflection at failure are recorded in Table 6.5.1

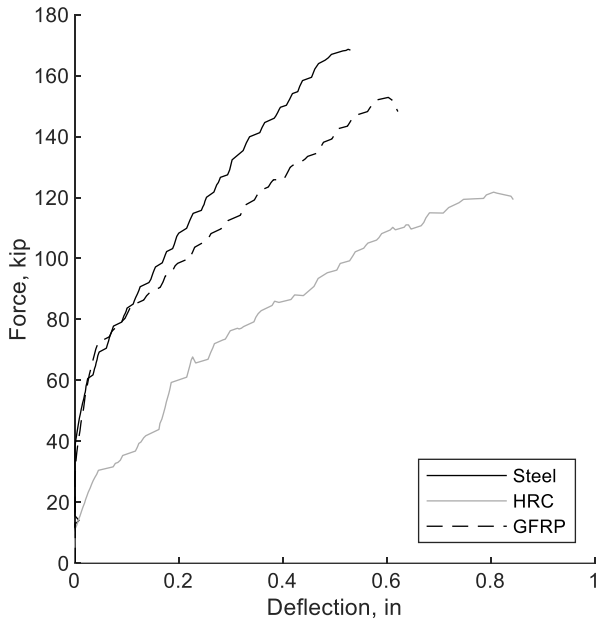

.

Figure 6.5.1 Force-deflection for post-fatigue punching shear decks (Imperial)

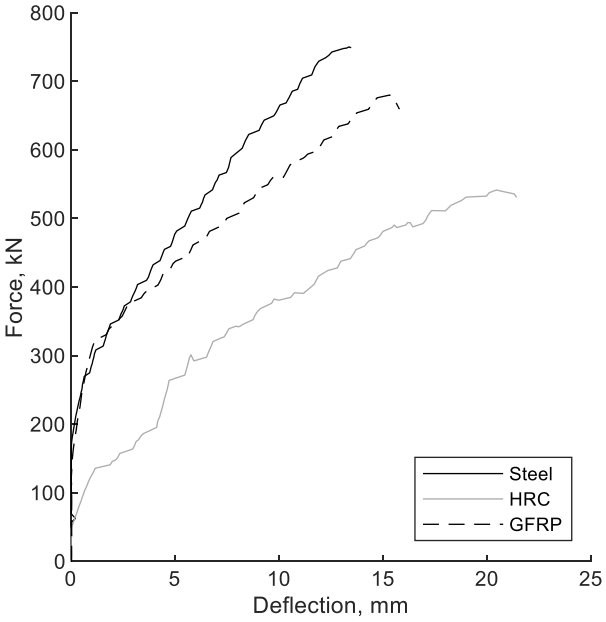

Figure 6.5.2 Force-deflection for post-fatigue punching shear decks (SI)

Table 6.5.1 Maximum forces and deflections for post-fatigue punching shear decks

Deck Type	Maximum Force, kip (kN)	Deflection at Failure, in (mm)
Steel	168.8 (750.9)	0.53 (13.5)
GFRP	153.0 (680.6)	0.61 (15.5)
HRC	121.8 (541.8)	0.81 (20.6)

7. DISCUSSION – FLEXURAL DECKS

7.1 Introduction

In this chapter, all of the results from the flexural experiment will be analyzed and discussed. The viability of HRC as an alternative bridge deck reinforcement strategy will be determined based on the data from Chapter 5. A perfect experiment that can account for all of the variability in bridge deck design, detailing, and fabrication cannot be executed, but the experiment performed provides useful information regarding the static and cyclic flexural behavior of HRC beams and deck panels. Understanding this mechanical behavior will enable a bridge engineer to design an HRC panel with a sufficient level of confidence.

This section is broken down into several parts. The first portion of this chapter contains the constitutive models of each material utilized to predict the flexural behavior of each deck type. After understanding the individual material responses, the fatigue data are analyzed to understand deflection and crack behavior at the service level loads. The effect of fatigue on the bridge decks is discussed, and normalizations that account for the strength and modulus of the concrete are performed to permit a direct comparison between different types of bridge deck types.

Following the discussion of the fatigue performance of each deck type, the strength limit state is analyzed. These include the moment-deflection response of each type. The experimentally obtained ultimate moment is compared with analytical predictions based on the material models created in the first portion of this chapter.

7.2 Material Models

7.2.1 Steel Reinforcement

In order to create a material model for the mild steel reinforcement used in this project, the rebar testing results from Chapter 5 were averaged and several assumptions were used to come up with the stress-strain constitutive relationship.

First, after the peak stress was reached, it was assumed that the stress remained constant after that point. The actual drop in stress from the peak to rupture is somewhere between 15% and 25%, but since this drop occurs at a strain of over 6.8% and is unlikely to occur for design reinforcement ratios prior to the rupture of the concrete, it is a valid assumption for this experiment. Equation 7.2.1 shows the stress level for each increment of strain:

$$\sigma = \begin{cases} \epsilon * E_s \; for \; \epsilon < \epsilon_y \\ \sigma_y \; for \; \epsilon_y \leq \epsilon < \epsilon_{sh} \\ \sigma_{sh} \; for \; \epsilon_{sh} \leq \epsilon < \epsilon_u \\ \sigma_u \; for \; \epsilon_u \leq \epsilon < \epsilon_r \\ 0 \; for \; \epsilon > \epsilon_r \end{cases} \tag{7.2.1}$$

Where

- σ = Stress in reinforcement
- σ_y = Yield stress
- σ_{sh} = Stress in steel after strain hardening and prior to peak
- σ_u = Peak stress
- E_s = Modulus of elasticity of steel

- ϵ = Strain in reinforcement
- ϵ_y = Yield strain
- ϵ_{sh} = Strain at onset of strain hardening
- ϵ_u = Strain corresponding to the peak stress
- ϵ_r = Strain at rupture

A quadratic relationship is assumed between the onset of strain hardening until the peak tensile stress is reached. This takes the form of Equation 7.2.2:

$$\sigma_{sh} = a_{coeff} * (\epsilon - \epsilon_u)^2 + F_u \quad (7.2.2)$$

Where

- a_{coeff} = Leading coefficient for parabolic standard form

The leading coefficient, a_{coeff}, is defined in Equation 7.2.3:

$$a_{coeff} = \frac{\sigma_y - \sigma_u}{(\epsilon_{sh} - \epsilon_u)^2} \quad (7.2.3)$$

Figure 7.2.1 and Figure 7.2.2 show this relationship between stress and strain for the steel reinforcement. This relationship is assumed to be equivalent for compression. This assumption holds since the steel is confined in the concrete and unable to buckle.

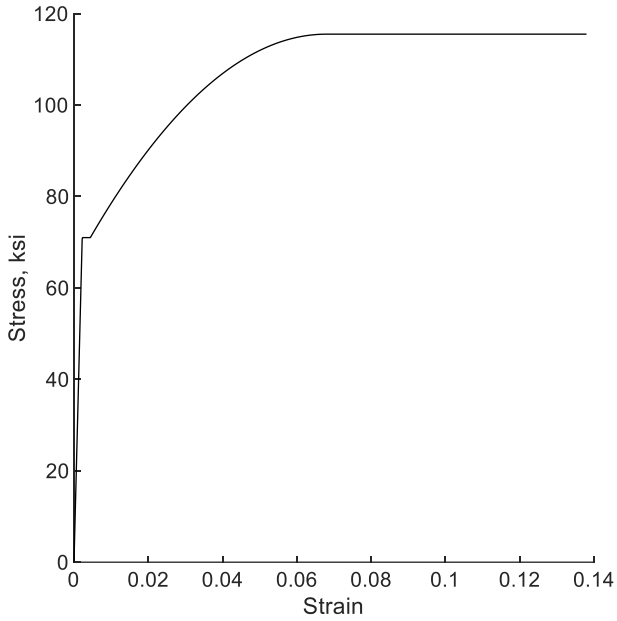

Figure 7.2.1 Steel stress-strain constitutive relationship (Imperial)

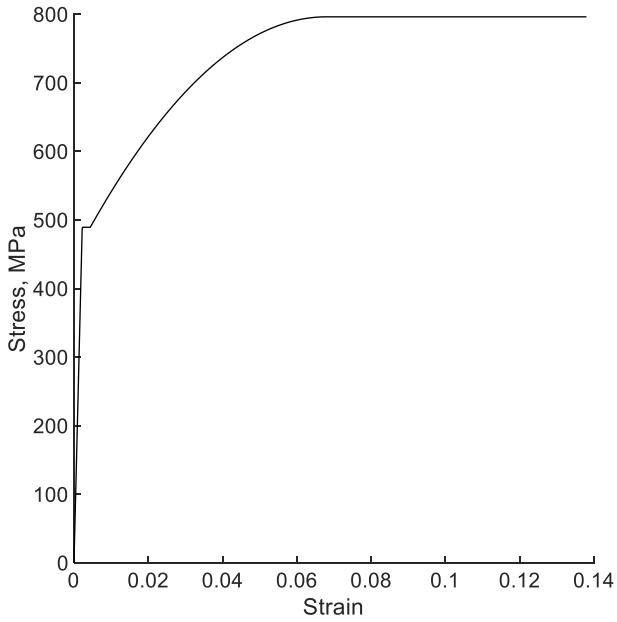

Figure 7.2.2 Steel stress-strain constitutive relationship (SI)

A more exact solution could be created by using the steel testing data directly as input data, but this more general solution can be derived for any steel test data and is very accurate within the stress ranges that bridge decks will experience.

7.2.2 GFRP Reinforcement

The GFRP model is much simpler to synthesize due to the linearity of the GFRP reinforcement until failure. Equation 7.2.4 demonstrates this linear constitutive relationship, and Figure 7.2.3 and Figure 7.2.4 show the stress-strain relationship of the GFRP reinforcement.

$$\sigma = \begin{cases} \epsilon * E_f \; for \; \epsilon < \epsilon_{fu} \\ 0 \; for \; \epsilon > \epsilon_{fu} \end{cases} \tag{7.2.4}$$

Where

- σ = Stress in reinforcement
- E_f = Modulus of elasticity of GFRP
- ϵ = Strain in reinforcement
- ϵ_{fu} = Rupture strain of GFRP

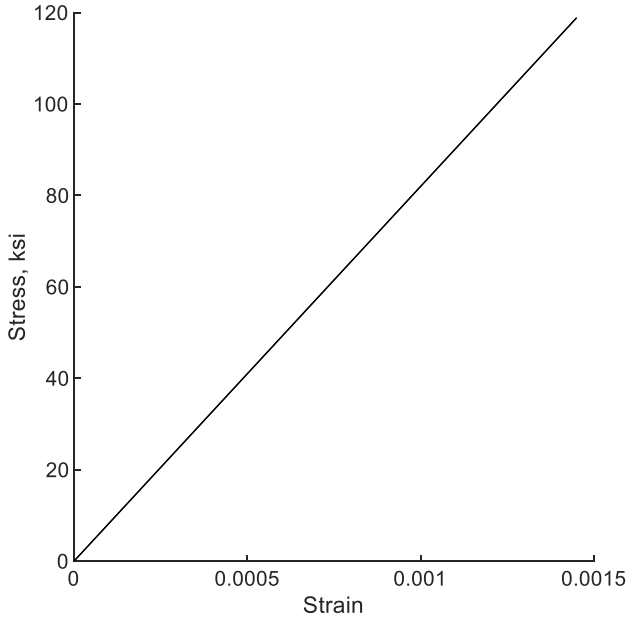

Figure 7.2.3 GFRP stress-strain constitutive relationship (Imperial)

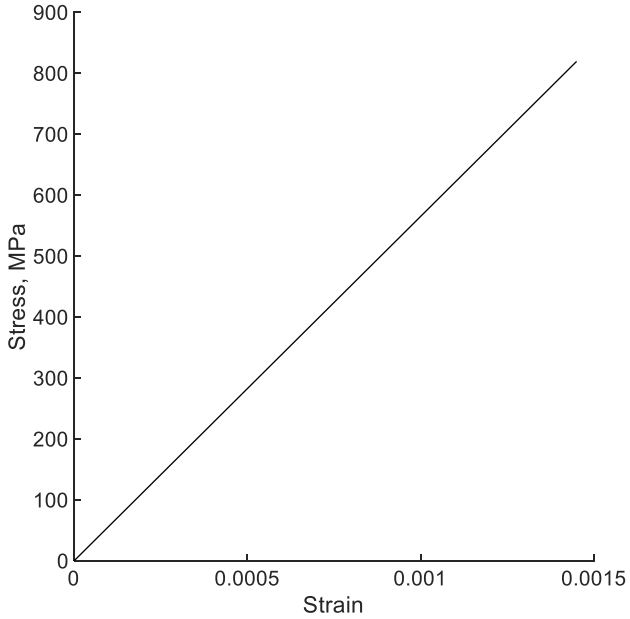

Figure 7.2.4 GFRP stress-strain constitutive relationship (SI)

Although the compressive stress in the GFRP is usually neglected, the GFRP in compression is so close to the neutral axis, that even including it in the calculations results in a nearly negligible stress value. In this experiment, in order to simplify the model, the GFRP contribution in compression was assumed to follow the same stress-strain relationship as the GFRP tension model.

7.2.3 Plain Concrete

The concrete compression model was assumed to follow a modified version of Hognestad's constitutive relationship for unconfined plain concrete in compression shown in Figure 7.2.5 (Hognestad, 1951). The value of the curved portion of the stress-strain curve prior to the peak is given in Equation 7.2.5:

$$f_c = f_c'' \left[2\frac{\epsilon}{\epsilon_0} - \left(\frac{\epsilon}{\epsilon_0}\right)^2 \right] \tag{7.2.5}$$

Where

- f_c = Compressive stress in concrete
- f''_c = Maximum stress in flexure
- ϵ = Strain in the concrete
- ϵ_0 = Strain corresponding to peak concrete stress

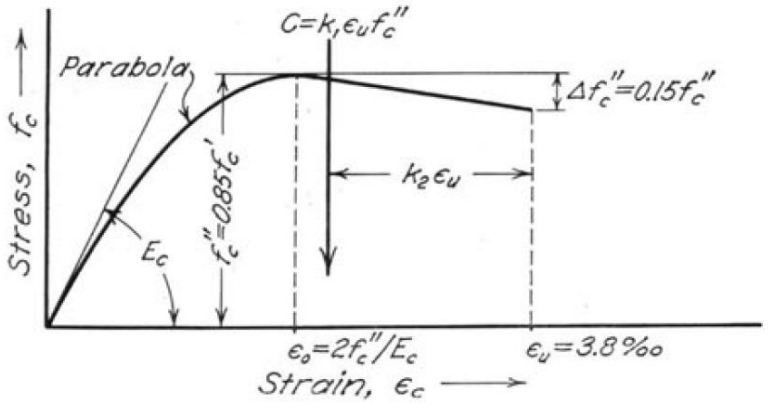

Figure 7.2.5 Hognestad relationship (adapted from Hognestad, 1951)

Following the peak stress, a linear relationship is assumed for a 15% drop from the peak stress up until the rupture strain of concrete. Kent and Park (1971) developed a modified version of the Hognestad relationship which assumes that the peak stress, f_c'', is the full concrete compressive strength, f_c' . They also determined that the peak strain, ϵ_0, is 0.002. We will also assume that our maximum compressive strain in the concrete is 3%, rather than the 3.8% assumed by Hognestad. Our model will incorporate all of these assumptions, therefore, the compressive model for the concrete of this experiment will use the constitutive relationship outlined in Equation 7.2.6:

$$f_c = \begin{cases} \sigma_1 \; for \; 0 \leq \epsilon < \epsilon_0 \\ \sigma_2 \; for \; \epsilon_0 \leq \epsilon < \epsilon_{cu} \\ 0 \; for \; \epsilon \geq \epsilon_{cu} \end{cases} \tag{7.2.6}$$

Where

- f_c = Compressive stress in concrete
- σ_1 = Stress in parabolic region prior to peak
- σ_2 = Stress in linear region after peak stress
- ϵ = Strain in concrete
- ϵ_0 = Strain at peak compressive stress
- ϵ_{cu} = Concrete rupture strain

The stress values for σ_1 and σ_2 are given in Equations 7.2.7 and 7.2.8, respectively:

$$\sigma_1 = f_c' \left[2\frac{\epsilon}{\epsilon_0} - \left(\frac{\epsilon}{\epsilon_0}\right)^2 \right] \tag{7.2.7}$$

$$\sigma_2 = f_c' \left[1 - 0.15\left(\frac{\epsilon - \epsilon_0}{\epsilon_0}\right) \right] \tag{7.2.8}$$

For each strength of concrete, a corresponding stress-strain relationship was constructed. An example relationship for 5 ksi (34.5 MPa) concrete is demonstrated in Figure 7.2.6 and Figure 7.2.7.

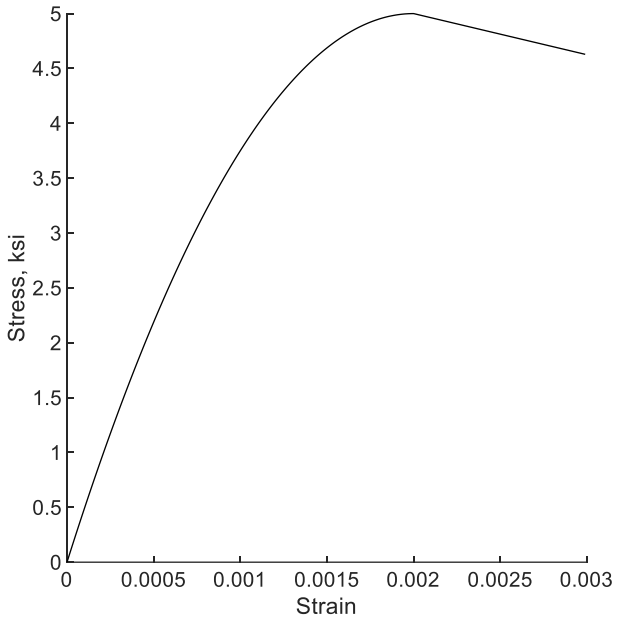

Figure 7.2.6 Concrete compressive stress-strain constitutive relationship (Imperial)

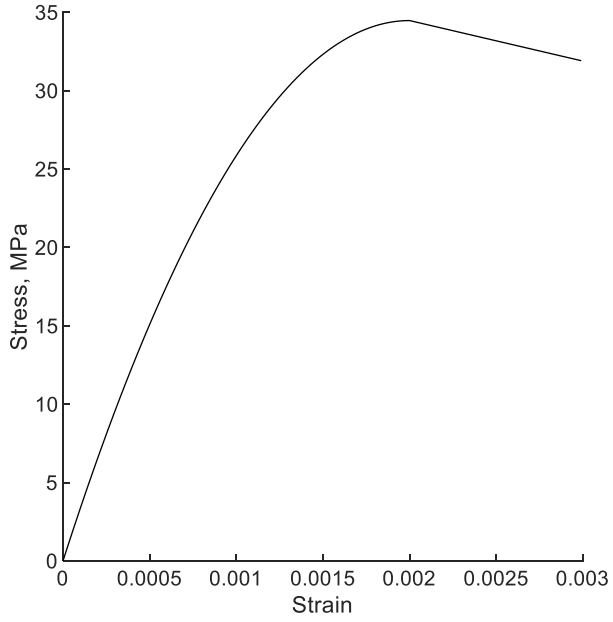

Figure 7.2.7 Concrete compressive stress-strain constitutive relationship (SI)

A very simplified concrete tension model is adopted for this study. It is assumed that the contribution of concrete in tension is negligible after rupture. In reality, there is some level of tension-stiffening, but this contribution is not included in this document due to the wide variability in tension-stiffening from steel, GFRP, and HRC reinforcing strategies. The model shown in Equation 7.2.9 demonstrates the linear nature of the concrete in tension up until the MOR.

$$f_t = \begin{cases} \epsilon * E_c \; for \; 0 \leq \epsilon < \epsilon_r \\ 0 \; for \; \epsilon > \epsilon_r \end{cases} \quad (7.2.9)$$

Where

- f_t = Tension stress in concrete
- E_c = Modulus of elasticity of concrete
- ϵ = Strain in concrete
- ϵ_r = Rupture strain in concrete

Figure 7.2.8 and Figure 7.29 show the linear stress-strain relationship of concrete in tension up until the MOR. A range of concrete models is developed for each batch of concrete, but for this example model, an MOR of 0.6 ksi (4.1 MPa), and a modulus of elasticity, E_c, of 4765 ksi (32850 MPa) is assumed.

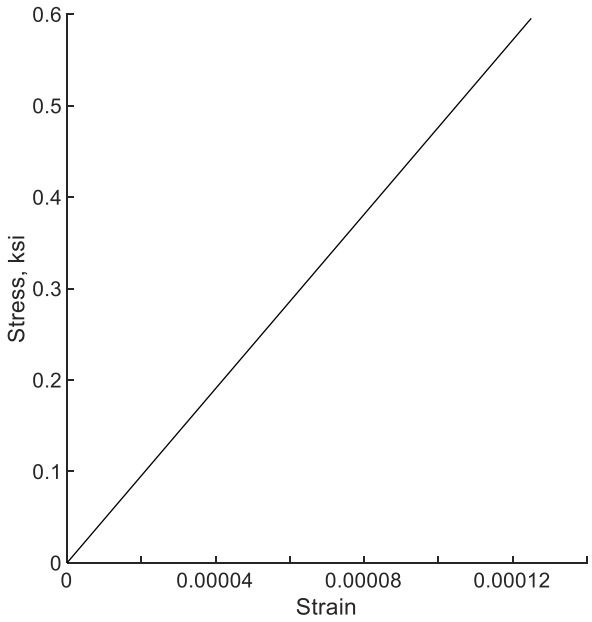

Figure 7.2.8 Concrete in tension stress-strain constitutive relationship (Imperial)

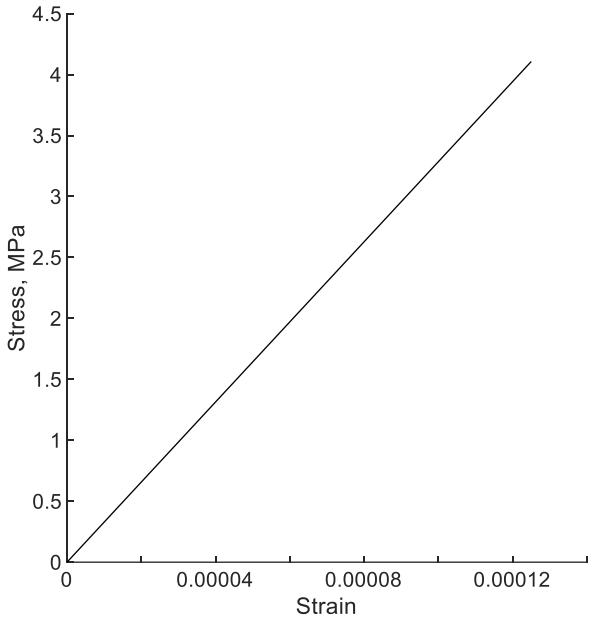

Figure 7.2.9 Concrete in tension stress-strain constitutive relationship (SI)

7.2.4 FRC

For the FRC, the plain concrete compressive model was used, but the tension model was modified according to the fib Model Code (CEB-FIB, 2013). For a variable strain distribution in the cross section, the Model Code requires that the rupture strain in tension is equal to 2%. The maximum permissible crack width is 0.1 in. (2.5 mm). For this project, the linear model described in Equations 7.2.10 and 7.2.11 was used.

$$f_{Fts} = 0.45 f_{R1} \tag{7.2.10}$$

Where

- f_{Fts} = Serviceability residual strength
- f_{R1} = Residual flexural tensile strength at CMOD1

$$f_{Ftu} = f_{Fts} - \frac{w_u}{CMOD_3}(f_{Fts} - 0.5 f_{R3} + 0.2 f_{R1}) \geq 0 \tag{7.2.11}$$

Where

- f_{Ftu} = Ultimate residual strength
- w_u = Maximum allowable crack opening
- $CMOD_3$ = 0.1 in. (2.5 mm) Crack mouth opening displacement

Using this model, the residual tensile strength of the concrete can be found for each value of strain. Since the FRC material properties range significantly depending on the type of fibers, the dosage of the fibers, and the properties of the concrete matrix, a generalized model is shown in Figure 7.2.10. The f_{Lk} in the figure is the limit of proportionality, or the modulus of rupture (MOR), ϵ_r in this case, is the strain at first crack, and ϵ_u is the maximum allowable design strain corresponding to w_u.

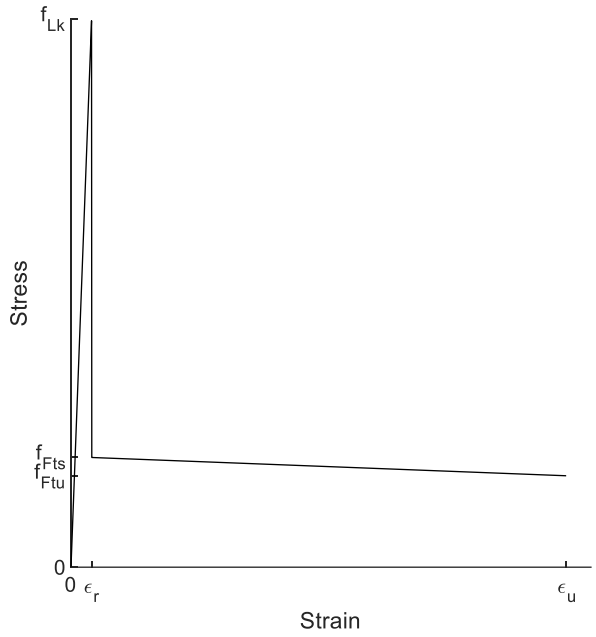

Figure 7.2.10 FRC in tension stress strain constitutive relationship

The scale of this figure is not representative of actual FRC tensile behavior, since the actual ultimate strain, ϵ_u, was defined as 0.02, which is roughly 200-300 times larger than the strain at first crack, ϵ_r. For ease of interpretation, Figure 7.2.10 shows an ultimate strain – cracking strain ratio of about 20, $\left(\frac{\epsilon_u}{\epsilon_r}\right) \approx 20$. It is clear from this plot that the fibers add a significant amount of post-cracking ductility to the concrete member through crack arresting behavior.

7.3 Service Limit State

7.3.1 Deflection

Deflection at the service level moment is highly dependent on the modulus of elasticity of the concrete and the effective moment of inertia of the section. Therefore, as the stiffness of the concrete increases, the deflection will increase. Because there was such a large range of concrete strength and stiffness, some sort of normalization is required to compare the live load deflection of the bridge deck panels. Without normalizing, the data are somewhat arbitrary since a stiffer concrete deck will outperform a lower stiffness concrete counterpart deck with regard to deflection.

It is proposed that a normalization is used to account for the variability in stiffness. This simple approach is achieved by multiplying the live load deflection response by the modulus of elasticity, E_c, directly. Although the output of this equation is meaningless with respect to units and design utility, the overall curves generated should give a general indication of how different concrete deck types behave without regard to the stiffness of the member.

Since a spreader beam was utilized, the beam shear and moment diagram are as shown in Figure 7.3.1.

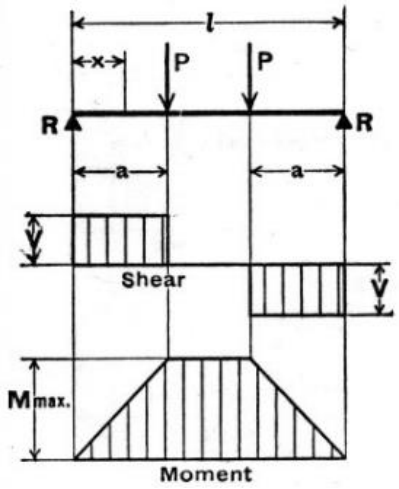

Figure 7.3.1 Simply supported beam - 4-point flexure (adapted - AISC Manual 2017)

Equation 7.3.1 gives the general maximum deflection of a beam under symmetrical 4-point loading as shown in Figure 7.3.1.

$$\Delta_{max} = \frac{Pa}{24EI}(3l^2 - 4a^2) \tag{7.3.1}$$

Where

- Δ_{max} = Maximum deflection at midspan
- P = Loading from spreader beam (as shown in Figure 7.3.)
- a = Width of constant shear region (as shown in Figure 7.3.)
- l = Length of beam
- E = Modulus of elasticity of beam
- I = Moment of inertia of beam

Finding the effective moment of inertia can be difficult, especially since the interaction between the fibers and the GFRP bars is difficult to model, so a simpler approach is taken by multiplying the stiffness out of the equation. Since the units are meaningless, only the imperial units are used to normalize the deflection curves. Figure 7.3.2 shows the original live load deflection plot, and Figure 7.3.3 shows the live load deflection modified by a scalar of E_c.

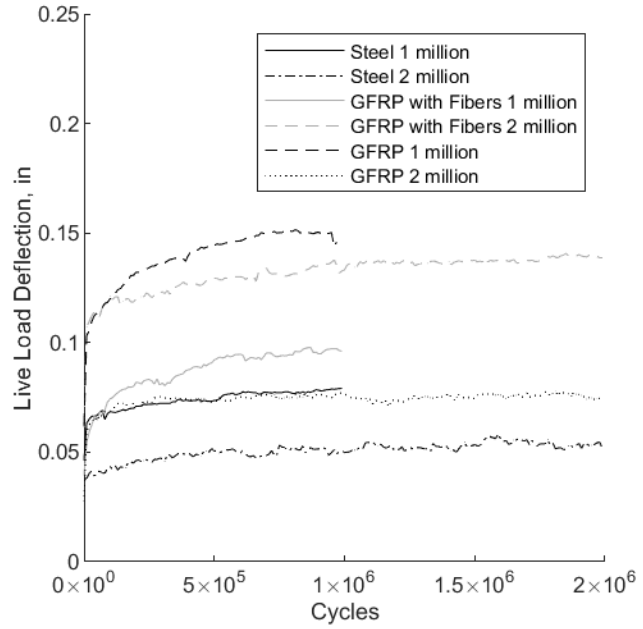

Figure 7.3.2 Live load deflection – fatigue loading

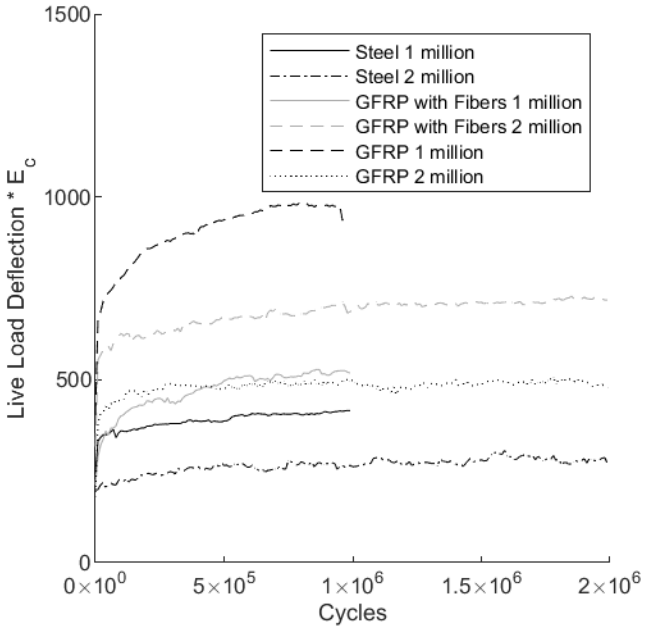

Figure 7.3.3 Live load deflection – normalized by E_c

For both plots, the steel-reinforced decks outperform the GFRP or HRC decks regarding live load deflection. This can be attributed to the stiffness of the steel reinforcement and the exceptional bond between the steel rebar and the concrete. The normalization shows that the GFRP-only gets farther away from the steel response, while the HRC decks approach the steel-reinforced deflection behavior. This is due to the high concrete stiffness of the GFRP decks. Without the fibers to bridge the cracks, the low modulus of elasticity of the GFRP decks results in increased deflections. Therefore, for a stiffness similar to the HRC or steel decks, the GFRP decks would exhibit larger live load deflections.

A more refined material prediction model could determine the displacements as a function of concrete strength, concrete stiffness, reinforcement stiffness, material bond, and, in the case of the HRC, crack bridging and pullout. This simple normalization is a only brief attempt, however, at examining the relative effect of the widely variable concrete strength and stiffness received in this experiment.

The acceptable element deflection for the bridge deck elements is L/800 for a non-pedestrian bridge. This equates to a 0.15 in. (3.8 mm) allowable deflection. Table 7.3.1 shows the adequacy ratio of the bridge deck elements for live load deflection after 1 or 2 million cycles. Numbers less than or equal to 1 are adequate for the live load deflection check.

Table 7.3.1 Adequacy of bridge decks for live load deflection

Deck Type	Cycle Count	Live Load Deflection, in. (mm)	Adequacy Ratio $\left(\frac{\Delta_{actual}}{\Delta_{allowable}}\right)$
Steel	1 Million	0.080 (2.0)	0.53
	2 Million	0.059 (1.5)	0.39
GFRP	1 Million	0.15 (3.9)	1.01
	2 Million	0.079 (2.0)	0.53
HRC	1 Million	0.10 (2.5)	0.67
	2 Million	0.14 (3.6)	0.93

Therefore, all of the decks are within the allowable deflection requirements except for the GFRP deck after 1 million cycles. In a real bridge deck section, the compressive membrane action and increased transverse stiffness would mitigate the deflection. Therefore, all three deck reinforcement strategies are viable options for service load deflections.

7.3.2 Crack Width

Before discussing the crack width results, several things must be noted. First, although care was taken to select the largest cracks to monitor, after several million cycles of fatigue, the cracks that initially were the largest were sometimes found to be similar in size or smaller than cracks in their vicinity. Second, although the LVDTs used were very well calibrated and stable, the magnitude of crack width is so small that even a difference of 0.01 in. (0.25 mm) appears to be large, when in actuality it is nearly negligible.

The live load crack opening was recorded and reported in Chapter 5 as the amount the crack varied from peak to valley, but the peak crack opening is the value that the AASHTO code attempts to limit by the spacing of the reinforcement.

For a class 1 exposure, the AASHTO LRFD specification states that the crack width equation is based on a crack equal to 0.017 in. (0.43 mm) (AASHTO, 2018c). The AASHTO Bridge Design Guide specifications for GFRP state that the allowable crack width can be increased to 0.028 in. (0.71 mm) (AASHTO, 2018b). This is due to the increased electrochemical corrosion resistance of the GFRP bars.

Without even attempting normalizations of the peak crack widths of the decks, it can be readily seen in Table 7.3.2 that each deck is within the crack width requirements suggested by AASHTO. The adequacy is defined as the ratio of the observed crack width, w_{actual}, to the allowable crack width, $w_{allowable}$. If the ratio is less than 1, then the deck is satisfactory for the crack opening requirements. For steel-reinforced decks, the allowable crack width is set to 0.017 in. (0.43 mm), and for GFRP-reinforced and HRC decks, the allowable crack width is set to 0.028 in. (0.71 mm).

Table 7.3.2 Adequacy of bridge decks for crack width

Deck Type	Cycle Count	Peak Crack Width, in. (mm)	Adequacy Ratio $\left(\frac{w_{actual}}{w_{allowable}}\right)$
Steel	1 Million	0.006 (0.14)	0.35
	2 Million	0.008 (0.20)	0.47
GFRP	1 Million	0.011 (0.29)	0.39
	2 Million	0.0073 (0.19)	0.26
HRC	1 Million	0.014 (0.36)	0.50
	2 Million	0.015 (0.37)	0.54

Therefore, all of the crack widths are adequate when compared to the AASHTO recommendations. The cracks would be even smaller when arching action and increased transverse stiffness is accounted for; therefore, all of the decks are viable when considering crack widths at service level conditions. The HRC decks counterintuitively experienced larger crack widths than the steel- and GFRP- reinforced deck sections, but the difference between all three was so small that it was nearly negligible.

7.4 Strength Limit State

7.4.1 Deflection

Even though a bridge deck will most likely never experience a flexural failure under ultimate limit state conditions due to punching shear, it is important to understand the failure mechanics of a bridge deck section in flexure since design engineers still use flexural capacity to size and space reinforcement. Failure in Chapter 5 was defined as the point at which the concrete crushes. This crushing occurs after the yielding of the steel in the steel-reinforced bridge decks, but before the GFRP rupture for both the GFRP-reinforced and HRC members.

Table 7.4.1 gives a summary of the deflections at failure for each bridge deck type pre- and post-fatigue. The average of the decks pre-fatigue is given.

Table 7.4.1 Bridge deck deflection at failure

Deck Type	Pre-fatigue	After 1 Million Cycles	After 2 Million Cycles
Steel	2.35 (59.6)	2.62 (66.5)	1.79 (45.5)
GFRP	3.50 (89.0)	3.87 (98.3)	3.75 (95.3)
HRC	4.56 (115.9)	4.84 (122.9)	4.96 (126.0)

From this table, it can be readily seen that at the ultimate load, the HRC decks show a marked improvement in ductility from both other deck types. Before fatigue loading, the HRC decks are 30% and 94% more ductile at failure than the GFRP and steel decks, respectively. After 1 million cycles, the HRC decks are 25% and 85% more ductile than the GFRP and steel decks. Following the 2 million fatigue cycles, the HRC decks are 32% and 177% more ductile than the GFRP- and steel-reinforced decks.

The deflection at failure before and after fatiguing increased for all three deck types after 1 million cycles. After 2 million cycles, however, there is a slight dip in the deflection at failure for the steel reinforced deck and GFRP deck. The HRC panel continued to see an increase in the deflection at failure even after 2 million cycles.

The post-peak energy absorption of the steel decks is considerably higher than both the GFRP and HRC decks. The GFRP decks exhibited very little post-peak ductility for each test, and the HRC decks saw some ductility after reaching the peak load as the fibers pulled out of the concrete. The linear behavior of the GFRP was expected, and since the GFRP rebar does not have any plasticity, the brittle response was expected. This post-peak behavior will not be seen in a typical bridge deck panel; therefore, even the low level of ductility shown by the GFRP decks is not concerning.

7.4.2 Moment Capacity

Using the constitutive models of each material, a moment-curvature program was created that sets increments in curvature and imposes equilibrium until certain criteria are met. The defined failure criteria for this project was a concrete strain of ϵ_u = 0.003. If the bottom layer of rebar ruptured, the program was also exited, and the previous moment and curvature was defined as the failure moment. Figure 7.4.1 shows a flow chart for the moment curvature program. The script for the program is included in Appendix B.

This program was run for each deck type, and the results are shown plotted in Figure 7.4.2 for the steel-reinforced decks, Figure 7.4.3 for the GFRP-reinforced decks, Figure 7.4.4for the first set of HRC decks corresponding with panels HRC 1 and HRC 2, and Figure 7.4.5 for the second set of HRC decks corresponding with HRC 3.

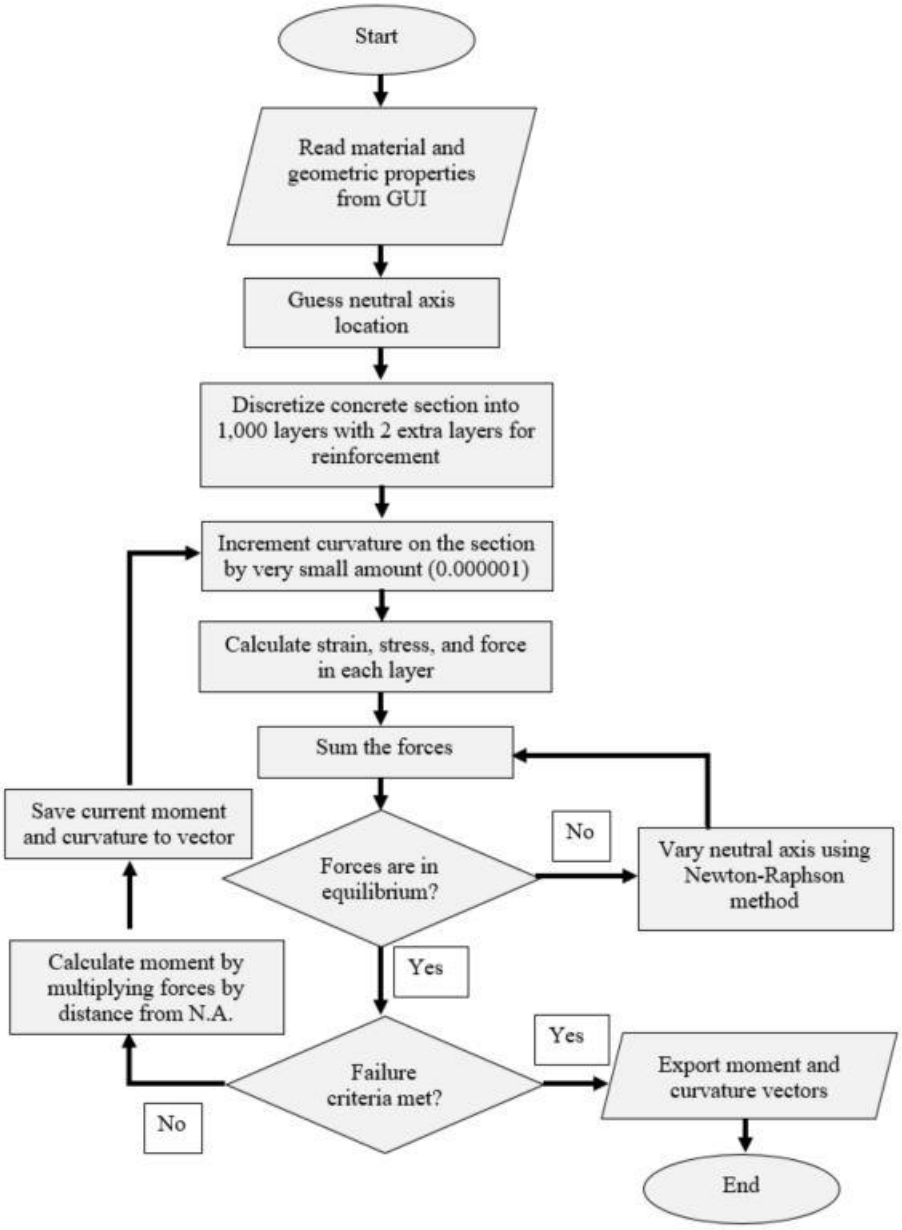

Figure 7.4.1 Moment curvature program flow chart

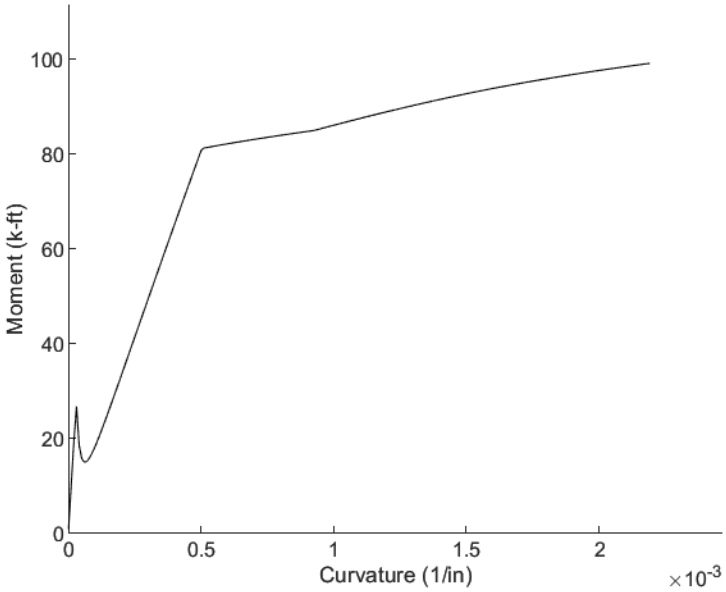

Figure 7.4.2 Steel moment-curvature relationship before fatigue

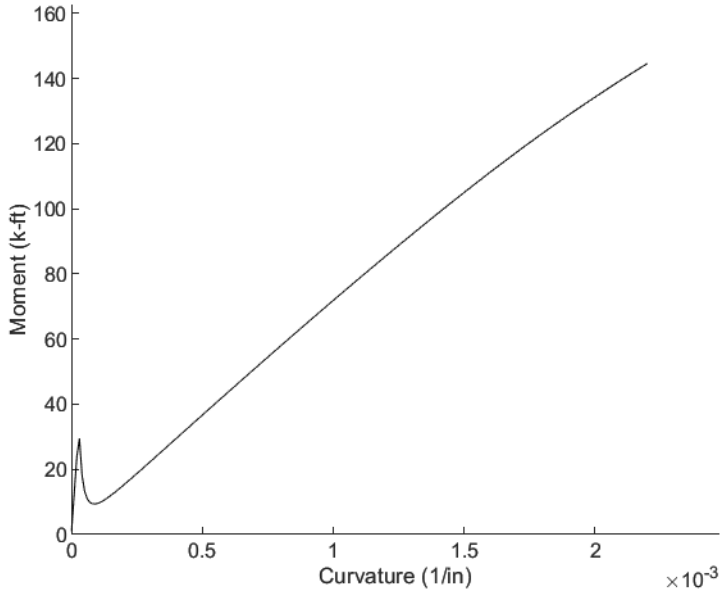

Figure 7.4.3 GFRP moment-curvature relationship before fatigue

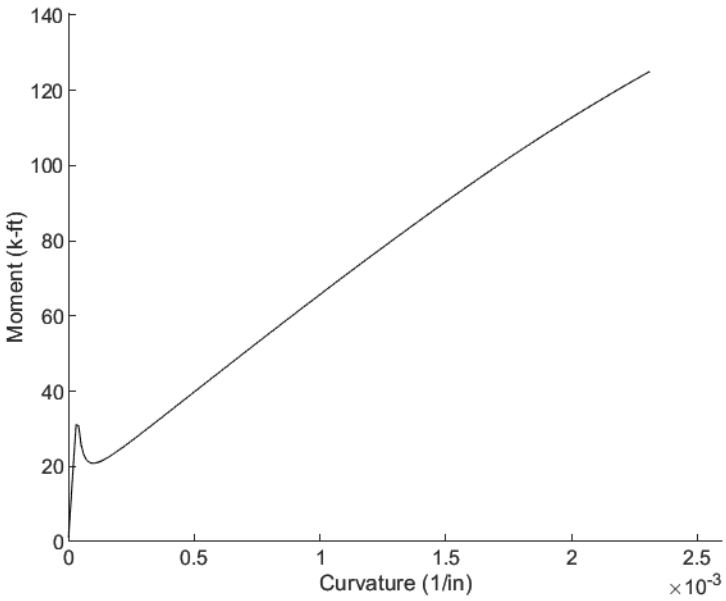

Figure 7.4.4 HRC set #1 moment-curvature relationship before fatigue

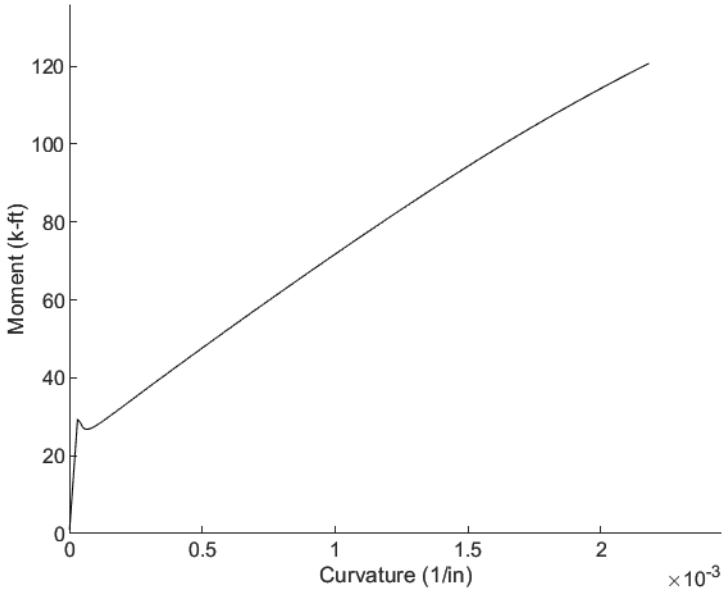

Figure 7.4.5 HRC set #2 moment-curvature relationship before fatigue

The model was also utilized for the post-fatigue decks to see if the damage accumulated during the fatiguing affected the ultimate capacity of the decks. Figure 7.4.6 shows the steel-reinforced deck moment-curvature relationship for the post-fatigue decks. The moment-curvature relationship for the GFRP post-fatigue deck is shown in Figure 7.4.7. Figure 7.4.8 contains the moment-curvature response for the HRC deck that experienced 1 million cycles, and Figure 7.4.9 shows the moment-curvature response for the HRC deck subjected to 2 million cycles.

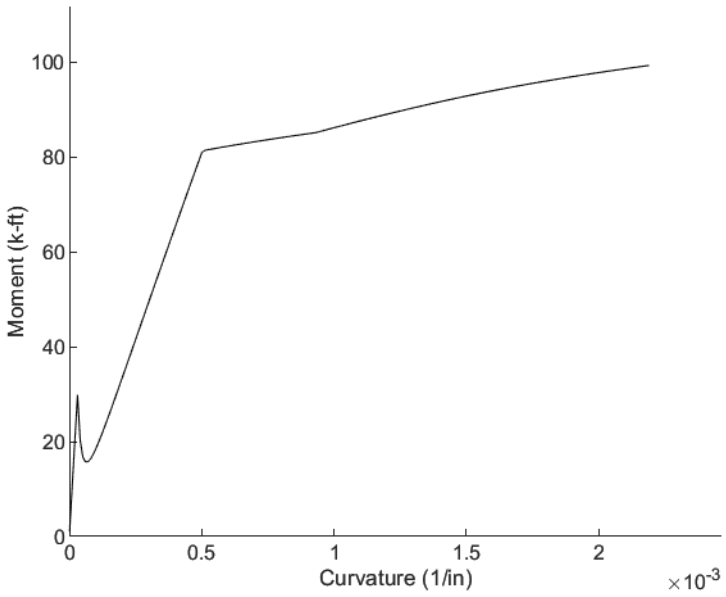

Figure 7.4.6 Steel moment-curvature relationship after fatigue

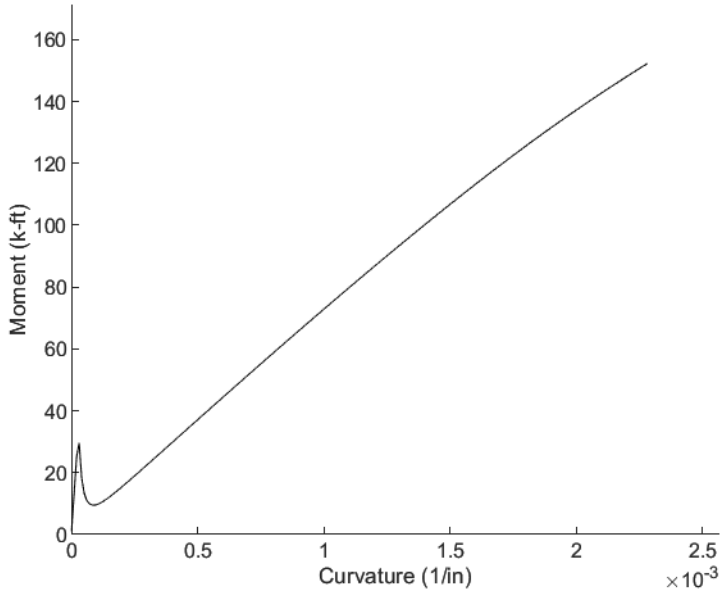

Figure 7.4.7 GFRP moment-curvature relationship after fatigue

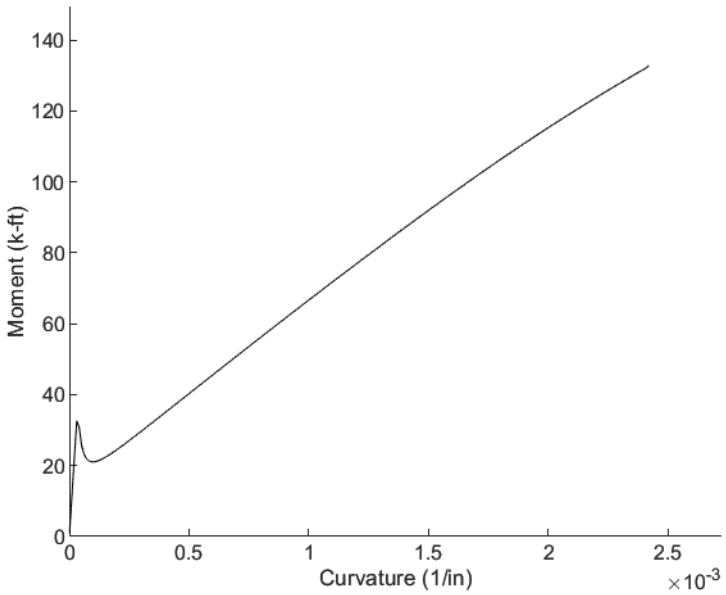

Figure 7.4.8 HRC set #1 moment-curvature relationship after fatigue

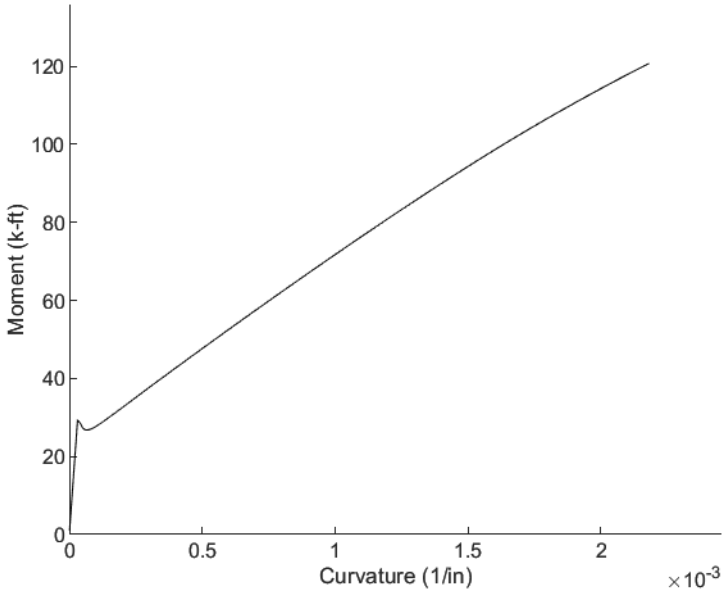

Figure 7.4.9 HRC set #2 moment-curvature relationship after fatigue

Table 7.4.2 compares the predicted ultimate moment from the moment curvature analysis to the actual peak moment for each deck. A simplified prediction based on Whitney's stress block and the equilibrium equations is given in Chapter 2 from the ACI 440.1R-15 and ACI 544.4R-18 design guides. The ratios given are the actual capacity compared to predicted capacity, $\frac{M_{actual}}{M_{predicted}}$. If this ratio is greater than 1, then the prediction was less than the actual moment, but if the ratio is less than 1, then the prediction exceeded the actual moment.

Table 7.4.2 Actual moment vs predicted moment for each specimen

Deck Type	Actual Moment k-ft (kN-m)	Predicted Moment k-ft (kN-m)	Predicted Moment (simplified) k-ft (kN-m)	MC Ratio	Simple Ratio
Steel 1	95.5 (129.5)	99.2 (134.5)	82.5	0.96	1.16
Steel 2	88.8 (120.4)	99.2 (134.5)	82.5	0.90	1.08
GFRP 1	127.4 (172.7)	144.6 (196.1)	132.3	0.88	0.96
GFRP 2	142.0 (192.5)	144.6 (196.1)	132.3	0.98	1.07
HRC 1	121.2 (164.3)	125.0 (169.5)	107.6	0.97	1.13
HRC 2	107.7 (146.0)	125.0 (169.5)	107.6	0.86	1.001
HRC 3	110.8 (150.2)	120.7 (163.6)	102.9	0.92	1.08
Steel 1 million	96.9 (131.4)	99.3 (134.6)	82.5	0.98	1.17
Steel 2 million	102.8 (139.4)	99.3 (134.6)	82.5	1.04	1.25
GFRP 1 million	148.9 (201.9)	152.3 (206.5)	139.6	0.98	1.07
GFRP 2 million	151.7 (205.7)	152.3 (206.5)	139.6	0.996	1.09
HRC 1 million	134.5 (182.4)	132.9 (180.2)	115.0	1.01	1.17
HRC 2 million	99 (134.2)	120.7 (163.6)	102.9	0.82	0.96
			Average:	0.95	1.09

This table shows the wide variability of the moments obtained for each test. In general, the moment-curvature (MC) model slightly over-predicts the maximum moment by an average of ≈ 5%. This is within a reasonable amount considering the simplicity of the material models utilized. The largest MC model over-prediction of 18% occurred for the HRC 2-million cycle deck. Another MC model over-prediction of 12% occurred for the first GFRP panel that was tested.

To provide a lower-bound simplified prediction model, Whitney's stress block was used on each section while also neglecting the compression reinforcement contribution. The average under-prediction ratio of this simplified approach is about 9%. This conservative design approach is most likely the method used by design engineers.

By comparing the pre- and post-fatigue MC model ratio for each deck type in Table 7.4.2, the relative change in capacity from before fatigue to after fatigue can be determined. For the steel decks, the average MC ratio before fatigue (0.93) is 8% less than the average MC ratio after fatigue (1.01). For the GFRP decks, the average MC ratio before fatigue (0.93) is 6% less than the average MC ratio after fatigue (0.988). Finally, for the HRC decks, the average MC ratio (0.92) is 0.5% larger than the average MC ratio after fatigue (0.915).

Both panels mentioned above that had large over-predictions experienced behavior that did not appear to coincide with a purely flexural failure. The GFRP-only deck appeared to be close to a flexural failure when a spontaneous shear failure occurred at the edge of the spreader beam. For all subsequent tests, the spreader beam was eliminated to preclude similar shearing failure. For the HRC 2-million cycle deck, the loading beam was slightly rotated, which could have introduced small stress concentrations on the side of the loading beam. The GFRP failure mode is shown in Figure 7.4.10, while the HRC deck failure mode is shown in Figure 7.4.11.

Figure 7.4.10 Shear failure on first GFRP specimen

Figure 7.4.11 HRC failure after 2 million cycles

By taking these two decks out of the prediction set, the over-prediction average for the MC model drops to 3.8%. The rest of the decks had failure modes primarily consistent with pure flexure, although some possible bond issues developed in the GFRP decks after fatigue. For the GFRP deck after 1 million cycles, the bottom surface delaminated after a large horizontal crack developed. The GFRP deck after 2 million cycles experienced similar delamination and cracking at the bottom layer of rebar. Figure 7.4.12 shows the large horizontal crack in the GFRP deck after 2 million cycles, Figure 7.4.13 shows the delamination of the bottom cover of the 1-million cycle GFRP deck from a profile view, and Figure 7.4.14 shows the bottom of the deck after testing.

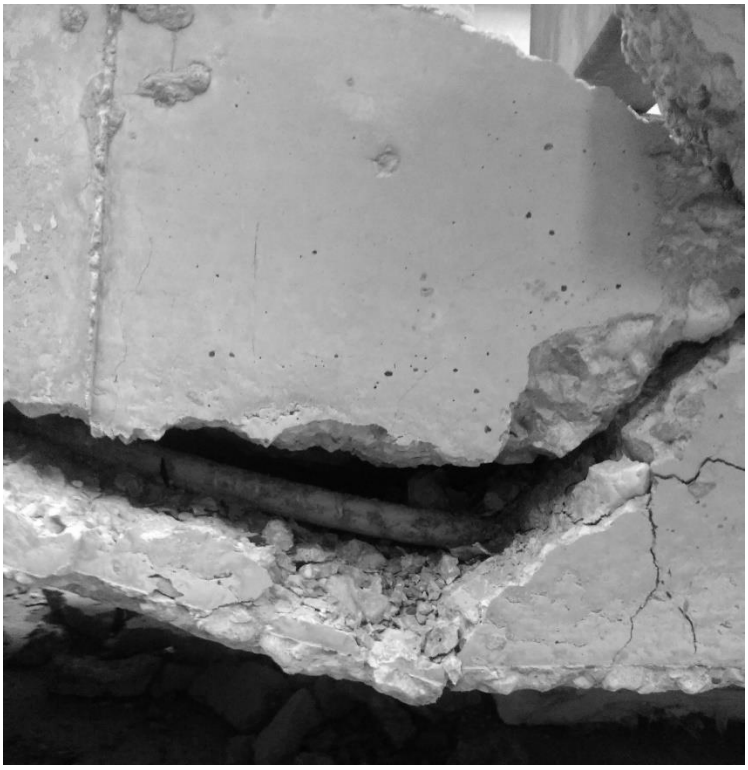

Figure 7.4.12 Bond failure on GFRP deck post-fatigue

Figure 7.4.13 Side view of 1 million cycle GFRP specimen at failure

Figure 7.4.14 Bottom view of GFRP specimen after failure

This effect did not cause much of a difference with regard to the failure moment, since both decks almost reached the predicted failure moment prior to this failure, but more research should be done to investigate the bond of the GFRP during fatigue loading. The delamination seen on the GFRP-only panels was not seen in any of the HRC decks; therefore, the fibers appear to improve the bond of the GFRP rebar before and after fatiguing.

In general, the fatigue cycles did not appear to adversely affect the overall sectional capacity. Before fatigue, the MC model over-predicted the moment capacity by an average of 7.6%. After fatigue, the model over-predicted the moment capacity by an average of 3%. This demonstrates that the post-fatigue decks performed adequately, if not better, when compared with the pre-fatigue decks as mentioned before.

Although the above figures show atypical flexural behavior for several decks, the majority failed in pure flexure as shown in Figure 7.4.15 for a steel deck, Figure 7.4.16 for a GFRP deck, and Figure 7.4.17 for a HRC deck.

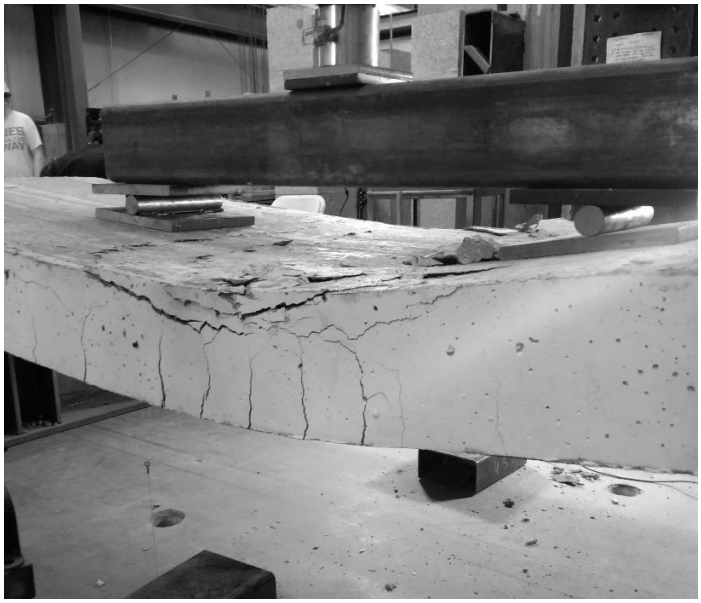

Figure 7.4.15 Steel deck at failure

Figure 7.4.16 GFRP deck at failure

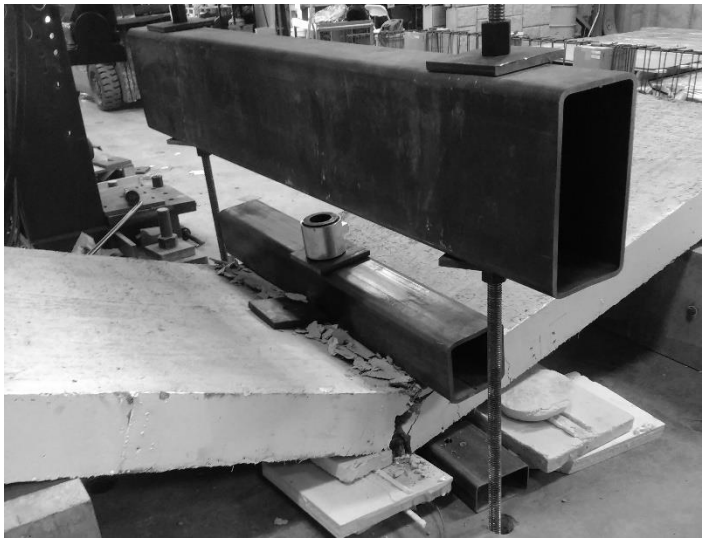

Figure 7.4.17 HRC deck at failure

The steel failure is the most desirable failure mechanism of the three, but the added ductility at maximum load and enhanced bond from the HRC compared with the GFRP-only decks makes the HRC decks a viable alternative for the capacity at the ultimate limit state.

8. DISCUSSION – PUNCHING SHEAR

8.1 Introduction

In the following chapter, all of the results from the punching shear portion of the experiment are analyzed and discussed. Due to the wide discrepancy in concrete strength between deck types, the results from the tests prior to fatigue as well as post-fatigue are normalized with consideration to their respective compressive strengths. The results are compared against predicted behavior according to the ACI 318 specification, the ACI 440.1R-15 guide, or a modified prediction based on the equations in Chapter 2 for the steel-reinforced, GFRP-reinforced, and HRC decks, respectively. At the end of the discussion of each section, the decks are evaluated to determine their viability as alternative reinforcement strategies.

8.2 Static Testing

As mentioned in Chapter 6, one 14’ x 12’ (4.3 x 3.7 m) deck of each type was tested monotonically until failure using a single concentrated load equivalent to the AASHTO HL-93 wheel contact area of 20” x 10” (508 x 254 mm). During testing, the load was recorded with a load cell under the actuator, and the deflection was monitored relative to the loading frame. These force-deflection results were plotted together in Figure 6.3.1 and Figure 6.3.2.

All three of the decks exhibited the same punching behavior on the top-side of the deck. For the entire test up until failure, the decks did not show any cracks on the surface. After reaching the peak load, the loading plate sunk into the deck. For the HRC and GFRP decks, the loading plate sheared the top mat of rebar; however, for the steel decks, the top and bottom mat of rebar deformed rather than demonstrating a shear rupture. Only the HRC decks had bottom reinforcement bars sheared for any of the deck types.

The load-deformation responses are plotted again in Figure 8.2.1 and Figure 8.2.2 for ease of comparison. It is clear in these figures that the steel-reinforced deck was much stiffer than both the GFRP and HRC decks. The HRC decks failed at a much lower load than the steel- and GFRP-reinforced decks, but due to the wide variability in concrete strength, some method of normalization must be attempted to compare the decks without bias.

By dividing by the square root of f_c', the force-deflection responses of each deck type were normalized so the responses can be compared more directly. The units are no longer significant in the normalized curves, but general trends can be observed. Figure 8.2.3 and Figure 8.2.4 show the normalized static punching shear results for the decks prior to fatigue.

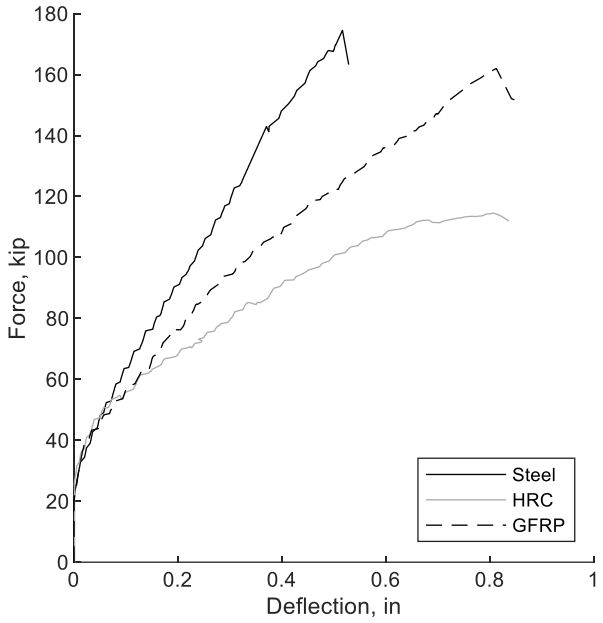

Figure 8.2.1 Force-deflection of punching shear decks (Imperial)

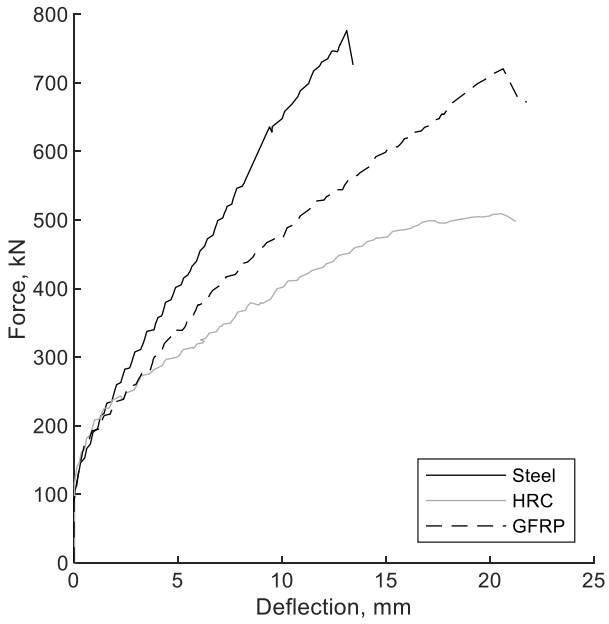

Figure 8.2.2 Force-deflection of punching shear decks (SI)

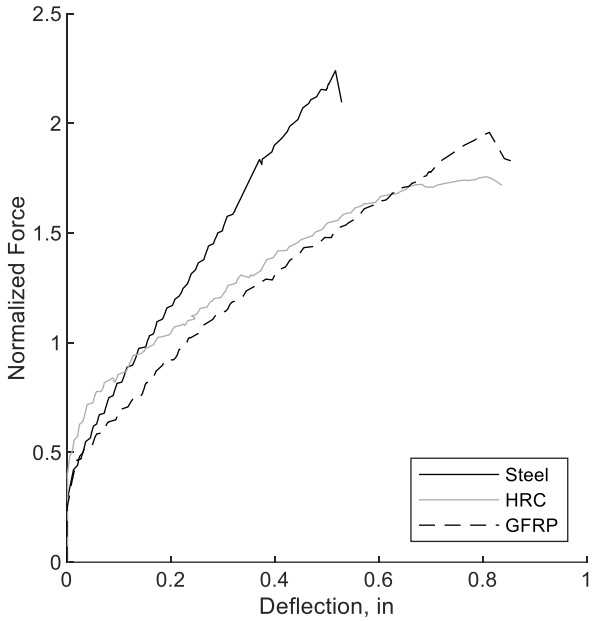

Figure 8.2.3 Normalized force-deflection of punching shear decks (Imperial)

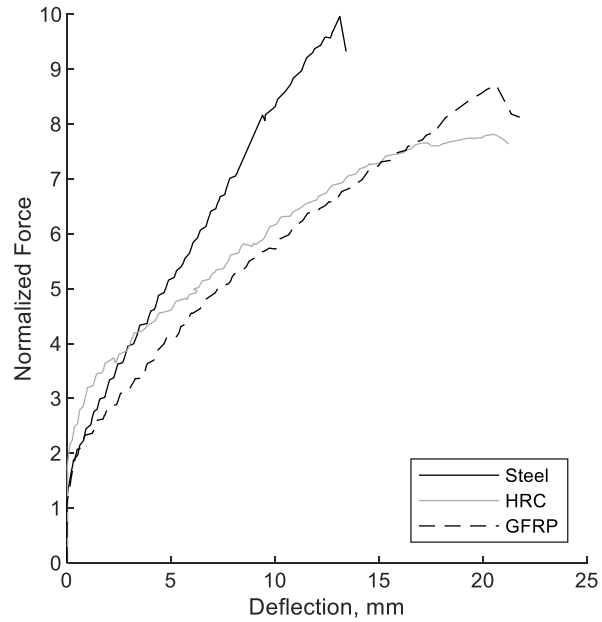

Figure 8.2.4 Normalized force-deflection of punching shear decks (SI)

By normalizing the punching shear response by the square root of f_c', the GFRP and HRC decks have a nearly identical response. Initially, the HRC decks have a stiffness similar to the steel-reinforced decks. This could be attributed to the initial tendency of the FRC to resist crack opening. Therefore, as the decks deflect, the cracks are bridged by the fibers, and exhibit a slightly stiffer response than the GFRP decks. At a certain point, the HRC decks and GFRP decks follow each other more closely, while the steel decks demonstrate the same stiffness for almost the entire response.

It appears that at the relatively low dosage of 15 lb/cy (8.9 kg/m^3) does not significantly improve the punching shear response as much as it did the flexural response. The punching shear area on the top surface of the steel deck, GFRP deck, and HRC deck is shown in Figure 8.2.5, Figure 8.2.6, and Figure 8.2.7, respectively. Figure 8.2.8 shows the rupture of the top layer of GFRP rebar in an HRC deck. Figure 8.2.9, Figure 8.2.10, and Figure 8.2.11 show the bottom surface of the deck following failure.

Figure 8.2.5 Top of steel punching shear deck

Figure 8.2.6 Top of GFRP punching shear deck

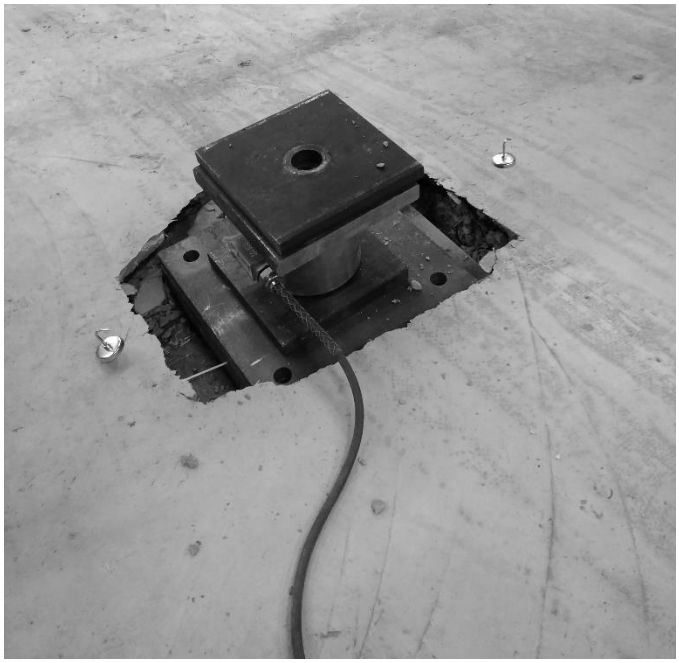

Figure 8.2.7 Top of HRC punching shear deck

Figure 8.2.8 Shear rupture of GFRP bar

Figure 8.2.9 Bottom surface of steel punching shear deck

Figure 8.2.10 Bottom surface of GFRP punching shear deck

Figure 8.2.11 Bottom surface of HRC punching shear deck

Table 8.2.1 contains the bottom surface punching dimensions, and maximum punching shear angle for the deck. By using the maximum angle, all of the predictions will be conservative.

Table 8.2.1 Bottom surface punching dimensions and shear angle

Deck Type	Length, in (mm)	Width, in (mm)	Maximum Punching Shear Angle
Steel	36 (915)	28 (711)	45.0°
GFRP	36 (915)	30 (762)	45.0°
HRC	28 (711)	24 (610)	63.4°

For the HRC deck, the angle is steeper than for the steel and GFRP decks. The steel- and GFRP-decks had 45° as their punching shear angle. Most researchers report shallower angles, but the exact angle is difficult to quantify since around the punching shear frustum there is significant spalling and surface delamination. Therefore, all of these measurements are approximate.

Predictions for the ultimate punching shear load are tabulated in Table 8.2.2. For the steel-reinforced decks, the ACI and AASHTO equations are used. Whereas, for the GFRP-reinforced decks, Equations 2.5.4 to 2.5.21 were used to predict the ultimate load capacities. Note that these equations were developed with various assumptions. A brief summary of those assumptions is given in Chapter 2. Finally, the ultimate load capacities of the HRC decks are given by increasing the GFRP-reinforced predictions by the fiber component.

Table 8.2.2 Punching shear prediction models for static tests

Prediction Method	**Force, kips (kN)**	**Ratio, Actual/Predicted**
Steel	*Tested: 176.8 (786.4)*	
ACI/AASHTO	163.4 (726.8)	1.082
GFRP	*Tested: 162.4 (722.4)*	
ACI 440	71.3 (317.2)	2.278
CSA S806-12	133.5 (593.9)	1.216
JSCE-97	121.6 (541.0)	1.336
IStruct (1999)	110.2 (490.1)	1.474
El-Ghandour et al (1999)	111.6 (496.6)	1.455
El-Ghandour et al (2000)	135.0 (600.4)	1.203
Matthys and Taerwe (2000)	115.1 (512.1)	1.411
Ospina et al (2003)	144.5 (642.9)	1.124
El-Gamal et al 2005	146.5 (651.6)	1.109
HRC	*Tested: 114.6 (509.8)*	
Fiber Contribution Only	46.7 (207.6)	N/A
ACI 440	96.0 (427.0)	1.194
CSA S806-12	150.2 (668.0)	0.763
JSCE-97	157.2 (699.3)	0.729
IStruct (1999)	132.1 (587.6)	0.868
El-Ghandour et al (1999)	134.7 (599.0)	0.851
El-Ghandour et al (2000)	151.3 (673.1)	0.757
Matthys and Taerwe (2000)	135.9 (604.6)	0.843
Ospina et al (2003)	158.7 (706.0)	0.722
El-Gamal et al 2005	151.6 (674.3)	0.756

From Table 8.2.2, it is clear the steel-reinforced deck prediction was the most accurate. It was 8% conservative, while the most accurate GFRP-reinforced prediction model was 11% conservative. Only the ACI 440 prediction equation was conservative when the fibers are added into the predicted force with an under-prediction of 19%. The rest of the models over-predicted the behavior. It is unclear what the fiber pull-out contribution was in the punching shear behavior when compared with the flexural tensile strengths in the fibers obtained from the EN 14651 testing. Table 8.2.3 was created for only the HRC decks without any contribution from the fibers accounted for in the punching shear capacity.

Table 8.2.3 HRC prediction models without fiber contribution

Prediction Method	Force, kips (kN)	Ratio, Actual/Predicted
HRC	*Tested: 114.6 (509.8)*	
ACI 440	49.3 (219.2)	2.325
CSA S806-12	103.5 (460.5)	1.107
JSCE-97	110.5 (491.5)	1.037
IStruct (1999)	85.4 (380.0)	1.342
El-Ghandour et al (1999)	88.0 (391.4)	1.302
El-Ghandour et al (2000)	104.6 (465.5)	1.096
Matthys and Taerwe (2000)	89.3 (397.0)	1.283
Ospina et al (2003)	112.1 (498.4)	1.022
El-Gamal et al 2005	104.9 (466.7)	1.092

The predictions in this table, without accounting for the contribution from the fibers, are much closer than those with the fiber contribution. All of the predictions in this table are still conservative. Therefore, without further investigation, it can be assumed that the fibers at the dosage used in this experiment are not sufficient to increase the capacity of the section in punching shear. For all of the predictions, the ACI equations under-predicted the behavior; therefore, the ACI methods are conservative for all deck types.

8.3 Fatigue Testing

One deck panel of each reinforcement type was subjected to 1 million cycles at 4 Hz, using a hydraulic actuator. The peak load was set equal to the AASHTO wheel load of 16 kips (71.2 kN). During the fatigue cycles, the decks were monitored using the same potentiometers used during the flexural fatigue testing. However, the relative displacement of the deck was so minimal from peak to valley that the noise threshold of 0.0009” (0.01 mm) was not enough to capture the displacement. Therefore, only the actuator displacement gives any insight into the fatigue behavior of the bridge decks.

Figure 6.4.1 and Figure 6.4.2 from Chapter 6 show this hydraulic actuator displacement recording plotted against the number of cycles. As mentioned, this measurement is recording multiple stray deflections in the test setup and other places. The steel- and GFRP-reinforced deck showed similar actuator displacement, but the HRC deck had a deflection that exceeded the AASHTO allowable limit for deflections. Prior to each fatigue test, shims were placed to minimize rocking behavior between the uneven supports and deck. For whatever reason, the HRC deck exhibited much greater rocking than any of the other two deck types. This rocking may account for the increased deflection from cycle to cycle. Since the potentiometers did not see a deflection larger than the noise threshold, all of the deck types are viable reinforcement options for the service limit state.

8.4 Post-Fatigue Testing

Following the fatigue loading, the three decks that experienced the 1 million cycles were subjected to a static load test equivalent to the static tests performed on the pre-fatigue decks. Once again, the load behavior was monitored with a load cell under the ram, and deflection measurements were made as the deck was loaded monotonically until failure. Following the failure, the punching shear frustum was measured by taking measurements on the bottom surface of the deck.

The load-deformation responses are plotted again in Figure 8.4.1 and Figure 8.4.2 for ease of comparison. The HRC decks failed at a lower load than the steel- and GFRP-reinforced decks, but due to the wide variability in concrete strength, a normalization is again used to compare the decks without bias.

By dividing by the square root of f_c', the force-deflection responses of each deck type were normalized so the responses can be compared. Once again, the units are no longer significant in the normalized curves, but general trends can be observed. Figure 8.4.3 and Figure 8.4.4 show the normalized static punching shear results for the decks prior to fatigue.

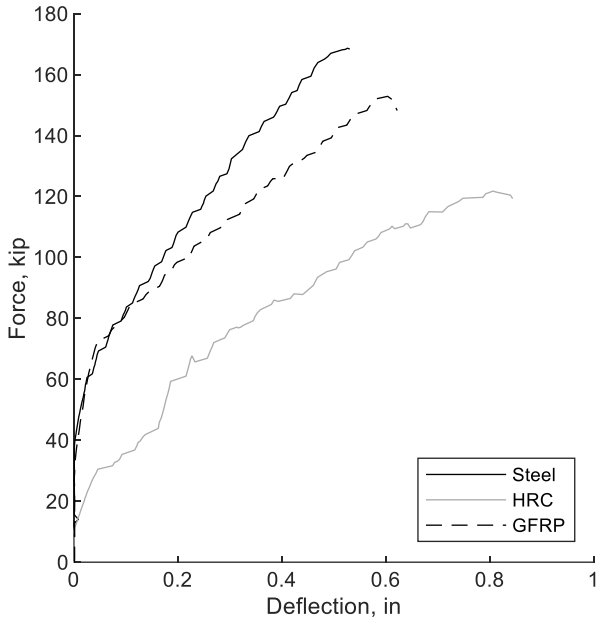

Figure 8.4.1 Force-deflection of punching shear decks after fatigue (Imperial)

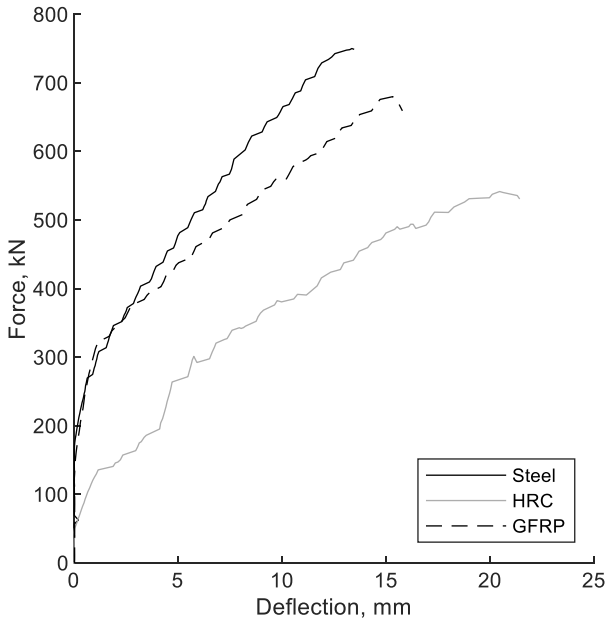

Figure 8.4.2 Force-deflection of punching shear decks after fatigue (SI)

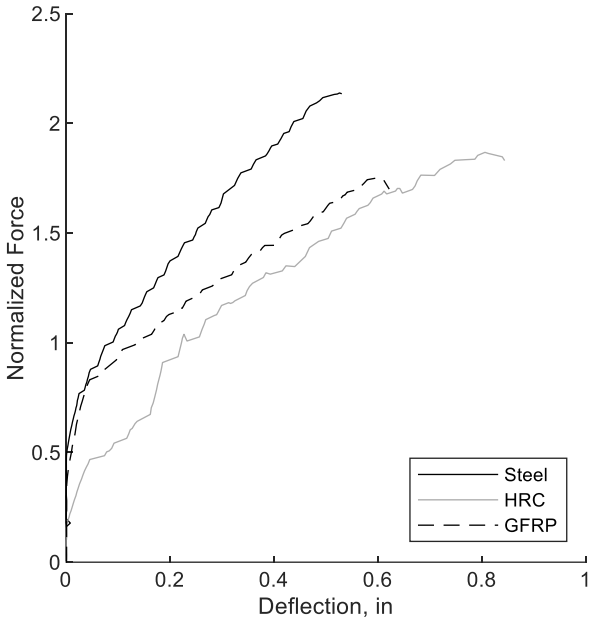

Figure 8.4.3 Normalized force-deflection of punching shear decks after fatigue (Imperial)

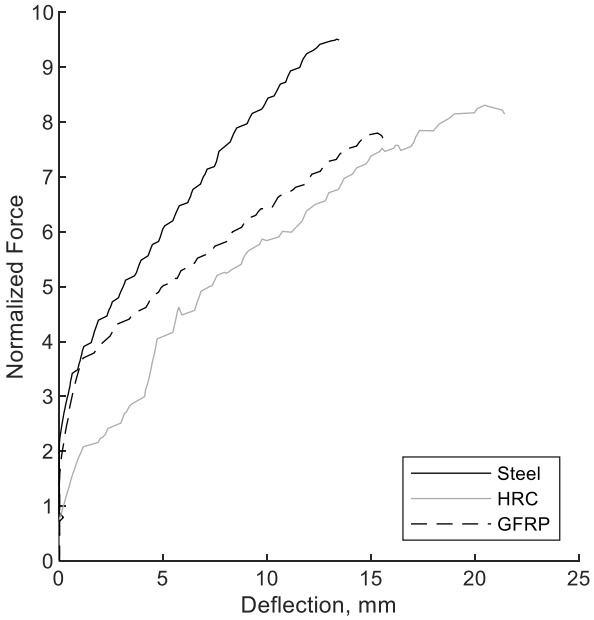

Figure 8.4.4 Normalized force-deflection of punching shear decks after fatigue (SI)

Several observations can be made for these decks. First, prior to normalization, the HRC decks appear to underperform significantly when compared with the GFRP or steel-reinforced decks. However, following the normalization, the HRC and GFRP decks once again show similar behavior. It can also be observed that the stiffness of the HRC decks following the fatigue is lower initially than the steel- or GFRP-reinforced decks. The cause of this is unknown, and more tests would be needed to determine whether this was an isolated occurrence, or if this is a pattern.

Figure 8.4.5, Figure 8.4.6, and Figure 8.4.7 show the top surface of the steel, GFRP, and HRC decks, respectively. Figure 8.4.8, Figure 8.4.9, and Figure 8.4.10 show the bottom surface of the steel, GFRP, and HRC decks, respectively.

Figure 8.4.5 Top of steel post-fatigue punching shear deck

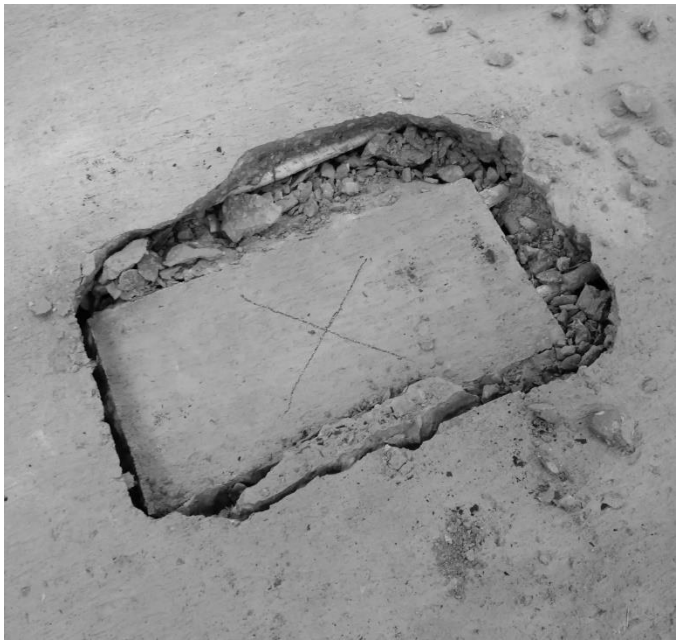

Figure 8.4.6 Top of GFRP post-fatigue punching shear deck

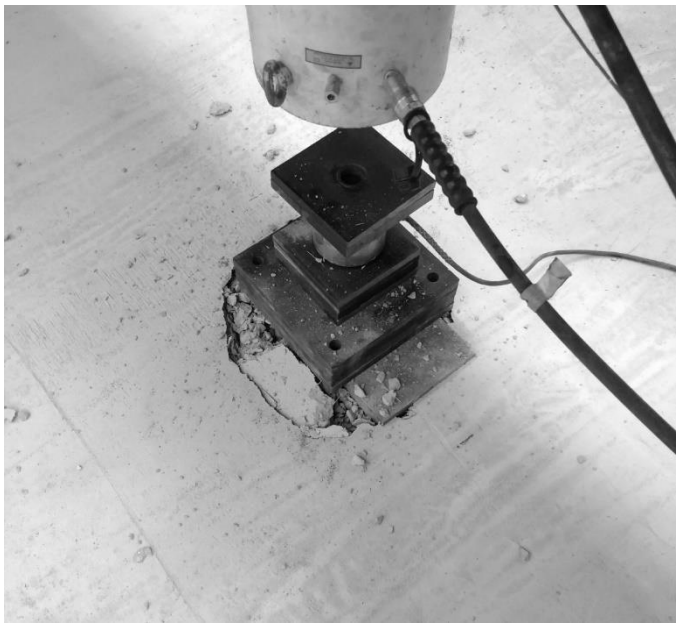

Figure 8.4.7 Top of HRC post-fatigue punching shear deck

Figure 8.4.8 Bottom of steel post-fatigue punching shear deck

Figure 8.4.9 Bottom of GFRP post-fatigue punching shear deck

Figure 8.4.10 Bottom of HRC post-fatigue punching shear deck

Table 8.4.1, contains the measured bottom surface of the punching shear cone, as well as the maximum punching shear angle, which will once again provide a conservative prediction.

Table 8.4.1 Bottom surface punching shear dimensions and shear angle (post-fatigue)

Deck Type	Length, in (mm)	Width, in (mm)	Maximum Punching Shear Angle
Steel	30 (915)	24 (711)	58.0°
GFRP	30 (915)	27 (762)	58.0°
HRC	34 (711)	32 (610)	48.8°

Unlike the decks prior to fatigue, the angle for the steel- and GFRP-reinforced decks was steeper than for the HRC deck. Once again, the punching angle was difficult to quantify due to the significant spalling and delamination around the punching area.

Predictions for the ultimate punching shear capacity after fatigue loading are again tabulated in Table 8.4.2. For the steel-reinforced decks, the ACI and AASHTO equations were used. Whereas, for the GFRP-reinforced decks, Equations 2.5.4 – 2.5.21 were used to predict the ultimate load capacities. Note that these equations were developed with various assumptions. A brief summary of those assumptions is given in Chapter 2. Finally, the ultimate load capacities of the HRC decks are given by increasing the GFRP-reinforced predictions by a contribution from the fibers as described in Chapter 2.

Table 8.4.2 Punching shear prediction models for post-fatigue static tests

Prediction Method	**Force, kips (kN)**	**Ratio, Actual/Predicted**
Steel	*Tested: 168.8 (750.9)*	
ACI/AASHTO	165.4 (735.9)	1.021
GFRP	*Tested: 153.0 (680.6)*	
ACI 440	75.2 (334.3)	2.035
CSA S806-12	138.3 (615.1)	1.106
JSCE-97	121.6 (541.0)	1.258
IStruct (1999)	114.1 (507.6)	1.341
El-Ghandour et al (1999)	117.7 (523.4)	1.300
El-Ghandour et al (2000)	139.8 (621.9)	1.094
Matthys and Taerwe (2000)	119.2 (530.4)	1.284
Ospina et al (2003)	149.7 (665.9)	1.022
El-Gamal et al 2005	154.4 (686.9)	0.991
HRC	*Tested: 121.8 (541.8)*	
Fiber Contribution Only	46.7 (207.6)	N/A
ACI 440	96.0 (427.0)	1.269
CSA S806-12	150.2 (668.0)	0.811
JSCE-97	157.2 (699.3)	0.775
IStruct (1999)	132.1 (587.6)	0.922
El-Ghandour et al (1999)	134.7 (599.0)	0.904
El-Ghandour et al (2000)	151.3 (673.1)	0.805
Matthys and Taerwe (2000)	135.9 (604.6)	0.896
Ospina et al (2003)	158.7 (706.0)	0.767
El-Gamal et al 2005	151.6 (674.3)	0.803

Once again, the steel decks predict the punching shear behavior closely. The prediction models used to predict the GFRP-only punching shear behavior were also fairly close. Only the method given by El-Gamal et al., 2005, over-predicted the behavior. Once again, by adding a contribution from the fibers, most of the prediction models over-predict the behavior; therefore, the deck capacity predictions without the fiber contribution are tabulated in Table 8.4.3.

.

Table 8.4.3 HRC punching shear predictions without fiber contribution (post-fatigue)

Prediction Method	Force, kips (kN)	Ratio, Actual/Predicted
HRC	*Tested: 121.8 (541.8)*	
ACI 440	49.3 (219.3)	2.471
CSA S806-12	103.5 (460.5)	1.177
JSCE-97	110.5 (491.5)	1.102
IStruct (1999)	85.4 (380.0)	1.426
El-Ghandour et al (1999)	88.0 (391.4)	1.384
El-Ghandour et al (2000)	104.6 (465.5)	1.164
Matthys and Taerwe (2000)	89.3 (397.0)	1.364
Ospina et al (2003)	112.1 (498.4)	1.087
El-Gamal et al 2005	104.9 (466.7)	1.161

Once again, the predictions in this table without accounting for the contribution from the fibers are much closer than those with the fiber contribution. Until further research is done to quantify the benefit of the fibers in the punching shear mechanism, any additional strength from the fibers should not be accounted for. By attempting to use the flexural tensile strength in the punching shear calculations, the models tend to over-predict the capacity by a significant amount. Just like the pre-fatigue decks, the ACI code equation is conservative for all deck types.

As a matter of comparison, the force-deflection responses for each deck type before and after fatigue are shown in Figure 8.4.11 and Figure 8.4.12.

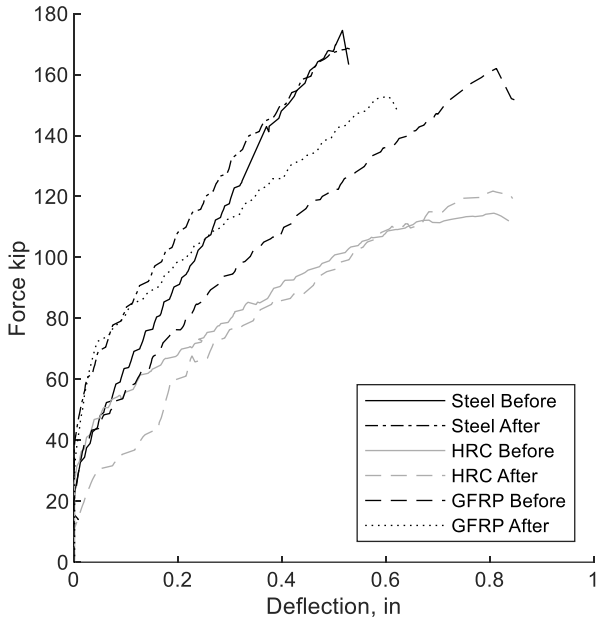

Figure 8.4.11 Force-deflection for punching shear decks before and after fatigue (Imperial)

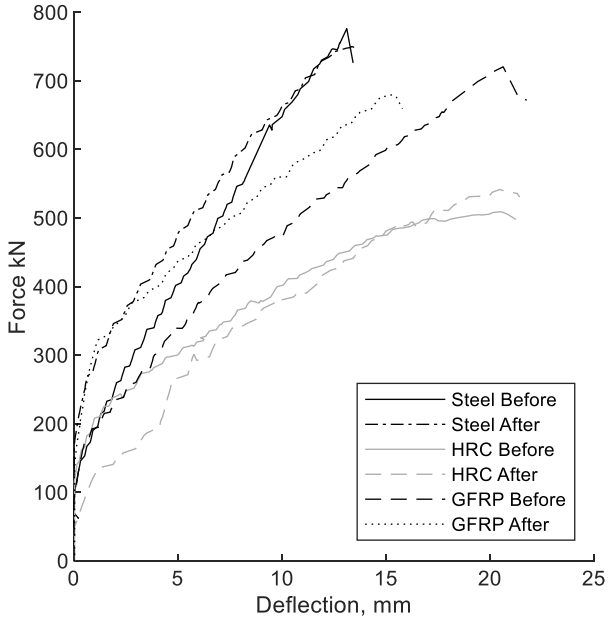

Figure 8.4.12 Force-deflection for punching shear decks before and after fatigue (SI)

Both the steel and HRC deck responses before and after fatigue are very similar. The GFRP deck shows a stiffer initial response and is followed by a reduced capacity. Table 8.4.4 contains the capacity and deflection at failure before and after fatigue. A ratio of before/after is also given for both capacity and deflection.

Table 8.4.4 Punching shear force and deflection comparisons before and after fatigue

Deck Type	Force Before, kip (kN)	Force After, kip (kN)	Force Ratio (Before/After	Deflection Before, in (mm)	Deflection After, in (mm)	Deflection Ratio (Before/After)
Steel	176.8 (786.4)	168.8 (750.9)	1.05	0.52 (13.2)	0.53 (13.5)	0.98
GFRP	162.4 (722.4)	153.0 (680.6)	1.06	0.82 (20.8)	0.61 (15.5)	1.3
HRC	114.6 (509.8)	121.8 (541.8)	0.94	0.81 (20.6)	0.81 (20.6)	1.0

Apart from the deflection of the GFRP, all of the forces and deflections were within 6% of each other for the decks before and after fatigue. Therefore, it can be assumed that under fatigue level loading for 1 million cycles, there is no apparent adverse effect on the bridge decks. The decks tested in this experiment were uncracked prior to fatigue loading. Future experiments should impose the fatigue loading on a cracked specimen to see if there is a significant difference.

9. CONCLUSIONS

In the United States, 9.1% of the bridges are structurally deficient (American Society of Civil Engineers, 2017). In 2002, the estimated annual cost of bridge deck corrosion was $2 billion (Koch et al., 2002). Finding a non-corrosive bridge deck reinforcement strategy that is not cost prohibitive is vital to creating a sustainable bridge infrastructure. The proposed corrosion resistant solution in this document of combining discrete GFRP rebar and AR-glass FRP composite macrofibers has been shown to be a viable reinforcement solution.

The testing of the full-scale bridge decks included both static loading as well as fatigue loading. The static load consisted of a monotonically increasing load until failure was reached. The fatigue loading was applied over 1 million cycles for the first set, and 2 million cycles for the second set. All fatigue loads were applied at a frequency of 4 Hz. Following the fatigue loading, the decks underwent a static test to compare pre- and post-fatigue behavior. Based on the testing results, the following conclusions can be made about the static flexural behavior:

- In static flexure, the HRC decks deflect an average of 29% more prior to failure than the GFRP decks for pre- and post-fatigue, and 119% more than the steel decks pre- and post-fatigue.
- Although the steel decks demonstrate much more energy absorption after failure, the HRC decks also show some post-peak ductility. The post-peak behavior of the GFRP is minimal due to the perfectly linear elastic behavior of the GFRP.
- A simple moment-curvature model can be created using the constitutive relationships of each material that predicts the pre- and post-fatigue static behavior. The model created here predicts behavior to within an average of 5.0%.
- A lower-bound prediction can also be provided using Whitney's stress block and neglecting contributions from the compression reinforcement. This simplified approach under-predicts the behavior of the decks by an average of 9.0%.
- The GFRP-reinforced deck sections experienced some bond loss after fatiguing. The same bond loss was not seen in the HRC or steel sections. This indicates that the fibers in the HRC aid in the bond behavior of the GFRP bars during fatigue loading.
- The fatigue loading did not adversely affect the behavior of the deck sections in static flexure. In some cases, the static flexural behavior actually improved following the cyclic loading.
- The steel reinforced decks experienced a tension-controlled failure, but the GFRP and HRC deck experienced a compression-controlled failure. This is consistent with the design of each deck type.
- All three options are viable bridge deck reinforcement strategies for the ultimate limit state. The GFRP deck exhibited the most brittle behavior, but the codified factors applied to GFRP reinforcement account for this, and the bridge decks are still viable. The HRC deck displayed some post-peak improvement and increased ductility from the GFRP deck.

In order to understand the service level behavior of the bridge decks, the deflection and crack widths were monitored throughout the cyclic fatigue loading, and these values were compared to recommended AASHTO limits. For the service level loads, the following conclusions can be made:

- In order to account for the variability of the concrete stiffness, two simple normalizations were performed by multiplying the modulus of elasticity or the square root of the modulus into the live load deflection. A more sophisticated model may be able to predict the live load deflection of the bridge decks during fatigue loading.
- All bridge decks except for the 1-million cycle GFRP deck were acceptable for the live load deflection criteria established by AASHTO. The 1-million cycle GFRP deck only exceeded the limit by 1%, which is essentially negligible.

- The steel decks outperformed both the GFRP and HRC decks with respect to the live load deflection. This can be attributed to the high modulus of elasticity of the steel. The HRC and GFRP deflections were similar.
- All the bridge decks performed exceptionally well with regard to the peak crack width. The ratio of actual crack width to allowable crack width was less than 1 for all cases, with the largest discrepancy being the 2-million cycle HRC deck experiencing a crack that was still only 54% of the allowable crack width.
- Since the HRC and GFRP decks are not susceptible to electrochemical corrosion, the crack limit established by AASHTO for GFRP is mostly for appearances and user-comfort.
- All three deck types are viable options for the service level loading and fall within the crack and deflection criteria established by AASHTO.

By examining the decks in both static and cyclic behavior, it was determined that the HRC decks with discrete GFRP bars and alkali-resistant fiberglass composite macrofibers are viable alternatives to steel-reinforced and GFRP-reinforced bridge decks for flexural behavior. Both the static and service level behavior of each bridge deck type was adequate, and the exceptional post-peak energy absorption demonstrated by the HRC will add ductility to previously elastic GFRP sections. By comparing the HRC decks to the GFRP decks after fatigue loading, it is also supposed that the bond behavior is enhanced by the crack bridging of the fibers.

Several conclusions can be drawn from the cyclic and static testing of the full-scale 14’ x 12’ (4.3 x 3.7 m) punching shear specimens. The first set of decks was loaded monotonically until a punching shear failure occurred. The subsequent set of decks was subjected to 1 million cycles of fatigue loading at 4 Hz, and then they were loaded statically until failure.

- The experimental capacity predicted by the ACI and AASHTO code always exceeded the experimental values. Therefore, the code equations are adequately conservative.
- By using a variety of prediction models for the GFRP and HRC decks, a range of predictive values were generated that are fairly consistent with the tested result.
- The contribution of the fibers in the FRC was nearly negligible with regard to the punching shear mechanism. More research needs to be conducted at variable dosages with more specimens to better understand the relationship between the flexural tensile stresses obtained in the beam tests and the fiber contribution to punching shear.
- The increased deflections shown by the GFRP and HRC decks are attributed to the lower modulus of elasticity. Therefore, the GFRP and HRC decks will see more deflection prior to failure than a steel deck. This is consistent with the flexural testing.
- By normalizing the test results by the square root of the concrete compressive strength, the GFRP and HRC force-deflection curves mimic each other very closely. This would once again suggest that the fiber contribution in punching shear is minimal.
- During the fatigue loading, the relative live load deflection was much less than the AASHTO requirements.
- The change in force and deflection from before fatigue loading to after is negligible. Only the GFRP deflection at failure had a change larger than 6% from the value prior to fatigue. Therefore, all three decks are viable for the fatigue loading.

By implementing pilot bridges of this hybrid reinforcement solution, steps will be made toward a more sustainable bridge design that will last many years without the need of bridge deck replacement common in steel-reinforced decks. These pilot bridges will need to be monitored much like the GFRP-only decks currently implemented in Canada and the United States.

Future research should include steps toward better understanding the shared crack bridging behavior of the discrete reinforcement and the fibers. A better and more widely accepted accelerated durability test should be developed to improve life-cycle predictions of GFRP-only decks as well as HRC decks.

REFERENCES

Aas-Jakobsen, K., & Lenschow, R. (1973). "Behavior of Reinforced Columns Subjected to Fatigue Loading." *Journal Proceedings*, *70*(3). https://doi.org/10.14359/11198

AASHTO. (2018a). AASHTO LFRD Bridge Design Guide Specifications for GFRP-Reinforced Concrete. *American Association of State Highway and Transportation Officials*, 121.

AASHTO. (2018b). *AASHTO LRFD Bridge Design Guide Specifications for GFRP-Reinforced Concrete.* AASHTO Washington, DC.

AASHTO. (2018c). AASHTO LRFD Bridge Design Specifications. *American Association of State Highway and Transportation Officials, Washington, DC*.

Abdel-Magid, B., Ziaee, S., Gass, K., & Schneider, M. (2005). "The combined effects of load, moisture and temperature on the properties of E-glass/epoxy composites." *Composite Structures*, *71*(3), 320–326. https://doi.org/https://doi.org/10.1016/j.compstruct.2005.09.022

Abdelkarim, O. I., Ahmed, E. A., Mohamed, H. M., & Benmokrane, B. (2019). "Flexural strength and serviceability evaluation of concrete beams reinforced with deformed GFRP bars." *Engineering Structures*, *186*, 282–296. https://doi.org/https://doi.org/10.1016/j.engstruct.2019.02.024

ACI Committee 318. (2014). *Building Code Requirements for Structural Concrete (ACI 318-14)[and] Commentary on Building Code Requirements for Structural Concrete (ACI 318R-14)*.

ACI Committee 440. (2015). *ACI 440.1R-15: Guide for the Design and Construction of Structural Concrete Reinforced with Fiber-Reinforced Polymer Bars*.

ACI Committee 544. (2018). ACI 544.4R-18: Guide to Design with Fiber-Reinforced Concrete. *American Concrete Institute*.

Adimi, M. R., Rahman, A. H., & Benmokrane, B. (2000). "New Method for Testing Fiber-Reinforced Polymer Rods under Fatigue." *Journal of Composites for Construction*, *4*(4), 206–213. https://doi.org/10.1061/(ASCE)1090-0268(2000)4:4(206)

Aguiniga Gaona, F. (2004). *Characterization of design parameters for fiber reinforced polymer composite reinforced concrete systems*. Texas A&M University.

Alexander, S. D. B., & Simmonds, S. H. (1992). "Punching shear tests of concrete slab-column joints containing fiber reinforcement." *Structural Journal*, *89*(4), 425–432.

Alliche, A. (2004). "Damage model for fatigue loading of concrete." *International Journal of Fatigue*, *26*(9), 915–921. https://doi.org/https://doi.org/10.1016/j.ijfatigue.2004.02.006

Almusallam, A. A., Khan, F. M., Dulaijan, S. U., & Al-Amoudi, O. S. B. (2003). "Effectiveness of surface coatings in improving concrete durability." *Cement and Concrete Composites*, *25*(4), 473–481. https://doi.org/https://doi.org/10.1016/S0958-9465(02)00087-2

Almusallam, T. H. (1997). "Analytical Prediction of Flexural Behavior of Concrete Beams Reinforced by FRP Bars." *Journal of Composite Materials*, *31*(7), 640–657. https://doi.org/10.1177/002199839703100701

Alsayed, S. H., & Alhozaimy, A. M. (1999). "Ductility of Concrete Beams Reinforced with FRP Bars and Steel Fibers." *Journal of Composite Materials*, *33*(19), 1792–1806. https://doi.org/10.1177/002199839903301902

American Society of Civil Engineers. (2017). *2017 Infrastructure report card*.

Amir, S., van der Veen, C., Walraven, J., & de Boer, A. (2015). "Punching shear capacity of bridge decks regarding compressive membrane action." *HERON*, *60*(3), 235.

ASTM A615. (2018). *Standard Specification for Deformed and Plain Carbon-Steel Bars for Concrete Reinforcement*. https://doi.org/10.1520/A0615_A0615M-18E01

ASTM C31. (2019). *Standard Practice for Making and Curing Concrete Test Specimens in the Field*. West Conshohocken, PA: ASTM International.

ASTM C39. (2012). "Standard test method for compressive strength of cylindrical concrete specimens." *ASTM C39/C39M-12*.

ASTM C469. (2014). *Standard Test Method for Static Modulus of Elasticity and Poisson's Ratio of Concrete in Compression*. https://doi.org/10.1520/C0469_C0469M-14

ASTM D7205. (2016). *Standard Test Method for Tensile Properties of Fiber Reinforced Polymer Matrix Composite Bars*. https://doi.org/10.1520/D7205_D7205M-06R16

ASTM E8. (2016). *Standard Test Methods for Tension Testing of Metallic Materials*. https://doi.org/10.1520/E0008_E0008M-16A

Barros, J. A. O., Taheri, M., & Salehian, H. (2015). "A model to simulate the moment–rotation and crack width of FRC members reinforced with longitudinal bars." *Engineering Structures*, *100*, 43–56. https://doi.org/https://doi.org/10.1016/j.engstruct.2015.05.036

Batchelor, B. D., Hewitt, B. E., & Csagoly, P. (1978). "An investigation of the fatigue strength of deck slabs of composite steel/concrete bridges." *Transportation Research Record*, (664).

Batson, G., Bailey, L., Landers, E., Hooks, J., & Ball, C. (1972). "Flexural Fatigue Strength of Steel Fiber Reinforced Concrete Beams." *Journal Proceedings*, *69*(11). https://doi.org/10.14359/11275

Bedard, C. (1992). "Composite Reinforcing Bars: Assessing Their Use in Construction." *Concrete International*, *14*(1).

Behnood, A., Van Tittelboom, K., & De Belie, N. (2016). "Methods for measuring pH in concrete: A review." *Construction and Building Materials*, *105*, 176–188. https://doi.org/https://doi.org/10.1016/j.conbuildmat.2015.12.032

Benmokrane, B., Masmoudi, R., & Chaallal, 0. (1996). "Flexural Response of Concrete Beams Reinforced with FRP Reinforcing Bars." *Structural Journal*, *93*(1). https://doi.org/10.14359/9839

Benmokrane, Brahim, & Ali, A. H. (2016). "Durability of FRP rebars in aggressive environments." *Proceedings of 8th International Conference on Fibre-Reinforced Polymer (FRP) Composites in Civil Engineering (CICE2016)*.

Benmokrane, Brahim, Desgagne, G., Lackey, T., & El-Salakawy, E. (2004). "FRP Bars for Bridges." *Concrete International*, *26*(8).

Benmokrane, Brahim, El-Salakawy, E., El-Gamal, S., & Goulet, S. (2007). "Construction and Testing of an Innovative Concrete Bridge Deck Totally Reinforced with Glass FRP Bars: Val-Alain Bridge on Highway 20 East." *Journal of Bridge Engineering*, *12*(5), 632–645. https://doi.org/10.1061/(ASCE)1084-0702(2007)12:5(632)

Benmokrane, Brahim, El-Salakawy, E., El-Ragaby, A., & Lackey, T. (2006). "Designing and Testing of Concrete Bridge Decks Reinforced with Glass FRP Bars." *Journal of Bridge Engineering*, *11*(2), 217–229. https://doi.org/10.1061/(ASCE)1084-0702(2006)11:2(217)

Benmokrane, Brahim, Wang, P., Ton-That, T. M., Rahman, H., & Robert, J.-F. (2002). "Durability of glass fiber-reinforced polymer reinforcing bars in concrete environment." *Journal of Composites for Construction*, *6*(3), 143–153.

Benzecry, V., Brown, J., Al-Khafaji, A., Haluza, R., Koch, R., Nagarajan, M., … Nanni, A. (2019). *Durability of GFRP Bars Extracted from Bridges with 15 to 20 years of Service Life*.

Bhargava, K., Ghosh, A. K., Mori, Y., & Ramanujam, S. (2006). "Analytical model for time to cover cracking in RC structures due to rebar corrosion." *Nuclear Engineering and Design*, *236*(11), 1123–1139. https://doi.org/https://doi.org/10.1016/j.nucengdes.2005.10.011

Blanco, A., Pujadas, P., de la Fuente, A., Cavalaro, S., & Aguado, A. (2013). "Application of constitutive models in European codes to RC–FRC." *Construction and Building Materials*, *40*, 246–259. https://doi.org/https://doi.org/10.1016/j.conbuildmat.2012.09.096

Bouguerra, K., Ahmed, E. A., El-Gamal, S., & Benmokrane, B. (2011). "Testing of full-scale concrete bridge deck slabs reinforced with fiber-reinforced polymer (FRP) bars." *Construction and Building Materials*, *25*(10), 3956–3965.

Breitenbücher, R., & Ibuk, H. (2006). "Experimentally Based Investigations on the Degradation-Process of Concrete Under Cyclic Load." *Materials and Structures*, *39*(7), 717–724. https://doi.org/10.1617/s11527-006-9097-9

British Standards Institution. (1997). *Structural use of concrete - code of practice for design and construction*. London, UK.

Brown, V. L., & Bartholomew, C. L. (1993). "FRP reinforcing bars in reinforced concrete members." *Materials Journal*, *90*(1), 34–39.

Byars, E. A., Waldron, P., Dejke, V., Demis, S., & Heddadin, S. (2003). "Durability of FRP in concrete–current specifications and a new approach." *International Journal of Materials and Product Technology*, *19*(1–2), 40–52.

Canadian Standards Association. (2012). *Design And Construction Of Building Structures With Fibre-Reinforced Polymers, CAN/CSA S806-12*. Toronto, ON, Canada.

Carrette, J. K., & El-Salakawy, E. (2018). "Evaluation of Punching Shear Strength Models for Glass Fibre-Reinforced Polymer (GFRP)-Reinforced Concrete (RC) Flat Plates Subjected to Unbalanced Moment-Shear Transfer." *Proceedings of Manitoba's Undergraduate Science and Engineering Research*, *3*.

Carvelli, V., Pisani, M. A., & Poggi, C. (2010). "Fatigue behaviour of concrete bridge deck slabs reinforced with GFRP bars." *Composites Part B: Engineering*, *41*(7), 560–567.

CEB-FIB. (2013). "Fib model code for concrete structures 2010." *Fédération Internationale Du Béton (Fib)*.

Chaallal, O., & Benmokrane, B. (1993). "Physical and mechanical performance of an innovative glass-fiber-reinforced plastic rod for concrete and grouted anchorages." *Canadian Journal of Civil Engineering*, *20*(2), 254–268.

Chandra, S. P. S. and S. (1970). "Fracture of Concrete Subjected to Cyclic and Sustained Loading." *Journal Proceedings*, *67*(10). https://doi.org/10.14359/7312

Chang, T. S., & Kesler, C. E. (1958). "Fatigue Behavior of Reinforced Concrete Beams*." *Journal Proceedings*, *55*(8). https://doi.org/10.14359/11352

Cheng, M.-Y., & Parra-Montesinos, G. J. (2010). "Evaluation of Steel Fiber Reinforcement for Punching Shear Resistance in Slab-Column Connections--Part I: Monotonically Increased Load." *ACI Structural Journal*, *107*(1).

Choi, K.-K., Reda Taha, M. M., Park, H.-G., & Maji, A. K. (2007). "Punching shear strength of interior concrete slab–column connections reinforced with steel fibers." *Cement and Concrete Composites*, *29*(5), 409–420. https://doi.org/https://doi.org/10.1016/j.cemconcomp.2006.12.003

Cleary, D. B., & Ramirez, J. A. (1991). "Bond strength of epoxy-coated reinforcement." *Materials Journal*, *88*(2), 146–149.

Clemmer, H. F. (1922). "Fatigue of concrete." *Proceedings, ASTM*, *22*(Part II), 402–419.

Construction, A. I. of S. (2017). *Manual of Steel Construction, 15th Edition*. Chicago: AISC.

Cornelissen, H. A. W. (1984). "Fatigue failure of concrete in tension." *HERON, 29 (4), 1984*.

Crepps, R. B. (1923). "Fatigue of mortar." *Proc. ASTM*, *23*(Part II), 329–340.

Darwin, D., Browning, J., Van Nguyen, T., & Locke Jr, C. E. (2002). *Mechanical and corrosion properties of a high-strength, high chromium reinforcing steel for concrete*. South Dakota Department of Transportation Office of Research.

Demers, C. E. (1998). "Tension–tension axial fatigue of E-glass fiber-reinforced polymeric composites: fatigue life diagram." *Construction and Building Materials*, *12*(5), 303–310. https://doi.org/https://doi.org/10.1016/S0950-0618(98)00007-5

Diaz, S. I., & Hilsdorf, H. K. (1971). *Fracture mechanisms of concrete under static, sustained, and repeated compressive loads*. University of Illinois Engineering Experiment Station. College of ….

Dorafshan, S., & Maguire, M. (2018). "Bridge inspection: human performance, unmanned aerial systems and automation." *Journal of Civil Structural Health Monitoring*, *8*(3), 443–476. https://doi.org/10.1007/s13349-018-0285-4

Dorafshan, S., Thomas, R. J., Coopmans, C., & Maguire, M. (2019). "A Practitioner's Guide to Small Unmanned Aerial Systems for Bridge Inspection." *Infrastructures*, *4*(4), 72.

Dorafshan, S., Thomas, R. J., & Maguire, M. (2019). "Benchmarking Image Processing Algorithms for Unmanned Aerial System-Assisted Crack Detection in Concrete Structures." *Infrastructures*, *4*(2), 19.

El-Gamal, S, El-Salakawy, E. F., & Benmokrane, B. (2005). "A new punching shear equation for two-way concrete slabs reinforced with FRP bars." *ACI Special Publication*, *230*, 877–894.

El-Gamal, Sherif, El-Salakawy, E., & Benmokrane, B. (2005). "Behavior of concrete bridge deck slabs reinforced with fiber-reinforced polymer bars under concentrated loads." *ACI Structural Journal*, *102*(5), 727.
El-Ghandour, A. W., Pilakoutas, K., & Waldron, P. (1999). "New approach for punching shear capacity prediction of fiber reinforced polymer reinforced concrete flat slabs." *Special Publication*, *188*, 135–144.
El-Ghandour, A. W., Pilakoutas, K., & Waldron, P. (2000). "Punching shear behaviour and design of FRP RC flat slabs." *Trita-BKN. Bulletin*, *57*, 359–366.
El-Ragaby, A., El-Salakawy, E., & Benmokrane, B. (2007). "Fatigue Life Evaluation of Concrete Bridge Deck Slabs Reinforced with Glass FRP Composite Bars." *Journal of Composites for Construction*, *11*(3), 258–268. https://doi.org/10.1061/(ASCE)1090-0268(2007)11:3(258)
El-Salakawy, E., Benmokrane, B., & Desgagné, G. (2003). "Fibre-reinforced polymer composite bars for the concrete deck slab of Wotton Bridge." *Canadian Journal of Civil Engineering*, *30*(5), 861–870. https://doi.org/10.1139/l03-055
El-Salakawy, E., Benmokrane, B., El-Ragaby, A., & Nadeau, D. (2005). "Field Investigation on the First Bridge Deck Slab Reinforced with Glass FRP Bars Constructed in Canada." *Journal of Composites for Construction*, *9*(6), 470–479. https://doi.org/10.1061/(ASCE)1090-0268(2005)9:6(470)
EN 14651. (2005). *Test Method for Metallic Fibre Concrete—Measuring the Flexural Tensile Strength*.
Falk, M. S. (1904). *Cements, mortars and concretes: their physical properties*. Clark.
Fang, I. K., Tsui, C. K. T., & Burns, N. H. (1990). "Fatigue Behavior of Cast-in-Place and Precast Panel Bridge Decks With Isotropic Reinforcement." *PCI Journal*, *35*(3), 28–39.
Fanous, F. S., & Wu, H.-C. (2000). "Service life of Iowa bridge decks reinforced with epoxy-coated bars." *Mid-Continent Transportation Symposium Proceedings*, 259–262.
Féret, R. (1906). *Etude Expérimentale du Ciment Armé*. Paris, France.
Florida DOT. (2011). *LRFD Design Example #1: Prestressed Precast Concrete Beam Bridge Design* (p. 347). p. 347. Retrieved from https://www.fdot.gov/structures/lrfddesignexamples.shtm
Frosch, R. J., Labi, S., & Sim, C. (2014). *Increasing Bridge Deck Service Life: Volume I - Technical Evaluation*. West Lafayette, IN.
Gallego, J. M., Zanuy, C., & Albajar, L. (2014). "Shear fatigue behaviour of reinforced concrete elements without shear reinforcement." *Engineering Structures*, *79*, 45–57. https://doi.org/https://doi.org/10.1016/j.engstruct.2014.08.005
Gopalaratnam, V. S., Meyer, J., De Young, K., Belarbi, A., & Wang, H. (2006). *Steel-free hybrid reinforcement system for concrete bridge decks, phase 1*. Missouri. Dept. of Transportation.
Graddy, J. C., Kim, J., Whitt, J. H., Burns, N. H., & Klingner, R. E. (2002). "Punching-shear behavior of bridge decks under fatigue loading." *Structural Journal*, *99*(3), 257–266.
Grimaldi, A., Meda, A., & Rinaldi, Z. (2013). "Experimental behaviour of fibre reinforced concrete bridge decks subjected to punching shear." *Composites Part B: Engineering*, *45*(1), 811–820.
Harajli, M. H., Maalouf, D., & Khatib, H. (1995). "Effect of fibers on the punching shear strength of slab-column connections." *Cement and Concrete Composites*, *17*(2), 161–170.
Hassan, M., Fam, A., & Benmokrane, B. (2016). "A new punching shear design formula for FRP-Reinforced interior slab-column connections." *7th International Conference on Advanced Composite Materials in Bridges and Structures*, 7. Vancouver, British Columbia.
Hatt, W. K. (1922). "Note of Fatigue of Mortar." *Journal Proceedings*, *18*(2). https://doi.org/10.14359/15682
Hatt, W. K. (1925). "Fatigue of concrete." *Highway Research Board Proceedings*, *4*.
Higashiyama, H., Ota, A., & Mizukoshi, M. (2011). "Design equation for punching shear capacity of SFRC slabs." *International Journal of Concrete Structures and Materials*, *5*(1), 35–42.
Hognestad, E. (1951). *Study of combined bending and axial load in reinforced concrete members*. University of Illinois at Urbana Champaign, College of Engineering ….
Hsu, T. T. C. (1981). "Fatigue of plain concrete." *Journal Proceedings*, *78*(4), 292–305.

Hussein, A. H., & El-Salakawy, E. F. (2018). "Punching Shear Behavior of Glass Fiber-Reinforced Polymer-Reinforced Concrete Slab-Column Interior Connections." *ACI Structural Journal*, *115*(4).
Issa, M. S., Metwally, I. M., & Elzeiny, S. M. (2011). "Influence of fibers on flexural behavior and ductility of concrete beams reinforced with GFRP rebars." *Engineering Structures*, *33*(5), 1754–1763. https://doi.org/https://doi.org/10.1016/j.engstruct.2011.02.014
IStructE. (1999). *Standard method of detailing structural concrete: A manual for best practice*. London, UK: The Institute of Structural Engineers.
Japan Society of Civil Engineering. (1997). *Recommendation for design and construction of concrete structures using continuous fibre reinforcing materials: Concrete engineering series 23*. Tokyo, Japan: JSCE.
Johnston, C. D., & Zemp, R. W. (1991). "Flexural Fatigue Performance of Steel Fiber Reinforced Concrete--Influence of Fiber Content, Aspect Ratio, and Type." *Materials Journal*, *88*(4). https://doi.org/10.14359/1875
Ju, M., Park, K., & Park, C. (2018). "Punching Shear Behavior of Two-Way Concrete Slabs Reinforced with Glass-Fiber-Reinforced Polymer (GFRP) Bars." *Polymers*, *10*(8), 893. https://doi.org/10.3390/polym10080893
Kahhaleh, K. Z., Vaca-Cortés, E., Jirsa, J. O., Wheat, H. G., & Carrasquillo, R. L. (1998). "Corrosion performance of epoxy-coated reinforcement–beam tests." In *Research Report No. 1265-4*. Texas Department of Transportation USA.
Kent, D. C., & Park, R. (1971). "Flexural members with confined concrete." *Journal of the Structural Division*.
Kessler-Kramer, C., Mechtcherine, V., & Müller, H. S. (2004). "Testing and modeling the behavior of concrete under cyclic tensile loading." *Proceedings of the 5th International Conference on Fracture Mechanics of Concrete Structures, Vail*.
Klowak, C., Memon, A., & Mufti, A. (2006). "Static and fatigue investigation of second generation steel-free bridge decks." *Cement and Concrete Composites*, *28*(10), 890–897.
Koch, G. H., Brongers, M. P. H., Thompson, N. G., Virmani, Y. P., & Payer, J. H. (2002). *Corrosion cost and preventive strategies in the United States*. United States. Federal Highway Administration.
Krauss, P. D., Lawler, J. S., & Steiner, K. A. (2009). "Guidelines for selection of bridge deck overlays, sealers and treatments." *NCHRP Project*, 7–20.
Krauss, P. D., & Rogalla, E. A. (1996). *Transverse Cracking in Newly Constructed Bridge Decks*. Washington, DC.
Krausz, A. S. (1988). *Fracture kinetics of crack growth* (Vol. 1). Springer Science & Business Media.
Kulicki, J. M., Wassef, W. G., Nowak, A. S., Mertz, D. R., Samtani, N. C., & Nassif, H. (2015). *Bridges for Service Life Beyond 100 Years: Service Limit State Design*. Transportation Research Board, National Research Council, Washington DC.
Kumar, S. V, & GangaRao, H. V. S. (1998). "Fatigue response of concrete decks reinforced with FRP rebars." *Journal of Structural Engineering*, *124*(1), 11–16.
Le Camus, B. (1945). "Recherches sur le Comportement du Beton et du Beton Arme soumis a des Efforts Repetes." *Compte Rendu Des Recherches Ejfectuees En 1945*, *46*.
Le, J.-L., & Bažant, Z. P. (2014). "Finite weakest-link model of lifetime distribution of quasibrittle structures under fatigue loading." *Mathematics and Mechanics of Solids*, *19*(1), 56–70.
Lee, J.-H., Yoon, Y.-S., Cook, W. D., & Mitchell, D. (2009). "Improving Punching Shear Behavior of Glass Fiber-Reinforced Polymer Reinforced Slabs." *ACI Structural Journal*, *106*(4).
Lee, M. K., & Barr, B. I. G. (2004). "An overview of the fatigue behaviour of plain and fibre reinforced concrete." *Cement and Concrete Composites*, *26*(4), 299–305. https://doi.org/https://doi.org/10.1016/S0958-9465(02)00139-7
Li, V. C., & Matsumoto, T. (1998). "Fatigue crack growth analysis of fiber reinforced concrete with effect of interfacial bond degradation." *Cement and Concrete Composites*, *20*(5), 339–351. https://doi.org/https://doi.org/10.1016/S0958-9465(98)00010-9

Lundgren, K. (2002). "Modelling the effect of corrosion on bond in reinforced concrete." *Magazine of Concrete Research*, *54*(3), 165–173.
Mai, S. H., Le-Corre, F., Foret, G., & Nedjar, B. (2012). "A continuum damage modeling of quasi-static fatigue strength of plain concrete." *International Journal of Fatigue*, *37*, 79–85. https://doi.org/https://doi.org/10.1016/j.ijfatigue.2011.10.006
Manning, D. G. (1996). "Corrosion performance of epoxy-coated reinforcing steel: North American experience." *Construction and Building Materials*, *10*(5), 349–365. https://doi.org/https://doi.org/10.1016/0950-0618(95)00028-3
Matthys, S., & Taerwe, L. (2000). "Concrete slabs reinforced with FRP grids. II: Punching resistance." *Journal of Composites for Construction*, *4*(3), 154–161.
Maya, L. F., Ruiz, M. F., Muttoni, A., & Foster, S. J. (2012). "Punching shear strength of steel fibre reinforced concrete slabs." *Engineering Structures*, *40*, 83–94.
Memon, A. H. (2005). *Comparative fatigue performance of steel-reinforced and steel-free concrete bridge deck slabs*.
Metwally, I. M. (2013). "Prediction of punching shear capacities of two-way concrete slabs reinforced with FRP bars." *HBRC Journal*, *9*(2), 125–133.
Micelli, F., Nanni, A., & La Tegola, A. (2001). "Effects of conditioning environment on GFRP bars." *International Conference, CNIT Paris*.
Michaluk, C. R., Tadros, G., Benmokrane, B., & Rizkalla, S. H. (1998). "Flexural Behavior of One-Way Concrete Slabs Reinforced by Fiber Reinforced Plastic Reinforcements." *Structural Journal*, *95*(3). https://doi.org/10.14359/552
Mobasher, B., Yao, Y., & Soranakom, C. (2015). "Analytical solutions for flexural design of hybrid steel fiber reinforced concrete beams." *Engineering Structures*, *100*, 164–177.
MoDOT. (2006). *Steel-Free Hybrid Reinforced Concrete Bridge Decks Avoid Corrosion*.
Mufti, A. A., Jaeger, L. G., Bakht, B., & Wegner, L. D. (1993). "Experimental investigation of fibre-reinforced concrete deck slabs without internal steel reinforcement." *Canadian Journal of Civil Engineering*, *20*(3), 398–406.
Murdock, John W, & Kesler, C. E. (1958). "Effect of Range of Stress on Fatigue Strength of Plain Concrete Beams*." *Journal Proceedings*, *55*(8). https://doi.org/10.14359/11350
Murdock, John Washburn. (1965). *A critical review of research on fatigue of plain concrete*. University of Illinois at Urbana Champaign, College of Engineering ….
Naaman, A. E. (2018). "Fiber Reinforced Concrete: Five Decades of Progress." *Composite Materials. Rio de Janeiro*.
Nanni, A. (1993). "Flexural behavior and design of RC members using FRP reinforcement." *Journal of Structural Engineering*, *119*(11), 3344–3359.
Natário, F., Fernández Ruiz, M., & Muttoni, A. (2015). "Experimental investigation on fatigue of concrete cantilever bridge deck slabs subjected to concentrated loads." *Engineering Structures*, *89*, 191–203. https://doi.org/https://doi.org/10.1016/j.engstruct.2015.02.010
National Academies of Sciences Engineering and Medicine. (2019). *Performance of Bridges that Received Funding Under the Innovative Bridge Research and Construction Program*. Washington, DC: The National Academies Press.
National Research Council. (1991). *Life Prediction Methodologies for Composite Materials*. Washington, DC.
Nguyen-Minh, L., Rovňák, M., Tran-Quoc, T., & Nguyenkim, K. (2011). "Punching shear resistance of steel fiber reinforced concrete flat slabs." *Procedia Engineering*, *14*, 1830–1837.
Nguyen, O., Repetto, E. A., Ortiz, M., & Radovitzky, R. A. (2001). "A cohesive model of fatigue crack growth." *International Journal of Fracture*, *110*(4), 351–369. https://doi.org/10.1023/A:1010839522926
Noël, M., & Soudki, K. (2014). "Fatigue Behavior of GFRP Reinforcing Bars in Air and in Concrete." *Journal of Composites for Construction*, *18*(5), 4014006. https://doi.org/10.1061/(ASCE)CC.1943-5614.0000468

Nordby, G. M. (1958). "Fatigue of Concrete- A Review of Research*." *Journal Proceedings*, *55*(8). https://doi.org/10.14359/11349
O'Neil, E. F. (1978). *Ultimate Strength of Fiber-Reinforced Concrete under Cyclic, Flexural Loading.* Army Engineer Waterways Experiment Station, Vicksburg Miss.
Oh, B. H. (1991). "Fatigue Life Distributions of Concrete for Various Stress Levels." *Materials Journal*, *88*(2). https://doi.org/10.14359/1870
Okada, K., Okamura, H., & Sonoda, K. (1978). "Fatigue failure mechanism of reinforced concrete bridge deck slabs." *Transportation Research Record*, *664*, 136–144.
Ospina, C. E., Alexander, S. D. B., & Cheng, J. J. R. (2003). "Punching of two-way concrete slabs with fiber-reinforced polymer reinforcing bars or grids." *Structural Journal*, *100*(5), 589–598.
Papa, E., & Taliercio, A. (1996). "Anisotropic damage model for the multiaxial static and fatigue behaviour of plain concrete." *Engineering Fracture Mechanics*, *55*(2), 163–179. https://doi.org/https://doi.org/10.1016/0013-7944(96)00004-5
Perdikaris, P. C., & Beim, S. (1988). "RC Bridge Decks Under Pulsating and Moving Load." *Journal of Structural Engineering*, *114*(3), 591–607. https://doi.org/10.1061/(ASCE)0733-9445(1988)114:3(591)
Perdikaris, P. C., Beim, S. R., & Bousias, S. N. (1989). "Slab continuity effect on ultimate and fatigue strength of reinforced concrete bridge deck models." *Structural Journal*, *86*(4), 483–491.
Picazo, Á., Alberti, M. G., Enfedaque, A., & Gálvez, J. C. (2018). "Assessment of the Shear Strength of Steel Fibre-Reinforced Concrete." In *High Tech Concrete: Where Technology and Engineering Meet* (pp. 405–412). Springer.
Porter, M. L., Hughes, B. W., Barnes, B. A., & Viswanath, K. P. (1993). *Non-corrosive tie reinforcing and dowel bars for highway pavement slabs. Final Report*.
Probst, E., & Treiber, F. (1932). "Reinforced concrete beams under frequently repeated loading." *Bouingenieur, Berlin*, *13*(21/22), 285–289.
Raithby, K. D. (1979). "Flexural fatigue behaviour of plain concrete." *Fatigue of Engineering Materials and Structures*, *2*.
Raithby, K. D., & Whiffin, A. C. (1968). *Failure of Plain Concrete Under Fatigue Loading-A Review of Current Knowledge*.
Ramakrishnan, V., Wu, G. Y., & Hosalli, G. (1989). "Flexural fatigue strength of fiber-reinforced concrete, endurance limit and impact strength." *Transportation Research Record No*, *1226*, 17.
Robert, M., & Benmokrane, B. (2013). "Combined effects of saline solution and moist concrete on long-term durability of GFRP reinforcing bars." *Construction and Building Materials*, *38*, 274–284. https://doi.org/https://doi.org/10.1016/j.conbuildmat.2012.08.021
Rossini, M., Nanni, A., Matta, F., Nolan, S., Potter, W., & Hess, D. (2019). "Overview of AASHTO Design Specifications for GFRP-RC Bridges 2nd Edition: Toledo Bridge as Case Study." *IABSE Symposium 2019 Guimaraes: Towards a Resilient Built Environment-Risk and Asset Management*, 1214–1221. International Association for Bridge and Structural Engineering (IABSE).
Sagüés, A. A., Powers, R. G., & Kessler, R. (2001). "Corrosion performance of epoxy-coated rebar in Florida Keys bridges." *CORROSION/2001, Paper*, (01642).
Salem, A., El Aghoury, I., Sayed-Ahmed, E., & Moustafa, T. (2002). "Composite steel-free deck bridges: Numerical modelling and pilot parametric study." *Canadian Journal of Civil Engineering*, *29*, 662–678. https://doi.org/10.1139/l02-060
Samples, L. M., & Ramirez, J. A. (1999). *Methods of Corrosion Protection and Durability of Concrete Bridge Decks Reinforced with Epoxy-coated Bars-Phase I*.
Scaletta, C. (2015). *Comparative study between steel-free and steel reinforced concrete bridge deck slabs subjected to fatigue loading*.
Schütz, W. (1996). "A history of fatigue." *Engineering Fracture Mechanics*, *54*(2), 263–300. https://doi.org/https://doi.org/10.1016/0013-7944(95)00178-6
Sen, R., Salem, T., & Mullins, G. (2002). "Durability of E-Glass/Vinylester Reinforcement in Alkaline Solution." *Structural Journal*, *99*(3). https://doi.org/10.14359/11921

Singh, S. P., & Kaushik, S. K. (2003). "Fatigue strength of steel fibre reinforced concrete in flexure." *Cement and Concrete Composites*, *25*(7), 779–786.
Sivagamasundari, R., & Kumaran, G. (2008). "A comparative study on the flexural behaviour of one-way concrete slabs reinforced with GFRP reinforcements and conventional reinforcements when subjected to monotonic and repeated loading." *Open Civil Engineering Journal*, *2*, 24–34.
Sonoda, K., & Horikawa, T. (1982). "Fatigue strength of reinforced concrete slabs under moving loads." *Fatigue of Steel and Concrete Structures*, 455–462.
Spadea, G., & Bencardino, F. (1997). "Behavior of Fiber-Reinforced Concrete Beams under Cyclic Loading." *Journal of Structural Engineering*, *123*(5), 660–668. https://doi.org/10.1061/(ASCE)0733-9445(1997)123:5(660)
Suresh, S. (1998). *Fatigue of materials*. Cambridge University Press.
Swamy, R. N., & Ali, S. A. R. (1982). "Punching shear behavior of reinforced slab-column connections made with steel fiber concrete." *Journal Proceedings*, *79*(5), 392–406.
Taerwe, L. R., & Matthys, S. (1999). "FRP for Concrete Construction: Activities in Europe." *Concrete International*, *21*(10).
Taheri, M., Barros, J. A. O., & Salehian, H. (2011). "A design model for strain-softening and strain-hardening fiber reinforced elements reinforced longitudinally with steel and FRP bars." *Composites Part B: Engineering*, *42*(6), 1630–1640.
Tan, K.-H., & Paramasivam, P. (1994). "Punching shear strength of steel fiber reinforced concrete slabs." *Journal of Materials in Civil Engineering*, *6*(2), 240–253.
Tan, K. H., & Venkateshwaran, A. (2019). "Punching Shear in Steel Fiber-Reinforced Concrete Slabs with or without Traditional Reinforcement." *Structural Journal*, *116*(3). https://doi.org/10.14359/51713291
Tannous, F. E. (1997). *Durability of non-metallic reinforcing bars and prestressing tendons*.
Tepfers, R., & Kutti, T. (1979). 'Fatigue Strength of Plain, Ordinary, and Lightweight Concrete." *Journal Proceedings*, *76*(5). https://doi.org/10.14359/6962
Tilly, G. P. (1979). "Fatigue Of Steel Reinforcement Bars In Concrete: A review." *Fatigue & Fracture of Engineering Materials & Structures*, *2*(3), 251–268. https://doi.org/10.1111/j.1460-2695.1979.tb01084.x
Treece, R. A., & Jirsa, J. O. (1989). "Bond strength of epoxy-coated reinforcing bars." *Materials Journal*, *86*(2), 167–174.
Valette, R. (1947). "Resistance des Ponts sous Rails en Beton Arme; Essais de Poutres aux Flexions Repetees." *Memoires, Association Internationale Des Ponts et Charpentes,(Zurich)*, *8*.
Van Ornum, J. L. (1903). "The fatigue of cement products." *Proceedings of the American Society of Civil Engineers*, *29*(6), 627–629. ASCE.
Wang, H. (2005). *Steel-free hybrid reinforcement system for reinforced concrete flexural members*. University of Missouri-Rolla.
Wang, H., & Belarbi, A. (2011). "Ductility characteristics of fiber-reinforced-concrete beams reinforced with FRP rebars." *Construction and Building Materials*, *25*(5), 2391–2401. https://doi.org/https://doi.org/10.1016/j.conbuildmat.2010.11.040
Wei, S., Yun, Y., & Jianming, G. (1996). "Study of the Fatigue Performance and Damage Mechanism of Steel Fiber Reinforced Concrete." *Materials Journal*, *93*(3). https://doi.org/10.14359/9804
Whaley, C. P., & Neville, A. M. (1973). "Non-elastic deformation of concrete under cyclic compression." *Magazine of Concrete Research*, *25*(84), 145–154.
Williams, H. A. (1943). "Fatigue Tests of Lightweight Aggregate Concrete Beams." *Journal Proceedings*, *39*. https://doi.org/10.14359/8638
Yang, B., Mall, S., & Ravi-Chandar, K. (2001). "A cohesive zone model for fatigue crack growth in quasibrittle materials." *International Journal of Solids and Structures*, *38*(22), 3927–3944. https://doi.org/https://doi.org/10.1016/S0020-7683(00)00253-5

Yang, J.-M., Min, K.-H., Shin, H.-O., & Yoon, Y.-S. (2012). "Effect of steel and synthetic fibers on flexural behavior of high-strength concrete beams reinforced with FRP bars." *Composites Part B: Engineering*, *43*(3), 1077–1086. https://doi.org/https://doi.org/10.1016/j.compositesb.2012.01.044

Yost, J., Dinehart, D., Gross, S., Reilly, P., & Reichmann, D. (2015). "Fatigue behavior of GFRP and steel reinforced bridge decks designed using traditional and empirical methodologies." *Bridge Structures*, *11*(3), 87–94.

You, Y.-J., Kim, J.-H. J., Park, Y.-H., & Choi, J.-H. (2015). "Fatigue performance of bridge deck reinforced with cost-to-performance optimized GFRP rebar with 900 MPa guaranteed tensile strength." *Journal of Advanced Concrete Technology*, *13*(5), 252–262.

Youn, S.-G., & Chang, S.-P. (1998). "Behavior of composite bridge decks subjected to static and fatigue loading." *Structural Journal*, *95*(3), 249–258.

Zadeh, H. J., & Nanni, A. (2013). "Reliability analysis of concrete beams internally reinforced with fiber-reinforced polymer bars." *Structural Journal*, *110*(6), 1023–1032.

Zaghloul, E. E.-D. R., Mahmoud, Z. I., & Salama, T. A. (2008). "Punching behaviour and strength of two-way concrete slabs reinforced with glass fiber reinforced polymer (GFRP) rebars." *Structural Composites for Infrastructure Applications*, 16. Hurghada, Egypt.

Zhang, J., Stang, H., & Li, V. C. (1998). "Fatigue Performance in Flexure of Fiber Reinforced Concrete." *Materials Journal*, *95*(1). https://doi.org/10.14359/351

Zhao, Y., Ren, H., Dai, H., & Jin, W. (2011). "Composition and expansion coefficient of rust based on X-ray diffraction and thermal analysis." *Corrosion Science*, *53*(5), 1646–1658. https://doi.org/https://doi.org/10.1016/j.corsci.2011.01.007

Zhaodong, D., & Jie, L. (2018). "A physically motivated model for fatigue damage of concrete." *International Journal of Damage Mechanics*, *27*(8), 1192–1212.

APPENDIX A. BRIDGE DECK DESIGNS AND FATIGUE LOADING

The calculations in the following sections were based on both the Florida DOT bridge design example as well as design examples provided to the author by Eriksson Technologies. There are no standards given for some of the required calculations, therefore, the assumptions are provided along with the calculations.

Steel-Reinforced Bridge Deck Design

Design Criteria:

Same as FDOT example https://www.fdot.gov/structures/lrfddesignexamples.shtm

Geometry:

Bridge Span ---------- $L_{span} := 90\ ft$

Girder Spacing ---------- $S := 10\ ft$

Deck Slab Thickness ---------- $t_{slab} := 8\ in$

Analysis Method ---------- "Equivalent Strip Method"

Cover distance ---------- $c_c := 1.5\ in$

Design Width ---------- $b_{slab} := 1\ ft$

Material Properties:

Design Concrete Strength ---------- $f'_c := 5000\ psi$

Design Steel Yield Strength ---------- $F_y := 60000\ psi$

Stress Block Factor ---------- $\beta_1 := 0.85 - \left(\frac{f'_c - 4000\ psi}{1000\ psi}\right) \cdot 0.05 = 0.8$

Modulus of Elasticity of Concrete ---------- $E_c := 57000 \cdot \sqrt{f'_c \cdot psi} = 4030.51\ ksi$

Modulus of Elasticity of Steel ---------- $E_s := 29000\ ksi$

Width of Equivalent Strips:

Width of strip for positive moment ---------- $E_{pos} := \left(26 + 6.6 \cdot \frac{S}{ft}\right) \cdot in = 92\ in$

Width of strip for negative moment ---------- $E_{neg} := \left(48 + 3.0 \cdot \frac{S}{ft}\right) \cdot in = 78\ in$

Following the FDOT Example, AASHTO Table A4-1 is used to find the live load design moments:

Positive Live Load Moment ---------- $M_{LLpos} := 6.89\ kip \cdot ft$

Negative Live Load Moment ---------- $M_{LLneg} := 4.25\ kip \cdot ft$

Dead Load Moments:

Again, the FDOT Example is utilized to come up with the dead load moment. The "DC" moment includes the self-weight of the deck, the traffic barriers, and median barrier.

The "DW" moment includes the future wearing surface and utilities. In their design example, they assumed the deck would act as the wearing surface, therefore, the DW moment is 0.

Dead Load Positive Moment ---------- $M_{Dpos} := 0.67\ kip \cdot ft$

Dead Load Negative Moment ---------- $M_{Dneg} := 0.43\ kip \cdot ft$

Design Limit States (AASHTO Table 3.4.1-1):

Service I:

Positive Service I Moment ---------- $M_{SIpos} := M_{Dpos} + M_{LLpos} = 7.56\ kip \cdot ft$

Negative Service I Moment ---------- $M_{SIneg} := M_{Dneg} + M_{LLneg} = 4.68\ kip \cdot ft$

Strength I:

Positive Strength I Moment ----- $M_{StrIpos} := 1.25\ M_{Dpos} + 1.75\ M_{LLpos} = 12.9\ kip \cdot ft$

Negative Strength I Moment ---- $M_{StrIneg} := 1.25 \cdot M_{Dneg} + 1.75 \cdot M_{LLneg} = 7.98\ kip \cdot ft$

Moment Design (AASHTO 5.6.3):

Assume Initially that ϕ = 0.9 and that the section is tension-controlled. Also, ignore the contribution of the compression reinforcement. Also, assume an inital guess of reinforcement and then iterate until convergence is achieved for the section.

Utilize the same reinforcement size and spacing for positive and negative reinforcement.

Assumed Resistance Factor ---------- $\phi := 0.9$

Assumed Size of Bar ---------- $bar := \text{“\#5”}$

Assumed Bar Spacing ---------- $spacing := 6\ in$

Bar Diameter ---------- $d_b := 0.625\ in$

Bar Area ---------- $A_b := \frac{\pi \cdot d_b^{\,2}}{4} = 0.31\ in^2$

Area of Steel per foot of deck ---------- $A_s := \frac{A_b \cdot ft}{spacing} = 0.61\ in^2$

Because we assumed a cover of 1.5", our example will vary slightly from the FDOT example after this point.

Depth to centroid of steel ---------- $d := t_{slab} - c_c - \frac{d_b}{2} = 6.19\ in$

Guess a value for the depth to the neutral axis:

Estimated Depth to N.A. ---------- $c := 1.5\ in$

Solve equilibrium for the correct depth:

$c := \mathbf{root}\left(0.85 \cdot f'_c \cdot b_{slab} \cdot \beta_1 \cdot c - A_s \cdot F_y, c\right) = 0.9\ in$

Depth to of Stress Block ---------- $a := c \cdot \beta_1 = 0.72\ in$

Capacity of the Section ---------- $\phi M_r := \phi \cdot A_s \cdot F_y \cdot \left(d - \frac{a}{2}\right) = 16.09\ kip \cdot ft$

$M_u := \max\left(M_{StrIpos}, M_{StrIneg}\right) = 12.9\ kip \cdot ft$

$\mathbf{if}\left(\phi M_r > M_u, \text{“Okay”}, \text{“Check”}\right) = \text{“Okay”}$ *Therefore, the section is okay for flexure.*

Check Minimum Area of Reinforcement (AASHTO 5.6.3.3):

The minimum reinforcement requirements ensure that the capacity of the section exceed the cracking moment by a certain factor.

Concrete Density Modification Factor ------ $\gamma := 1.0$ (AASHTO 5.4.2.8)

Modulus of Rupture of Concrete ---------- $f_r := 0.24 \cdot \gamma \cdot \sqrt{f'_c \cdot ksi} = 0.54\ ksi$

Slab Moment of Inertia ---------- $I_{slab} := \frac{b_{slab} \cdot t_{slab}^{3}}{12} = 512\ in^4$

Distance from N.A. to Extreme Tension ---- $y := \frac{t_{slab}}{2} = 4\ in$

Section Modulus ---------- $S_c := \frac{I_{slab}}{y} = 128\ in^3$

Flexural Cracking Factor ---------- $\gamma_1 := 1.6$

Yield/Ultimate Ratio Factor ---------- $\gamma_3 := 0.67$

Cracking Moment ---------- $M_{cr} := \gamma_3 \cdot (\gamma_1 \cdot f_r) \cdot S_c = 6.14\ kip \cdot ft$

Minimum Reinforcement --------- $A_{min} := \frac{\frac{M_{cr}}{\phi}}{F_y \cdot \left(d - 0.5 \cdot \left(\frac{A_s \cdot F_y}{0.85 \cdot f'_c \cdot b_{slab}}\right)\right)} = 0.23\ in^2$

*The steel provided for flexure must exceed the minimum of 1.33*Required Steel for Flexure, or Amin from Cracking moment:*

Required Steel for Flexure:

$$A_{sreqd} := \mathbf{root}\left(\phi \cdot A_s \cdot F_y \cdot \left(d - \frac{A_s \cdot F_y}{2 \cdot 0.85 \cdot f'_c \cdot b_{slab}}\right) - M_u, A_s\right) = 0.49\ in^2$$

Minimum Reinforcement ---------- $A_{smin} := min\left(A_{sreqd}, A_{min}\right) = 0.23\ in^2$

$\mathbf{if}\left(A_s > A_{smin}, \text{“Okay”}, \text{“Check”}\right) = \text{“Okay”}$

Therefore, the section meets the minimum steel requirements.

Check Minimum Spacing of Reinforcement for Cracking (AASHTO 5.6.3.3):

We will assume Exposure Class 1, which is based on an assumed crack width of 0.017 in.

Exposure factor (Class 1) ---------- $\gamma_e := 1.0$ (AASHTO 5.6.3.3)

Thickness of slab ---------- $t_{slab} = 8\ in$

Positive Moment Check

Depth from tension to bar ---------- $d_c := c_c + \frac{d_b}{2} = 1.81\ in$

Ratio of strain from tension face to bar ------ $\beta_s := 1 + \frac{d_c}{0.7 \cdot (t_{slab} - d_c)} = 1.42$
(AASHTO Eq. 5.6.7-2)

To determine the stress in the tension reinforcement, the neutral axis must be determined.

Initialize a guess for the neutral axis --------- $x := 2\ in$

Solve for the neutral axis:

$$x := \mathbf{root}\left(\frac{1}{2} \cdot b_{slab} \cdot x^2 - \frac{E_s}{E_c} \cdot A_s \cdot (d - x), x\right) = 1.8\ in$$

Tensile Force in steel - service moment ----- $T_s := \frac{M_{SIpos}}{d - \frac{x}{3}} = 16.23\ kip$

Tensile Stress in steel - service moment ----- $f_s := \frac{T_s}{A_s} = 26.46\ ksi$

Required Reinforcement Spacing ---------- $s_{required} := \frac{700 \cdot \gamma_e \cdot \left(\frac{kip}{in}\right)}{\beta_s \cdot f_s} - 2 \cdot d = 6.28\ in$
(AASHTO Eq 5.6.7-1)

$\mathbf{if}\left(spacing < s_{required}, \text{“Okay”}, \text{“Check”}\right) = \text{“Okay”}$

Negative Moment Check

Depth from tension to bar ---------- $d_c := c_c + \frac{d_b}{2} = 1.81\ in$

Ratio of strain from tension face to bar ------ $\beta_s := 1 + \frac{d_c}{0.7 \cdot (t_{slab} - d_c)} = 1.42$
(AASHTO Eq. 5.6.7-2)

To determine the stress in the tension reinforcement, the neutral axis must be determined.

Initialize a guess for the neutral axis --------- $x := 2\ \textbf{\textit{in}}$

Solve for the neutral axis:

$$x := \text{root}\left(\frac{1}{2} \cdot b_{slab} \cdot x^2 - \frac{E_s}{E_c} \cdot A_s \cdot (d - x), x\right) = 1.8\ \textbf{\textit{in}}$$

Tensile Force in steel - service moment ----- $T_s := \frac{M_{SIneg}}{d - \frac{x}{3}} = 10.05\ \textbf{\textit{kip}}$

Tensile Stress in steel - service moment ----- $f_s := \frac{T_s}{A_s} = 16.38\ \textbf{\textit{ksi}}$

Required Reinforcement Spacing ---------- $s_{required} := \frac{700 \cdot \gamma_e \cdot \left(\frac{\textbf{\textit{kip}}}{\textbf{\textit{in}}}\right)}{\beta_s \cdot f_s} - 2 \cdot d = 17.76\ \textbf{\textit{in}}$
(AASHTO Eq 5.6.7-1)

$\text{if}(spacing < s_{required}, \text{“Okay”}, \text{“Check”}) = \text{“Okay”}$

Check Temperature and Shrinkage Reinforcement (AASHTO 5.10.6):

Assume #5 bars at 8 inches o/c initially.

Temperature and Shrinkage Bar Diameter -- $d_{bTS} := 0.625\ in$

Area of T+S Steel ---------- $A_{bTS} := \frac{\pi \cdot d_{bTS}^{2}}{4} = 0.31\ in^2$

Spacing of T+S Steel ---------- $s_{TS} := 8\ in$

Design width ---------- $b_{slab} = 12\ in$

Thickness of slab ---------- $t_{slab} = 8\ in$

Required T+S Steel *(AASHTO 5.10.6-1)* and *(AASHTO 5.10.6-2)*:

$$A_{TS} := min\left(0.6\ \frac{in^2}{ft}, \max\left(0.11\ \frac{in^2}{ft}, \frac{1.3 \cdot \frac{kip}{in \cdot ft} \cdot b_{slab} \cdot t_{slab}}{2 \cdot (b_{slab} + t_{slab}) \cdot F_y}\right)\right) = 0.11\ \frac{in^2}{ft}$$

Max T+S Spacing ---------- $s_{maxTS} := min\left(\frac{A_{bTS}}{A_{TS}}, 3 \cdot t_{slab}, 18\ in\right) = 18\ in$

$\text{if}\left(s_{TS} < s_{maxTS}, \text{“Okay”}, \text{“Check”}\right) = \text{“Okay”}$

Check Distribution Steel Requirements (AASHTO 5.12.2.1):

According to AASHTO, transverse distribution reinforcement shall be placed in the bottoms of all slabs. We will check to see if the Temperature and Shrinkage Steel provided is adequate for the distribution.

Required Distribution Percentage ---------- $D := min\left(\frac{220}{\sqrt{\frac{S}{ft}}}, 67\right)\% = 0.67$

Required Distribution Area/ft ---------- $A_{dist} := D \cdot A_s = 0.41\ in^2$

Max Spacing for Distribution Steel ---------- $s_{maxdist} := \frac{b_{slab}}{\left(\frac{A_{dist}}{A_{bTS}}\right)} = 8.96\ in$

$\text{if}\left(s_{TS} < s_{maxdist}, \text{“Okay”}, \text{“Check”}\right) = \text{“Okay”}$

Check Deflections (AASHTO 5.6.3.5.2):

The Service Limit State deflections will be checked against the allowable deflections of L/800. The load is assumed to act as a uniform LL with fixed ends.

Gross Moment of Inertia ---------- $I_g := \frac{b_{slab} \cdot t_{slab}^3}{12} = 512\ in^4$

Neutral Axis ---------- $x = 1.8\ in$

Cracked Moment of Inertia ---------- $I_{cr} := \frac{b_{slab} \cdot x^3}{3} + \frac{E_s}{E_c} \cdot A_s \cdot (d - x)^2 = 108.31\ in^4$

Design Service Moment ---------- $M_a := \max(M_{SIpos}, M_{SIneg}) = 7.56\ kip \cdot ft$

Distance from NA to tension ---------- $y_t := \frac{t_{slab}}{2} = 4\ in$

Cracking Moment ---------- $M_{cr} := f_r \cdot \frac{I_g}{y_t} = 5.72\ kip \cdot ft$
(AASHTO Eq. 5.6.3.5.2-2)

Effective Moment of Inertia (AASHTO Eq. 5.6.3.5.2-2):

$$I_e := min\left(\left(\frac{M_{cr}}{M_a}\right)^3 \cdot I_g + \left(1 - \left(\frac{M_{cr}}{M_a}\right)^3\right) \cdot I_{cr}, I_g\right) = 283.56\ in^4$$

Assumed Uniform Load ---------- $w_{eq} := \max\left(M_{LLpos} \cdot \frac{24}{S^2}, M_{LLneg} \cdot \frac{12}{S^2}\right) = 1.65\ klf$

Deflection Limit ---------- $\Delta_{limit} := \frac{S}{800} = 0.15\ in$

Max Deflection ---------- $\Delta_{max} := \frac{1}{384} \cdot \frac{w_{eq} \cdot S^4}{E_c \cdot I_e} = 0.07\ in$

if $(\Delta_{max} < \Delta_{limit}, \text{“Okay”}, \text{“Check”}) = \text{“Okay”}$

GFRP-Reinforced Bridge Deck Design

Design Criteria:

Same as FDOT example https://www.fdot.gov/structures/lrfddesignexamples.shtm
The AASHTO References in this example refer to the AASHTO GFRP Design Guide.

Geometry:

Bridge Span ---------- $L_{span} := 90\ ft$

Girder Spacing ---------- $S := 10\ ft$

Deck Slab Thickness ---------- $t_{slab} := 8\ in$

Analysis Method ---------- "Equivalent Strip Method"

Cover distance ---------- $c_c := 1.5\ in$

Design Width ---------- $b_{slab} := 1\ ft$

Material Properties:

Design Concrete Strength ---------- $f'_c := 5000\ psi$

Stress Block Factor ---------- $\beta_1 := 0.85 - \left(\frac{f'_c - 4000\ psi}{1000\ psi}\right) \cdot 0.05 = 0.8$

Concrete Crushing Strain ---------- $\varepsilon_{cu} := 0.003$

Modulus of Elasticity of Concrete ---------- $E_c := 57000 \cdot \sqrt{f'_c \cdot psi} = 4030.51\ ksi$

Modulus of Elasticity of GFRP ---------- $E_f := 6700\ ksi$

Environmental Reduction Factor ---------- $C_e := 0.7$
(AASHTO 2.4-1)

Ultimate GFRP Strength ---------- $f_{fu'} := 100000\ psi$

Design GFRP Strength ---------- $f_{fu} := f_{fu'} \cdot C_e = 70000\ psi$

Ultimate Strain ---------- $\varepsilon_{fu'} := 0.0149$

Design Ultimate Strain ---------- $\varepsilon_{fu} := \varepsilon_{fu'} \cdot C_e = 0.0104$

Width of Equivalent Strips:

Width of strip for positive moment ---------- $E_{pos} := \left(26 + 6.6 \cdot \frac{S}{ft}\right) \cdot in = 92\ in$

Width of strip for negative moment ---------- $E_{neg} := \left(48 + 3.0 \cdot \frac{S}{ft}\right) \cdot in = 78\ in$

Following the FDOT Example, AASHTO Table A4-1 is used to find the live load design moments:

Positive Live Load Moment ---------- $M_{LLpos} := 6.89\ kip \cdot ft$

Negative Live Load Moment ---------- $M_{LLneg} := 4.25\ kip \cdot ft$

Dead Load Moments:

Again, the FDOT Example is utilized to come up with the dead load moment. The "DC" moment includes the self-weight of the deck, the traffic barriers, and median barrier.

The "DW" moment includes the future wearing surface and utilities. In their design example, they assumed the deck would act as the wearing surface, therefore, the DW moment is 0.

Dead Load Positive Moment ---------- $M_{Dpos} := 0.67\ kip \cdot ft$

Dead Load Negative Moment ---------- $M_{Dneg} := 0.43\ kip \cdot ft$

Design Limit States (LRFD AASHTO Table 3.4.1-1):

Service I:

Positive Service I Moment ---------- $M_{SIpos} := M_{Dpos} + M_{LLpos} = 7.56\ kip \cdot ft$

Negative Service I Moment ---------- $M_{SIneg} := M_{Dneg} + M_{LLneg} = 4.68\ kip \cdot ft$

Strength I:

Positive Strength I Moment ----- $M_{StrIpos} := 1.25\ M_{Dpos} + 1.75\ M_{LLpos} = 12.9\ kip \cdot ft$

Negative Strength I Moment ---- $M_{StrIneg} := 1.25 \cdot M_{Dneg} + 1.75 \cdot M_{LLneg} = 7.98\ kip \cdot ft$

Moment Design (AASHTO 5.6.3):

Assume Initially that ϕ = 0.9 and that the section is tension-controlled. Also, ignore the contribution of the compression reinforcement. Also, assume an inital guess of reinforcement and then iterate until convergence is achieved for the section.

Utilize the same reinforcement size and spacing for positive and negative reinforcement.

Assumed Size of Bar ---------- $bar := \text{"\#6"}$

Assumed Bar Spacing ---------- $spacing := 6\ in$

Bar Diameter ---------- $d_b := 0.75\ in$

Bar Area ---------- $A_b := \frac{\pi \cdot d_b^{\,2}}{4} = 0.44\ in^2$

Area of GFRP per foot of deck ---------- $A_f := \frac{A_b \cdot ft}{spacing} = 0.88\ in^2$

Because we assumed a cover of 1.5", our example will vary slightly from the FDOT example after this point.

Depth to centroid of steel ---------- $d := t_{slab} - c_c - \frac{d_b}{2} = 6.13\ in$

GFRP Reinforcement Ratio ---------- $\rho_f := \frac{A_f}{b_{slab} \cdot d} = 0.01202$

Balanced GFRP Reinforcement Ratio: $\rho_{fb} := 0.85 \cdot \beta_1 \cdot \frac{f'_c}{f_{fu}} \cdot \left(\frac{E_f \cdot 0.003}{E_f \cdot 0.003 + f_{fu}} \right) = 0.01084$

Since the reinforcement ratio is greater than the balanced ratio, the section is compression-controlled.

Stress in FRP (AASHTO Eq. 2.6.3.1-1):

$$f_f := min\left(\sqrt{\frac{(E_f \cdot \varepsilon_{cu})^2}{4} + \frac{0.85 \cdot \beta_1 \cdot f'_c}{\rho_f} \cdot E_f \cdot \varepsilon_{cu}} - 0.5 \cdot E_f \cdot \varepsilon_{cu}, f_{fu} \right) = 66.01\ ksi$$

Depth of Stress Block ---------- $a := \frac{A_f \cdot f_f}{0.85 \cdot f'_c \cdot b_{slab}} = 1.14$ ***in***

Depth to N.A. ---------- $c := \frac{a}{\beta_1} = 1.43$ ***in***

Nominal Moment Capacity ---------- $M_r := A_f \cdot f_f \cdot \left(d - \frac{a}{2}\right) = 26.99$ ***kip·ft***

Strain in GFRP ---------- $\varepsilon_f := \left(\frac{d-c}{c}\right) \cdot \varepsilon_{cu} = 0.0099$

Resistance Factor ---------- $\phi := 1.55 - \frac{\varepsilon_f}{\varepsilon_{fu}} = 0.61$
(AASHTO 2.5.5.2-1)

Factored Moment Capacity ---------- $\phi M_r := \phi \cdot M_r = 16.34$ ***kip·ft***

Required Moment ---------- $M_u := \max\left(M_{StrIpos}, M_{StrIneg}\right) = 12.9$ ***kip·ft***

if $\left(\phi M_r > \max\left(M_{StrIpos}, M_{StrIneg}\right), \text{“Okay”}, \text{“Check”}\right) = \text{“Okay”}$

Check Minimum Area of Reinforcement (AASHTO 2.6.3.3):

The minimum reinforcement requirements ensure that the capacity of the section exceed the cracking moment by a certain factor.

Concrete Density Modification Factor ------ $\gamma := 1.0$ (AASHTO 5.4.2.8)

Modulus of Rupture of Concrete ---------- $f_r := 0.24 \cdot \gamma \cdot \sqrt{f'_c \cdot ksi} = 0.54\ ksi$

Slab Moment of Inertia ---------- $I_{slab} := \frac{b_{slab} \cdot t_{slab}^{3}}{12} = 512\ in^4$

Distance from N.A. to Extreme Tension ---- $y := \frac{t_{slab}}{2} = 4\ in$

Section Modulus ---------- $S_c := \frac{I_{slab}}{y} = 128\ in^3$

Flexural Cracking Factor ---------- $\gamma_1 := 1.6$

Cracking Moment ---------- $M_{cr} := (\gamma_1 \cdot f_r) \cdot S_c = 9.16\ kip \cdot ft$

Minimum Reinforcement --------- $A_{min} := \frac{\frac{M_{cr}}{\phi}}{f_f \cdot \left(d - 0.5 \cdot \left(\frac{A_f \cdot f_f}{0.85 \cdot f'_c \cdot b_{slab}}\right)\right)} = 0.5\ in^2$

*The GFRP provided for flexure must exceed the minimum of 1.33*Required GFRP for Flexure, or Amin from Cracking moment:*

Required Steel for Flexure:

$$A_{freqd} := \mathbf{root}\left(\phi \cdot A_f \cdot f_f \cdot \left(d - \frac{A_f \cdot f_f}{2 \cdot 0.85 \cdot f'_c \cdot b_{slab}}\right) - M_u, A_f\right) = 0.68\ in^2$$

Minimum Reinforcement ---------- $A_{fmin} := min\left(A_{freqd}, A_{min}\right) = 0.5\ in^2$

$\mathbf{if}\left(A_f > A_{fmin}, \text{“Okay”}, \text{“Check”}\right) = \text{“Okay”}$ *Therefore, the section meets the minimum GFRP requirements.*

Check Distribution Reinforcement (AASHTO 2.10.2.1):

In bridge decks, a percentage of the primary reinforcement must be provided in deck type bridges.

Required Distribution Percentage ---------- $D := min\left(\frac{100}{\sqrt{\frac{S}{ft}}}, 50\right)\% = 0.32$

Required Distribution Area/ft ---------- $A_{dist} := D \cdot A_f = 0.28\ in^2$

Max Spacing for Distribution GFRP --------- $s_{maxdist} := \frac{b_{slab}}{\left(\frac{A_{dist}}{A_b}\right)} = 19\ in$

Spacing for Distribution GFRP ---------- $s_{dist} := 9\ in$

Check Temperature and Shrinkage Reinforcement (AASHTO 5.10.6):

Assume #6 bars at 9 inches o/c initially.

Temperature and Shrinkage Bar Diameter -- $d_{bTS} := 0.75\ in$

Area of T+S GFRP ---------- $A_{bTS} := \frac{\pi \cdot {d_{bTS}}^2}{4} = 0.44\ in^2$

Ratio of T+S (AASHTO 2.9.6-1):

$$\rho_{fTS} := min\left(\max\left(\frac{3.132\ ksi \cdot ksi}{E_f \cdot f_{fu}}, 0.0014\right), 0.0036\right) = 0.0014$$

Required Area of T+S ---------- $A_{fTS} := \frac{\rho_{fTS} \cdot b_{slab} \cdot d}{ft} = 0.103\ \frac{in^2}{ft}$

Thickness of slab ---------- $t_{slab} = 8\ in$

Max T+S Spacing ---------- $s_{maxTS} := min\left(\frac{A_{bTS}}{A_{fTS}}, 3 \cdot t_{slab}, 18\ in\right) = 18\ in$

$\text{if}\left(s_{dist} < s_{maxTS}, \text{“Okay”}, \text{“Check”}\right) = \text{“Okay”}$

Check Deflections (AASHTO 2.6.3.4.2):

The Service Limit State deflections will be checked against the allowable deflections of L/800. The load is assumed to act as a uniform LL with fixed ends.

Gross Moment of Inertia ---------- $I_g := \frac{b_{slab} \cdot t_{slab}^3}{12} = 512\ in^4$

Initialize a guess for the neutral axis --------- $x := 2\ in$

Solve for the neutral axis:

$$x := \mathbf{root}\left(\frac{1}{2} \cdot b_{slab} \cdot x^2 - \frac{E_f}{E_c} \cdot A_f \cdot (d - x), x\right) = 1.11\ in$$

Neutral Axis ---------- $x = 1.11\ in$

Cracked Moment of Inertia ---------- $I_{cr} := \frac{b_{slab} \cdot x^3}{3} + \frac{E_f}{E_c} \cdot A_f \cdot (d - x)^2 = 42.41\ in^4$

Design Service Moment ---------- $M_a := \max(M_{SIpos}, M_{SIneg}) = 7.56\ kip \cdot ft$

Distance from NA to tension ---------- $y_t := \frac{t_{slab}}{2} = 4\ in$

Cracking Moment ---------- $M_{cr} := f_r \cdot \frac{I_g}{y_t} = 5.72\ kip \cdot ft$
(AASHTO Eq. 2.6.3.4.2-2)

Variable Stiffness Factor ---------- $\gamma_d := 1.72 - 0.72 \cdot \left(\frac{M_{cr}}{M_a}\right) = 1.17$
(AASHTO Eq. 2.6.3.4.2-1)

Effective Moment of Inertia:

$$I_e := min\left(\frac{I_{cr}}{1 - \gamma \cdot \left(\frac{M_{cr}}{M_a}\right)^2 \cdot \left(1 - \frac{I_{cr}}{I_g}\right)}, I_g\right) = 89.44\ in^4$$

Assumed Uniform Load ---------- $w_{eq} := \max\left(M_{LLpos} \cdot \frac{24}{S^2}, M_{LLneg} \cdot \frac{12}{S^2}\right) = 1.65\ klf$

Deflection Limit ---------- $\Delta_{limit} := \frac{S}{800} = 0.15\ in$

Max Deflection ---------- $\Delta_{max} := \frac{1}{384} \cdot \frac{w_{eq} \cdot S^4}{E_c \cdot I_e} = 0.21\ in$

$\mathbf{if}(\Delta_{max} < \Delta_{limit}, \text{“Okay”}, \text{“Check”}) = \text{“Check”}$

Check Deflections (AASHTO 2.6.3.4.2):

This check shall ensure that the max crack is less than 0.028 in by distributing the reinforcement sufficiently.

Crack Width Limit ---------- $w_{max} := 0.028\ in$

Bond Reduction Factor ---------- $C_b := 0.83$

Design Service Moment ---------- $M_a = 7.56\ kip \cdot ft$

Find the Neutral Axis, assuming that the compression reinforcement is not contributing:

$$x := \mathbf{root}\left(\frac{1}{2} \cdot b_{slab} \cdot x^2 - \frac{E_f}{E_c} \cdot A_f \cdot (d - x), x\right) = 1.11\ in$$

Tensile Force in GFRP - service moment --- $T_{fs} := \dfrac{M_{SIpos}}{d - \dfrac{x}{3}} = 15.76\ kip$

Tensile Stress in GFRP - service moment --- $f_{fs} := \dfrac{T_{fs}}{A_f} = 17.84\ ksi$

Maximum Allowable Spacing:

$$s_{max} := min\left(1.15 \cdot \frac{C_b \cdot E_f \cdot w_{max}}{f_{fs}} - 2.5 \cdot c_c, 0.92 \cdot \frac{C_b \cdot E_f \cdot w_{max}}{f_{fs}}\right) = 6.29\ in$$

Design Spacing of Rebar ---------- $spacing = 6\ in$

$\mathbf{if}\left(spacing < s_{max}, \text{“Okay”}, \text{“Check”}\right) = \text{“Okay”}$

HRC-Bridge Deck Design

Design Criteria:

Same as FDOT example https://www.fdot.gov/structures/lrfddesignexamples.shtm
The AASHTO References in this example refer to the AASHTO GFRP Design Guide.

Geometry:

Bridge Span ---------- $L_{span} := 90\ ft$

Girder Spacing ---------- $S := 10\ ft$

Deck Slab Thickness ---------- $t_{slab} := 8\ in$

Analysis Method ---------- "Equivalent Strip Method"

Cover distance ---------- $c_c := 1.5\ in$

Design Width ---------- $b_{slab} := 1\ ft$

Material Properties:

Design Concrete Strength ---------- $f'_c := 4500\ psi$

Stress Block Factor ---------- $\beta_1 := 0.85 - \left(\frac{f'_c - 4000\ psi}{1000\ psi}\right) \cdot 0.05 = 0.83$

Concrete Crushing Strain ---------- $\varepsilon_{cu} := 0.003$

Modulus of Elasticity of Concrete ---------- $E_c := 57000 \cdot \sqrt{f'_c \cdot psi} = 3823.68\ ksi$

Modulus of Elasticity of GFRP ---------- $E_f := 6700\ ksi$

Environmental Reduction Factor ---------- $C_e := 0.7$
(AASHTO 2.4-1)

Ultimate GFRP Strength ---------- $f_{fu'} := 100000\ psi$

Design GFRP Strength ---------- $f_{fu} := f_{fu'} \cdot C_e = 70000\ psi$

Ultimate Strain ---------- $\varepsilon_{fu'} := 0.0149$

Design Ultimate Strain ---------- $\varepsilon_{fu} := \varepsilon_{fu'} \cdot C_e = 0.0104$

Fiber dosage ---------- $dosage := 15\ \frac{lbf}{yd^3}$

Assumed Orientation Factor ---------- $K := 1.0$

Residual Tensile Strength for CMOD1 ------ $f_{R1} := 203\ psi$

Residual Tensile Strength for CMOD3 ------ $f_{R3} := 226\ psi$ <--- *These values came from a data sheet provided by the fiber manufacturer.*

Limit of Proportionality ---------- $f_{Lk} := 455\ psi$

Check FRC Structural Use Requirments:

fib Model Code (5.6-4) ---------- $\frac{f_{R1}}{f_{Lk}} = 0.4462$

$$\text{if}\left(\left(\frac{f_{R1}}{f_{Lk}}\right) > 0.4, \text{“Okay”}, \text{“Check”}\right) = \text{“Okay”}$$

fib Model Code (5.6-3) ---------- $\frac{f_{R3}}{f_{R1}} = 1.1133$

$$\text{if}\left(\left(\frac{f_{R3}}{f_{R1}}\right) > 0.5, \text{“Okay”}, \text{“Check”}\right) = \text{“Okay”}$$

Width of Equivalent Strips:

Width of strip for positive moment ---------- $E_{pos} := \left(26 + 6.6 \cdot \frac{S}{ft}\right) \cdot in = 92\ in$

Width of strip for negative moment ---------- $E_{neg} := \left(48 + 3.0 \cdot \frac{S}{ft}\right) \cdot in = 78\ in$

Following the FDOT Example, AASHTO Table A4-1 is used to find the live load design moments:

Positive Live Load Moment ---------- $M_{LLpos} := 6.89\ kip \cdot ft$

Negative Live Load Moment ---------- $M_{LLneg} := 4.25\ kip \cdot ft$

Dead Load Moments:

Again, the FDOT Example is utilized to come up with the dead load moment. The "DC" moment includes the self-weight of the deck, the traffic barriers, and median barrier.

The "DW" moment includes the future wearing surface and utilities. In their design example, they assumed the deck would act as the wearing surface, therefore, the DW moment is 0.

Dead Load Positive Moment ---------- $M_{Dpos} := 0.67\ kip \cdot ft$

Dead Load Negative Moment ---------- $M_{Dneg} := 0.43\ kip \cdot ft$

Design Limit States (LRFD AASHTO Table 3.4.1-1):

Service I:

Positive Service I Moment ---------- $M_{SIpos} := M_{Dpos} + M_{LLpos} = 7.56\ kip \cdot ft$

Negative Service I Moment ---------- $M_{SIneg} := M_{Dneg} + M_{LLneg} = 4.68\ kip \cdot ft$

Strength I:

Positive Strength I Moment ----- $M_{StrIpos} := 1.25\ M_{Dpos} + 1.75\ M_{LLpos} = 12.9\ kip \cdot ft$

Negative Strength I Moment ---- $M_{StrIneg} := 1.25 \cdot M_{Dneg} + 1.75 \cdot M_{LLneg} = 7.98\ kip \cdot ft$

Moment Design:

Several Assumptions will be made to assist in the design of the HRC Section. First, the Rigid-Plastic model allowable ultimate tensile stress in the FRC will be utilized. Second, instead of a variable tension stress in the HRC, a uniform rectangular stress will be observed to simplify analysis.
Utilize the same reinforcement size and spacing for positive and negative reinforcement.

Axial Tensile Capacity (FRC) ---------- $f_{Ftu} := \frac{f_{R3}}{K \cdot 3} = 75.33\ psi$

Bar Size ---------- $bar := \text{“\#6”}$

Assumed Bar Spacing ---------- $spacing := 8\ in$

Bar Diameter ---------- $d_b := 0.75\ in$

Bar Area ---------- $A_b := \frac{\pi \cdot d_b^{\,2}}{4} = 0.44\ in^2$

Area of GFRP per foot of deck ---------- $A_f := \frac{A_b \cdot ft}{spacing} = 0.66\ in^2$

We will be ignoring the contribution of the GFRP bar in compression.

Because we assumed a cover of 1.5", our example will vary slightly from the FDOT example after this point.

Depth to centroid of steel ---------- $d := t_{slab} - c_c - \frac{d_b}{2} = 6.13\ in$

GFRP Reinforcement Ratio ---------- $\rho_f := \frac{A_f}{b_{slab} \cdot d} = 0.00902$

Balanced GFRP Reinforcement Ratio: $\rho_{fb} := 0.85 \cdot \beta_1 \cdot \frac{f'_c}{f_{fu}} \cdot \left(\frac{E_f \cdot 0.003}{E_f \cdot 0.003 + f_{fu}} \right) = 0.01006$

Since the reinforcement ratio is less than the Balanced Ratio, the section is tension-controlled. This is disregarding the fiber contribution, however, and since it is so close, the section will be assumed to be a compression-controlled section and then the assumption will be checked.

GFRP Tensile Force ---------- $T_{GFRP}(c) := A_f \cdot E_f \cdot \left(\frac{d-c}{c}\right) \cdot 0.003$

FRC Tensile Force ---------- $T_{FRC}(c) := f_{Ftu} \cdot (t_{slab} - c) \cdot b_{slab}$

Concrete Compression Force ---------- $C_{con}(c) := -0.85 \cdot f'_c \cdot \beta_1 \cdot c \cdot b_{slab}$

Assumed Neutral Axis ---------- $c := 1.5\ \textit{in}$

$c := \textbf{root}\left(T_{GFRP}(c) + T_{FRC}(c) + C_{con}(c), c\right) = 1.37\ \textit{in}$

GFRP Tensile Force ---------- $T_{GFRP} := A_f \cdot E_f \cdot \left(\frac{d-c}{c}\right) \cdot 0.003 = 46.05\ \textit{kip}$

FRC Tensile Force ---------- $T_{FRC} := f_{Ftu} \cdot (t_{slab} - c) \cdot b_{slab} = 5.99\ \textit{kip}$

Concrete Compression Force ---------- $C_{con} := -0.85 \cdot f'_c \cdot \beta_1 \cdot c \cdot b_{slab} = -52.04\ \textit{kip}$

Equivalent GFRP Reinforcing ---------- $A_{eff} := A_f \cdot \left(\frac{T_{GFRP} + T_{FRC}}{T_{GFRP}}\right) = 0.75\ \textit{in}^2$

Strain in GFRP ---------- $\varepsilon_f := \left(\frac{d-c}{c}\right) \cdot 0.003 = 0.01$

Resistance Factor ---------- $\phi := 1.55 - \frac{\varepsilon_f}{\varepsilon_{fu}} = 0.56$
(AASHTO 2.5.5.2-1)

Moment Capacity (Datum at top)

$M_r := T_{GFRP} \cdot (d) + T_{FRC} \cdot \left(t_{slab} - \left(\frac{t_{slab} - c}{2}\right)\right) - C_{con} \cdot \left(\frac{c \cdot \beta_1}{2}\right) = 28.3\ \textit{kip} \cdot \textit{ft}$

Factored Moment Capacity ---------- $\phi M_r := \phi \cdot M_r = 15.73\ \textit{kip} \cdot \textit{ft}$

Required Moment ---------- $M_u := \max\left(M_{StrIpos}, M_{StrIneg}\right) = 12.9\ \textit{kip} \cdot \textit{ft}$

$\textbf{if}\left(\phi M_r > \max\left(M_{StrIpos}, M_{StrIneg}\right), \text{“Okay”}, \text{“Check”}\right) = \text{“Okay”}$

Check Minimum Area of Reinforcement (AASHTO 2.6.3.3):

The minimum reinforcement requirements ensure that the capacity of the section exceed the cracking moment by a certain factor.

Concrete Density Modification Factor ------ $\gamma := 1.0$ (AASHTO 5.4.2.8)

Modulus of Rupture of Concrete ---------- $f_r := 0.24 \cdot \gamma \cdot \sqrt{f'_c \cdot ksi} = 0.51\ ksi$

Slab Moment of Inertia ---------- $I_{slab} := \frac{b_{slab} \cdot t_{slab}^{3}}{12} = 512\ in^4$

Distance from N.A. to Extreme Tension ---- $y := \frac{t_{slab}}{2} = 4\ in$

Section Modulus ---------- $S_c := \frac{I_{slab}}{y} = 128\ in^3$

Flexural Cracking Factor ---------- $\gamma_1 := 1.6$

Cracking Moment ---------- $M_{cr} := (\gamma_1 \cdot f_r) \cdot S_c = 8.69\ kip \cdot ft$

Stress in GFRP ---------- $f_f := \varepsilon_f \cdot E_f = 69.49\ ksi$

Minimum Reinforcement --------- $A_{min} := \frac{\frac{M_{cr}}{\phi}}{f_f \cdot \left(d - 0.5 \cdot \left(\frac{A_f \cdot f_f}{0.85 \cdot f'_c \cdot b_{slab}}\right)\right)} = 0.48\ in^2$

*The GFRP provided for flexure must exceed the minimum of 1.33*Required GFRP for Flexure, or Amin from Cracking moment:*

Required Steel for Flexure:

$$A_{freqd} := \mathbf{root}\left(\phi \cdot A_f \cdot f_f \cdot \left(d - \frac{A_f \cdot f_f}{2 \cdot 0.85 \cdot f'_c \cdot b_{slab}}\right) - M_u, A_f\right) = 0.72\ in^2$$

Minimum Reinforcement ---------- $A_{fmin} := min\left(A_{freqd}, A_{min}\right) = 0.48\ in^2$

$\mathbf{if}\left(A_{eff} > A_{fmin}, \text{“Okay”}, \text{“Check”}\right) = \text{“Okay”}$ *Therefore, the section meets the minimum GFRP requirements.*

Check Distribution Reinforcement (AASHTO 2.10.2.1):

In bridge decks, a percentage of the primary reinforcement must be provided in deck type bridges.

Required Distribution Percentage ---------- $D := min\left(\frac{220}{\sqrt{\frac{S}{ft}}}, 67\right)\% = 0.67$

Tension Force in Primary Direction --------- $P_{Tension} := T_{GFRP} + T_{FRC} = 52.04\ kip$

Net Force Required for Distribution ------ $P_{dist} := \frac{D \cdot P_{Tension}}{ft} - \left(f_{Ftu} \cdot t_{slab}\right) = 27.63\ klf$

Distribution Spacing ---------- $s_{distrequired} := \frac{f_{fu} \cdot A_b}{P_{dist}} = 13.43\ in$

Selected Spacing ---------- $s_{dist} := 13\ in$

Check Temperature and Shrinkage Reinforcement:

Assume #6 bars at 13"

Temperature and Shrinkage Bar Diameter -- $d_{bTS} := 0.75\ in$

Area of T+S GFRP ---------- $A_{bTS} := \frac{\pi \cdot {d_{bTS}}^2}{4} = 0.44\ in^2$

Ratio of T+S (AASHTO 2.9.6-1):

$$\rho_{fTS} := min\left(\max\left(\frac{3.132\ ksi \cdot ksi}{E_f \cdot f_{fu}}, 0.0014\right), 0.0036\right) = 0.0014$$

Required Area of T+S ---------- $A_{fTS} := \frac{\rho_{fTS} \cdot b_{slab} \cdot d}{ft} = 0.103\ \frac{in^2}{ft}$

Thickness of slab ---------- $t_{slab} = 8\ in$

Max T+S Spacing ---------- $s_{maxTS} := min\left(\frac{A_{bTS}}{A_{fTS}}, 3 \cdot t_{slab}, 18\ in\right) = 18\ in$

$\text{if}\left(s_{dist} < s_{maxTS}, \text{“Okay”}, \text{“Check”}\right) = \text{“Okay”}$

Check Deflections (AASHTO 2.6.3.4.2):

The Service Limit State deflections will be checked against the allowable deflections of L/800. The load is assumed to act as a uniform LL with fixed ends.

Gross Moment of Inertia ---------- $I_g := \frac{b_{slab} \cdot t_{slab}^3}{12} = 512\ in^4$

Initialize a guess for the neutral axis --------- $x := 2\ in$

Solve for the neutral axis:

$$x := \mathbf{root}\left(\frac{1}{2} \cdot b_{slab} \cdot x^2 - \frac{E_f}{E_c} \cdot A_f \cdot (d - x), x\right) = 1\ in$$

Neutral Axis ---------- $x = 1\ in$

$$I_{cr} := \frac{b_{slab} \cdot x^3}{3} + \frac{E_f}{E_c} \cdot A_f \cdot (d - x)^2 + \frac{E_f}{E_c} (A_{eff} - A_f) \cdot \left(\frac{t_{slab} - x}{2}\right)^2 = 36.35\ in^4$$

Design Service Moment ---------- $M_a := \max(M_{SIpos}, M_{SIneg}) = 7.56\ kip \cdot ft$

Distance from NA to tension ---------- $y_t := \frac{t_{slab}}{2} = 4\ in$

Cracking Moment ---------- $M_{cr} := f_r \cdot \frac{I_g}{y_t} = 5.43\ kip \cdot ft$
(AASHTO Eq. 2.6.3.4.2-2)

Variable Stiffness Factor ---------- $\gamma_d := 1.72 - 0.72 \cdot \left(\frac{M_{cr}}{M_a}\right) = 1.2$
(AASHTO Eq. 2.6.3.4.2-1)

Effective Moment of Inertia:

$$I_e := min\left(\frac{I_{cr}}{1 - \gamma_d \cdot \left(\frac{M_{cr}}{M_a}\right)^2 \cdot \left(1 - \frac{I_{cr}}{I_g}\right)}, I_g\right) = 85.85\ in^4$$

Assumed Uniform Load ---------- $w_{eq} := \max\left(M_{LLpos} \cdot \frac{24}{S^2}, M_{LLneg} \cdot \frac{12}{S^2}\right) = 1.65\ klf$

Deflection Limit ---------- $\Delta_{limit} := \frac{S}{800} = 0.15\ in$

Max Deflection ---------- $\Delta_{max} := \frac{1}{384} \cdot \frac{w_{eq} \cdot S^4}{E_c \cdot I_e} = 0.23\ in$

$\mathbf{if}(\Delta_{max} < \Delta_{limit}, \text{“Okay”}, \text{“Check”}) = \text{“Check”}$

Check Crack Widths:

This check shall ensure that the max crack is less than 0.028 in by distributing the reinforcement sufficiently.

Crack Width Limit ---------- $w_{max} := 0.028\ in$

Bond Reduction Factor ---------- $C_b := 0.83$

Design Service Moment ---------- $M_a = 7.56\ kip \cdot ft$

Ratio of Depth of NA to h ---------- $k := \frac{c}{t_{slab}} = 0.17$

Maximum Stress at Bottom ---------- $f_{max} := M_a \cdot \frac{t_{slab} - k \cdot d}{I_{cr}} = 17.34\ ksi$

Strain at Tensile Face ---------- $\varepsilon_{SLS} := \frac{f_{max}}{E_c \cdot C_b} = 0.55\%$

We will assume that the Characteristic length is equal to the distance from the N.A. to the bottom face of the deck:

N.A. to Bottom ---------- $y_{max} := t_{slab} - k \cdot d = 6.95\ in$

Strain at CMOD1 ---------- $\varepsilon_1 := \frac{0.5\ mm}{y_{max}} = 0.28\%$

Strain at CMOD3 ---------- $\varepsilon_3 := \frac{2.5\ mm}{y_{max}} = 1.42\%$

Service crack width:

$$w_{SLS} := 0.5\ mm + \frac{(2.5\ mm - 0.5\ mm)}{(\varepsilon_3 - \varepsilon_1)} (\varepsilon_{SLS} - \varepsilon_1) = 0.038\ in$$

$\text{if}\left(w_{SLS} < w_{max}, \text{“Okay”}, \text{“Check”}\right) = \text{“Check”}$

Static Flexure Fatigue Load

Design Criteria:

In this document, the fatigue level load for the simply supported bridge deck panels is determined.

Geometry:

Girder Spacing ---------- $S := 10\ ft$

Number of Widths ---------- $N := 4$

Deck Slab Thickness ---------- $t_{slab} := 8\ in$

Analysis Method ---------- "Equivalent Strip Method"

Cover distance ---------- $c_c := 1.5\ in$

Design Width ---------- $b_{slab} := 1\ ft$

Spreader Beam Width ---------- $b_{spreader} := 4\ ft$

Shear Region Width ---------- $b_{shear} := \frac{\langle S - b_{spreader} \rangle}{2} = 3\ ft$

AASHTO Factors:

The AASHTO LRFD Design Code requires a dynamic load allowance and multiple presence factor. The service level factors must be scaled to the fatigue level load.

Service - Dynamic Load Allowance --------- $IM_{service} := 1.33$ (Table 3.5.2.1-1)

Fatigue - Dynamic Load Allowance --------- $IM_{fatigue} := 1.15$

Service - Multiple Presence Factor ---------- $m_{service} := 1.2$ (Table 3.6.1.1.2-1)

Fatigue - Multiple Presence Factor ---------- $m_{fatigue} := 1.0$

AASHTO Live Load Moment:

Using the Equivalent Strip Method, under certain conditions, the designer can interpolate from Table A4-1 in Appendix A4 to find the live load negative and positive moment for the bridge deck. This includes a multiple presence factor of 1.2 and a dynamic load allowance of 1.33, so to get the fatigue load that must be applied to the bridge deck, these loads must

be scaled accordingly.

Positive Live Load Moment ---------- $M_{positive} := 6.89\ kip \cdot ft$

Negative Live Load Moment ---------- $M_{negative} := 4.25\ kip \cdot ft$

Fatigue Positive Live Load Moment:

$$M_{fatiguepos} := M_{positive} \cdot \frac{m_{fatigue}}{m_{service}} \cdot \frac{IM_{fatigue}}{IM_{service}} = 4.96\ kip \cdot ft$$

Fatigue Negative Live Load Moment:

$$M_{fatigueneg} := M_{negative} \cdot \frac{m_{fatigue}}{m_{service}} \cdot \frac{IM_{fatigue}}{IM_{service}} = 3.06\ kip \cdot ft$$

Maximum Fatigue Moment:

$$M_{fatigue} := \max\left(M_{fatiguepos}, M_{fatigueneg}\right) = 4.96\ kip \cdot ft$$

Required Maximum Fatigue Force ---------- $P_{Req} := N \cdot \frac{M_{fatigue} \cdot 2}{b_{shear}} = 13.24\ kip$

Therefore, to impose a fatigue level moment in the 4 ft (1.3 m) uniform moment region, a maximum applied load of 13.24 kip (58.9 kN) must be applied to the spreader beam. A minimum fatigue load of 10% will be used to maintain sufficient contact between the ram and the set-up.

Required Minimum Fatigue Force ---------- $P_{min} := P_{Req} \cdot 10\% = 1.32\ kip$

APPENDIX B. MOMENT CURVATURE PROGRAM SCRIPT

Figure , shows the opening page of the program. Figure B- shows the page to input the geometric properties of the section such as bar size, spacing, and width/depth of the section. Figure B- shows the steel-reinforced section moment-curvature GUI, Figure B- shows the GFRP-reinforced section moment-curvature GUI, and Figure B- shows the HRC section moment curvature GUI.

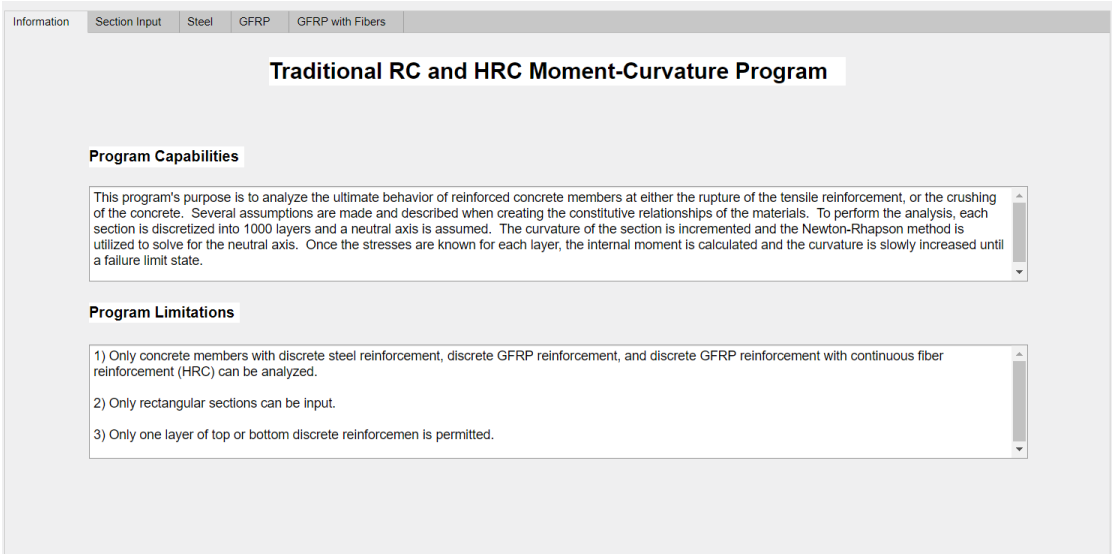

Figure B-1 Introduction page of moment-curvature program

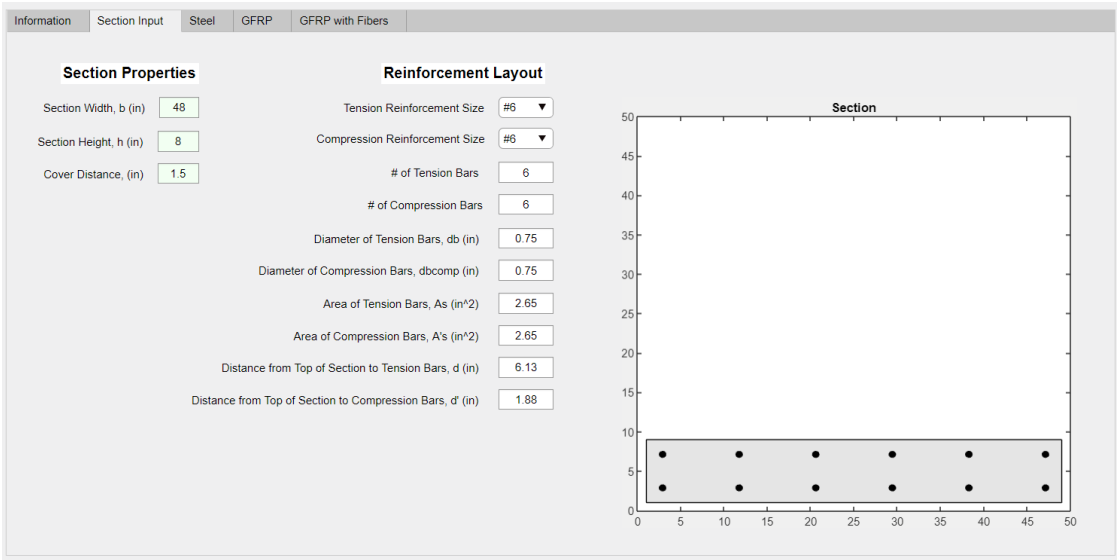

Figure B-2 Sectional input

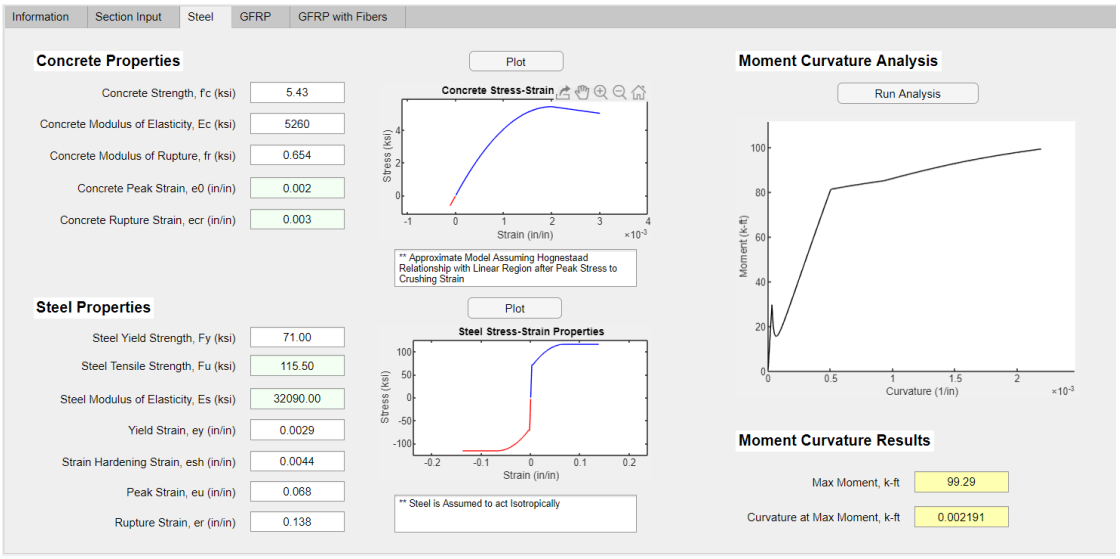

Figure B-3 Steel reinforced moment-curvature analysis

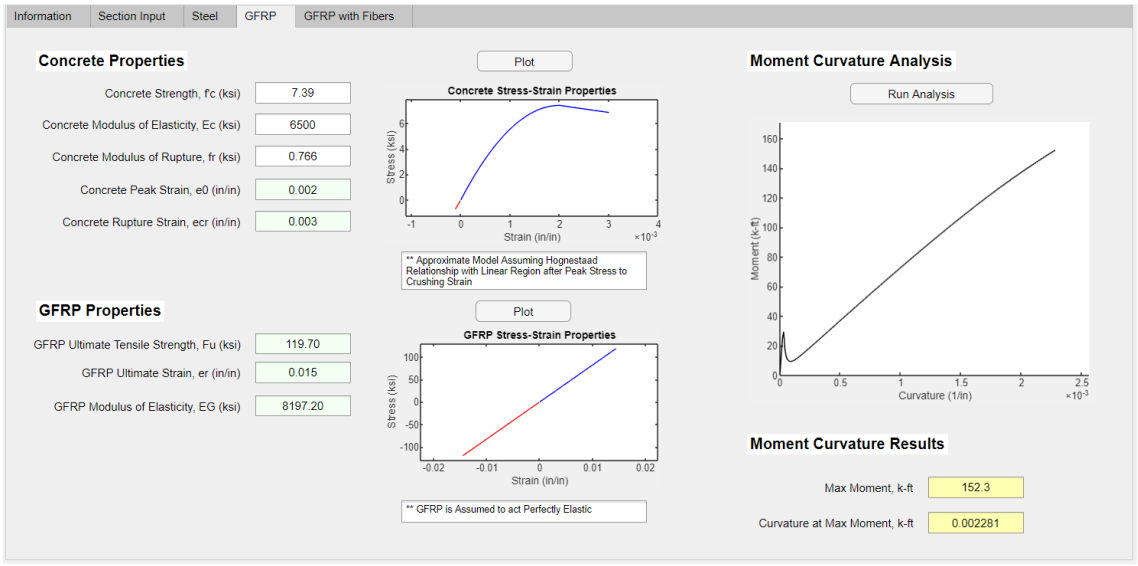

Figure B-4 GFRP reinforced moment-curvature analysis

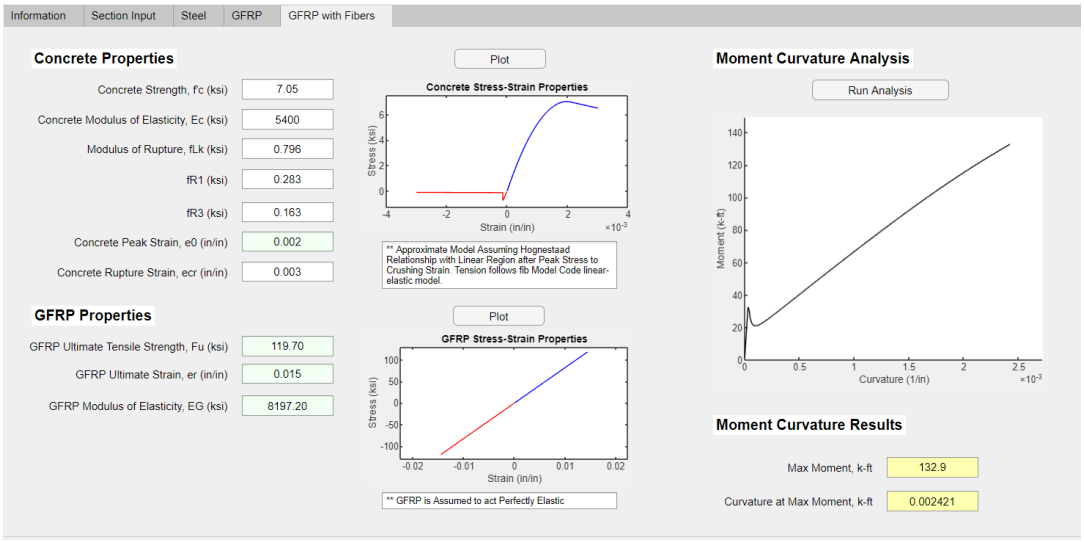

Figure B-5 HRC moment-curvature analysis

An example script for the HRC section moment-curvature iteration script is given below:

```
% Button pushed function: HRC_RunAnalysisButton
function HRC_RunAnalysisButtonPushed(app, event)
 % Guess Neutral Axis Location
 cguess = 1.5;
 % Discretize Element into layers
 Layers = (1:1000);
 NumLayers = numel(Layers);
 % Find Layer Locations
 Location = (0:app.h.Value/(Layers(end)-1):app.h.Value);
 LayerHeight = Location(2);
 % Find Layer Areas where top and bottom layers are 1/2 of mid
 % layers.
 LayerArea = zeros(1,NumLayers);
 LayerArea(2:NumLayers-1) = app.b.Value*LayerHeight;
 LayerArea(1,NumLayers) = app.b.Value*LayerHeight/2;
 LayerArea(1,1) = app.b.Value*LayerHeight/2;
 % Call Rebar Areas from app.SectionProperties tab.
 RebarArea = [app.AComp.Value app.ATension.Value];
 % Initialize Curvature vector and increments
 curvature = 0.000001:0.00001:0.1;
 Ncurvature = numel(curvature);
 M = zeros(1,Ncurvature);
 for j = 1:Ncurvature
 c = cguess;
 % Call Rebar Locations from app.SectionProperties tab.
 RebarLocation = [app.dcomp.Value app.d.Value];
 % Initialize sum of forces and counter
 F = 1;
 k = 1;
 m = 0.01;
 % Set Tolerance for Error
```

```
   tol = 0.001;
   %Perform Newton-Rhapson Method to Converge on Neutral Axis
   while abs(F) > tol
    if c <0 || c>app.h.Value
     % Ensure convergence by starting from a different
     % location on beam.
     c = 0+m;
     m = m+0.01;
    end
    LayerStrain = (c-Location)*curvature(j);
    RebarStrain = (c-RebarLocation)*curvature(j);
    LayerStress =
HRCConcreteStress(app,LayerStrain,app.HRC_ConcreteStrength.Value,app.HRC_Concrete
Modulus.Value,app.HRC_MOR.Value,app.HRC_e0.Value,app.HRC_ecr.Value,
app.HRC_fR1.Value,app.HRC_fR3.Value);
    RebarStress =
(GFRPStress(app,RebarStrain,app.HRC_Fu.Value,app.HRC_EG.Value,app.HRC_er.Value));
    % Find f(x0)
    F = dot(LayerStress,LayerArea)+dot(RebarStress,RebarArea);
    % Make a small change in x0
    c = c*1.01;
    % Find f(x0 + Increment)
    LayerStrain = (c-Location)*curvature(j);
    RebarStrain = (c-RebarLocation)*curvature(j);
    LayerStress =
HRCConcreteStress(app,LayerStrain,app.HRC_ConcreteStrength.Value,app.HRC_Concrete
Modulus.Value,app.HRC_MOR.Value,app.HRC_e0.Value,app.HRC_ecr.Value,
app.HRC_fR1.Value,app.HRC_fR3.Value);
    RebarStress =
(GFRPStress(app,RebarStrain,app.HRC_Fu.Value,app.HRC_EG.Value,app.HRC_er.Value));
    FF = dot(LayerStress,LayerArea)+dot(RebarStress,RebarArea);
    % dFdc = f'(x0) = (f(x0+Increment)-f(x0))/(Increment)
    dFdc = (FF-F)/(c-(c/1.01));
    % Change from (x0 + Increment) back to x0
    c = c/1.01;
    % x0 = x0 + f(x0)/f'(x0)
    c = c-F/dFdc;
    % Find new Force to check convergence
    LayerStrain = (c-Location)*curvature(j);
    RebarStrain = (c-RebarLocation)*curvature(j);
    LayerStress =
HRCConcreteStress(app,LayerStrain,app.HRC_ConcreteStrength.Value,app.HRC_Concrete
Modulus.Value,app.HRC_MOR.Value,app.HRC_e0.Value,app.HRC_ecr.Value,
app.HRC_fR1.Value,app.HRC_fR3.Value);
    RebarStress =
(GFRPStress(app,RebarStrain,app.HRC_Fu.Value,app.HRC_EG.Value,app.HRC_er.Value));
    F = dot(LayerStress,LayerArea)+dot(RebarStress,RebarArea);
    if F == 0
     F = 1;
    end
    % Exit Loop if no Convergence is achieved
    k = k+1;
```

```
    if k > 1000
     break
    else
     % Nothing
    end
   end
   % Find Forces for the final time for curvature(j)
   LayerStrain = (c-Location)*curvature(j);
   RebarStrain = (c-RebarLocation)*curvature(j);
   LayerStress =
HRCConcreteStress(app,LayerStrain,app.HRC_ConcreteStrength.Value,app.HRC_Concrete
Modulus.Value,app.HRC_MOR.Value,app.HRC_e0.Value,app.HRC_ecr.Value,
app.HRC_fR1.Value,app.HRC_fR3.Value);
   RebarStress =
(GFRPStress(app,RebarStrain,app.HRC_Fu.Value,app.HRC_EG.Value,app.HRC_er.Value));
   LayerForce = LayerStress.*LayerArea;
   RebarForce = RebarStress.*RebarArea;
   %Find Moment Capacity at each Incremental Curvature and Convert
   %to k-ft
   M(j) = abs((dot(Location,LayerForce)+dot(RebarLocation,RebarForce))*(1/12));
   if LayerStrain(1) >= app.HRC_ecr.Value || RebarForce(2) == 0
    % If Concrete Crushing strain is exceeded or the bottom bar ruptures, only
the
    % previous Moments and curvatures are taken and the curvature
    % loop is exited.
    M = M(1:j-1);
    curv = curvature(1:j-1);
    break
   end
   end
   %Plot the Moment-Curvature Diagram
   plot(app.HRC_MomentCurvatureFigure,curv,M,'k');
   xlim(app.HRC_MomentCurvatureFigure,[0 curv(end)+curv(end)/8]);
   ylim(app.HRC_MomentCurvatureFigure,[0 M(end)+M(end)/8]);
   % Output max Moment and Curvature
   [app.HRC_MaxMoment.Value, Index] = max(M);
   app.HRC_MaxCurvature.Value = curv(Index);
   app.HRC_MaxMomentValueChanged
   app.HRC_MaxCurvatureValueChanged
  end
```

APPENDIX C. PRELIMINARY COST ANALYSIS

The numbers in this section are highly dependent upon the supplier used and some variability in labor/material costs and other factors. This is meant to provide an approximate cost and demonstrate a quick method to calculate the costs of the different bridge deck types per square foot. The reader should not rely on these numbers, but they give an idea of the costs. Table C- gives upper and lower bounds for each reinforcing material used in this project. The figures are pulled from several documents and reports, as explained in the bottom of Table C-. Included into these costs are figures for installation and labor.

Table C-1 Unit costs of reinforcing materials

Material	Lower Bound Cost	Upper Bound Cost
Plain Steel	$0.94/lb	$1.48/lb
Epoxy Coated Steel	$1.34/lb	$1.68/lb
GFRP	$1.47/ft	$1.94/ft
Macrofibers	$5/lb	$7/lb
The lower bounds for the steel are from an Engineering News Record (ENR) from 2018. The upper bound for steel and lower bound for GFRP are from figures from FHWA in 2013. The upper bound for GFRP comes from a FDOT report in 2016.		

The steel reinforcement is quoted in dollars/lb., whereas the GFRP reinforcement is quoted in dollars/foot. By calculating the number of bars for each bridge deck type and figuring the cost per square foot, the relative cost of these reinforcement strategies used in this project can be estimated. Table C- gives the upper and lower bound costs of each deck reinforcement strategy, based on the pricing information given.

Table C-2 Cost per square foot for each reinforcement scheme

Material	Transverse Reinforcement	Dist. Reinforcement	Lower Bound $/sf	Upper Bound $/sf
Plain Steel	#5 @ 6” o.c.	#5 @ 8”	$6.86	$10.81
Epoxy Coated Steel	#5 @ 6” o.c.	#5 @ 6” o.c.	$9.78	$12.27
GFRP	#6 @ 6” o.c.	#6 @ 9” o.c.	$9.80	$11.47
HRC (15 lb/cy)	#6 @ 8” o.c.	#6 @ 13” o.c.	$8.97	$11.99

As shown in Table C-, the HRC decks have the least expensive lower bound, except for the plain steel rebar. Therefore, although these figures are just a rough comparison, it is clearly shown that by adding fibers, the cost of GFRP decks can be reduced and become more economically viable depending on the cost of the fibers. More cost analysis would need to be performed during the concept design phase, but preliminary analysis suggests that HRC decks are cost neutral to epoxy coated rebar.

One key aspect that has not been considered herein is the increase in cost due to the addition of fibers. Only the material costs have been included in this brief analysis. Perhaps the cost of super-plasticizer and labor would offset the savings, but this would need to be further researched and examined.